SENSORLESS CONTROL FOR SWITCHED RELUCTANCE MOTOR DRIVES

A THESIS

SUBMITTED TO

THE DEPARTMENT OF ELECTRONICS AND ELECTRICAL ENGINEERING

OF

THE UNIVERSITY OF GLASGOW

FOR THE DEGREE OF

DOCTOR OF PHILOSOPHY

By

Gabriel Gallegos López

November 1998

ProQuest LLC.
789 East Eisenhower Parkway
P.O. Box 1346
Ann Arbor, MI 48106 – 1346

Abstract

The thesis presents the work carried out on two methods for indirect sensing of the rotor position in switched reluctance motors.

In the first method, PWM voltage control is used to control the motor. The method, called *current gradient sensorless method*, uses the change of the derivative of the phase current to detect the position where a rotor pole and stator pole start to overlap, giving one position update per energy conversion stroke. As no *a priori* knowledge of motor parameters is required (except for the numbers of stator and rotor poles), the method is applicable to most switched reluctance motor topologies in a wide power and speed range and for several inverter topologies. A single current sensor and detection stage is enough to drive a multiphase SRM. To start up the motor a feedforward method is used which assures robust start-up from stand-still up to a minimum speed even under load. The method is comparable to the back-EMF position estimation for brushless DC motors in performance and cost. The major contributions to the *current gradient sensorless method* are its real-time implementation, its experimental test and the reduction of current sensors and detection stages from three to one.

The second method proposes a principle of high resolution sensorless position estimation for a switched reluctance motor drive, using either flux linkage or current to correct for errors in rotor position. The estimation algorithm makes full use of the non-linear magnetic characteristics of the SRM through correlation of current, flux linkage and rotor position. The estimation model is simple, but with no loss in accuracy, leading to few real-time computations. Furthermore, a criterion is proposed to choose the

phase most suited for position estimation when more than one phase conducts. The algorithm can also predict flux linkage, which in turn may be used to correct the position estimate further, and the features of this are discussed. The major contributions to this algorithm are the use of a simpler model for the observer, the introduction of a novel method to estimate the rotor position form the best phase from all conducting phases, and the experimental validation of the algorithm.

Simulation and experimental results, which include steady-state with and without load, and dynamic transient tests, are presented, and confirm the concept and the robust functionality of both methods. The detailed operation and real-time implementation of both methods are described. However, it should be noted that these methods present advantages and disadvantages as other methods proposed before in the literature. Therefore, it is fair to say that these methods cannot replace in fully the mechanical sensor such as encoder or resolver, however they can offer a simpler and a better way than previous methods to estimate the rotor position.

A second topic covered in this thesis is a functionality study of the classic switched reluctance motor inverter utilising a resonant dc-link to provide current regulation with zero-voltage switching. Although this topic is not directly related to the major part of the thesis on sensorless control, it is important in the wider study of power electronic converters for SR machines, and could form the basis for extended research in the combination of soft switching and sensorless control.

Contents

Acknowledgements

Thanks to my supervisor Professor Timothy J.E. Miller for his advice and guidance during my PhD studies. Special thanks to Dr. Philip Kjær and Mr. Calum Cossar for their technical support and sharing ideas through many productive discussions.

I gratefully acknowledge the financial support for my PhD studies given by Consejo Nacional de Ciencia y Tecnología México (CONACyT). I would like to acknowledge the Department of Electronics and Electrical Engineering of University of Glasgow and specially to the *SPEED* consortium for the facilities provided.

Many thanks to Dr. Jeremy Gribble for his helpful feedback and positive discussions on this thesis. I also want to thank Mr. Ian Young, Mr. Peter Miller and Mr Jimmy Kelly for their support and help in the hardware and test equipment. On the software side, I would like to thank Mr. Malcolm McGilp for his support. Thanks to my friends and all my colleagues, former and present, in the *SPEED* team for their permanent help. Special thanks to Mr. Tadashi Sawata and Miss Marielle Piron for their constant support and many interesting discussions.

Special acknowledges to my parents Timoteo and Esther, my aunt Clara and all my family in México for their support and motivation over the years. Finally, I would like to thank, *mi amor*, Elena for her understanding.

List of Figures

List of Tables

List of Symbols

$\hat{}$	Superscript indicating estimated value	
$_b$	Subscript indicating value at θ_b	
$_{b-}$	Subscript indicating value just before θ_b	
$_{b+}$	Subscript indicating value just after θ_b	
$_o$	Subscript indicating value at θ_o	
$_{o-}$	Subscript indicating value just before θ_o	
$_{o+}$	Subscript indicating value just after θ_o	
α	Phase displacement	[rad]
θ	Rotor Position in mechanical degrees	[^{o} mech.]
θ_a	Aligned position	[^{o} mech.]
θ_{actual}	True value of rotor position	[^{o} mech.]
θ_b	Rotor position overlap	[^{o} mech.]
θ_e	Estimated rotor position	[^{o} mech.]
θ_{elec}	Rotor position in electrical degrees	[^{o} mech.]
θ_m	Measured rotor position	[^{o} mech.]
θ_o	Rotor position overlap	[^{o} mech.]
θ_{off}	Turn off angle	[^{o} mech.]
θ_{og}	Mechanical rotor position overlap	[^{o} mech.]
θ_{om}	Magnetic rotor position overlap	[^{o} mech.]

θ_{on}	Turn on angle	[^{o} mech.]
θ_p	Predicted rotor position	[^{o} mech.]
θ_{pitch}	Rotor pitch	[^{o} mech.]
θ_r, θ_{ref}	Reference rotor position	[^{o} mech.]
θ_{stroke}	Stroke angle	[^{o} mech.]
θ_u	Unaligned position	[^{o} mech.]
σ	resolution	[^{o} mech.]
ω	Angular speed	[rad/s]
ω_1	Angular speed before acceleration	[rad/s]
ψ	Flux linkage	[V-s]
ψ_{actual}	True value of flux linkage	[^{o} mech.]
ψ_c	Corrected flux linkage	[V-s]
ψ_e	Estimated flux linkage	[V-s]
ψ_{ex}	Expected flux linkage	[V-s]
ψ_{error}	Error in flux linkage, $\psi_p - \psi_{actual}$	[V-s]
ψ_i	Calculated flux linkage	[V-s]
ψ_m	Measured flux linkage	[V-s]
ψ_{ml}	Mutual flux linkage	[V-s]
ψ_{old}	Previous flux linkage	[V-s]
ψ_p	Predicted flux linkage	[V-s]
ψ_r, ψ_{ref}	Reference flux linkage	[V-s]
$\Delta\theta$	Increment in rotor position	[^{o} mech.]
$\Delta\theta$	Error in rotor position, $\theta_{actual} - \theta_e$	[^{o} mech.]
$\Delta\theta_b$	Increment in rotor position of *the best phase*	[^{o} mech.]
$\Delta\theta_g$	The difference between $\hat{\theta}_{om} - \hat{\theta}_{og}$	[^{o} mech.]

$\Delta\theta_m$	The difference between $\hat{\theta}_{om} - \hat{\theta}_{om}$	[° mech.]
$\Delta\psi$	Increment in flux linkage	[V-s]
Δi, ΔI	Increment in current	[A]
ΔT	Time step	[s]
$\Delta W'$	Increment in coenergy	[J]
a	zero in PI controller	
A/D	Analog-digital	
A, B, C, D	Motor phases	
AC	Alternate current	
ACRDCL	Active clamp resonant dc-link	
ACRDCL-SR	Active clamp resonant dc-link switched reluctance	
B	Viscous damping	[Nm·rads]
BJT	Bipolar Junction Transistor	
BW	Band Width	
c	Integer constant	
C	Capacitor	[F]
C_c	Clamp capacitor	[F]
C_{dump}	Dump capacitor	[F]
C_r	Resonant capacitor	[F]
CGPE	Current gradient position estimation	
CGSM	Current gradient sensorless method	
D	Duty cycle	[%]
D	Diode	
D_c	Clamp diode	
D_{dc}	Diode in the dc-link	

D_h	Duty cycle for hard chopping	[%]
D_s	Duty cycle for soft chopping	[%]
D_{sup}	Suppression diode	
D_{zener}	Zener diode	
D/A	Digital-analog	
DC	Direct current	
DMA	Direct memory access	
DP	Decoded pulses	
DPM	Discrete Pulse Modulation	
DSP	Digital signal processor	
e	Back-EMF	[V]
e	Control error	
$Enable\ on\ S_{dc}$	Enable on signal for S_{dc}	
$Enable\ on\ S_c$	Enable on signal for S_c	
$Enable\ off\ S_c$	Enable off signal for S_c	
EMF	Electromotive force	
EMI	Electromagnetic interference	
f_{mod}	Modulation frequency	[Hz]
f_r	Resonant frequency	[Hz]
f_s	Sampling frequency	[Hz]
f_{sw}	Switching frequency	[Hz]
F	Constant factor	
F	Counter frequency of the commutation stage	[Hz]
F_θ	Position vector gain	
F_ψ	Flux linkage matrix gain	
F_ω	Speed matrix gain	
FE	Finite element	

FPGA	Field Programmable Gate Array	
G	Inverse inductance function	
$G_{S_{dc}}$	Gate signal for S_{dc}	
G_{S_c}	Gate signal for S_c	
GTO	Gate turn off thyristor	
H	Inverse inductance function	[1/H]
HS	Hard swiching	
i	Phase current	[A]
i_{active}	Current in active phase	[A]
i_b, i_e, i_m	Sampling current values	[A]
i_{bus}	Current in the lower transistor bus	[A]
i_e	Estimated current	[A]
i_{load}, I_o	Load current	[A]
i_m	Measured current	[A]
i_{peak}	Peak current of probing pulses	[A]
i_{ref}	Resonant current reference	[A]
i_{rf}	Current reference	[A]
i_{sw}	Current in the switching transition	[A]
i_{L_r}	Resonant inductor current	[A]
I	Current	[A]
I_c	Clamp diode current	[A]
I_{clamp}	Clamp current	[A]
I_{curve}	Current function	[A]
I_m	The difference between $i_{L_r} - i_{load}$	[A]
I_{max}	Maximum rated current	[A]
I/O	Input-output	
IC	Integrated circuit	

IGBT	Isolated gate bipolar transistor	
INT0	External DSP interrupt	
J	System moment of inertia	[kg·m^2]
k	Weighting factor	
K	Clamp constant	
K	Control gain	
K_i	Integral control gain	
K_p	Proportional control gain	
K_I	Integral control gain equal to $K_i \cdot T_s$	
l	Incremental phase inductance	[H]
L	Phase inductance	[H]
L	Inductor	[H]
L_{ao}	Unsaturated aligned inductance	[H]
L_{dump}	Dump inductor	
L_r	Resonant inductor	[H]
L_{ref}	Reference inductance	[H]
L_u	Unaligned inductance	[H]
LC	Inductor-capacitor circuit	
m	Integer factor	
MC	Microcontroller	
MFLOPS	Million floating-point instructions per second	
MIPS	Million instructions per second	
MOSFET	Metal oxide semiconductor field-effect transistor	
n	Number of conducting phases	

N	Number of phases	
N_r	Number of rotor poles	
N_s	Number of stator poles	
OD, ID	Outer, Inner Diameter	
OPAM	Operational amplifier	
p	Number of poles per phase	
P_c	Conduction power losses	[W]
P_{new}	New position variable	
P_{old}	Previous position variable	
P_{sw}	Switching power losses	[W]
P_t	Average power semiconductor dissipation	[W]
PI	Control signal	
PI	Proportional Integral control	
PIT	Periodic microcontroller interrupt	
PLL	Phase locked loop	
PM	Permanent magnet	
PWM	Pulse Width Modulation	
Q	Switch	
r	Current ripple	[%]
R	Phase resistance	[Ω]
R	Resistor in commutation delay circuit	[Ω]
R_{ESR}	Equivalent system resistance	[Ω]
R_{on}	On device resistance	[Ω]
R_{sup}	Suppression resistance	
R_{JA}	Thermal resistance	[°C/W]

RAM	Random access memory	
RDCL	Resonant dc-link	
RL	Resistance-inductor circuit	
RLC	Resistance-inductor-capacitor circuit	
S	Switch	
S_{dc}	Switch in the dc-link	
SOA	Switch Operating Area	
SR	Switched reluctance	
SRDL	Switched Reluctance Drives ltd	
SRM	Switched reluctance motor	
SS	Soft switching	
t	Time	[s]
t_1, t_2, t_3	Time windows and timer values of microcontroller	[s]
t_{fall}	Fall time	[s]
t_{on}	Conduction time	[s]
t_{rise}	Rise time	[s]
t_{toff}	Transition turn off time	[s]
t_{ton}	Transition turn on time	[s]
T	Torque	[Nm]
T_{avg}	Average torque	[Nm]
T_f	Frictional load torque	[Nm]
T_s	Sampling time	[s]
T_{sw}	Switching period	[s]
T_A	Ambient temperature	[^{o}C]
T_J	Junction temperature	[^{o}C]
UART	Asynchronous communication element	

v, v_{ph}	Phase voltage	[V]
v	Injected voltage signal	[V]
v_{ind}	Induced voltage	[V]
V	Voltage	[V]
V_{clamp}	Clamp voltage	[V]
V_d	Voltage drop in a diode	[V]
V_{dc}	Voltage in the dc-link	[V]
V_{drp}, v_{drop}	Condution voltage drop	[V]
V_{ref}	Reference voltage	[V]
V_{res}	Resonant voltage	[V]
V_{supply}	Supply voltage	[V]
V_t	Voltage drop in a switch	[V]
V_z	Zero voltage period	
V_{D_z}	Voltage in the zener diode	[V]
VA	Volts-Amperes	
VMSM	Voltage magnitude sensorless method	
W'	Coenergy	[J]
W_f	Stored magnetic field energy	[J]
W_{on}	Conduction losses	[J]
W_{toff}	Turn off energy losses	[J]
W_{ton}	Turn on energy losses	[J]
z^{-1}	Delay of one sample period	
Z_o	Resonant tank impedance	[Ω]
ZCS	Zero current switching	
ZVS	Zero voltage switching	

Chapter 1

Introduction

This chapter gives a brief review of SRM technology and identifies its main advantages and drawbacks. A review of mechanical position sensors used for switched reluctance motors is also given. The project motivation, objectives, and original thesis contribution are presented. Finally the content of each chapter is described.

This thesis presents research carried out on sensorless control for switched reluctance motor (SRM) drives [1]. Two new sensorless methods have been developed, implemented and tested experimentally.

The aim of the first sensorless method is to detect the rotor position electronically in a simple way in order to minimize the implementation cost, while keeping reasonable performance of the drive itself. In other words, the method is able to estimate the rotor position in applications that do not require high "dynamic" performance (4-quadrant). The second sensorless method detects the rotor position based on either current or flux linkage using an observer machine model. The aim of this method is to achieve high resolution of rotor position in order to maximize the performance of the drive regardless of cost, which means that robustness and high dynamic performance are of high priority.

[1] The elimination of the mechanical position sensor by an electronic method is known as *sensorless control.*

It is worthy to note that the thesis also includes an Appendix on soft switching (SS), i.e. the design and implementation of a resonant dc-link converter. This research was done in the first year of the PhD studies as an introductory project with the aim of getting good insight of the switched reluctance motor technology. Although this is not part of the logical development of the sensorless control, it represents an important part of the wider study of power electronic converter for SRM's, and if soft-switched converters are applied to the SRM the sensorless control methods would need to be extended. Appendix A therefore could contribute a basis for extended research going beyond the scope of the current thesis. Soft switching is a well known technique to reduce switching losses in power converters which has been applied to high efficiency AC drives and static energy control. However little work has been done on the application of soft switching to switched reluctance motors. The Appendix A describes the investigation of the functionality of a SRM converter using a front-end resonant dc-link to provide current regulation with zero-voltage switching. Simulated and experimental results are presented. Note that the Sensorless control of SRM project was started by the end of the first year of the PhD studies.

1.1 Background

The principle of the switched reluctance motor was introduced many years ago, however, the boom in its development started around 25 years ago with the rapid growth of power electronics devices and microcontroller technologies. The SRM drive, as other motor technologies, has benefited enormously from advances over the years in solid-state switching devices, such as diodes and transistors. This has opened the window to control the SRM drive electronically and more efficiently.

Nasar [1] published an early paper in 1969, which studies the performance of an axial single phase step gap SRM and this is the first instance of the term "switched reluctance motor". Patents [2, 3], by Bedford, describe a regular and step gap motor together with the commutation inverter. Harris introduced expressions to approximate the torque

capability of the saturated doubly-salient motor [4] in 1974. In 1984, Miller presented a detailed and interesting analysis of the converter volt-ampere requirements of the SRM [5]. In the 80's, the commercial potential of the SRM was developed by Lawrenson [6, 7] at the University of Leeds, who reported the interesting design and performance of a SRM for traction application, and claimed advantages such as robustness, cheapness, inverter with one switch per phase, simple to control, high efficiency over the whole torque-speed characteristic, magnetic and electric phase independence, and therefore, fault tolerant. Later the SRDL company was formed and led to a range of commercial applications of SRM technology in the range of 100W up to over 300kW. One of the best known SRDL designs is the 4-phase Oulton motor produced by TASC drives introduced in 1983. In 1995, SRDL became part of Emerson, and in 1997 the first washing machine driven by a SRM was introduced by Maytag in the USA.

Two commercial applications areas of the SRM drive have been mainly explored during the last two decades. The first is the low cost applications where the primary priority is cost of the overall system. SRDL has pushed this market strongly and licensed various commercial products, for instance, the electronic door-opener manufactured by Besam. The other market which seems very promising is aircraft applications, where the robustness of the drive itself is very important. GE, Sundstrand, Allied Signal and Lucas are leading the research in this area, where actuators, pumps, starter/generators and generators have been investigated. Robustness and fault tolerance play an important role in this market due to the harsh environment where the motor is operated. Research and development of the design of a 30kW SR starter/generator is presented by Ferreira *et al* in [8]. A design for a multi channel switched reluctance generator of 250kW is described in [9, 10] by Richter and Ferreira.

1.2 Why Switched Reluctance Motors: Advantages and drawbacks

The variable speed drive market continually demands more and more efficient and cheaper drives, while keeping their robustness, and low price production and maintenance. Energy saving and quality of motion control are the first priorities in most variable speed applications. The motivation to use switched reluctance motors in variable speed applications is that the overall drive cost may be commercially attractive compared with the AC and DC systems. In other words, the saving on the switched reluctance motor production itself should compensate the power electronics required to drive it. One trend in the drives industry is the integration of the motor, power electronics, control system and load in a single unit. With low cost power electronics and more compact integrated control electronics, the switched reluctance motor is becoming a serious contender with potential to compete with AC and DC systems.

SRM technology is not as well established as AC or DC machines, however, it has inherent advantages which make it very attractive. The main advantages are:

- High efficiency.
- Robustness.
- No permanent magnets.
- Simple construction.
- Suitable for high speeds.
- Good thermal properties.
- Low core losses.
- Easy access for cooling.
- Fault tolerant.

- High torque-speed range.
- High torque/inertia ratio.
- Low maintenance.

On the other hand its main drawbacks are:

- Tendency to be noisy i.e. acoustic noise.
- Inherent torque ripple.
- Needs rotor position feedback.
- High copper losses.
- High number of leads connecting inverter and motor.
- Its controller is unique, and complex for high efficiency drives.

It has been claimed in the literature that the switched reluctance drive can perform the same job equally well or better than the AC or DC machines. However, its drawbacks have not been fully overcome, and therefore, the introduction of the SRM technology in the commercial market has been limited. The strong advantages that the SRM drive can offer have been the main motivation of engineers in academia and industry to develop design and control techniques for reduction of the SRM's drawbacks. This has given rise to a number of patents and papers that are available in the literature.

Noise

The switched reluctance motor tends to present higher levels of acoustic noise than other motor technologies. Varies researchers have investigated the source of noise of the SRM and its possible cures. The first study of acoustic noise of the SRM was carried out by Cameron *et al* [11]. Through a series of experiments, they concluded that the main

source of acoustic noise is stator ovalisation due to the magnetic attraction between stator and rotor poles, and they proposed to introduce dither in the commutation angles in order to reduce the noise generation. Wu and Pollock made further investigation, and proposed a simple, but effective technique to reduce acoustic noise. They identified that the commutation turn off angle generated higher noise level than the turn on angle, and proposed to turn off the phase in two stages by introducing a zero voltage loop [12] or three stages by a turning off-on-off sequence [13]. Michaelides and Pollock generalised the previous method and proposed to turn off the phase in two stages but this time by introducing an average negative voltage between the voltage before commutation and the negative power supply voltage [14]. An analysis of vibration and acoustic noise by finite element analysis was carried out by Colby *et al* [15]. They proposed a formula to approximate the fundamental vibration frequency, and gave an interesting guide to motor design considerations for acoustic noise reduction.

Torque ripple

Higher torque ripple compared to other motor technologies is a significant disadvantage of switched reluctance motors. To overcome this drawback, several methods have been proposed in the literature. The basic principle of these methods is based on torque sharing between two phases and current profile. The instantaneous torque concept was introduced by Spong *et al* [16]. They developed the fundamental principle of instantaneous torque control, and suggested current profiling for reduction of torque ripple. Further work was carried out by Wallace and Taylor [17, 18], who analysed the design consideration of the pole arc for torque ripple minimisation, and they defined a critical commutation angle where two consecutive phases produce the same torque at constant current. Filicori *et al* [19] made use of torque sharing waveforms and suggested two optimization criteria, minimum copper losses, and minimum motor-feeding voltage. Husain and Ehsani [20] proposed the use of simple contour function, such that zero torque ripple is obtained in the period of excitation overlap. An example

of reducing the torque ripple and minimising the required voltage magnitude is presented by Stankovic [21]. Kjaer *et al* [22] demonstrated that the criterion of both minimum copper losses (low speed range) and minimum motor-feeding voltage (high speed range) for low torque ripple have to be combined to cover and enhance the torque speed characteristic.

1.3 Why is Sensorless Control of Switched Reluctance Motors desired?

Proper control of the switched reluctance motor requires careful commutation of phases synchronised with rotor position. Usually the rotor position is obtained from a mechanical position sensor coupled to the motor shaft. However, recently there has been enormous interest in eliminating the mechanical rotor sensors mainly for two reasons:

Reduction of the SRM drive cost: The mechanical sensor may be a significant part of the overall system cost in those cost-sensitive applications for fractional-kW power drives. The size of the mechanical sensor and number of leads required also play an important role in this kind of applications, where the resolution required of the rotor position sensor is low.

Operation of the SRM in harsh environment: In applications where the motor is operated in extreme environmental conditions, such as, high pressure, temperature, humidity and extremely high speeds, the use of a mechanical sensor may lead to reliability problems. Usually, a high resolution of rotor position is necessary for this kind of application.

Other factors that motivate the elimination of the mechanical sensors are: reduction of maintenance, increase of robustness, and the need of proper and robust mechanical mounting of the mechanical sensor.

Several sensorless methods have been proposed in the literature, and an extensive review of these methods is given in Chapter 3. Most of the methods use the magnetic characteristic of the SRM in one way or another to estimate the rotor position. However there is, as yet, no single sensorless method that can replace fully the mechanical sensor. Therefore, it is evident that there is a need for new sensorless methods or combinations of them to cover the whole torque-speed characteristic of the switched reluctance motor.

The aim of this thesis is the investigation and study of new sensorless methods for low-cost applications and high resolution applications. These methods are fully explained in Chapters 4 and 5.

1.3.1 Review of methods with mechanical position sensor

To obtain direct rotor position information, there are basically four methods which are briefly explained as follows:

Opto-interrupter with slotted disk: This simple method has been proposed in the literature by several researchers [23, 24, 25, 26, 27]. A slotted disk is mounted in the rotor shaft, and the opto-interrupters are placed in specific angular positions from the reference position. As the disk rotates, the opto-interrupters generate directly the commutation signal for each phase. Forward, reverse and braking operation with fixed dwell angle can be obtained by using simple logic of opto-interrupters signals. This method provides low resolution of rotor position, but may be used in combination with phase-lock-loop techniques to increase its resolution. The main advantage of this method is that it is very simple and cheap to implement but on the other hand, it limits the freedom of changing turn on and off angles, and therefore, it puts some constraints in efficiency and torque ripple of the drive.

Hall sensors: This option makes use of Hall-effect sensors with a magnetised ring. The resolution with this method is similar to opto-interrupters with slotted disk.

The main difference is that commutation signals are obtained from magnetic effect rather than optically.

Encoder: The digital incremental position encoder uses basically the same principle of the opto-interrupter with slotted disk, but the resolution is increased due to the number of slots in the disk. The disk has a number of marks around its perimeter, a light source is placed at one side of the disk while in the other side a light detector, as the disk rotates, the detector generates a stream of pulses which indicate the angular position. Most of these encoders have a second light source and detector placed in such a way in relation to the first detector that their signals are electrically in quadrature, this is used to obtained direction information. A third light source and detector gives one pulse per revolution which is used as revolution index. Other type of encoder is the absolute encoder which can provide absolute rotor position at any time i.e. unambiguous shaft angle. In this device the disk is divided in N sectors, each sector is divided in a number of sections and so on. The sectors are arranged such that a digital word is obtained from the N light sources and detectors. A variety of encoder with different characteristics exist in the commercial market. The resolution of an incremental encoder is counted by pulses per revolution. Encoders of low resolution give from 50 to 600 pulses per revolution, encoders of medium and high resolution are in the range from 600 up to 90000 pulses per revolution. There are encoder with super high resolution which can give up to 230 millions pulses per revolution, this is the case of the Laser Rotary Encoder X-1M from CANON. On the other hand, the resolution of an absolute encoder is measured by the number of bits in the range of 10 to 16 bits. The price of an encoder basically depends on its resolution, speed range and robustness of the operation conditions.

Resolver: The resolver is similar to a small machine. A simple resolver has only one winding in the rotor and two windings in the stator shifted 90 degrees each other. If the rotor is excited by a pure sinusoidal reference signal, the output

Technology	Typical resolution [ppr]	Typical cost [£]	Application areas
Slotted disk	3 to 10	5 to 15	Air moving, pumps.
Hall sensor	3 to 10	5 to 15	Air moving, pumps.
Encoder	low: 50 to 600	15 to 150	The above plus compressors and high speed applications.
	med.: 600 to 10000	200, 1000	Servo drives, actuators, robotics.
	high: 10000 to 90000		Robotics, machine and cluster tools.
	very high: up to 230 millions		Scientific measuring instruments.
Resolver	med./high: 2^{10} to 2^{16}	300 to 2000	Servo drives, robotics, actuators, antenna positioning systems.

Table 1.1: Comparison of the four position sensor technologies for switched reluctance motors.

signal induced in the stator windings are $\sin(\theta)$ and $\cos(\theta)$ where θ is the shaft angular position. The analog signals obtained from the resolver are processed by an external circuit which generates the digital pulses in similar manner as an incremental or absolute encoder. The resolver technology offers high resolution for good price, and it is used in applications where a high resolution is required.

The most popular position sensor for the switched reluctance motor is the incremental encoder. However, there is always a trade-off between the resolution and the cost of the position sensor. In common practice, the application requirements impose the type of position sensor that should be used. Table 1.1 summarises and compares the four mechanical sensor used for rotor position feedback in switched reluctance motors.

1.4 Project motivation and objectives

The development of the switched reluctance motor technology through more than two decades has revealed that this technology is a serious candidate for variable speed drives, and can offer the same performance or even better compared to the well established and conventional AC and DC drives. As discussed before, the switched reluctance motor drive has the added attractive and strong advantages of absence of magnets, brushes and rotor conductors, and its simple construction.

On the other hand, SR technology has significant drawbacks, one of them being the necessity of precise rotor position information, which limits its full acceptance in variable speed drive applications. Currently there are few companies that manufacture SRM drives, although this may increase as it seems that the SRM technology is gaining more acceptance in applications such as aircraft generators, electric power assisted steering, brake by wire, pumps, fans, and even domestic appliances.

Hence, the main motivation of this thesis is the development and investigation of electronic methods of rotor position estimation, called *Sensorless Methods*, for switched reluctance motors, which permit the elimination of the mechanical position sensor. The research reported in this thesis had two objectives. The first study was focus in sensorless method for low resolution, while the second study was to create a sensorless method for high resolution. The goals of the thesis are listed more explicitly as follows,

The low resolution sensorless method should have the following main features:

- Simple implementation.
- No requirement for magnetisation motor curves.
- No requirement for the inductance profile.
- Able to handle transient torque.
- Good performance in speed transient.

- Flexibility in commutation angles.
- Two-quadrant operation.
- Closed-loop speed control.
- Applicable to any regular switched reluctance motor.
- Should not compromise the motor performance.
- Coverage of a wide speed range.

On the other hand, the high resolution sensorless method should offer:

- High resolution.
- High accuracy in rotor position estimation.
- Simple and minimal calculation suitable for real time implementation.
- Identification of *the best phase* for position estimation from all conducting phases.
- High performance in torque and speed transients.
- Dynamic four-quadrant operation.
- Closed-loop speed and position control.
- Current and voltage control, current profiling and single pulse operation.
- Applicable to any regular switched reluctance motor.
- Coverage of the whole torque-speed range.
- Robustness and no limitation of the performance of the motor.
- Robust start-up.

Apart from the research carried out in sensorless control, this thesis has as secondary objective the study of the functionality of the switched reluctance motor drive with a resonant dc-link front-end to provide high bandwidth current regulation with zero voltage switching. The motivation of this work is born in the necessity of a high efficient switched reluctance motor drive for high power applications, for instance, electric vehicle traction. It should be noticed that this research was carried out in the first year of the PhD studies. The main features of the resonant dc-link SR drive should be:

- High band width current regulation.
- Reduction of switching losses.
- Should not limit the motor performance.
- Simple implementation.
- Robustness.

1.5 Original contribution

An overview of the original contribution of the thesis is given here. The new developments and findings obtained are listed in three groups as follows.

1. *Low resolution sensorless method:*
    - Real time implementation of the *current gradient sensorless method* for switched reluctance motors.
    - Identification of the advantages and limitations of the *current gradient sensorless method.*
    - Development of the *current gradient sensorless method*'s theory for switched reluctance generators.

- Experimental study of start-up procedures for the *current gradient sensorless method*, in particular self-synchronisation and feedforward.
- Experimental study of accuracy and dynamic performance of the *current gradient sensorless method.*
- Reduction of current sensors and detection stages for rotor position information.
- Implementation of two-quadrant closed-loop speed sensorless control using *current gradient sensorless method.*
- Experimental test of speed and torque transients using *current gradient sensorless method.*

The work carried out in the *current gradient sensorless method* has resulted in three publications [28, 29, 30], one of them being a refereed journal article. Chapter 4 presents in detail the systematic study of this method.

2. *High resolution sensorless method:*

- Development of the theory of sensorless control for switched reluctance motor based on flux linkage and current observer.
- A novel method of how to chose *the best phase* for position estimation among all conducting phases is introduced.
- Identification of advantages and drawbacks of the new sensorless method.
- Implementation of the flux linkage observer sensorless method in Simulink^{R}.
- Study of the flux linkage observer sensorless method using probing pulses in unenergised phases.
- Performance investigation of flux linkage and current observer.
- Performance investigation of a second stage for flux linkage correction.
- Real time implementation of the flux linkage observer for position estimation.

- Experimental test of PWM voltage control in sensorless mode.
- Experimental test of closed-loop current control in sensorless mode.

The results of this high resolution sensorless method have been published in [31]. The study and the full development of this method is the aim of Chapter 5, which gives a detailed description of the work carried out.

3. *Soft switching applied to switched reluctance motor drives:*

   Note that this work is presented in Appendix A.

   - Simulation study of the proposed classic switched reluctance inverter with a front-end resonant dc-link and the active clamp resonant dc-link.
   - Real implementation of the active resonant dc-link front-end switched reluctance inverter for the first time.
   - Experimental test of the active clamp resonant switched reluctance inverter.

   This work gave place to two publication [32, 33]. The detail study and implementation of the proposed topology is presented in Appendix A.

A list of author's publications is given in Appendix D, page 310.

1.6 Thesis structure

In this section the outline of the thesis organisation is given.

As an introduction, Chapter 1 has given a general overview of the history of the switched reluctance motor and its advantages/disadvantages. Also the motivation of the thesis and its original contributions have been presented.

The principle and the basic equations of the switched reluctance motor are presented in Chapter 2. The most common switched reluctance motor and drives topologies are

also described. The basic model of the switched reluctance drive and a list of the available packages that can be used are presented.

An extensive and detailed review of the state of the art of sensorless methods for switched reluctance motors is given in Chapter 3 based on more than 50 references including papers and patents. The basic principles of existing sensorless methods are briefly explained and classified into three major groups.

Chapter 4 presents the investigation and development carried out on low resolution sensorless methods. The theory of the *current gradient sensorless method* and the *voltage magnitude sensorless method* are given. The *current gradient sensorless method* is implemented in real time in a simple manner. Full description of the implementation is given. Start-up methods are also investigated and presented. The experimental results from open-loop and closed-loop speed sensorless control are also shown.

The high resolution sensorless method for switched reluctance motors is studied and investigated in Chapter 5. Sensorless control based on flux linkage and current observer are investigated. The theory is developed and the simplest models are identified. An analysis of the performance of the flux linkage and current model is also presented. The study of a second stage in the method for flux linkage correction is given. A new method of how to chose *the best phase* for position estimation from all conducting phases is proposed. The detail of real-time implementation of the flux linkage sensorless model is presented, and the experimental results obtained using this method with PWM voltage control and closed-loop current regulation are shown.

Finally, general conclusions and further possible future work are presented in Chapter 6.

Chapter 2

The SRM drive and its simulation model

This chapter discusses the most important characteristics of a number of topologies of the switched reluctance motor and the most common inverters to drive it. The basic equations together with the magnetisation curves that govern the SRM are also explained. Then the basic SRM drive model and a few of the commercial packages available are briefly described.

2.1 Switched Reluctance Motors

The switched reluctance motor has salient poles in both rotor and stator, it does not have any permanent magnets, rotor conductors or brushes. The torque is developed by the tendency of the rotor to minimise the reluctance of the magnetic circuit when a phase is excited. A phase is formed by two coils connected either in series or parallel [34]. Note that, for simplicity, the effects of saturation are often ignored in first explanations of the principles of operation of SR machines, in particular the ratio $\frac{L_{ao}}{L_u}$ between the no saturated aligned inductance L_{ao} and the unaligned inductance L_u. However the saturation is siginificant in the actual operation of the machine and this will be included in the discussion where appropiate.

There are regular and irregular motors. A regular motor has poles in the stator and rotor equally spaced and the lateral poles sides are symmetric with respect to the axis of the pole. The irregular motor is simply that one that does not match with the above definition. The SRM can have an interior or an exterior rotor, being the most common the interior rotor. There are linear, axial and radial versions of the SRM, and the windings can be short or full pitch windings. The work carried out here makes use of the radial regular SRM with short pitch windings (one coil per stator pole).

The stator poles and rotor poles for a regular motor have the following relationship (except single phase):

$$N_s = N_r \pm p \tag{2.1}$$

where N_s is the number of stator poles, N_r is the number of rotor poles and p the number of poles per phase. The SRM can be classified by its number of phases as follows:

One phase: The single phase motor is very attractive due to its simplicity and low cost of its inverter. However it has 100% of torque ripple and obviously the motor cannot produce the necessary torque to start-up from standstill if the rotor is either at aligned position or close to it. Hence it needs some kind of assistance to start-up. The load has to have enough inertia to allow the motor to pass the band where there is no positive torque production. There has been proposed by Horst [35] the use of a parking magnet i.e. the rotor is parked at a specific position to be able to start-up. An advantage of the single phase motor is the big slot area because it has more space for phase windings which means that wire with bigger diameter can be used and therefore the copper losses are reduced. Another advantage is the low commutation frequency which reduces core losses, although this may not apply at very high speed. Examples of single phase SRM are: 2/2 or with multipoles 4/4, 6/6, 8/8. Fig.2.1 (a) depicts the 8/8 topology.

Two phase: The two phase SRM is still attractive due to simplicity and low cost of its inverter. The regular 4/2 two phase SRM has the starting problem and needs some assistance for start-up, however the starting problem is alleviated in a 4/2 two phase irregular SRM with a step gap but only in one direction, The stepped gap is useful to increase the band of raising inductance, but at the same time increases the unaligned inductance and it may reduce the inductance ratio $\frac{L_{ao}}{L_u}$. The SRM two phase can have the following number of stator/rotor poles: 4/2, 4/6, 8/4, 8/12. The 4/2 with a step gap is shown in Fig.2.1 (b).

The common characteristics of one and two phases are:

- Fewer leads to connect between the power inverter and the motor.
- Big slot area that permits thicker wire, leading to low copper losses.
- Low commutation frequency which tends to reduce the core losses.
- Tend to have high efficiency.
- Suitable for high speed.
- High torque because of their high inductance ratio $\frac{L_{ao}}{L_u}$.
- Low strokes per revolution in topologies with minimum number of stator and rotor poles.
- Simple electronics for control due to few phases to control.
- High torque ripple.
- Start-up problem (the problem may be solved with step-gap rotor or parking magnets).
- It is not possible to change the direction of rotation when it is already rotating in one direction.

The SRM with one and two phases may be suitable for high speed, due to their relative low commutation frequency. However they suffer from high torque ripple and dynamic four-quadrant operation is not possible. Another big disadvantage

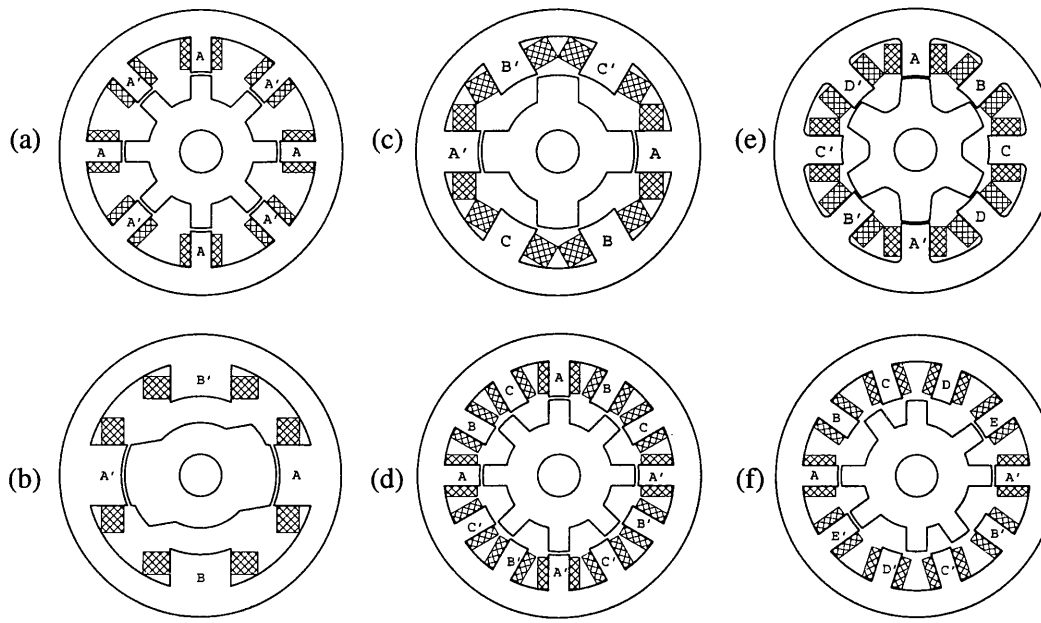

Figure 2.1: SRM a: 8/8 single phase, b: 4/2 two phase, c: 6/4 three phase, d: 12/8 three phase, e: 8/6 four phase, f: 10/8 five phase.

is the difficulty in start-up from standstill. However, this argument does not apply in the case of generating.

Three phase: At least three phases are required to start-up in any direction and to have dynamic 4-quadrant operation. It depends on the excitation sequence of the phases. The three phase SRM can have the following configuration: 6/2, 6/4, 6/8, 12/8, 24/16. Other possible topologies are: 12/10 with two teeth per stator pole and 12/10 irregular stator with poles grouped in pairs. Another special motor is the Megatorque with 144/150 teeth which is for low speed and high torque applications manufactured by NSK Japan. Fig.2.1 (c) and (d) show the 6/4 and 12/8 machine respectively.

Four phase: In four phase SRM the torque ripple is smaller than motors with fewer phases because there is more torque sharing between phases. Possible configurations are: 8/6 with 24 strokes/rev and 8/10 40 with strokes/rev. However the six rotor poles is preferable due to its bigger inductance ratio and less strokes/rev which means less core losses. The 8/6 machine is shown in Fig.2.1 (e)

Higher number of phases: For a five phase SRM there is a significant current overlap that helps in reducing the torque ripple, but core losses are higher due to the high number of strokes per revolution. However, reduction to half of strokes per revolution is possible for two pole-pitch rotor. In this topology the motor can work with short flux-paths. The combination of less strokes/rev and short flux-paths may reduce the core losses compared with the regular 10/8 SRM The 10/8 five phase with short flux-paths is depicted in Fig.2.1 (f).

The SRM with higher number of phases have the following common characteristics:

- More leads to connect between the power inverter and the motor.
- Small slot area that causes more copper losses.
- High commutation frequency which increases the core losses.
- They are less suitable for high speed than the motor with low number of phases due to core losses.
- Small inductance ratio $\frac{L_{ao}}{L_u}$.
- High number of strokes per revolution.
- Expensive inverter to control the motor.
- Low torque ripple.
- Great fault tolerance, i.e. if one phase fails the motor can still generate enough torque with the healthy phases.

2.2 SRM Inverters

To produce motoring torque the SRM needs current to be applied in a phase when the inductance of the phase in question is increasing from unaligned to aligned position, and to switch off the current when the inductance is maximum (aligned position). The torque depends only on the sign of phase inductance slope and not on the direction of

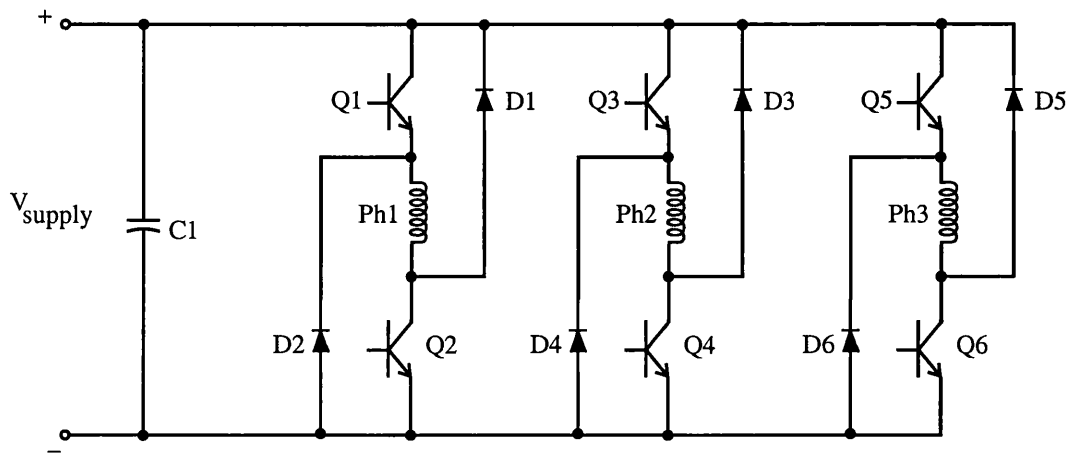

Figure 2.2: Classic SR inverter.

the current. However the phase voltage needs to be reversed in order to de-flux the phase as quickly as possible.

There are a number of proposed SRM inverters in the literature which have their own advantages and disadvantages. The inverter must be chosen according to application requirements. In this section the most well known inverter topologies and their states (shown for one phase) are summarised. The following apply thereafter, N= Number of phases, V_{dc}= Supply voltage and I_{max}= Maximum phase current.

Classic inverter: It is the most popular due to its flexibility in controlling each phase independently. It has two switches and two diodes per phase as shown in Fig.2.2. It is capable of producing unidirectional phase current. V_{dc} is applied to phase one when Q1 and Q2 are turned on, reverse voltage is applied when Q1 and Q2 are turned off, then current freewheels through diodes D1 and D2. Zero voltage loop is possible when only one transistor is on. Its states are summarised in Table 2.1.

Configurations with one switch per phase: There has been great interest on reducing the number of switches per phase without compromising the performance of the drive. However no such inverter topology has yet been found. In most inverters with one switch per phase, the power rating of the devices has to be

Q1	Q2	D1	D2	Voltage in Ph1	Action
on	on	off	off	V_{dc}	Magnetisation
off	on	off	on	0	Freewheeling
on	off	on	off	0	Freewheeling
off	off	on	on	$-V_{dc}$	Demagnetisation

Table 2.1: Classic inverter states

Q1	D1	Voltage in Ph1				Action
		D_{sup}	R_{sup}	D_{zener}	Bifilar	
on	off	V_{dc}	V_{dc}	V_{dc}	V_{dc}	Magnetisation
off	on	0	$-R_{sup}$	$-(R_{sup}+V_{Dz})$	$-V_{dc}$	Freewheeling Demagnetisation

Table 2.2: One switch per phase inverter states

twice the power rating that the motor requires. The common characteristics of these inverters are shown in Table 2.2.

Diode suppression (Fig.2.3 (a))

For this topology, it is not possible to reverse the voltage in the phase. The phase de-fluxing is slower and depends on the volt-drop in the diode and the winding resistance. This leads to a long current tail which affects the efficiency of the motor by producing negative torque, and limits the dwell angle at high speed.

Resistance suppression (Fig.2.3 (b))

In this circuit an external resistance is added to increase the suppression voltage across the winding during the freewheeling and phase demagnetisation. However the suppression voltage decays as function of the current, and the energy is dissipated through the resistance decreasing the efficiency of the drive.

Diode zener suppression (Fig.2.3 (c))

This topology uses a diode zener to sustain a higher suppression voltage. The demagnetisation time is reduced but still wasting energy in the resistance.

Q1	D2	Voltage in Ph1	Action
on	off	$\frac{V_{dc}}{2}$	Magnetisation
off	on	$-\frac{V_{dc}}{2}$	Demagnetisation

Table 2.3: Split rail inverter states

These topologies are not suitable for high power due to their limitation in de-fluxing phases, and low efficiency of the drive. This kind of inverter may be suitable for low power drives.

Bifilar winding (Fig.2.3 (d))

The phase winding is composed by two coils in each stator pole. One is connected between the positive rail and the switch and the other between the positive rail and the diode. It does not permit soft chopping, but permits full reversal voltage. It should be noted that the number of out-leads increases to 4 per phase. For further information refer to [6, 36, 37].

Split rail inverter

The split inverter shown in Fig.2.3 (e) has a minimum number of transistor per phase without adding passive components, but is suitable only for even number of phases and it is not possible soft chopping. One disadvantage of this topology is that the motor uses half of the voltage supply and that the voltage in the split capacitor has to be kept balanced. The states of this inverter are shown in Table 2.3.

Inverter with (N+1) number of switches: The transistor Q works for all three phases, while Q1, Q2, and Q3 commutate the phases, refer to Fig.2.3 (g). In this circuit the phase independency is lost. The demagnetisation of any phase depends on the average voltage in node A. If it is sufficiently small, one phase can still be demagnetized. This topology is not suitable for high speed where there is long current excitation overlap between phases, see [38, 39]. A variant of this circuit for four phases is shown in Fig.2.3 (h), where the chopping transistors Qa

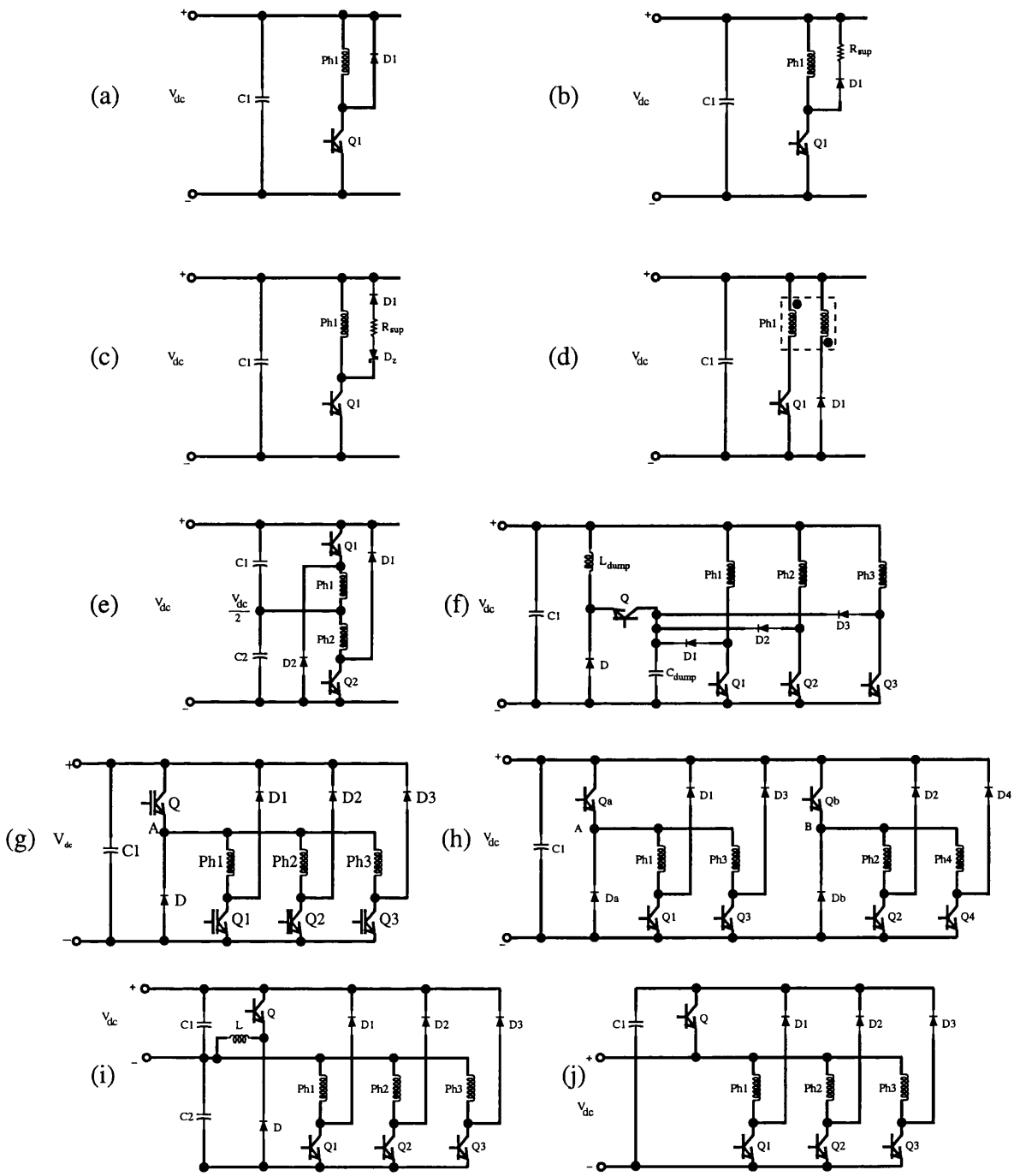

Figure 2.3: SRM inverters. a: Diode suppression, b: Resistance suppression, c: Diode Zener suppression, d: Bifilar inverter, e: Split rail inverter, f: C-Dump inverter, g: $N+1$ switches inverter, h: $2 \cdot (N+1)$ switches inverter, i: Buck-Boost inverter, j: Dual-rail inverter.

Q	Q1	D	D1	Voltage in Ph1	Action
on	on	off	off	V_{dc}	Magnetisation
off	on	on	off	Depends on the average voltage in A	Freewheeling
off	off	on	on	Depends on the average voltage in A	Demagnetisation

Table 2.4: N+1 inverter rating

Q	Q1	D	D1	Voltage in Ph1	Action
off	on	off	off	V_{dc}	Magnetisation
off	off	off	on	$V_{dc} - V_{C_{dump}}$	Demagnetisation C is discharged and C_{dump} charged
on	off	off	off		C_{dump} discharges through L_{dump}
off	off	on	off		C1 is charged as L_{dump} transfers its energy

Table 2.5: C-Dump inverter rating

and Qb are connected to phases (Ph1 and Ph3) and (Ph2 and Ph4) respectively. The problem of overlap is reduced and all phases can have maximum reverse voltage up to certain speed. The states of this inverter are shown in Table 2.4.

C-Dump inverter: All phases freewheel into the dump capacitor C_{dump}. The voltage in C_{dump} is controlled by Q, D and L_{dump} to an average value approximately of $2 \cdot V_{dc}$ [40]. Soft chopping is not possible and needs extra control to regulate the voltage in C_{dump}. Q1, Q2, and Q3 are the chopping and the commutation transistors. The states of this inverter are presented in Table 2.5, and its configuration in Fig.2.3 (f).

Buck-boost inverter: The Buck-Boost Inverter is similar to C-dump Inverter but in this topology Q1, Q2 and Q3 are only commutation transistors and the magnetisation voltage is V_{C2} which is controlled by Q, D and L. Table 2.6 show the states of this inverter and the circuit diagram is depicted in Fig.2.3 (i), see [41].

The Dual-Rail inverter: The main characteristic of this topology is that there is no dc-link capacitor. In this circuit V_{dc} is unfiltered rectified voltage. The phases are magnetised either from V_{dc} or V_{C1}. This topology needs such a control to maintain

Q	Q1	D	D1	Voltage in Ph1	Action
off	on	off	off	V_{C2}	Magnetisation
off	off	off	on	$-V_{dc}$	Demagnetisation, C1 is charged with the energy from phase winding
on	off	off	off	0	$C1$ is discharged through L
off	off	on	off	0	$C2$ is charged as L transfer its energy

Table 2.6: Buck-boost inverter states

Q	Q1	D	D1	Voltage in Ph1	Action
off	on	off	off	V_{dc}	Magnetisation when $V_{dc} > V_{C1}$
on	on	off	off	V_{C1}	Magnetisation when $V_{dc} < V_{C1}$
on	off	off	on	0	Demagnetisation-Freewheeling
off	off	off	on	$V_{C1} - V_{dc}$	Demagnetisation-Charging C1, the phase winding charges C1

Table 2.7: Dual-Rail inverter states

the voltage in the capacitor stable around the peak voltage of the unfiltered rectified voltage. The circuit is shown in Fig.2.3 (j), Q1, Q2, and Q3 are the chopping and the commutation transistors, see [41, 42]. Table 2.7 summarises its characteristics.

The components, power rating and control capability of all the inverters are summarised in Table 2.8, 2.9 and 2.10 respectively. It is easy to see that inverters with one switch per phase either need double power rating for the switches, compromise the performance of the drive or both. Furthermore their control is more complex. In contrast the Classic inverter offers full phase control independency and is easy to control.

Converter	Switches per Phase	Diodes per Phase	Extra Switches	Extra Diodes	Extra Passive Component
Classic	2	2	-	-	-
Diode Sup.	1	1	-	-	-
Resistor Sup.	1	1	-	-	Resistor
Dzener Sup.	1	1	-	-	Res., D_z
Bifilar	1	1	-	-	-
Split rail	1	1	-	-	-
$(N+1)$-sw.	1	1	1	1	-
$2\cdot(N+1)$-sw.	1	1	2	2	-
C-Dump	1	1	1	1	C_{dump}, L_{dump}
Buck-Boost	1	1	1	1	C, L
Dual rail	1	1	1	-	C^*

Table 2.8: Summary of the components of SRM inverters. *, this topology does not use capacitor in the dc-link.

Converter	Phase Switch Rating	Extra Switch Rating	Total kVA Rating $W = V_{dc}\cdot I_{max}$
Classic	V_{dc}, I_{max}	-	$2\cdot N\cdot W$
Diode Sup.	$2\cdot V_{dc}$, I_{max}	-	$2\cdot N\cdot W$
Resistor Sup.	$2\cdot V_{dc}$, I_{max}	-	$2\cdot N\cdot W$
Dzener Sup.	$2\cdot V_{dc}$, I_{max}	-	$2\cdot N\cdot W$
Bifilar	$2\cdot V_{dc}$, I_{max}	-	$2\cdot N\cdot W$
Split rail	V_{dc}, I_{max}	-	$N\cdot W$
$(N+1)$-sw.	V_{dc}, I_{max}	V_{dc}, $2\cdot I_{max}$	$(2+N)\cdot W$
$2\cdot(N+1)$-sw.	V_{dc}, I_{max}	V_{dc}, $2\cdot I_{max}$	$(2+N)\cdot W$
C-Dump	$2\cdot V_{dc}$, I_{max}	$2\cdot V_{dc}$, $2\cdot(1+r)\cdot I_{max}$	$2\cdot(N+2\cdot(1+r))\cdot W$
Buck-Boost	$2\cdot V_{dc}$, I_{max}	$2\cdot V_{dc}$, $2\cdot\frac{1+r}{1-D}\cdot I_{max}$	$2\cdot(N+2\cdot\frac{1+r}{1-D})\cdot W$
Dual rail	$2.27\cdot V_{dc}$, I_{max}	$2.27\cdot V_{dc}$, $2\cdot I_{max}$	$2.27\cdot(N+2)\cdot W$

Table 2.9: Power rating of the SRM inverters. r is the current ripple in the dc-link divided by 100. D is the duty cycle of the extra transistor.

Converter	Soft Chop.	Hard Chop.	Power Range	Speed Range	Phase Indep.	Number of Phases	Number of Leads
Classic	Yes	Yes	Any	Any	Full	No lim.	$2 \cdot N$
Diode Sup.	Yes	No	Low	Med.	Full	No lim.	$N+1$
Resistor Sup.	Yes	No	Low	Med.	Full	No lim.	$N+1$
Dzener Sup.	Yes	No	Low	Med.	Full	No lim.	$N+1$
Bifilar	No	Yes	Any	Any	Full	No lim.	$4 \cdot N$
Split rail	No	Yes	Med.	Any	Shared	Even	$N+1$
$(N+1)$-sw.	Yes	No	Any	Low	Shared	No lim.	$N+1$
$2 \cdot (N+1)$-sw.	Yes	No	Any	Med.	Shared	Even	$2 \cdot (N+1)$
C-Dump	No	Yes	Med.	Any	Shared	No lim.	$N+1$
Buck-Boost	No	Yes	Any	Any	Shared	No lim.	$N+1$
Dual rail	Yes	Yes	Any	Any	Shared	No lim.	$N+1$

Table 2.10: Control capability of the SRM inverters.

2.3 Basic equations

The ideal phase inductance $L(\theta)$ is shown in Fig.2.4. The subscript u, a and o correspond to unaligned, aligned and start of overlap position respectively. Positive torque is generated when current is applied in the positive slope of the inductance $(\theta_o - \theta_a)$ regardless of the direction of the current, and negative torque is produced when current flows in the negative slope of the inductance. The stroke angle is given by,

$$\theta_{stroke} = \frac{360^o}{N \cdot N_r} \tag{2.2}$$

where N = number of phases and N_r = number of rotor poles.

The cross section of a 4 phase 8/6 machine is depicted in Fig.2.1 (e). The rotor is aligned with phase A while phase C is in unaligned position. Phase B and D are in intermediate position. The non-saturated phase inductance at aligned position L_{ao} and the phase inductance at unaligned position L_u are useful values for motor design. A good design maximises the ratio $\frac{L_{ao}}{L_u}$. The most important factor that influences L_u and L_{ao} is the airgap, in contrast the saturated L_a is affected mostly by the steel material. The rotor pitch (one electrical cycle) is given by,

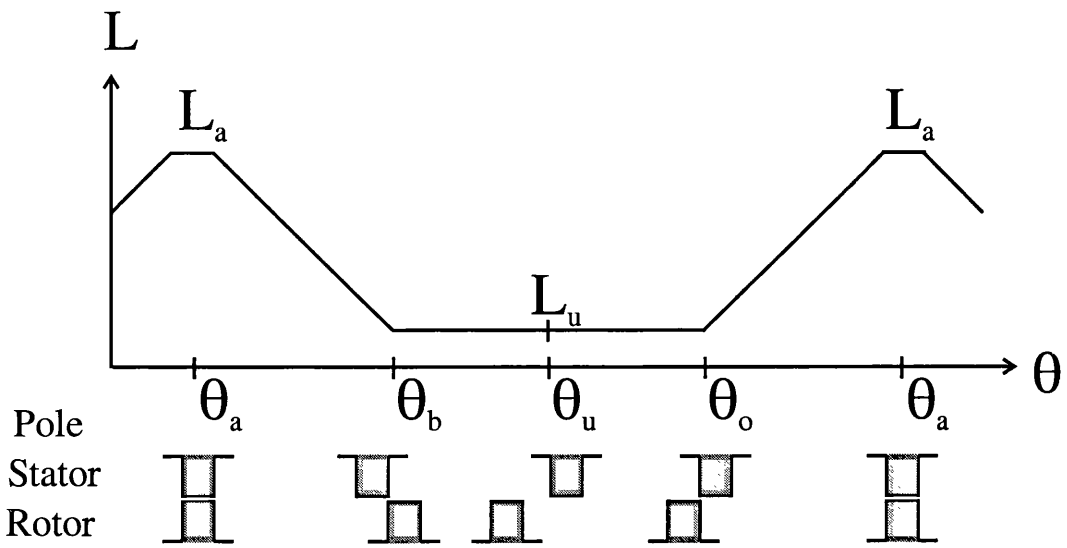

Figure 2.4: Ideal inductance profile.

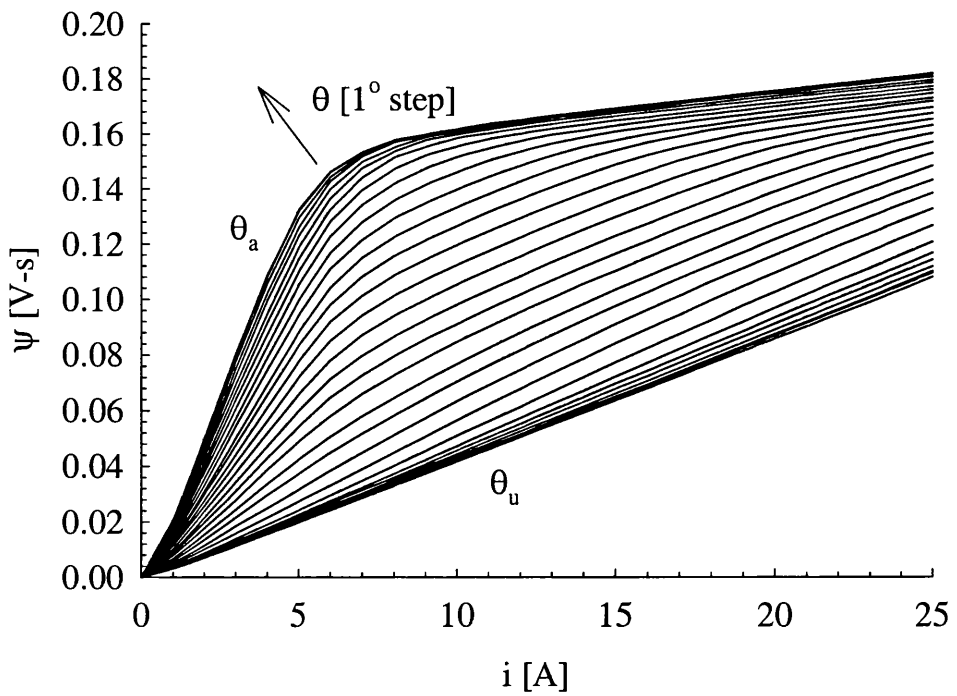

Figure 2.5: Measured magnetisation curves of the SR motor used in Chapter 5. The set of magnetisation curves were measured using the method explained in [43].

$$\theta_{pitch} = \frac{360^o}{N_r} \tag{2.3}$$

2.3.1 Magnetisation curves

The magnetisation curves, also called magcurves, represent the magnetic characteristic of the machine at discrete rotor positions. Half an electrical cycle is enough to represent the whole electrical cycle for a regular motor i.e. from θ_u to θ_a because the θ_u is in the middle of the electrical cycle. In contrast, the whole electrical cycle is needed for an irregular motor because the minimum inductance is not exactly in the middle of the electrical cycle.

A set of measured magcurves of a 4 phase 8/6 SRM is shown in Fig.2.5, for further information about magcurve measurements see [43]. This motor is the one used for the validation of high-grade sensorless algorithm presented in Chapter 5.

It can be observed that the curve at unaligned position θ_u is a straight line. In contrast, the curve for the aligned position θ_a shows a deflection around 5A where the saturation effect starts. Notice that the intermediate positions present two deflections, the first one around 5A which is mainly caused by the local saturation of the stator and rotor pole corners, and the second appears at higher current level depending on the rotor position. The main cause of this deflection is the stator and rotor yoke saturation.

Fig.2.6 depicts two electrical cycles of the measured magcurves plotted at constant current. It can be observed that the flux linkage increases from θ_u to θ_a. Note that the step in flux linkage is large at low current levels close to θ_a, however this step is reduced significantly at high current levels which results in a flatness of the curves, this is due to the saturation effect. In contrast, the step in flux linkage is kept constant at all current levels close to θ_u.

Another way to represent the magcurves is at constant flux linkage. Fig.2.7 shows two electrical cycles of the measured magcurves plotted in this form. It can be seen

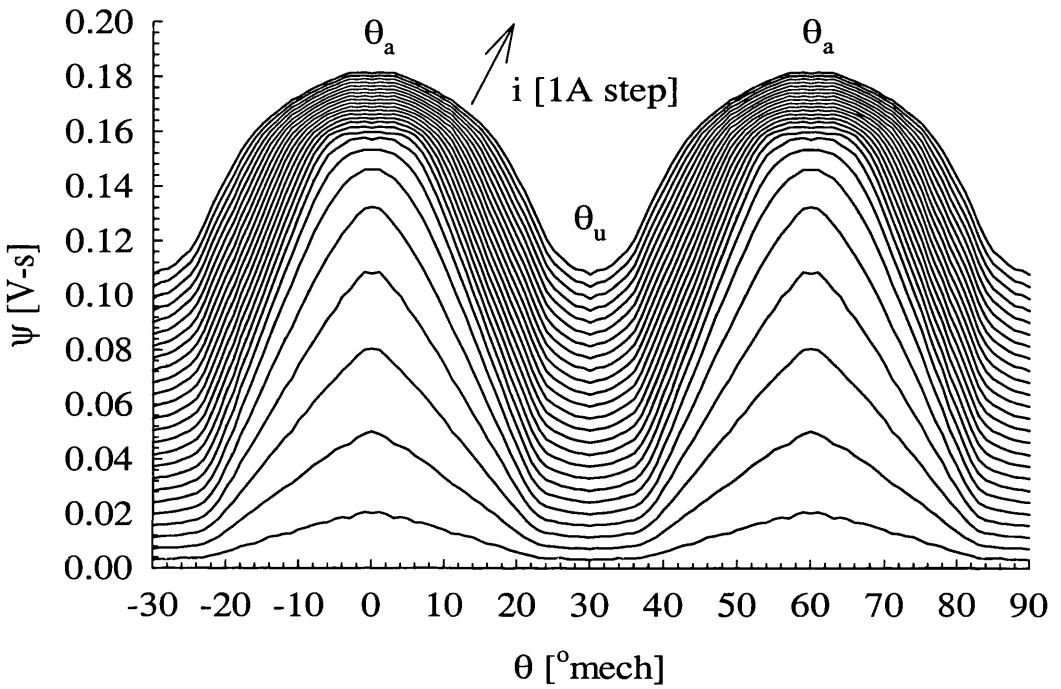

Figure 2.6: Measured magnetisation curves plotted at constant current. Note that this is the same data of Fig.2.5 plotted in different way.

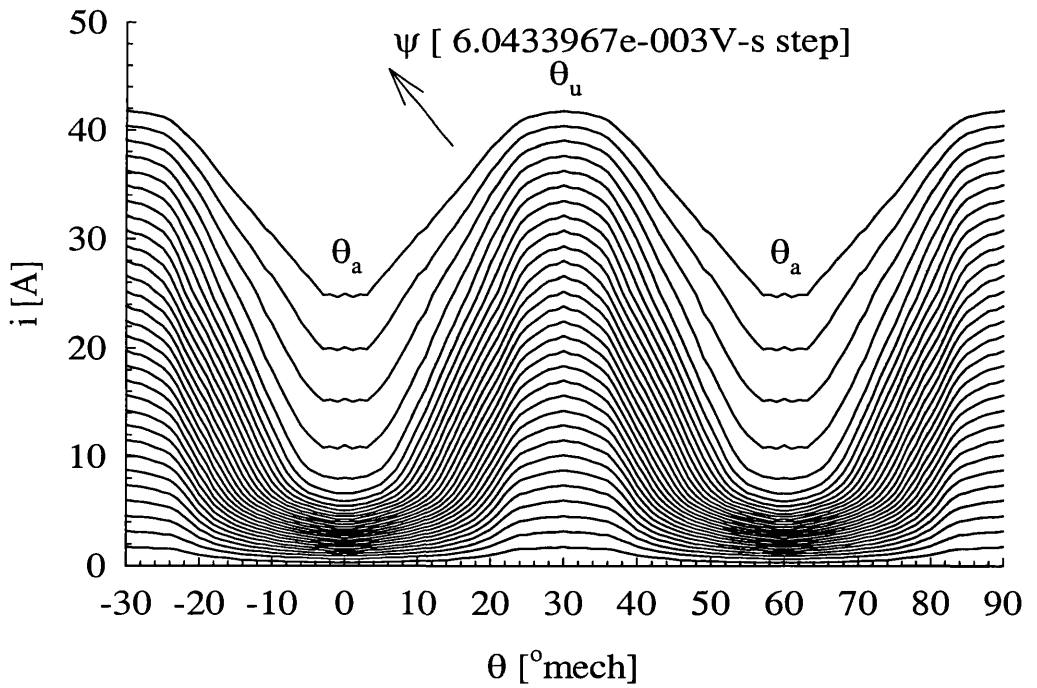

Figure 2.7: Measured magnetisation curves plotted at constant flux linkage. Note that this is the same data of Fig.2.5 plotted in different way.

that the current level decreases from θ_u to θ_a. Note that the step in current is constant for any value of flux linkage close to θ_u, in contrast, there is a change in current step close to θ_a due to the saturation effect.

The phase inductance is calculated as:

$$L(i,\theta) = \frac{\psi(i,\theta)}{i} \tag{2.4}$$

and plotted in Fig.2.8 for two electrical cycles. It is clear that the phase inductance is not only a function of position but current level as well. The phase inductance is constant at θ_u but not at θ_a and intermediate positions where it decreases as the current is raised. The phase inductance at θ_a is always higher than at θ_u, however the ratio $\frac{L_a}{L_u}$ is reduced as a function of current level due to the saturation effect.

The incremental phase inductance is calculated as:

$$l(i,\theta) = \left[\frac{\partial\psi(i,\theta)}{\partial i}\right]_{\theta=cst} \tag{2.5}$$

The incremental phase inductance is depicted in Fig.2.9 for two electrical cycle. We observe that even it may be smaller at θ_a than θ_u due to the saturation effect.

2.3.2 Torque

The magnetization curves are of great importance for the calculation of torque. The general equation which represent the torque generated by a phase is,

$$T(i,\theta) = \left[\frac{\partial W'(i,\theta)}{\partial\theta}\right]_{i=cst} \tag{2.6}$$

The coenergy W' is defined as the area between a given magnetisation curve and the

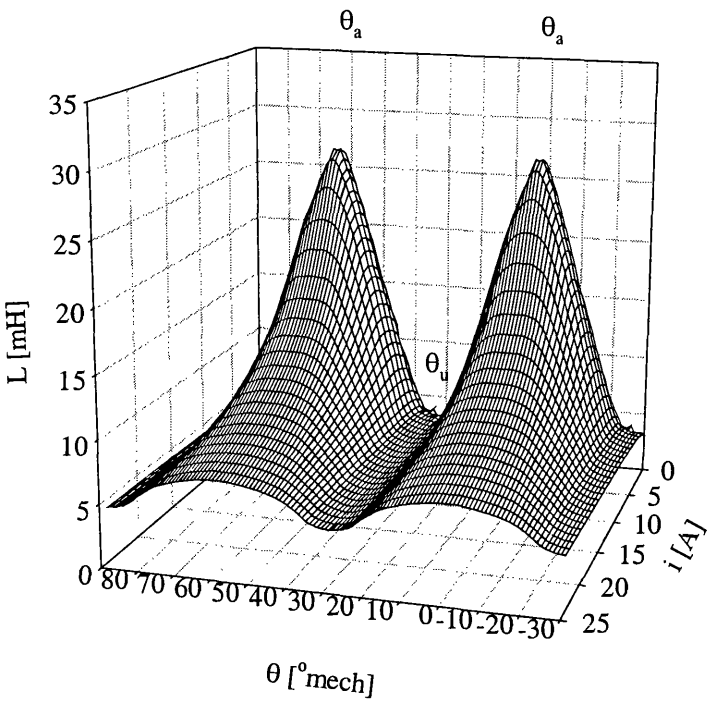

Figure 2.8: Phase inductance of the motor used in Chapter 5.

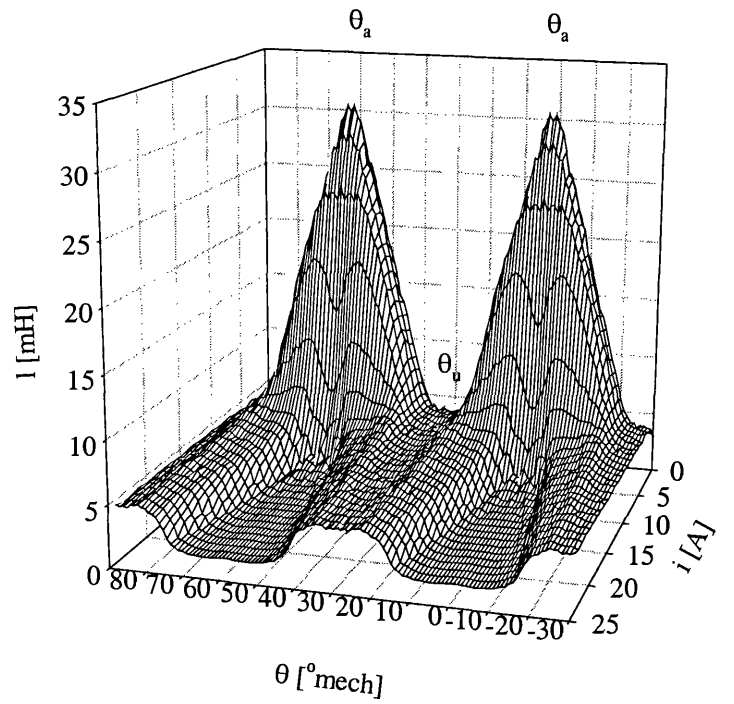

Figure 2.9: Incremental phase inductance of the motor used in Chapter 5.

current axis, while the stored magnetic field energy W_f is defined as the area between a given magnetisation curve and the flux linkage axis, see Fig.2.10.

The instantaneous torque is generated by the work $\delta W'$ divided by the infinitesimal displacement of the rotor $\delta\theta$. For the ideal case of a non-saturable machine the torque becomes,

$$T(i,\theta) = \frac{1}{2} \cdot i^2 \cdot \frac{dL}{d\theta} \tag{2.7}$$

The total energy supplied by the inverter, is the addition of W' and W_f, but only W' is transformed to mechanical work and W_f is returned to the power supply. In the case of the non-saturable machine only half of the total amount of energy is converted to mechanical work i.e. the ratio ($\frac{W_f}{W'} = \frac{1}{2}$). Fortunately there is a saturation effect in a real machine. As the saturation is higher the ratio $\frac{W_f}{W'}$ is smaller which means that the volt-ampere rating of the inverter is smaller for a given shaft power [5].

The instantaneous torque calculated from the magcurves is depicted in Fig.2.11 at constant current. It is clear that at θ_a and θ_u the torque generated is zero and that the peak torque is at an intermediate position. Fig.2.12 shows the instantaneous torque at constant flux linkage. This shows that neither constant current control nor constant flux linkage generates a constant torque output in an electrical cycle, hence either the current or the flux linkage may be profiled to produce constant torque and therefore to reduce torque ripple.

The energy enclosed by the $i - \psi$ trajectory in an electrical cycle ($\Delta W'$) represents the total electromagnetic energy converted to mechanical torque, refer to Fig.2.10. The average torque is calculated as,

$$T_{avg} = \Delta W' \cdot \frac{N \cdot N_r}{2 \cdot \pi} \tag{2.8}$$

In this equation, it is clear that in order to increase the average torque, the number of strokes ($N \cdot N_r$) and the area W' (ie. larger inductance ratio $\frac{L_{ao}}{L_u}$) should be

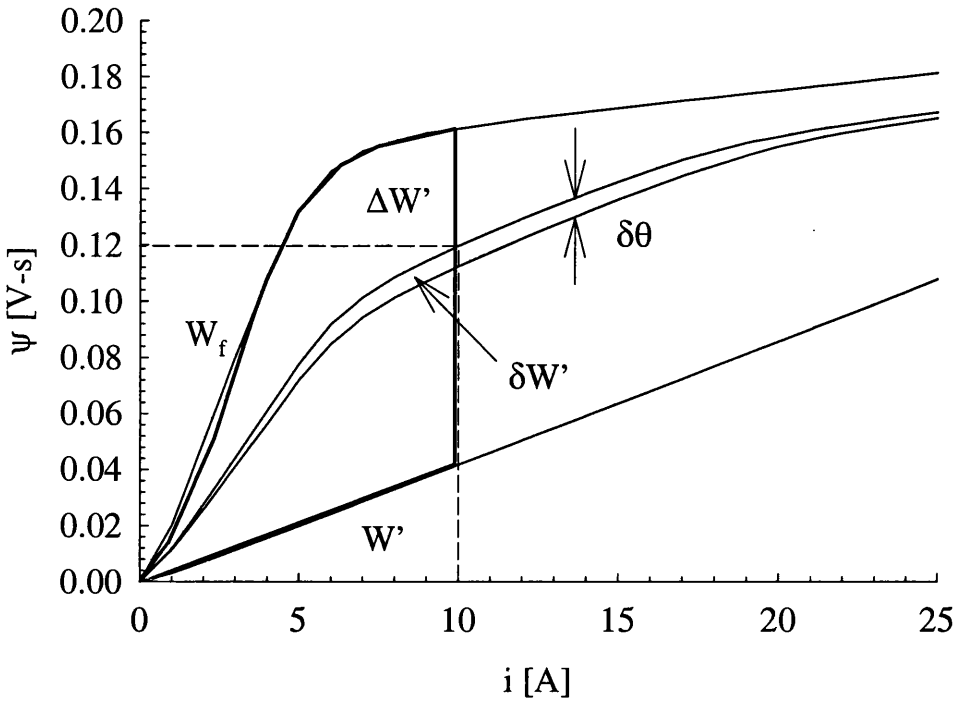

Figure 2.10: Coenergy in the $\psi - i$ plane.

increased. However these variables work against each other, in other words, if the number of strokes is increased, the inductance ratio tends to be reduced and viceversa. In three and four phase machines, the maximisation of inductance ratio and number of strokes/rev. may be found without these effects cancelling each other.

2.3.3 Phase voltage

The phase voltage in a phase can be expressed by

$$\begin{aligned} v(i,\theta) &= R \cdot i + \frac{d\psi(i,\theta)}{dt} \\ &= R \cdot i + \left[\frac{\partial\psi(i,\theta)}{\partial i}\right]_{\theta=cst} \cdot \frac{di}{dt} + \left[\frac{\partial\psi(i,\theta)}{\partial\theta}\right]_{i=cst} \cdot \frac{d\theta}{dt} \\ &= R \cdot i + l(i,\theta) \cdot \frac{di}{dt} + e \end{aligned} \tag{2.9}$$

The first term corresponds to the voltage due to the phase resistance R, the second term is the contribution of the inductive voltage and the third term corresponds to the

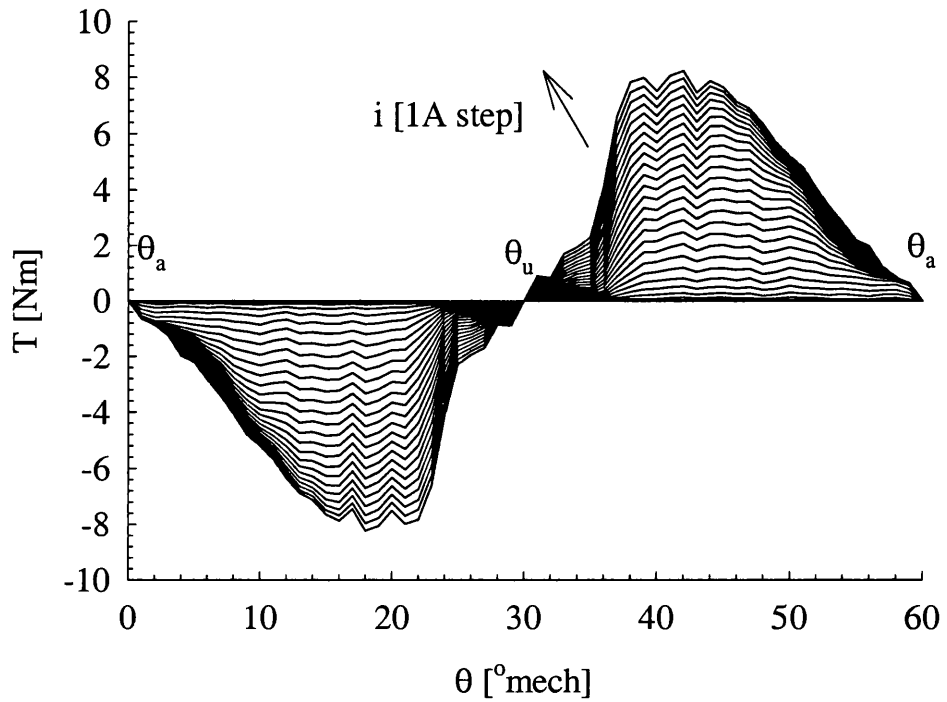

Figure 2.11: Instantaneous torque calculated from the measured magnetisation curve at constant current.

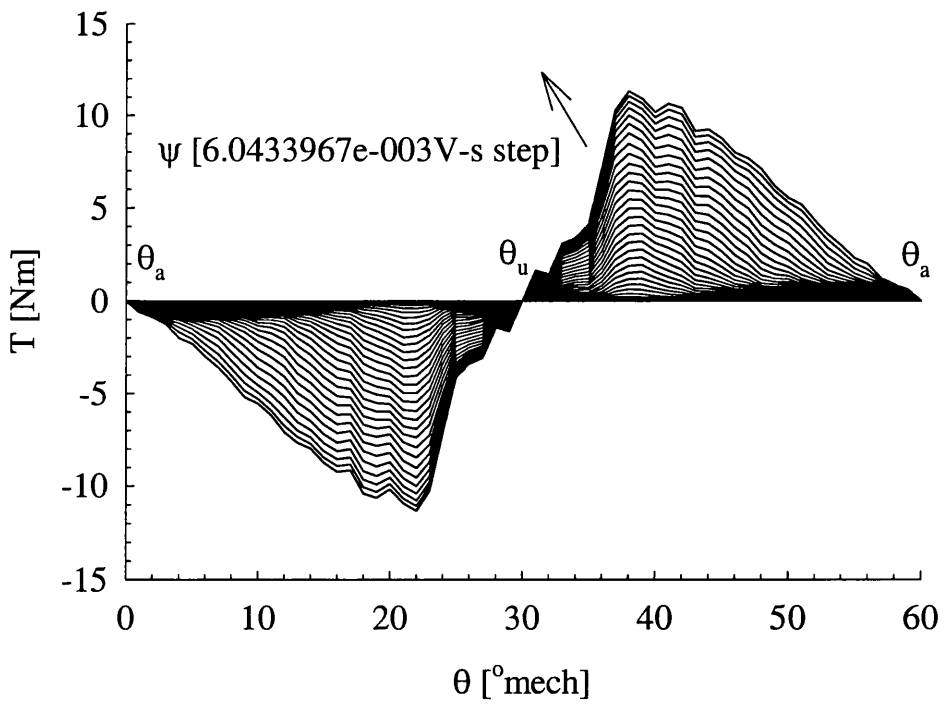

Figure 2.12: Instantaneous torque calculated from the measured magnetisation curve at constant flux linkage.

back-EMF e. The second and third term vary strongly as functions of current level and position.

2.3.4 Mutual coupling

When more than one phase is energised there is a sharing mainly in the flux linkage path of the stator and rotor yoke. This may cause a drop in the total phase flux linkage and therefore the magnetisation curves are affected, which means that they are not only a function of the current of the phase in question but also a function of all conducting phases, i.e. $\psi(i_1, i_2, i_3, \cdots, i_n, \theta)$. Hence the torque becomes a function of all phase current as,

$$T(i_1, i_2, i_3, \cdots, i_n, \theta) = \frac{\partial W'(i_1, i_2, i_3, \cdots, i_n, \theta)}{\partial \theta} \tag{2.10}$$

This is called mutual coupling and the effect is worst when the stator, rotor yoke or both are thin. The magnetisation curves may be affected significantly and hence also the torque production. A good SRM design tends to have at least the same thickness in the stator and rotor yoke as the pole width in order to minimise this effect.

2.4 SRM model

A good model of the SRM must take into account all the non-linearities in enough detail in order to approximate it to the real machine. It must simulate the current and voltage signals of the motor and inverter, and the control signal in time-stepping. It should give the torque-speed characteristic of the machine and be able to simulate the closed-loop torque, speed and position control.

To have an analytical expression to represent the SRM is difficult due to its strong non-linearities. A simple way to include the non-linearities of the machine is by representing the magnetisation curves and static torque curves as a look-up table and

calculating intermediate values by linear interpolation.

The main steps of the basic time-stepping simulation model are:

- Increment rotor position as a function of the speed and time step ΔT.
- Calculate the status of the inverter's transistors as a function of the selected firing angles, and in consequence the voltage in each phase.
- Calculate the flux linkage by $(v_{ph} - R \cdot i) \cdot \Delta T$.
- Calculate phase current from the look-up table as a function of position and flux linkage.
- Calculate instantaneous torque from look-up table as a function of current and position.

There are various powerful tools for modelling the SRM drive. The choice of tool depends on how much detail is required and the time available. Examples of this tools are:

Simulink^{R} - Matlab^{R}: This program is very popular for motor drives modelling because it is very powerful and easy to use. The model of the motor is based on look-up tables of the magnetisation and instantaneous torque curves. It does not have power device models, hence the inverter must be modelled with ideal switches.

Saber^{TM}: This program has an extended library of electronic and mechanical devices. Therefore a more detailed complex model can be created. The motor can be modelled, for example, using a lumped parameter equivalent circuit which may give more accurate results. Other similar programs are PSPICE^{R} and Simplora.

PC-SRD: This is a design tool for an SRM and its control. This program allows to size very fast the machine according to the application requirements with reasonable accuracy [44, 45].

FE time stepping (MEGA): The approach of this program is to link FE with the control electronics. The machine is modelled with FE which offers the advantage of high accuracy in the magnetic circuit model, however at expense of the long simulation time.

Writing your own code: This approach is very useful when a fast and simple SRM drive model is required, however the complexity of the model can be increased and customised as the application requires.

2.5 Conclusions

There is a vast variety of SRM topologies and there is no single topology that matches the requirements of all applications. The same happens with other types of motor, however in the case of SRM the scope is more open due to its high non-linearities.

For a high number of phases, the following trends can be summarised:

Increase of:

- Strokes per revolution, therefore increase of commutation frequency which means more core losses.
- Number of leads brought out.
- Current overlap, hence decrease of torque ripple.

Decrease of:

- Inductance ratio which tends to reduce the maximum torque.
- Slot area, therefore increase of copper losses.
- Pole arc decreases maximum inductance.

The torque in the SRM is proportional to the rate of change of the coenergy and the number of strokes per revolution. That is why the effect of high inductance ratio and high number of strokes/rev. is desired. However, a high inductance ratio requires few rotor poles while a high number of strokes/rev. demands a large number of rotor poles. The motor topology and its entire design has to be chosen according to the specifications of the application in question, ie. speed range, power, load, quadrant operation, starts per hour, load torque at start-up, torque ripple, bidirectional rotation.

Following the idea that the SR motor can operate with unidirectional current, most of the circuits that have been proposed are with one switch and one diode per phase. However the voltage should be reversed after the commutation angle in each stroke in order to de-flux the phase. Hence topologies with one switch per phase require extra switches, passive components or both. The disadvantages of such topologies is that the switches suffer at least twice the voltage or current of the nominal values of the motor. Furthermore the phase control independency is lost and, in topologies where phases share components, there is a risk that if the shared component fails the inverter loses its control capability. On the other hand, the main advantage of these topologies is that the number of leads brought out from the motor is reduced.

The most widely accepted topology is the Classic inverter with two switches and two diodes per phase. This is due to its simplicity, flexibility and independency in controlling the phase current. However the SRM inverter has to be chosen according to the specifications of each application, and it is often necessary a close design coordination between load, motor, inverter and its control.

It has been explained that the instantaneous torque is a nonlinear function of the current level and rotor position. The standard way to represent and model the SRM is based on its magnetisation curves from which instantaneous torque capability is obtained. The SRM poses a unique magnetic characteristic for each SRM design due to the high non-linearities of its magnetic circuit. This is well observed in Fig.2.5, 2.6 and 2.7. Usually one set of magnetisation curves is enough to model the SRM, however

it may not be the case when there is saturation in the stator and rotor yoke (mutual coupling) which means that the magnetisation curves are disturbed.

An analytical expression that represent torque in function of current and position may be very complex if there is one. On the other hand, there have been attempted to represent the measured magnetisation curves with mathematical functions as polynomial fitting, curves fitting and splines curves. [46], [47], [48], [49].

A fast model of the magnetisation curves with reasonable accuracy is explained in [47], where the linear part of the magnetic curve (flux linkage & current) before the saturation effect point is represented by a linear function and is joined to a quadratic function after the saturation point. The normalised flux linkage against position is expressed in a nonlinear function called *gauge curve*, an improvement of this technique is presented in [48, 44].

There are many commercial packages that can be used to model the complete SRM drive. However writing your own code in your favourite language is always a flexible and handy option. All depends on how much accuracy is required and time available for the development of the application in question. There is always a trade-off between these two variables. The general steps of the basic model for time-stepping simulation have been discussed in section 2.4.

Chapter 3

Review of sensorless methods for SRM

This chapter reviews the state of the art of existing rotor position estimation methods for switched reluctance motors. The sensorless methods are classified and their basic principles are discussed. The main advantages and disadvantages of the methods are also given.

3.1 Introduction

In recent years the SRM has received considerable attention for variable-speed drive applications. Its simple construction due to the absence of permanent magnets, rotor conductors and brushes, and high system efficiency over a wide range of speed make the SRM drive an interesting alternative to compete with permanent magnet brushless DC motor and induction motor drives. To obtain optimum performance from the SRM drive it is necessary to schedule carefully the excitation current from phase to phase synchronously with the rotor position. This has necessitated the use of a mechanical position transducer attached to the motor shaft. Hall sensors, optical sensors together with slot disc, encoder or resolver attached to the shaft are normally used to supply the rotor position.

The incorporation of these rotor position sensors may lead to reliability problems in harsh environments or the cost of the direct position sensor may become an important part of the overall drive system cost for drives below one horse power. Also they increase the overall physical envelope, the weight of the motor drive and the number of extra wires. Furthermore the requirement for mechanical mounting of the rotor position transducer complicates the SRM drive design and increases the requirement for maintenance. All these are the major reasons why the SRM drive has been excluded from many cost-sensitive applications.

For the last 25 years, the dependence of the SRM drive on rotor position information has stimulated researchers to investigate methods of eliminating the position sensor and a large variety of methods have been suggested [50]. The rotor position information appears in the phase voltage equation (2.10) and therefore position estimation may be obtained from it. However accurate measurements of the inductive voltage drop and the back-EMF are difficult when the motor is running as both change strongly as a function of the motor operating point.

3.2 Classification of sensorless method for SRM

The fundamental principle of most of sensorless rotor position detection methods is that the rotor position information can be obtained from the stator circuit measurements (current, voltage at the motor terminals) or their derived parameters. The magnetic characteristics of the SRM are influenced indeed by the saturation of the stator and rotor poles. In section 2.3.1, it was shown that the relation among current, flux linkage and rotor position is strongly non-linear which complicates the detection.

The sensorless methods mainly fall into three major groups:

1. Open loop.
    - Dwell angle compensation.
    - Commutation angle compensation.
2. Energised phase.
    - Chopping waveform.
    - Regenerative current.
    - Flux linkage.
    - State observers.
    - Irregularities in stator/rotor poles.
    - Current waveform.
3. Unenergised phase.
    - Active probing.
    - Modulated signal injection.
    - Regenerative current.
    - Mutually induced systems.

The first group, also called stability torque control, does not provide a direct position indication. The motor works in open loop as a stepper motor from a variable frequency oscillator in a traditional synchronous manner, however adjustment is made to the dwell angle or commutation angle to give improved stability in pull-out torque with maximum efficiency.

The second group uses the excitation current waveform and voltage (i.e. the phase that is generating torque) to detect the rotor position indirectly. An early method

[51] senses the change in di/dt when the motor is in hysteresis current regulation. A method that makes use of the regenerative current of the phase when the rotor crosses the aligned position also belongs to this group. These methods mainly are for low speed where the current can be chopped. On the other hand, there are methods involving the detection of flux linkage or phase inductance when the rotor passes through a particular threshold value representing a specific rotor position, that may provide a continuous estimate of rotor position. Alternatively a lumped parameter reluctance network model of the motor has been proposed which indicates instantaneous rotor position. State observer methods are based on a mathematical motor model which is run in real time. Chapter 5 presents the work carried out using methods based on observers for instantaneous rotor position estimation. These methods suffer at low speed where it is difficult to measure accurately the flux linkage because of the variation on the phase resistance. On the other hand, the methods that include a full model of the motor may be limited at high speed because of the large amount of computation, in other words, the speed of the Digital Signal Processor to cope with calculations may limit the use of these sensorless methods for high speed applications. Other methods include irregularities in the stator poles, rotor poles or both. In this way the inductance profile is modified so that when the phase is excited, it is easy to detect the irregularity in the phase current which indicates a specific rotor position. The last method of this group uses the shape of the current waveform to detect if the commutation angle in leading or lagging. The commutation angle is compensated in order to have the desired current waveform. The new methods *current gradient* and *voltage magnitude sensorless method* studied in Chapter 4 belong to this group. These methods identify one specific rotor position per stroke.

In the third group, different kinds of test signals are introduced or measured during the time when a phase is normally unenergised, usually during the negative slope of the phase inductance and around the minimum phase inductance period. The test signal needs to be of low amplitude for the following reasons:

- to avoid negative torque production.
- to avoid saturation effects.
- to avoid back EMF effects.
- to minimise the power rate of additional injection circuitry where this is necessary.

The principle of these methods is to detect the inductance or flux variation from the injected signal. The methods that belong to this group are: active probing, modulated signal injection, regenerative current and mutually induced systems. These methods suffer at high speed where there may not be enough time to inject the test signal between the extinction and turn on because the excitation waveform is non-zero over the majority of the electrical cycle. Furthermore the test or measured signal is sensitive to mutual interference from excitation currents in other phases.

The basic principle, main advantages and disadvantages, speed range, dynamic capability, computational overheads, and resolution of the three major groups of sensorless methods are discussed as follows.

3.3 Open loop

In this method the motor is running synchronously from a variable frequency oscillator. The basic principle of these methods is to improve the stability of open loop drive by adjusting the dwell angle or advancing the commutation angle in order to maximise efficiency with stable pull-out torque.

When the SRM is operated in open loop, the motor frequency and the dwell angle are controlled, but load torque fixes the torque angle. Miller [52, 53] shows that the maximum pull-out torque is proportional to the dwell angle, i.e. at maximum dwell angle there is maximum pull-out torque. Also it is shown that the efficiency is inversely proportional to the dwell angle, in other words, at minimum dwell angle there

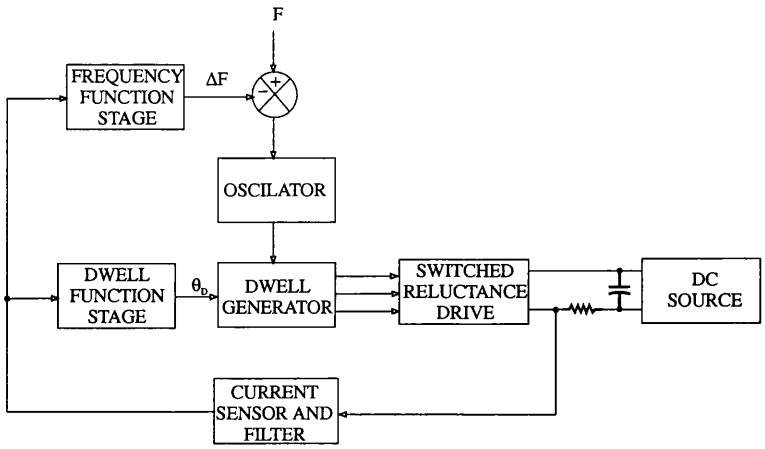

Figure 3.1: Block diagram for stabilised control by dwell angle control.

is maximum efficiency. Furthermore the two maxima (pull-out torque and efficiency) are around the same torque angle. Therefore, the dwell angle is adjusted to maintain a constant torque angle which maximises the efficiency for different load torques. When there is a load transient the dwell angle is increased to compensate the load torque maintaining in this way the torque angle. The feedback signal is the average dc-link current which is used to adjust the dwell angle i.e. with an increase in dc link current, dwell angle must be increased in order to maintain the torque angle. To improve more the stability, the frequency oscillator is also adjusted when there is a transient in load torque. Fig.3.1 shows the block diagram of the implementation. Oldenkamp [54] made some improvements to this method by adding a controller circuit which allow changes in the speed and direction of rotation. Vukosavic [55] proposed a similar method. The main difference is that the dwell angle is fixed and the commutation angle is advanced. The feedback signal is the average energy returned to the power supply i.e. the current that flows through the converter diodes.

The main advantages of these methods are: maximised efficiency with improved stability compared with the open loop control, and its low-cost implementation. The main disadvantage is that it is poor in dynamic performance because of the nature of the feedback signal, therefore it is not applicable for variable speed drives. It seems that it is applicable to motors working at constant speed with approximately constant

load. Zero speed is not possible and the method does not provide a direct rotor position signal since it assumes synchronism of the firing angles with the rotor position.

3.4 Energised phase

The methods that belong to this group are those which make use of the phase that is generating torque. The first two major publications concerning indirect detection of rotor position were published by Acarnley *et al* [51, 56] who proposed three methods. Two of them fall into this group and are explained later in this section. Another method in this group, uses the regenerative current when the rotor passes the aligned position. Alternatively, methods that use the intrinsic flux linkage characteristics of the SRM belong to this group. Furthermore, methods based on lumped parameter network and state observers make use of the energised phase for detecting rotor position. On the other hand, a method has been proposed which introduces irregularities in the inductance profile in a specific position. This method uses the energised phase to detect those irregularities. Methods which use the shape of the current waveform or its derivative also belong to this group. All these methods are explained in detail as follows.

3.4.1 Chopping waveform

Acarnley *et al* [51, 56] proposed this method in which the motor is controlled by hysteresis current regulation. The current is maintained approximately constant by a chopper in a hysteresis band $I \pm \frac{\Delta i}{2}$ as shown in Fig.3.2. The current swings around the required level at a rate dictated by the incremental inductance l. As the incremental inductance is rotor-position dependent, the instantaneous rotor position can be detected indirectly from the chopping characteristics. Rearranging 2.10 we have:

$$t_{rise} = \frac{l(i,\theta) \cdot \Delta i}{v_{ph} - R \cdot i - \left[\frac{\partial \psi}{\partial \theta}\right]_{i=cst} \cdot \omega} \tag{3.1}$$

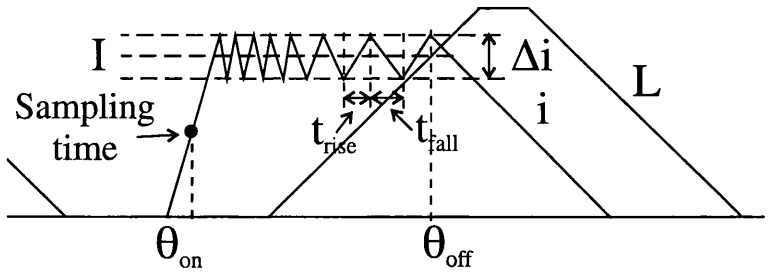

Figure 3.2: Chopped current in active phase for waveform detection method.

$$t_{fall} = \frac{l(i,\theta) \cdot \Delta i}{R \cdot i + \left[\frac{\partial \psi}{\partial \theta}\right]_{i=cst} \cdot \omega} \tag{3.2}$$

From (3.1) and (3.2), it can be observed that both t_{rise} and t_{fall} are a function of l and therefore the position can be detected assuming that the current swings in a small band relative to the mean current level. However, there are other variables which appear in these formulas, for instance the voltage drop across the phase resistance and the back-EMF which vary significantly as a function of speed operating point. The uncertainty in the phase resistance and back-EMF complicates rotor position detection using this principle. In practice $v_{ph} >> R \cdot i$ and $R \cdot i$ can be neglected. However the back-EMF, which can be comparable to the voltage supply at high speeds, cannot be neglected. Furthermore the incremental inductance is current dependent which contributes to ambiguity and extra complexity of rotor position detection. The use of t_{rise} for detecting rotor position is preferable instead of t_{fall}. The reason is that t_{rise} depends on v unlike t_{fall}, and therefore the back-EMF and $R \cdot i$ can be neglected at low speed. However, this assumption will not apply at high speed and should be compensated. A further study of this method was done by Panda [57, 58, 59] and the results showed the difficulty of estimating the position with this method. In [60] a comparison between the open loop method and the chopping current waveform method is shown which suggests some modifications to improve the stability of the method.

The main advantage of this method is that can be implemented with simple electronics. Its main application may be for drives $<$ 1kW at low speed. The major

problems of this method are: the back-EMF should be known which is difficult to measure while the motor is running, the fact that the incremental inductance also depends on the current introduces ambiguity at high current levels and the assumption of current chopping limits this method to low speeds where the back-EMF is not significant. It seems that instantaneous rotor position estimation is very difficult.

The second method proposed by Acarnley [51] is the use of the initial current gradient rather than the rise time in the chopping waveform. Obradovic [61] expanded this idea and proposed to sample at a predetermined time the current after the beginning of the commutation as shown in Fig.3.2. The current at that time being a function of rotor position governed by (3.1) (the drive still being controlled by hysteresis current control). The sampled current value is compared with a reference value representative of rotor position and the difference between them is used to control the hysteresis current reference in order to correct the desired rotor position during the next cycle. Feedback compensation is necessary to give acceptable stability. Using the current gradient at the beginning of commutation for position estimation has the advantage that the effect of the back-EMF and saturation is minimised because the sampling is done close to the unaligned position where the current is low compared with the rated current. However the method is still limited to low speed where current regulation is possible.

3.4.2 Regenerative current

This method, proposed by Reichard [62], senses the regeneration current in the energised phase, the phase is de-energised in response to such current. The SRM drive is controlled by current control with the characteristic that when the current is above the current reference the phase is off for a constant period of time (i.e. no hysteresis control). The control is in soft chopping and the freewheeling current is observed. When the rotor is in the region where the inductance is increasing, normally the freewheeling

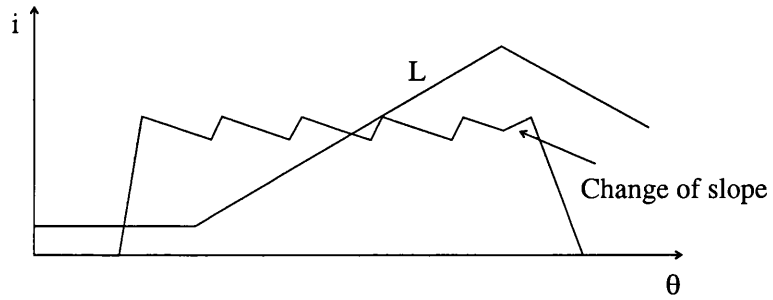

Figure 3.3: Chopped current in active phase for regenerative current detection method.

current decays along a negative slope, however when the rotor passes the aligned position the inductance starts to decrease, therefore, the negative slope of the freewheeling current is interrupted and starts to increase along a positive slope. This change from negative to positive slope of the freewheeling current indicates when the rotor passed the aligned position. Fig.3.3 shows a typical current waveform used in this method.

The main disadvantage of this method is that normally the energised phase is turned off just after the aligned position, where considerable negative torque may be generated and therefore ends up in poor efficiency of the drive. Other drawbacks are that the commutation angles cannot be advanced, and the speed range is limited to low speed where chopping is possible. This method is not applicable at standstill. It may be applicable to small motors at low constant speed operation.

3.4.3 Flux linkage

Several methods have been proposed which make use of pre-stored values of either inductance or flux linkage for detecting rotor position. For instance, Hedlund *et al* [63] proposed to identify a particular inductance value per stroke which corresponds to a rotor position in the rising inductance region. The signal which identifies the specific rotor position is created from the current in and the voltage across the phase winding without the motor drive being affected directly by the measuring process. According to the method, a known position is reached when the inductance L of the phase winding in question reaches a predetermined inductance value L_{ref}. The condition $L > L_{ref}$ is

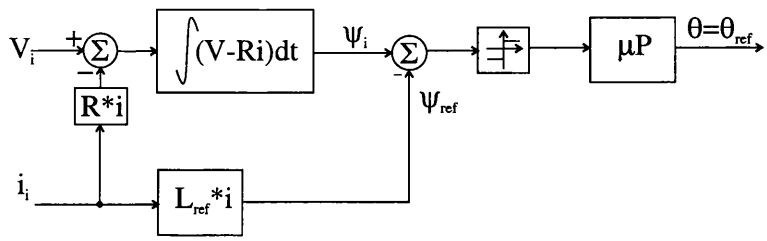

Figure 3.4: Block diagram of Hedlund's method.

calculated by comparing the integrated voltage in the phase winding to the product of the value of the actual phase current and the predetermined inductance L_{ref} as shown in (3.3).

$$\psi = \int (v_{ph} - R \cdot i)dt > L_{ref} \cdot i \tag{3.3}$$

The block diagram of the method is shown in Fig.3.4. The method uses two extra compensation factors implemented in the microcontroller box (μP). The current-dependent factor corrects the errors caused by the fact that the phase inductance varies as a function of the phase current. The second factor introduces a delay for phase commutation as a function of speed.

The method of Lyons *et al* [64, 65] makes use of a set of magnetisation curves stored in a multi-dimensional table. Phase flux linkage (calculated by integrating the phase voltage) and phase current measurements are made during motor operation in predetermined sensing regions defined over a range of rotor position. For a given flux linkage and current, the rotor position of the energised phase is estimated from the magnetisation curves taking into account mutual coupling effects. Measurements of voltage and current are made simultaneously in each phase and the rotor position is estimated continuously over the sensing region. The block diagram of the method is depicted in Fig.3.5. In order to minimise the amount of stored data, Lyons *et al* [66] proposed to store only one magnetisation curve which represents a reference position θ_{ref} between the unaligned and the aligned positions instead of a multi-dimensional table of a range of positions. The flux linkage and current of the active phase is measured continuously from the beginning of phase commutation, the current is used as an

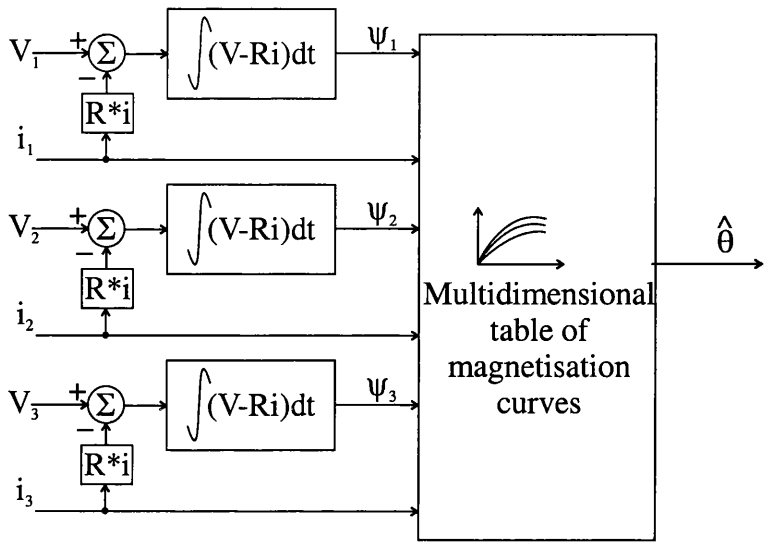

Figure 3.5: Block diagram of Lyon's method for a three phase machine.

index to look-up the reference flux linkage in a table. In Fig.3.6 the block diagram of the method is presented. Initially the measured flux linkage ψ_i is smaller than the flux reference ψ_{ref} but at some point ψ_i starts to exceed ψ_{ref}, at this time it is assumed that the rotor position has just passed the reference rotor position θ_{ref}. The calculation of rotor position is done continuously until the reference value is reached. Some extra factors are added in the calculation of rotor position to include mutual coupling coefficients. This method is quite similar to Hedlund's one. The main difference is that Lyons makes use of a vector of a magnetisation curve rather than an inductance reference with compensation factors.

Ray [67, 68], like Lyons, makes use of only one magnetisation curve which represents a rotor position between the unaligned and the aligned position. The main difference is that the calculation of flux linkage and current to estimate the rotor position is done only once. The calculation of rotor position is done after a specific time when the phase was turned on. Referring to Fig.3.7 (a), ψ_{ex} is the flux linkage which would be expected if the rotor position were identical to the reference position θ_r. The error in position is estimated by multiplying the difference $\psi_m - \psi_{ex} = \Delta\psi$ by the value of

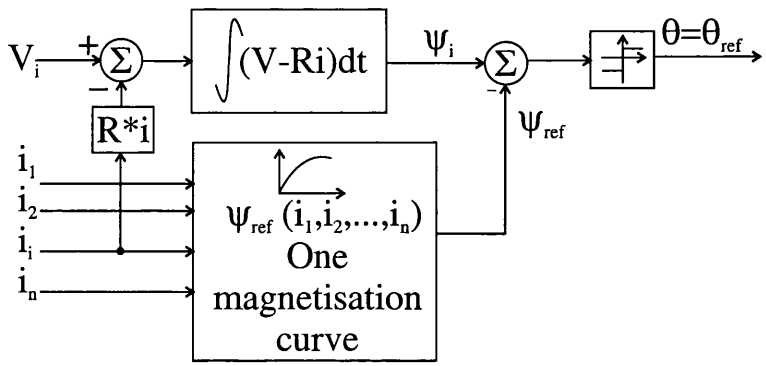

Figure 3.6: Block diagram of optional Lyon's method.

$\left[\frac{\partial\theta}{\partial\psi}\right]_{i_m}$ at the measured current i_m. This is expressed by,

$$\Delta\theta = \left[\frac{\partial\theta}{\partial\psi}\right]_{i_m} \cdot \Delta\psi \tag{3.4}$$

Since the reference position θ_r is known, the true rotor position at the measured instant may be calculated as

$$\theta_m = \theta_r + \Delta\theta \tag{3.5}$$

Fig.3.7 (b) shows the variation of $(\frac{\partial\theta}{\partial\psi})$ as a function of current for the reference rotor position θ_r. Ray also proposed to estimate the rotor position in the same way at low speed by injecting a test pulse in unenergised phase.

Alternatively, Lyons *et al* [69] proposed a lumped parameter reluctance network model of the motor, i.e. the model includes a network lump of stator, rotor and airgap reluctance terms and many of the reluctance elements are functions of rotor angle θ. Such a model takes into account multi-phase saturation, leakage and mutual coupling effects. Flux linkage and current for each phase are measured simultaneously, from which the reluctance terms of the model are determined, and then the position is estimated.

Recently, an interesting sensorless method based on current observer has been studied by Acarnley *et al* [70, 71] and Elmas [72]. This method is explained and studied in detail in Chapter 5. An example of a fuzzy logic algorithm applied to sensorless

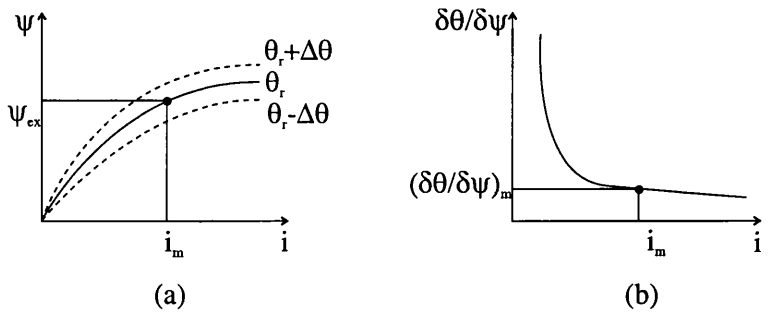

Figure 3.7: (a) Magnetisation curve, (b) $\partial\theta/\partial\psi$ as a function of current.

control of SRM is [73] by Cheok. A modification of this method to reduce the amount of computation time is done by Xu [74]. Recently, Mese [75] applied neural networks for rotor position estimation, and high performance of the drive is claimed.

The main disadvantage of all these methods is the calculation of flux linkage by integrating the phase voltage, this is because the phase resistance varies strongly with temperature, its effect is worse at low speeds where integration errors can be large. Other drawback is the necessity of pre-stored data on magnetisation curves which increases the amount of operations to be computed ending up with speed limitation of the drive. Examples of efforts to reduce computed time in these methods are [63, 66, 67]. However the price to be paid is the reduction of resolution in the estimation of rotor position. It should be noted that all these methods need an initial rotor position, therefore an initialisation routine is required at standstill.

On the other hand, the advantages offered by these methods are: immunity to the effect of saturation, applicable in a wide speed range, the mutual effect can be taken into account, good accuracy, four quadrant operation of the drive is possible. It seems that these methods are more suitable for medium and high speed applications due to the difficulty of calculating flux linkage.

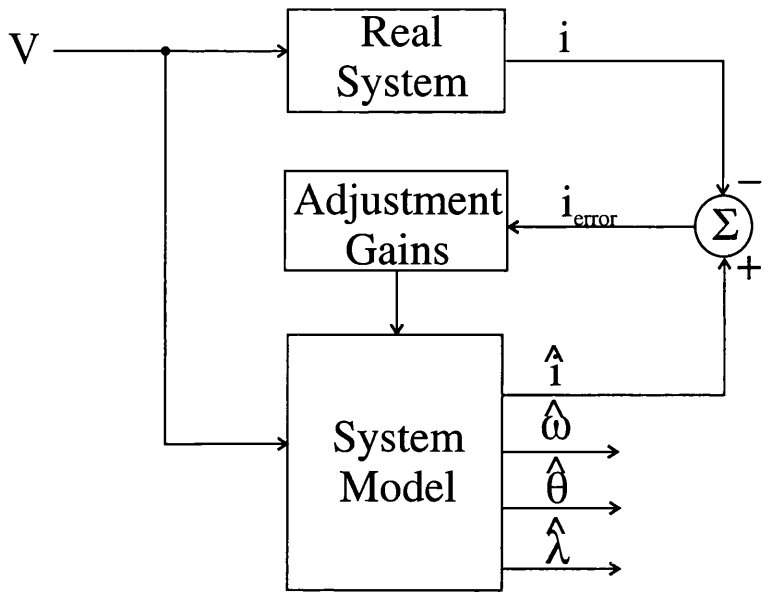

Figure 3.8: Block diagram of the system based on state observer for rotor position estimation.

3.4.4 State observers

This method was proposed by Lumsdaine [76]. A mathematical model of the complete system which includes the mechanical load is run simultaneously with the real system. In such a model, the voltage is considered to be the input and current is considered to be the output. The state variables are flux linkage, speed and rotor position. The model (3.6)-(3.9) assumes constant inertia J and viscous damping B and an inverse inductance function $H(\theta) = L^{-1}(\theta)$ which is independent of current[1]. The estimated current is compared with the measured current and the error is used as an input to the model to adjust the gains F_ψ (matrix gain), F_ω, and F_θ (vector gain). Fig.3.8 shows a block diagram of the system.

$$\frac{d\hat{\psi}}{dt} = -R \cdot H(\hat{\theta}) \cdot \hat{\psi} + v_{ph} + F_\psi(\hat{\psi}, \hat{\theta}) \cdot (\hat{i} - i) \tag{3.6}$$

$$\frac{d\hat{\omega}}{dt} = -\frac{B}{J} \cdot \hat{\omega} - \frac{1}{2 \cdot J} \cdot \hat{\psi}^T \cdot \frac{dH(\hat{\theta})}{d\hat{\theta}} \cdot \hat{\psi} + F_\omega(\hat{\psi}, \hat{\theta}) \cdot (\hat{i} - i) \tag{3.7}$$

$$\frac{d\hat{\theta}}{dt} = \hat{\omega} + F_\theta(\hat{\psi}, \hat{\theta}) \cdot (\hat{i} - i) \tag{3.8}$$

$$\hat{i} = H(\hat{\theta})\hat{\psi} \tag{3.9}$$

[1]The use of inductance independent of current implies that saturation is neglected.

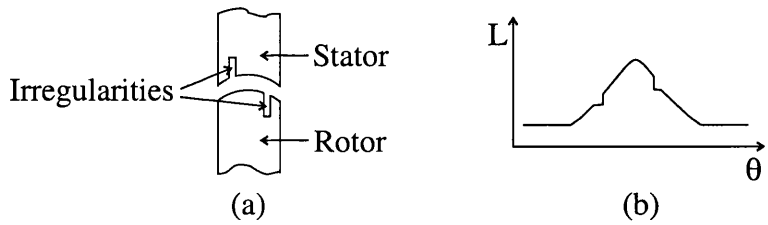

Figure 3.9: (a) Stator/rotor irregularities, (b) Modified inductance profile.

The success of this method relies on the accuracy of the mathematical model and the computational power of the hardware. The main disadvantages of this method are: complex algorithms of the complete system should run simultaneously with the real system and therefore a high speed DSP is needed which can cope with the amount of calculations, the implementation of the method requires a significant amount of extra circuitry which increases in great degree the cost, furthermore it may be limited at high speed by the speed of the DSP.

On the other hand, the advantages are: high resolution in detecting rotor position, high accuracy in estimating rotor position, applicable in the whole speed range, good performance in load torque transient, it is applicable at standstill.

3.4.5 Irregularities in stator/rotor poles

This method was proposed by Bartos *et al* [77]. The method suggests the alteration of the inductance profile by introducing an irregularity such as a notch, at least in one of the stator pole faces and/or at least one of the rotor pole phases. Fig.3.9 (a) depicts the irregularities in the stator and rotor poles and their effect in the inductance profile is shown in Fig.3.9 (b). A typical current waveform profile using this method is illustrated in Fig.3.10. The current peak is typically 30% of the peak current which is detected for rotor position estimation. One rotor position per electrical cycle can be detected. The motor should be controlled using PWM voltage control or single pulse.

The main disadvantage is that the inductance profile is affected, and therefore the torque "profile" produced by the irregular motor deteriorates and torque ripple

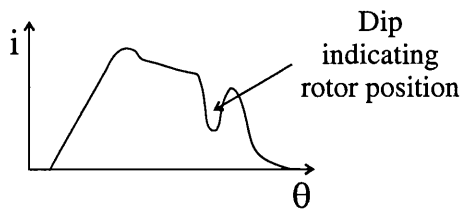

Figure 3.10: Typical current waveform with stator/rotor irregularities.

increased. The extra problem is to make the notches in the stator/rotor poles which increases the mechanical work. Rotor position estimation is not possible at standstill, and the phase should be energised over the inductance irregularity.

3.4.6 Current waveform

Sood *et al* [78] proposed a method which compensates the commutation angle as a function of the rate of change of the current waveform in an energised phase. If the actual current waveform does not match with the desired current waveform, the commutation angle is adjusted. It does not detect a specific rotor position. The motor is operated in single pulse with a constant dwell angle and the feedback signal is the DC bus current. Fig.3.11 (a)-(c) depict a current profile in the DC bus current which indicates if the commutation angle is leading or lagging. In (a), (b) and (c) commutation is considered "in phase", "lagging" and "leading" respectively. The current profile is sampled twice, one at the middle (i_1) of the commutation angle and the second just before the phase is turned off (i_2). From this information di/dt is calculated and compared with the desired value. The error indicates if the commutation angle is "in phase" and it is adjusted accordingly. Marcinkiewicz *et al* [79] improved this method introducing the sampling of three current values. The samples are made at 1/3, 2/3 of the commutation angle and the last one just before the phase is turned off. This is illustrated in Fig.3.11 (d). The sampled data is used in (3.10) which gives a more or less linear function of commutation angle at constant speed.

$$I_{curve} = 3i_e - 3i_m + i_b \tag{3.10}$$

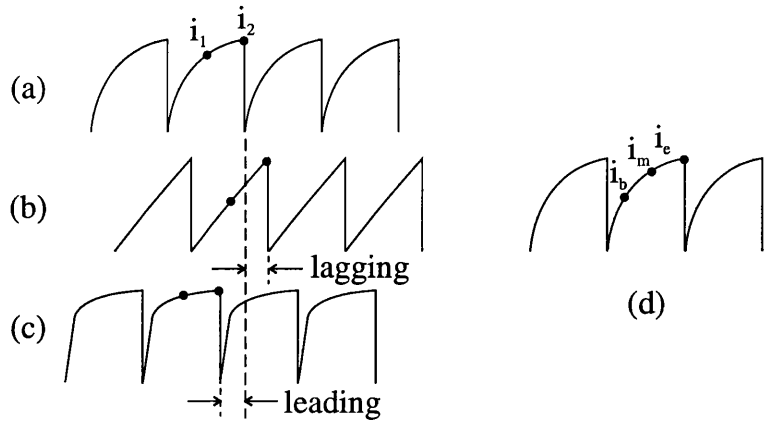

Figure 3.11: DC bus current waveforms. (a) commutation "in phase" with rotor, (b) commutation lags rotor, (c) commutation leads rotor.

The main disadvantages of this method are: the current waveform information of the specific motor is needed for a number of speeds before driving the motor, no specific rotor position is estimated. The current waveform is speed-dependent and therefore a large amount of data may be needed in order to cover the whole motor speed range. The dwell angle must be fixed at $(360/N)$ degrees. However the potential advantages are: reasonable stability for speed transients, easy implementation and four-quadrant operation.

A recent method was patented by Lim *et al* [80]. Fig.3.12 shows the circuit block diagram for one phase. The current waveform of an excited phase is differentiated direct from each phase. The resulted signal (di/dt) is amplified and compared to a reference value, the output of the comparator is used as a commutation signal (Commutation pulses 1). As an alternative option, the signal di/dt is passed through a low pass filter in order to introduce a delay. This signal is amplified and compared with a second reference value, the output of the second comparator is "OR" with the signal of the first comparator to obtain commutation signal (Commutation pulses 2). The motor is controlled in voltage control or single pulse, the dwell angle is fixed and it is suggested that the angles can be advance by adjusting the resistances and capacitances of the low pass filter. The main disadvantages of this method are: it is not applicable at standstill, inflexibility in advancing the commutation angle and the dwell angle is

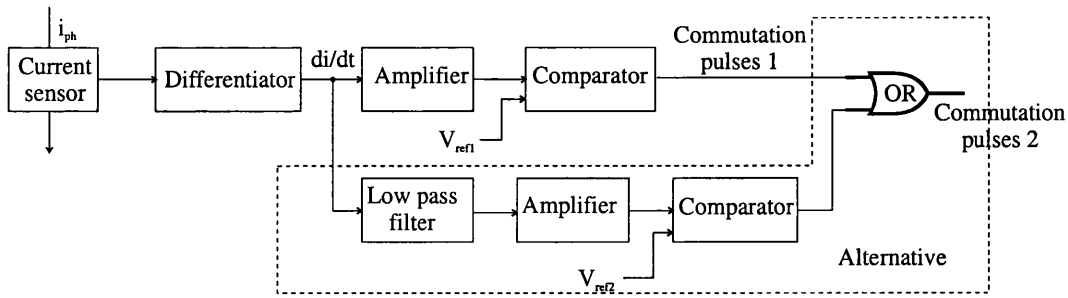

Figure 3.12: Block diagram of differentiation current waveform.

fixed, no applicable to low speed range. It seems that it is applicable to constant speed operation and limited to 2-quadrant operation. The advantages of this method are its low cost and simple implementation.

Current gradient and *voltage magnitude sensorless method* use the phase current derivative and the phase voltage respectively. Their study, development and test is explained in detail in Chapter 4.

3.5 Unenergised phase

Most of the methods of this group measure the phase inductance $L(\theta)$ in an unenergised phase which is used to estimate the rotor position. In other words, position estimation is done when the phase is not needed for torque production. Acarnley proposed a third method which uses the injection of a low level chopping current waveform in an unexcited phase. This method minimises the effect of the back-EMF and eliminates the effect of saturation, problems found in the chopping waveform method for an active phase. The current rise or fall time may be measured in an unexcited phase for rotor position estimation, in a similar manner to the use of the chopping waveform for an active phase. This method has been investigated and improved by other researches. Other sensorless methods proposed apply modulation techniques, similar to those used in communication systems, or a modulated resonant frequency to calculate the phase inductance and hence the rotor position. In another approach a lumped parameter

reluctance network model is used also in an unexcited phase by injecting low probing pulses. The last methods in this group are: the use of low level regenerative current in an unexcited phase, and the use of mutual induced voltage in an unexcited phase for indication of rotor position.

3.5.1 Active probing

Acarnley [51, 56] suggested using a low chopping current waveform in a non-torque productive phase. The probing pulses are injected at high frequency from the main power circuit. The current peak of the probing pulses is relatively small (usually 10% of the rated current) so that any negative torque produced can be neglected. The pulses are normally of fixed duration at frequencies in the range of 3 to 15 kHz.

Assuming that the pulse period is short enough, the peak current is small, and the voltage phase can be approximated as:

$$v \approx L(\theta)\frac{i_{peak}}{\Delta T} \tag{3.11}$$

Rearranging (3.11), it is found that the peak current is inversely proportional to the instantaneous value of the phase inductance

$$i_{peak} \approx \frac{v_{ph} \cdot \Delta T}{L(\theta)} \tag{3.12}$$

The phase commutation is found simply by comparing i_{peak} with a threshold value. The commutation angle can be advanced or retarded by reducing or increasing such a threshold value respectively. An alternative is to measure the inductance profile continuously which is used either as an index in a look-up table or by using an inverse function (3.13) for calculation of rotor position. Fig.3.13 depicts typical probing pulses in an unexcited phase. The probing pulses normally are injected in the phase next to be energised.

$$\hat{\theta} = G^{-1}(\hat{L}) \tag{3.13}$$

McMinn *et al* [81, 82, 83] suggested estimating the rotor position in two unenergised

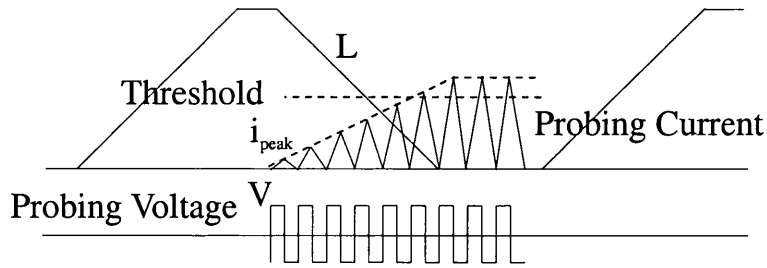

Figure 3.13: Probing pulses in an unexcited phase.

phases simultaneously to detect corruption due to switching noise or mutual coupling. If two phases are not unenergised during the sampling period, it is suggested that the extrapolated rotor position should be used instead of the instantaneous estimated value. They also suggested monitoring the variation of the supply voltage for more accurate rotor position estimation. Van Sistine [84] suggested comparing the peak current of the probing pulses in two unenergised phases. When both peak currents are equal the next phase in the sequence is energised. Hedlund *et al* [85] proposed improvements in inductance measurement by introducing a compensation factor which takes into account the mutual coupling effect. He measures $L_A(\theta, i_B)$ of phase "A" in the presence of current i_B in the active phase and adjusts this according to the equation.

$$L_A(\theta, 0) = (1 + c \cdot i_B) L_A(\theta, i_B) \tag{3.14}$$

Some of the most important disadvantages of these methods are: it is usually difficult to implement them at high speed because current flows in a phase almost over the whole electrical cycle, hence there is little room for probing pulses. For this reason the speed range is limited up to medium speed. The current in the active phase induces voltage in the unenergised phase which strongly distorts the probing pulses i.e. these methods are very sensitive to mutual coupling. There is the necessity of knowing the specific incremental inductance as a function of rotor position. It is difficult to estimate rotor position close to unaligned position due to the flatness of the phase inductance in this region.

The main advantages are: four-quadrant operation is possible, the probing pulses

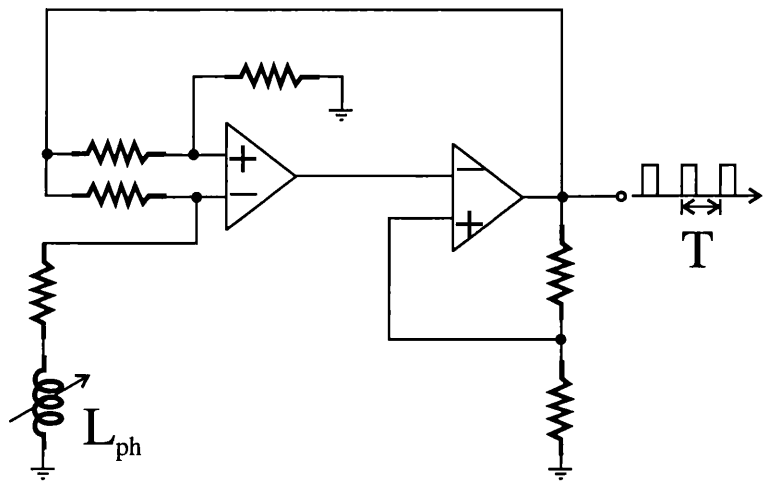

Figure 3.14: Oscillator.

are injected by the main converter itself and no extra circuit is required, it is applicable at standstill, unique rotor position information can be obtained if two phases are probed, the effect of the back-EMF and saturation are minimised for inductance measurement due to the low current used.

3.5.2 Modulated signal injection

Ehsani *et al* [86, 87, 88, 89, 90] proposed to measure the incremental inductance in an unenergised phase by different modulation techniques like those used in communication systems (frequency, amplitude and phase modulation). In the frequency injection method [86, 88], the phase winding of an unenergised phase is connected to an oscillator shown in Fig.3.14. The oscillator is designed such that the frequency f is inversely proportional to the phase inductance (3.15).

$$L(\theta) = \frac{1}{K \cdot f_{mod}} \tag{3.15}$$

The probing phase should be connected to an external frequency modulator-demodulator circuit as in Fig.3.16. The method requires a multiplexer for connection and disconnection of the modulator from the inverter. In [87, 89, 90], Ehsani *et al* suggests an alternative of the frequency injection method. Here, a low level sinusoidal voltage with fixed frequency and amplitude is applied to an unexcited phase from an oscillator

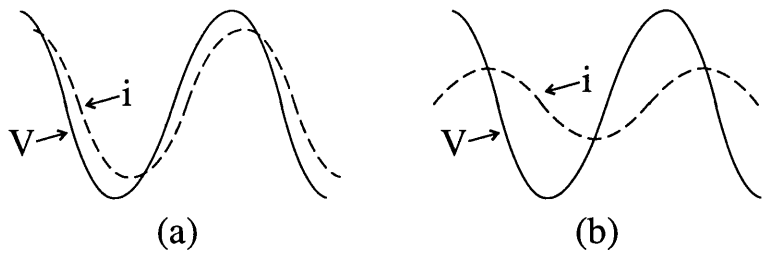

Figure 3.15: Typical signals for phase/amplitude modulation (a) aligned position, (b) unaligned position.

via a resistance. The phase displacement between voltage and current (3.16) and the current amplitude (3.18) varies between the oscillator voltage and current in function of the variation of the phase inductance. Therefore the inductance can be measured by detecting the change in either phase displacement (3.17) or amplitude (3.19). He shows that phase modulation is more sensitive at lower inductance while amplitude modulation is better at higher inductance (refer to Fig.3.15), therefore a combination of both is suggested in order to obtain better sensitivity and robustness to switching noise over the whole electrical cycle.

$$\alpha = tan^{-1}\frac{\omega \cdot L(\theta)}{R} \tag{3.16}$$

$$L(\theta) = \frac{R \cdot tan\alpha}{\omega} \tag{3.17}$$

$$I = \frac{v \cdot sin(\omega \cdot t - \alpha)}{\sqrt{R + (\omega \cdot L(\theta))^2}} \tag{3.18}$$

$$L(\theta) = \frac{1}{\omega}\sqrt{\frac{v^2}{I^2} - R^2} \tag{3.19}$$

The main disadvantages of the modulation techniques are: the connection of the oscillator to the power circuit i.e. the isolation of the sensing circuit from the power inverter. It is susceptible to corruption of the test signal due to mutual coupling effects, the specific incremental inductance should be known, an external modulator-demodulator circuit is required, hence increasing the analogue circuitry, the speed range is limited up to medium speed. On the other hand, these methods may offer four quadrant operation, the effect of the back-EMF and saturation is overcome, the inductance is

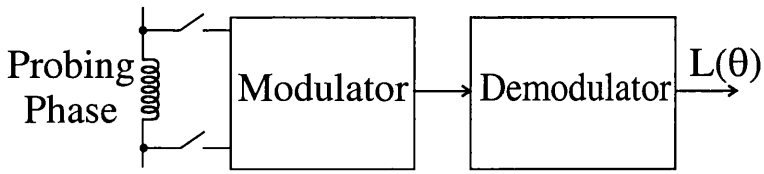

Figure 3.16: Block diagram of the modulated signal technique.

measured rather than impedance and the rotor position can be estimated with reasonably good accuracy. It may be applicable at standstill and unique rotor position information can be obtained.

The method proposed by Harris *et al* [91] includes a resonant tank (RLC) connected to an unenergised phase. A low power signal is injected into the tank of a unenergised phase similar to Ehsani's method. The characteristic resonant frequency of the tank varies between maximum and minimum values because of variation of the phase inductance. The variation of the resonant frequency is used to estimate the rotor position. The low power resonant circuit is connected to the power circuit by coupling capacitors and therefore no mutiplexer is required.

Laurent *et al* [92] shows that the use of resonant tank (RLC) increases the accuracy of inductance measurement compared with a RL circuit. Also he suggested in [93] the use of eddy current variation to estimate rotor position when the motor is operated in PWM voltage control. The main disadvantages of this method are: the motor cannot be operated in single pulse and saturation affects the rotor position estimation.

3.5.3 Regenerative current

A recent method proposed by Van Sistine *et al* [94] uses the regenerative current in unenergised phase. The phase is turned off before the aligned position, but approximately 15° after the aligned position, the upper and the lower transistor are turned on again. The upper transistor is chopped at fixed frequency in order to maintain the current about 4% of the rated current, hence no significant negative torque is generated. The

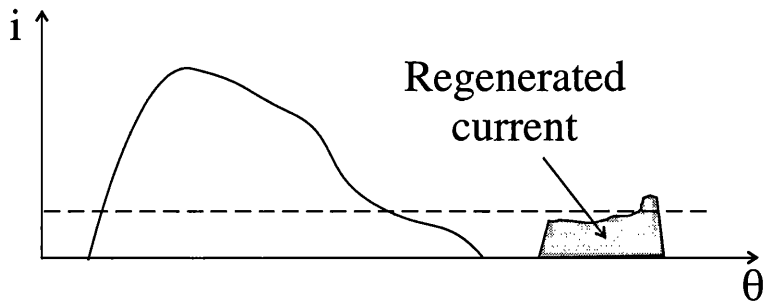

Figure 3.17: Regenerative current in an unenergised phase.

peak current is monitored and when exceeds a reference value the next phase in the sequence is energised. Fig.3.17 illustrates the principle of the method.

The disadvantages of this method are: it may not be applicable to high speed, it may generate considerable negative torque, it is not applicable at standstill. It may be difficult to advance the commutation angles, it seems that is applicable to constant speed operation. The advantages could be its easy implementation and that precise inductance data are not required.

3.5.4 Mutually induced systems

Austermann [95] proposed to use the mutually induced voltage in an unenergised phase produced by the current in the conducting phases. The induced voltage is expressed in function of the mutual flux linkage ψ_{ml} by (3.20) which varies significantly with rotor position.

$$v_{ind} = \frac{d\psi_{ml}(i_{active}, \theta)}{dt} = \left[\frac{\partial \psi_{ml}}{\partial i_{active}}\right]_{\theta=cst} \cdot \frac{di_{active}}{dt} + \left[\frac{\psi_{ml}}{\partial \theta}\right]_{i=cst} \cdot \frac{d\theta}{dt} \tag{3.20}$$

He claims that ψ_{ml} passes through zero at a known position independent of i_{active}, and therefore a position estimator is obtained. Husain [96] used practically the same method and claims good results over low speed range. The method seems to be limited to systems using current regulation because the mutual voltage induced depends on the level of the current in the excited phase and therefore the current should be constant over the conduction period (current regulation). This is the main disadvantage of this

method. Furthermore the speed range is limited at low speed. The possible advantage is that the method estimates rotor position by the direct measurement of an internal signal which is available without the injection of any diagnostic pulses.

3.6 Conclusion

All SR motors possess a unique relationship between phase inductance, phase current and rotor position. This makes it possible to measure the rotor position indirectly given information about the inductance and current. In the last few years researchers have proposed a large number of methods for rotor position estimation for SRMs, all making use of the inductance variation in one way or another. The fundamental principle of most of the methods is the detection of incremental inductance or flux linkage. It is evident that extra circuitry and computing time are required to implement any sensorless scheme. There is no method suitable for a wide range of speeds over which the torque capability of the motor is not limited, i.e. a method that replaces fully the mechanical sensor attached to the motor shaft.

The sensorless method used may differ according to the application. For instance, methods which use probing signal in an unenergised phase are more suitable for low speed because at high speed the current flows in a phase for almost all the electrical cycle and therefore there is a limited time for a probing signal. On the other hand, methods that make use of the flux linkage and current in an energised phase work better for high speed than at low speed where the calculation of the flux linkage ends up with large errors. It seems that the most suitable sensorless approach for SRM to cover the whole speed range, should combine a method of probing pulses for low speed, and a method based on active phase observers for high speed. Lyons [97] suggested using the flux linkage method to cover all the speed range. The flux linkage and current are measured using probing pulses in an unenergised phase at low speed, and the values in the energised phase are used instead at high speed.

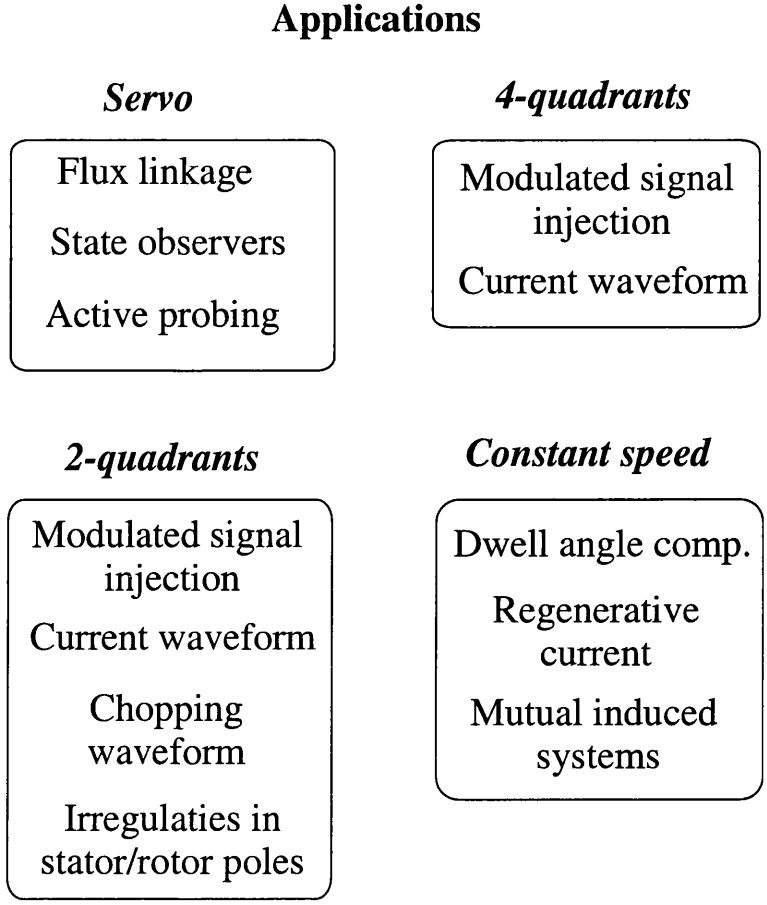

Figure 3.18: Possible application of sensorless methods.

There are many applications that require different motor performance which depends on the type of load that is driven. Fig.3.18 classifies the sensorless methods discussed here according with four main applications. For example servo applications require precise feedback of position and speed of the motor over all the speed range, in these applications an instantaneous rotor position is required. The most promising sensorless methods for servo applications may be: flux linkage, state observers and active probing which offer instantaneous estimation of rotor position. On the other hand there are applications where precise knowledge of the rotor position is not important, but four-quadrant operation is still required.

For this kind of application the most suitable sensorless methods could be: modulated frequency injection and current waveform. For applications that only require 2-quadrant operation of the motor, i.e. the motor is driven in both directions but no

braking is required, the above methods can be used with good performance but other methods, like chopping waveform and irregularities in stator/rotor poles, may be applicable. There are applications which require to drive the load at constant speed with modest load torque transient. In these applications sensorless methods like dwell angle compensation, regenerative current and mutual induced systems may be useful.

Methods such as flux linkage and state observers can be suitable for high resolution rotor position estimation in applications where the cost in not an issue but the robustness and accuracy of the system in a harsh environment are important. It is evident that there is a trade off between the resolution of rotor position and cost of extra components required for rotor position estimation. There is no cheap solution for high resolution of rotor position estimation. However the fact that every day there are more powerful digital signal processors with a lower cost may open the window of high resolution sensorless methods for most of the drive applications even those considered for low cost.

Chapter 4

Low cost sensorless methods for SRM

This chapter presents the work carried out in the study of low cost sensorless methods for switched reluctance motors. The theory of the new *current gradient (CGSM) and voltage magnitude (VMSM) sensorless methods* is introduced. Claims, advantages and limitations of these methods are presented as well. The *CGSM* is developed, implemented and tested experimentally for a three phase SRM. The detail of the implementation and experimental results are presented.

4.1 Introduction

The SRM is usually controlled in either closed-loop current control or open-loop PWM voltage control. In the former method, a current reference is kept constant in a phase winding during a stroke, in this method usually a hysteresis band is used to limit the switching frequency. In the latter method a fixed switching frequency is used and the duty cycle is varied to change the average phase voltage.

$$V_{ph} = D \cdot V_{dc}, \tag{4.1}$$

where V_{dc} = DC-link voltage and D = PWM duty cycle which is defined as the fraction of time that the switch is on with respect to the period of the switching frequency.

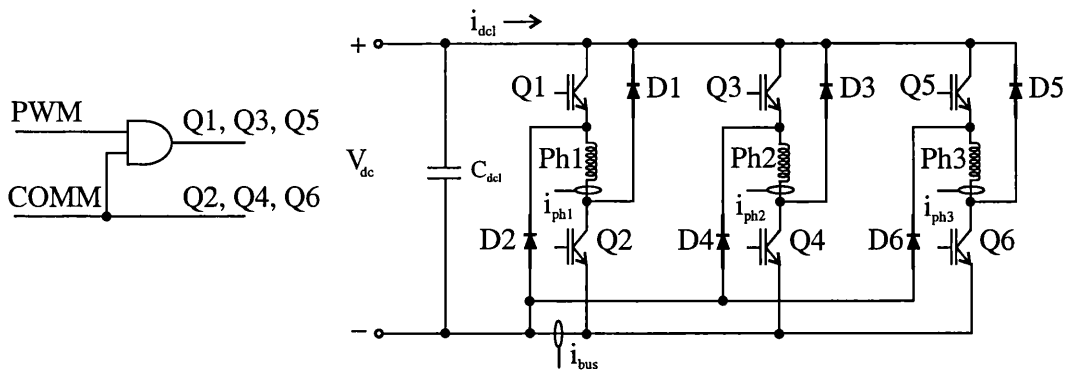

Figure 4.1: Classic SRM inverter.

The simplest way is to leave Q2, Q4 and Q6 on from θ_{on} to θ_{off} and chop Q1, Q3 and Q5 at fixed frequency with its corresponding duty cycle, i.e. soft-chopping (refer to Fig.4.1).

A common characteristics of most of the sensorless methods that have been proposed, is that they need some knowledge of the phase inductance profile. Moreover, the high non-linearities of the SRM, and changes in its parameters from one motor to another even with the same size and geometry, make these sensorless methods specific to each motor.

In these circumstances, a new method which permits:

- True rotor position detection.
- Minimum information of the SRM.
- Suitable in a wide speed range.
- Minimum risk of loss of synchronism.
- No compromise of the performance of the machine.
- Minimum computing.
- Cost effective.

is needed.

New and attractive sensorless methods proposed by Kjær *et al* [98] are *current gradient* (CGSM) and *voltage magnitude* (VMSM) *sensorless methods.* However they do not test the closed loop sensorless methods experimentally. The former is based on a differentiation of the phase current waveform when the motor is controlled by PWM voltage control. The latter is based on the change of magnitude of the average phase voltage when the motor is controlled by hysteresis current control.

These methods estimate one rotor position per stroke which corresponds to the beginning of overlap of rotor and stator poles. They belong to the subgroup *Current waveform* in the group *Energised phase* of sensorless control methods discussed in section 3.2. The main advantage of these methods is that no previous knowledge of the motor parameters is required, apart from the pole geometry.

4.2 Theory

CGSM and *VMSM* make use of phase current and average phase voltage respectively, signals. These already exist in an excited phase and are fully accessible in the motor terminals and the motor performance is not compromised by the measurement of these signals. Furthermore no probing signal in an unexcited phase, either from the main power amplifier or from external circuitry, is required. It is applicable to any regular switched reluctance machine and therefore introduction of irregularities in either stator or rotor poles is not needed.

For SRM control it is the usual practice that a phase is always excited (turned on) before the position θ_o (Fig.4.2) to avoid discontinuous torque production and guarantee sufficient current in the torque production area, i.e. from the beginning of overlap to the aligned position $(\theta_o - \theta_a)$, refer to Fig.4.2. Also the phase advance $(\theta_{on} - \theta_o)$ is varied depending on the speed and torque requested.

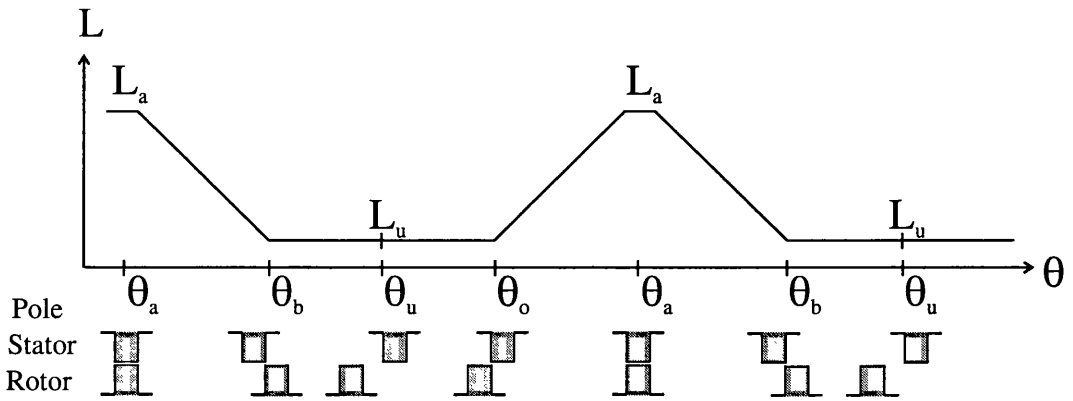

Figure 4.2: Ideal phase inductance profile for constant current.

The voltage in the phase winding, considering,

$$\psi = L \cdot i \tag{4.2}$$

$$\omega = \frac{d\theta}{dt} \tag{4.3}$$

where, L = inductance, and ω = speed. Using 4.2 and 4.3, the phase voltage is represented by,

$$v = R \cdot i + \omega \cdot L \cdot \frac{di}{d\theta} + \omega \cdot i \cdot \frac{dL}{d\theta}, \tag{4.4}$$

Let define θ_o as the rotor position where a rotor pole and a stator pole start to overlap (i.e. where the phase inductance begins to increase), and consider two situations, one just before reaching θ_o referred as "$o-$" and other just after passing θ_o referred as "$o+$". The voltage equations applied to these two situations, neglecting the voltage drop $R \cdot i$ becomes:

$$v_{o-} = \omega \cdot L_{o-} \cdot \frac{di_{o-}}{d\theta} + \omega \cdot i_{o-} \cdot \frac{dL_{o-}}{d\theta}, \tag{4.5}$$

$$v_{o+} = \omega \cdot L_{o+} \cdot \frac{di_{o+}}{d\theta} + \omega \cdot i_{o+} \cdot \frac{dL_{o+}}{d\theta}. \tag{4.6}$$

And they are valid for two rotor position near θ_o. The phase inductance at rotor position θ_o is ideally equal to the inductance at unaligned rotor position L_u (see Fig.4.2).

$$L_{o-} \approx L_u, \tag{4.7}$$

which yields

$$\frac{dL_{o-}}{d\theta} = 0 \tag{4.8}$$

Therefore, the voltage equations for the two rotor positions can be rewritten as,

$$v_{o-} = \omega \cdot L_u \cdot \frac{di_{o-}}{d\theta}, \tag{4.9}$$

$$v_{o+} = \omega \cdot L_u \cdot \frac{di_{o+}}{d\theta} + \omega \cdot i_{o+} \cdot \frac{dL_{o+}}{d\theta}. \tag{4.10}$$

4.2.1 Current Gradient Sensorless Method for PWM voltage control

Using PWM voltage control the voltage is given by

$$v = D \cdot v_{dc} \tag{4.11}$$

$$v_{o-} = v_{o+} \tag{4.12}$$

where v_{dc}, D are the DC-link voltage and duty cycle respectively. The phase is turned on before θ_o and voltage is maintained constant in a stroke, therefore (4.12) is true. Now combining and reordering (4.9), (4.10) and (4.12), it is obtained

$$\left(\frac{di_{o-}}{d\theta} - \frac{di_{o+}}{d\theta}\right) = \frac{i_{o+} \cdot \frac{dL_{o+}}{d\theta}}{L_u}. \tag{4.13}$$

As all factors on the right hand side of (4.13) are positive, it follows that the parenthesis on the left hand side must be positive as well. Hence the following inequality is always true.

$$\frac{di_{o-}}{d\theta} > \frac{di_{o+}}{d\theta} \tag{4.14}$$

The slope of the phase current

is always larger for $\theta < \theta_o$ than for $\theta > \theta_o$.

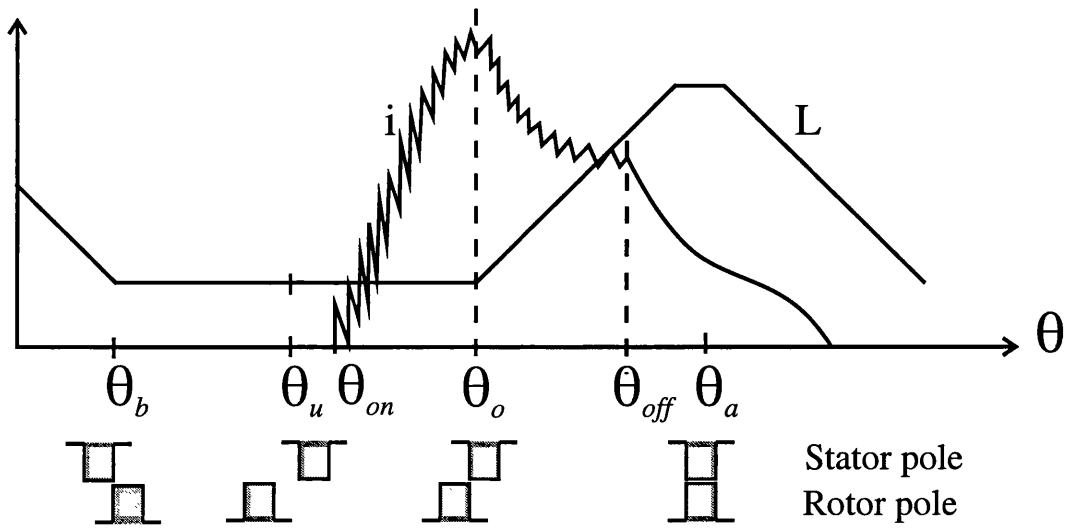

Figure 4.3: Typical current waveform for PWM voltage control.

From the aforementioned, one can say that an accurate indication of the rotor position θ_o can be detected by simply detection of the change in $\frac{di}{dt}$ (assuming constant speed). This well known rotor position is where the rotor pole and stator pole start to overlap. This is the core principle of *CGSM* as presented in [98]. Fig.4.3 shows a typical current waveform for PWM voltage control. It is clear that when the phase inductance starts to increase at θ_o, $\frac{di}{dt}$ must decrease or even become zero.

Most important, detecting the change in $\frac{di}{dt}$ indicates a rotor position which is given by motor geometry. One rotor position is estimated per stroke (energy conversion), where the stroke angle in mechanical degrees is defined as:

$$\Delta\theta = \frac{360^o}{N \cdot N_r} \tag{4.15}$$

where N_r and N are number of rotor poles and number of phases, respectively.

Current Gradient Sensorless Method for switched reluctance generator

The same principle of *CGSM* can be applied to a switched reluctance generator. For generating normally the phase is turned on before the aligned position θ_a and is turned off after θ_a but before the following θ_b, refer to Fig.4.2. Now let define θ_b as the rotor position where a rotor pole and a stator pole cease to overlap, (i.e. where the phase

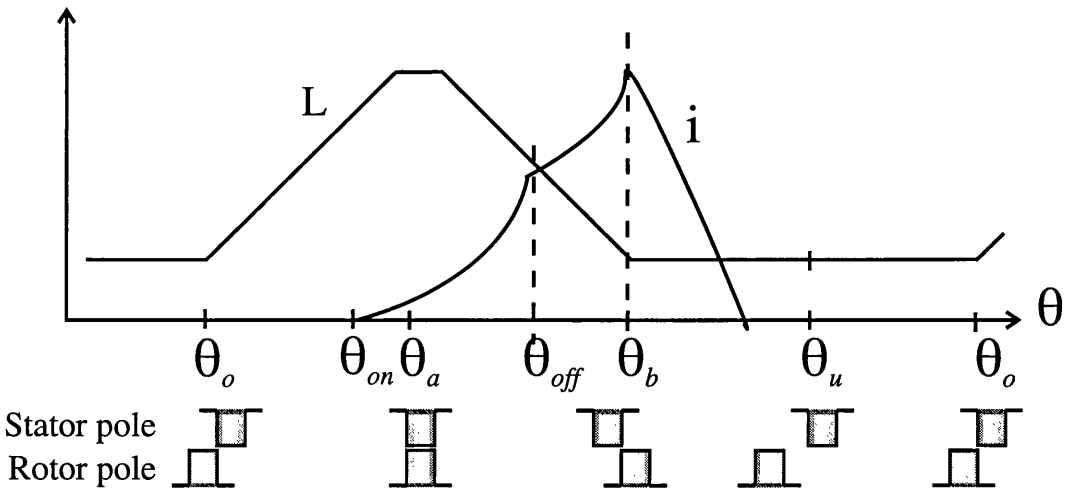

Figure 4.4: Typical generated phase current.

inductance reaches its minimum value L_u). Considering the same two situation as when motoring, the subscript "$o-$" and "$o+$" become "$b-$" and "$b+$" respectively.

$$\frac{dL_{b-}}{d\theta} = 0 \tag{4.16}$$

Assuming an ideal inductance, (4.16) is true for $\theta > \theta_b$ and therefore the voltage equations for the two rotor positions can be rewritten as:

$$v_{b+} = \omega \cdot L_u \cdot \frac{di_{b+}}{d\theta}, \tag{4.17}$$

$$v_{b-} = \omega \cdot L_u \cdot \frac{di_{b-}}{d\theta} + \omega \cdot i_{b-} \cdot \frac{dL_{b-}}{d\theta} \tag{4.18}$$

Now combining and reordering (4.17) and (4.18) assuming that the phase voltage is maintained constant i.e. $v_{b+} = v_{b-}$, while the currents freewheels through the diodes. we obtain,

$$\left(\frac{di_{b+}}{d\theta} - \frac{di_{b-}}{d\theta}\right) = \frac{i_{b-} \cdot \frac{dL_{b-}}{d\theta}}{L_u}. \tag{4.19}$$

As the right hand side of (4.19) is always negative, therefore, it is a fact that the parenthesis on the left hand side must be negative as well, so the following inequality is always true.

$$\frac{di_{b-}}{d\theta} > \frac{di_{b+}}{d\theta} \tag{4.20}$$

The slope of the generated phase current
is always larger for $\theta < \theta_b$ than for $\theta > \theta_b$.

Based on the forementioned, an accurate indication of the rotor position θ_b can be detected by simply detection of the change in $\frac{di}{dt}$. Fig.4.4 shows a typical generated current waveform. It is clear that when the phase inductance reaches its minimum value L_u at θ_b, $\frac{di}{dt}$ must decrease or even become zero. This well known rotor position is where the rotor pole and stator pole cease to overlap. Again, by simply detecting the change in $\frac{di}{dt}$ indicates a rotor position which is given by motor geometry.

4.2.2 Voltage Magnitude Sensorless Method for current control

The phase current can be assumed constant, if the hysteresis window is narrow,

$$i = i_{o-} = i_{o+} = i_{rf} = \text{constant} \tag{4.21}$$

Hence the phase current derivative before and after θ_o is considered zero.

$$\frac{di_{o-}}{d\theta} = \frac{di_{o+}}{d\theta} = 0 \tag{4.22}$$

Under this condition, the voltage equations become,

$$v_{o-} = 0 \tag{4.23}$$

$$v_{o+} = \omega \cdot i_{o+} \cdot \frac{dL_{o+}}{d\theta} \tag{4.24}$$

(4.24) is always positive, which yields,

$$v_{o-} < v_{o+} \tag{4.25}$$

The mean value of the phase voltage
is always larger for $\theta > \theta_o$ than for $\theta < \theta_o$.

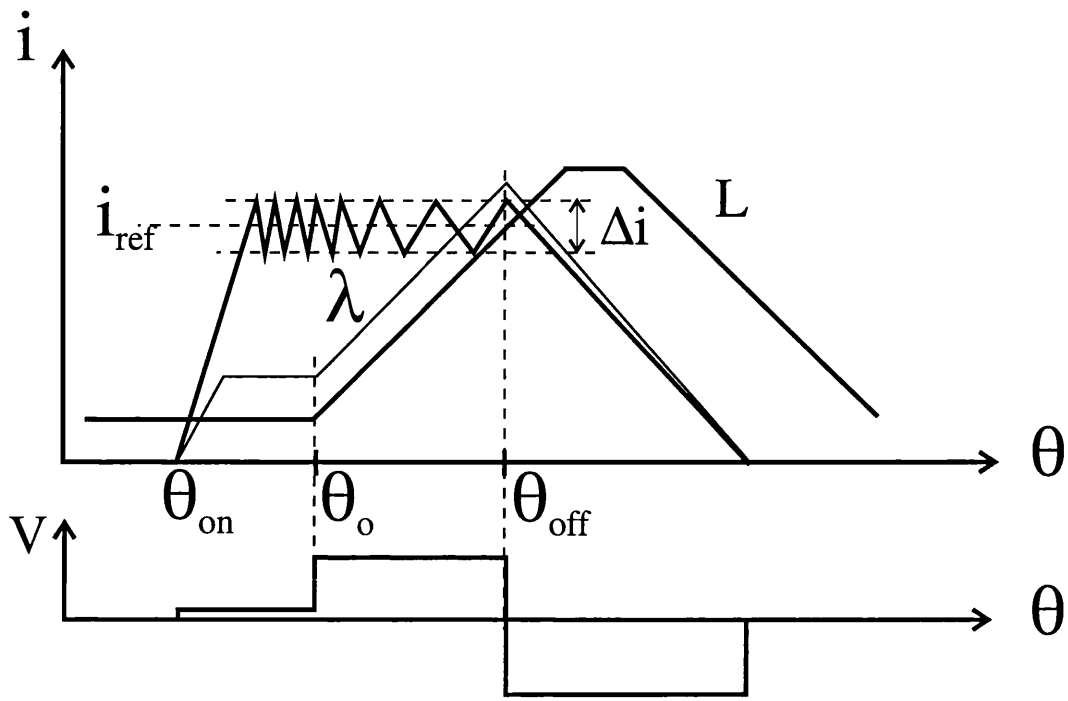

Figure 4.5: Typical phase current and average voltage waveform for current control.

This means that θ_o can be estimated by detecting the change in the average phase voltage. This is the core principle of *VMSM*. A typical current waveform for current control is shown in Fig.4.5. It is clear that the average voltage increases after the stator and rotor poles start to overlap which corresponds to well known rotor position θ_o. *VMSM* estimates one rotor position per stroke according where the mechanical angle per stroke is given by (4.15) as before.

4.2.3 Characteristics of Current Gradient Sensorless Method

Based on the theory aforementioned the following characteristics can be summarised:

1. For motoring the method is based on: *The slope of the phase current is always larger for* $\theta < \theta_o$ *than for* $\theta > \theta_o$, $(\frac{di_{o-}}{dt} > \frac{di_{o+}}{dt})$. θ_o is detected using this principle.

2. For generating the method is based on: *The slope of the generated phase current is always larger for* $\theta < \theta_b$ *than for* $\theta > \theta_b$, $(\frac{di_{b-}}{dt} > \frac{di_{b+}}{dt})$. θ_b is detected using this principle.

3. The current can be measured either independently from each phase (i.e. one current sensor per phase) or preferable from only one current sensor (i_{bus}, see Fig.4.1) in the lower commutation transistor bus (in the case of using the classic inverter or its variants in the case of other inverter topologies).

4. When using the preferable current waveform (i_{bus}) and there is excitation overlap, a simple logic is used to neglect wrong pulses and detect the correct pulse for the rotor position θ_o.

5. Two subsequent pulses which indicate θ_o as set forth in point 1 are used to interpolate linearly the instantaneous rotor position. Interpolation can be done by Phase-Locked-Loop methods. The instantaneous rotor position is used for accurate phase commutation.

6. Alternatively, pulses which indicate θ_o as set forth in 1 are delayed in function of the speed for a specific commutation angle.

7. Commutation angles can be changed freely. For motoring the only condition is that the turn on angle must be before θ_o. For generating the only condition is that the turn off angle must be before θ_b.

8. The drive must be controlled by PWM voltage control or single pulse.

9. The duty cycle can be adjusted for torque compensation.

10. The commutation angles can be adjusted for torque compensation.

4.2.4 Advantages and Disadvantages of Current Gradient Sensorless Method

The main advantage of *current gradient sensorless method* is that no *a priori* knowledge of motor parameters is required except from the number of phases and rotor poles.

Advantages

- No knowledge of inductance profile is required.
- It is applicable to any regular switched reluctance motor.
- No pre-stored data of magnetisation curves are needed.
- It is applicable for four quadrants operation of the drive.
- It does not compromise the performance of the motor.
- It allows closed-loop speed control by changing the duty cycle, commutation angles or both.
- The commutation angles can be set freely, subject to minor restriction explained as follows. In the case of motoring the condition is that the turn on angle must be before the phase inductance starts rising (θ_o). In the case of generating the condition is that the turn off angle must be before the inductance reaches its minimum value (θ_b).
- Implementation is simple with minimum extra components.
- Either the lower transistor bus current waveform (i_{bus}) or the current sensed in each phase are used as a feedback. i_{bus} allows operation with one current sensor.
- No extra computation, control requirements or compensation factors are needed.
- It allows excitation overlap.
- It allows single pulse operation.
- It permits medium load torque transients, i.e up to 0.5 pu.
- It is suitable for medium and high speed (constant power range), given that the peak in the current waveform becomes more prominent with increased speed.

The main disadvantage is that is not applicable at standstill, therefore a start-up method is required.

Disadvantages

- It is not applicable at standstill.
- It is not suitable for low speed.
- It needs a start-up procedure.
- It does not allow full load torque transients.
- Because the algorithm requires a peaky current waveform to work well, this conflicts with the preference for flat-topped current waveforms at low speeds that are used to improve efficiency.
- Current profiling is not allowed for reduction of torque ripple or noise.

4.2.5 Characteristics of Voltage Magnitude Sensorless Method

Based on the theory aforementioned the following characteristics can be summarised:

1. The method is based on: *The smoothed value of the phase voltage is always larger for* $\theta > \theta_o$ *than for* $\theta < \theta_o$, $(v_{o-} < v_{o+})$. θ_o is detected using this principle.
2. The phase voltage can be measured directly from each phase or calculated from the on time of the chopping transistor.
3. Two subsequent pulses which indicate θ_o as set forth in 1 are used to interpolate linearly the instantaneous rotor position. Interpolation can be done by Phase-Locked-Loop methods. The instantaneous rotor position is used for accurate phase commutation.
4. Alternatively, pulses which indicate θ_o as set forth in point 1 are delayed as a function of the speed for a specific commutation angle.
5. Commutation angles can be changed freely with the condition that the turn on must be before θ_o.

6. The drive must be controlled by hysteresis current control.

7. The current reference is adjusted for torque compensation.

8. Commutation angles can be adjusted for torque compensation.

4.2.6 Advantages and Disadvantages of Voltage Magnitude Sensorless Method

The main advantage of *voltage magnitude sensorless method* is that no *a priori* knowledge of motor parameters, except the number of phases and rotor poles, is required.

Advantages

- No knowledge of inductance profile is required.
- It is applicable to any regular switched reluctance motor.
- No pre-stored data of magnetisation curves are needed.
- It is applicable for two-quadrant operation of the drive.
- It does not compromise the performance of the motor.
- It allows closed-loop speed control by changing the current reference, commutation angles or both.
- The commutation angles can be set freely with the only condition that the turn on angle must be before the inductance starts rising (θ_o).
- Implementation with minimum extra components.
- It uses the phase voltage as a feedback, which already exist, to estimate the rotor position θ_o.
- No extra computation, control requirements or compensation factors are needed.

- It allows excitation overlap.

The main disadvantage is that is not applicable at standstill, therefore a start-up method is required.

Disadvantages

- It is not applicable at standstill.
- It is applicable only at low speed where current regulation is possible.
- It does not allow single pulse operation.
- It is not suitable for high speed.
- It needs a start-up procedure.

4.2.7 Summary

The theory of *current gradient* and *voltage magnitude sensorless method* has been described, which demonstrates estimation of one rotor position per stroke.

The basic principle of *CGSM* indicates that the method is applicable for four quadrant operation when the SRM drive is controlled by PWM voltage control. The feedback signal may be the current waveform of each phase, however, it is preferable the use of only one current sensor for the current waveform of the lower transistor bus i_{bus} due to significant reduction of components. It is stated that *CGSM* is suitable to medium and high speed but not at low speed. It is a fact that *CGSM* requires current flowing in the motor windings, and since at standstill there is not any current flowing through phase windings, the motor has to be started-up some how. Theoretically, it is possible to start-up the motor using *CGSM*, however practically it is not reliable. Other methods for start-up can be applied instead, for instance, feedforward method or

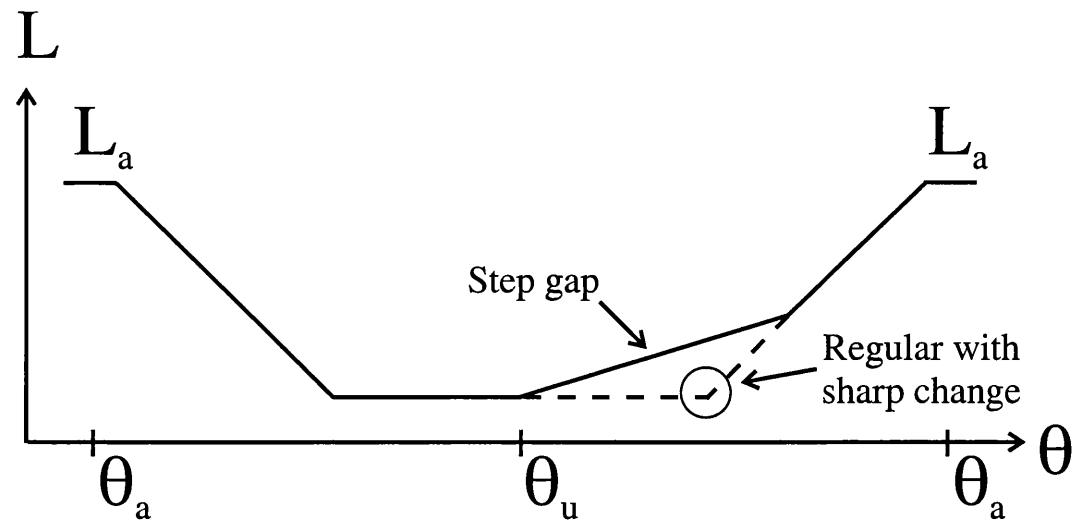

Figure 4.6: Inductance profile for a irregular motor with step gap.

injecting probing pulses in unenergised phase. These methods for the start-up sequence are explained in detail in section 4.4.

On the other hand, *VMSM* is applicable only for motoring when the SRM drive is controlled by hysteresis current regulation. The feedback signal is the average phase voltage which may be calculated from the on-time of the chopping transistor. This method is applicable only at low speed where the current can be regulated. Moreover, the characteristics, advantages and disadvantages of *CGSM* and *VMSM* have been stated. Their main advantage is that no *a priori* knowledge of motor parameters is required apart from the number of phases and rotor poles. The main disadvantage is that both methods require a start-up method. The sensitivity of these methods depends on the sharp change of phase inductance when the stator and rotor pole start to overlap (θ_o) or cease to overlap (θ_b) in the case of generating for *CGSM*. It should be noted that the ability to detect those positions is reduced or even cancelled in irregular switched reluctance motors with step gap. The step gap smooths the sharp change of phase inductance at (θ_o) which is illustrated in Fig.4.6.

Table 4.1 indicates the resolution obtained with *CGSM* and *VMSM* for different motor topologies according with (4.15). *CGSM* is comparable to the back-EMF zero-crossing method of position estimation for brushless DC motors [99]. In a 3-phase

Phases	Geometry	Stroke angle
2	4/2	90^o
3	6/4	30^o
3	6/8	15^o
3	12/8	15^o
4	8/6	15^o
5	10/8	9^o

Table 4.1: Stroke angle for different motor topologies

brushless dc machine the zero crossing of the back-EMF indicates two positions per phase per cycle while *current gradient* method according to (4.14) indicates one position per phase per cycle, and from these pulses, commutation angles can be obtained. Both motors need a start-up procedure (feedforward), when operated without mechanical position sensor.

In summary, *CGSM* is applicable to most SRM topologies in a wide power and speed range and for most inverter topologies. The method allows four quadrants operation and it is mainly suitable for medium and high speed applications.

4.3 Single current sensor for inverter topologies

Based on the theory, *CGSM* needs the current waveform of each phase as a feedback signal. The current waveform can be measured from each phase, however it requires a current sensor per phase. Alternatively, it is preferred the use of only one current sensor in the lower transistor bus (i_{bus}) in Fig.4.1 which contains the same information required by *CGSM* as all phase currents.

Fig.4.1 depicts the classic inverter topology with two transistors and two diodes per phase with the special characteristic of splitting the lower transistor bus, so that the current in the commutating transistors can be observed. The information of current waveform for each phase can also be obtained from the dc-link current, however this

signal is noisy and is changing from $\pm i_{load}$ in case of hard chopping or form i_{load} to 0 in case of soft chopping. Therefore, reconfiguration of the most common topologies is needed in order to have access to a cleaner current signal for all phases from a single current sensor. The way in which this can be done is outlined in the following paragraphs.

Diode suppression inverter topology: In order to have access to the current in each phase from one current sensor, the positive rail is split in two. One bus connects all the phase windings and the other connects all the freewheeling diodes. The current sensor is put as shown in Fig.4.7 (a) which measures current when either the transistor is on or off. The current signal i_{bus} can be used as a feedback for *CGSM*. The same configuration applies to inverters with resistance and zener diode suppression.

Bifilar inverter topology: To access the current in each phase from one current sensor the positive rail is split in two. The first bus is for the phase coil connected in series with the transistor and second bus is for the phase coil connected in series with the diode. The second bus passes through the current sensor i_{bus} in the direction shown in Fig.4.7 (b) in order to measure the correct current polarity.

Split rail inverter topology: The configuration which allows the current measurement of each phase from a single current sensor is shown in Fig.4.7 (c), the lead from the middle rail to the lead of the second phase winding is passed through the current sensor i_{bus} as shown.

$N+1$ **switches inverter:** For this topology it is not necessary to split any rail, the current sensor i_{bus} is simple put as shown in Fig.4.7 (d) for measuring the excitation current of every phase.

C-dump inverter: The current sensor i_{bus} is placed as shown in Fig.4.7 (e) to have access to the current information of each phase required by *CGSM*.

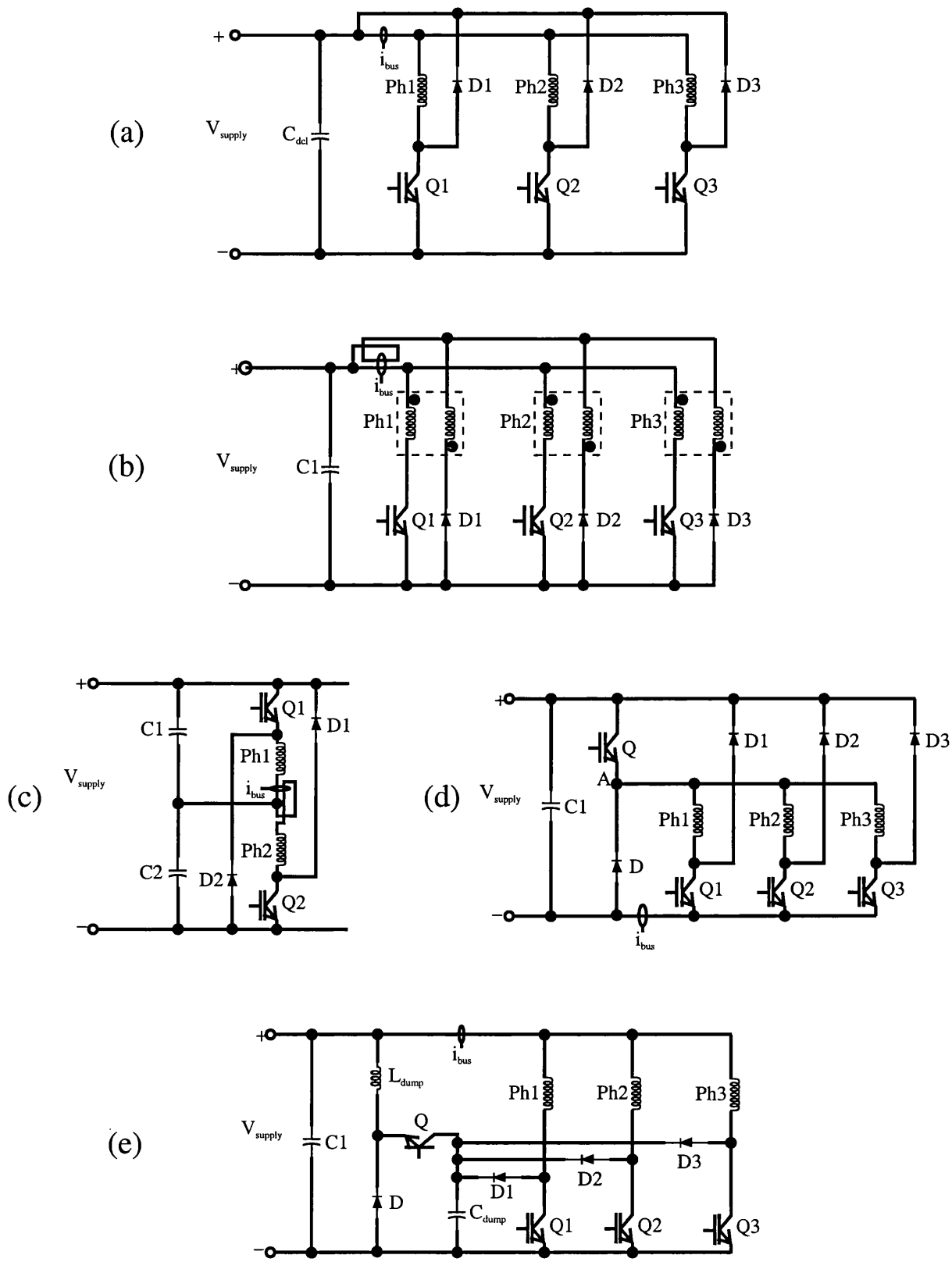

Figure 4.7: Placement of current sensor in different inverters. a: Diode suppression inverter, b: Bifilar inverter, c: Split rail inverter, d: N+1 switches inverter, e: C-dump inverter.

In any system, the use of minimum components for implementation is desired without compromising the quality of the information required. Minor modification or a place where to put the current sensor of the most common inverter topologies has been suggested in order to obtain the excitation current waveform of every phase from only one current sensor.

4.4 Start-up procedures

As explained in section 4.2, *CGSM* and *VMSM* make use of the phase current waveform and the average phase voltage waveform respectively which are signals that already exist in the excited winding. However, the problem arises at standstill where there are no currents flowing through the motor windings. Based on the theory aforementioned, it is possible to start-up the motor with *CGSM* and *VMSM*, but practically may not be reliable.

Therefore, three possible methods are suggested for start-up. These are applicable to both *CGSM* and *VMSM*, however they are discussed only for *CGSM*. A brief description of each one is given before the details of each option are explained.

Self-synchronisation: This method is based on the basic principle of *CGSM*. First the motor is aligned to phase one, then the next phase in the sequence, according to the desired direction, is energised. The current is observed and a pulse is obtained which may correspond to θ_o. This pulse is used as the rotor position for phase commutation. After three or four electrical cycles the motor is in synchronism.

Feedforward: The motor is controlled in feedforward open-loop as a stepper motor. A train of pulses with an initial frequency is applied to the motor windings in a sequence according to the desired direction. The frequency is increased linearly and it is assumed that the rotor follows it. In this manner the motor is accelerated up to the speed where sensorless pulses can be detected by *CGSM*.

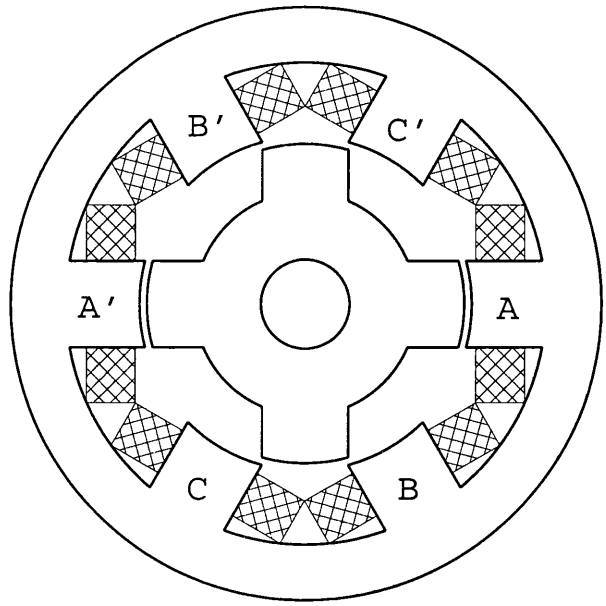

Figure 4.8: 6/4 3-phase SR Motor.

Active probing: This method makes use of small probing pulses in all phase windings in order to identify the rotor position at standstill. With this information, the correct phase is energised according to the desired direction of rotation. Once the first phase in energised, small probing pulses are injected in the next phase to be energised. The rotor position is extracted by probing pulses, and used for phase commutation. The motor is accelerated up to the speed where sensorless pulses can be detected by *CGSM*.

4.4.1 Self-synchronisation

Depending on the desired direction of rotation, the rotor can be aligned either to phase B or C, in order to place phase A in a position with enough torque to start up. It should be noted that in a three phase machine when one phase is at aligned position θ_a the others two are in θ_o, refer to Fig.4.8. The same principle can be applicable to other motor topologies.

After the initial rotor alignment, phase A is energised. In the first electrical cycle, an uncontrolled high peak current appears, the current is observed and the detection

circuit produces a pulse when there is a significant change in $\frac{di}{dt}$, which may not correspond to θ_o, i.e. it is at a random position between θ_u and θ_a. However this initial pulse allows commutation of the phases sequentially according to the direction of rotation (A-B-C or A-C-B). After two or three electrical cycles the correct rotor position is detected. This method permits a start-up of the motor even under load but neither efficient or optimal. At the first electrical cycle a peaky current waveform is observed, which can be reduced if a duty cycle smaller than 100% is applied.

The disadvantage of this method are the non-controlled high peak current in the first electrical cycle which may damage the phase windings and generate excessive torque, and most important the uncertainty of rotor position estimation θ_o. This method is erratic and the motor may not start smoothly.

4.4.2 Feedforward

It is a requirement of the CGSM that the phases conduct non-zero current but also that the waveform resembles that of Fig.4.3. Therefore a feedforward (open-loop) procedure, in similar manner as stepper motor [100], is used to accelerate the motor from standstill to a take-over speed where the waveform conditions are met.

The goal is for the motor to generate enough torque to accelerate up to the speed at which the sensorless pulses from *CGSM* can be detected. The take-over speed is defined as the speed at which the motor goes from being operated in feedforward (essentially as a stepper motor), to true sensorless operation (feedback).

The starting characteristic (pull-in torque) of a SRM when operated in open-loop is load dependent. There is a range of frequencies where the motor can start without losing synchronism. In Fig.4.9 it is shown that the pull-in torque range decreases if load inertia increases. Therefore, it is very important to take into account the inertia coupled to the motor shaft. The equation of motion of the motor is,

$$T = J \cdot \frac{d\omega}{dt} + B \cdot \omega + T_f \tag{4.26}$$

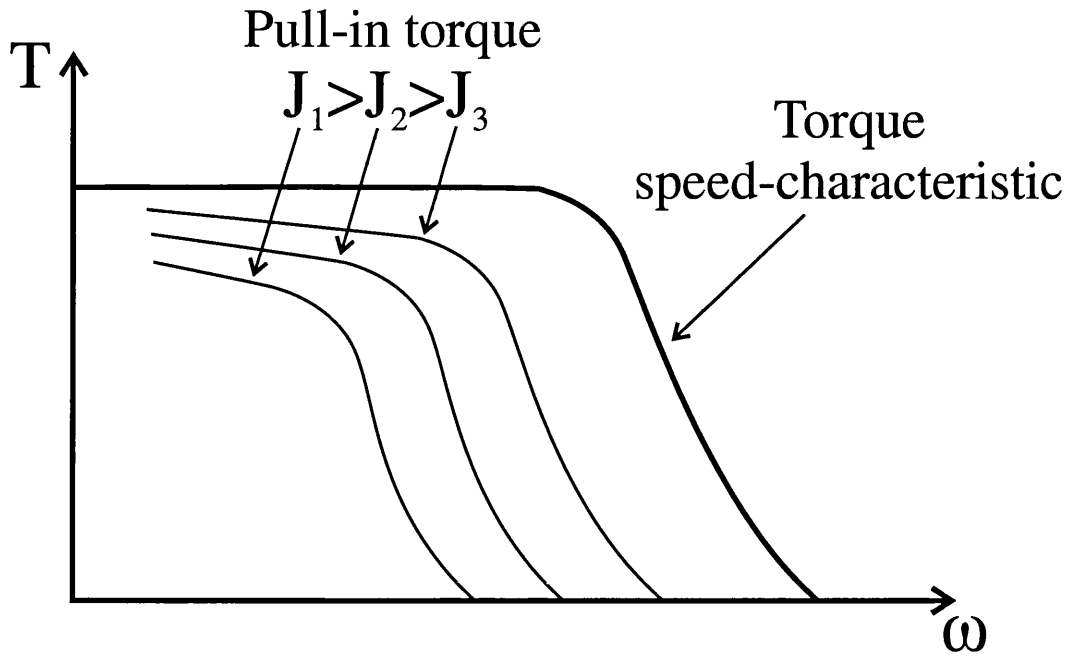

Figure 4.9: Variation of pull-in curves with load inertia.

where, T = torque produced by the rotor, J = total inertia of rotor and load, B = viscous frictional damping, T_f = frictional load torque independent of speed.

If the viscous friction term is negligible and the motor torque is constant in the speed range under consideration, the integration of (4.26) is obtained,

$$\omega = \frac{T - T_f}{J} \cdot t + \omega_1 \tag{4.27}$$

where, ω_1 = angular speed before acceleration starts.

Thus the motor can be accelerated linearly (at a constant rate) as shown in Fig.4.10. The motor must be capable of starting without missing steps at the initial frequency ω_1. The time of the ramp is dependent on load torque inertia. When the load torque is increased, the time of the ramp must be decreased to such value which assures the synchronism of the motor.

The feedforward method works as follows: a train of pulses is applied to each phase in sequence according to the direction of rotation. Each phase pulse-train is phase shifted 30° mech. (120° elec.). To start the motor, first the frequency of pulses applied is fixed to a such low value that the motor can follow it, after the frequency

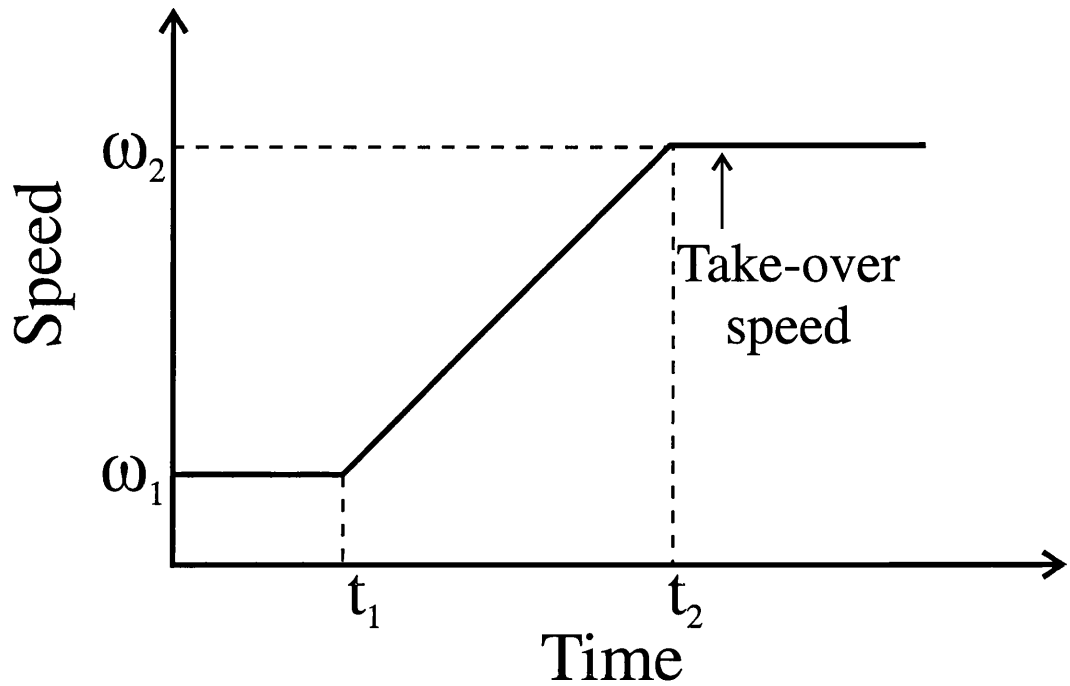

Figure 4.10: Linear acceleration in the start-up sequence.

is increased linearly to a value determined by a pre-defined take-over speed. When the SRM is operated with PWM voltage control in open loop, the variables that can be controlled are the motor frequency, the dwell angle and duty cycle, while the load torque fixes the torque angle (i.e. where the phase is commutated).

For the start-up sequence, the following is considered: set the take-over speed (i.e. the final value of frequency ramp), and control either the dwell angle or the duty cycle. However, a fixed dwell angle of 30^o mech is desired in order to assure a large range of pull-out torque and avoid discontinuous torque production, [53, 34]. Therefore, control of the duty cycle is preferable in order to obtain a current waveform like that shown in Fig.4.3, i.e. a waveform with at least one peak. Note that there is a duty cycle which produces such a current waveform at given take-over speed.

There are two options to control the duty cycle: (a) apply an initial low duty cycle and increase it to the final value which gives the desired current waveform, (b) apply maximum duty cycle (100%) and decrease it down to the final value which gives the desired current waveform. In the former, the initial and final duty cycle need to be

set according to the load attached to the motor shaft, while in the latter only the final duty cycle requires to be set. At the beginning the current is limited but as the motor is accelerated the back-EMF increases and the current limit goes off. Option (b) is preferable because only the final duty cycle needs to be set and gives maximum pull-out range at standstill, which assures a robust start-up in a range of load torque. Once the motor is accelerated and the current waveform conditions are met, *current gradient position estimation* (CGPE) pulses from *CGSM* are detected and used for phase commutation.

It should be noted that the limitation for the minimum take over speed is the torque pulsation because, this makes that the speed changes significantly in an electrical cycle. In consequence, the linear extrapolation of rotor position by PLL between two sensorless pulses is not correct.

The proposed start-up sequence is summarised as follows:

- Set a maximum current limit.
- Set the duty cycle at 100%.
- Apply a train of pulses with low fixed frequency ω_1 to the motor windings for a short time.
- Increase the motor frequency linearly up to the take-over speed.
- Decrease the duty cycle linearly down to the final value according to load torque.
- Swap from open-loop to true sensorless operation.
- Adjust the time of the ramp according to the load.

The start-up procedure for a take-over speed of 500, 750 and 1000 rpm was simulated, and the PWM duty cycle was decreased to 33%, 50% and 67%, respectively in order to assure the current waveform where CGPE pulses can be detected. The top

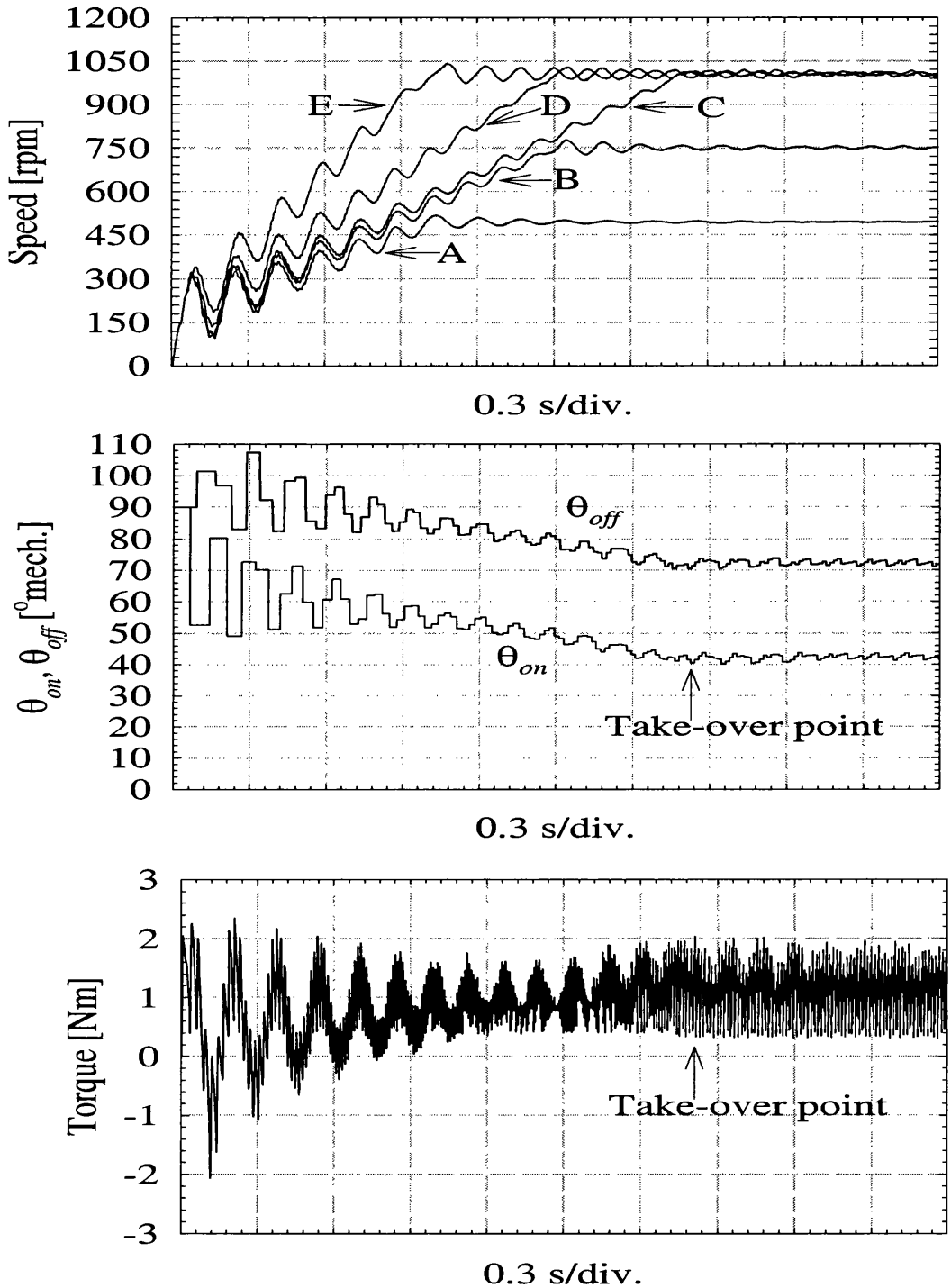

Figure 4.11: CGSM feedforward start-up (simulated). Top: speed for different accelerations, A: 500 rpm, 1s, B: 750 rpm, 1.5s, C: 1000 rpm, 2s, D: 1000 rpm, 1.5s, E: 1000 rpm, 1s. Centre: firing angles. Bottom: instantaneous torque.

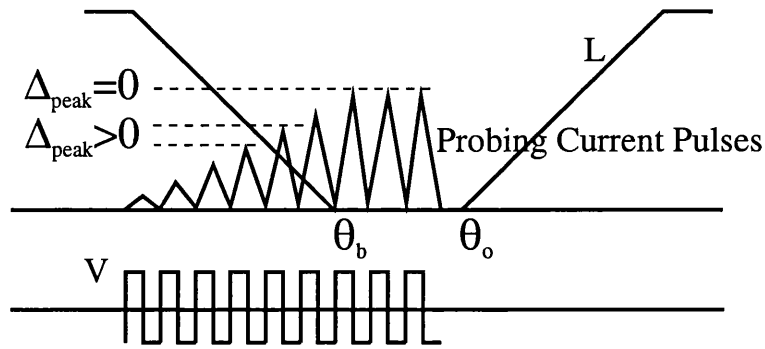

Figure 4.12: Probing method for start-up sequence.

graph of Fig.4.11 shows the results. For the case of take-over at 1000 rpm, three traces are shown which correspond to different accelerations. The ramp time can be adjusted depending on the load-torque. It is important to mention that the condition required for *current gradient* sensorless method may not be met for speeds below 200 rpm, for the particular drive analysed here. Fig.4.11 (center) depicts θ_{on} and θ_{off} corresponding to a take-over speed of 1000 rpm with a ramp time of 2s. The ripple shows how the commutation angles move in order to match the load-torque during the start-up sequence (as a stepper). It is clear that θ_{on} occurs before θ_a and θ_{off} occurs after θ_a. At the take-over speed, θ_{on} is around 43° and θ_{off} is around 73°, at this time θ_o can be estimated. Fig.4.11 (bottom) depicts the instantaneous torque during start-up. It shows that at the beginning there are significant torque oscillations, but these are limited at the take-over point. This method assures robust start-up even with load but neither efficient nor optimal start-up of the motor.

4.4.3 Active probing

Active probing method is based on high-frequency-low-power testing pulses in unenergised phases [51]. At standstill, probing pulses are injected in all phases in order to determine the actual rotor position. From this information the correct phase in the sequence is energised according with the desired direction.

The method proposed here to start-up the motor is as follows. The testing phase

is the unenergised phase next to be energised. The probing pulses are injected at fixed frequency with a with a duty cycle less than 50%. When the rotor position reaches θ_b (refer to Fig.4.12) the inductance is approximately constant and equal to L_u, in consequence the peak of the probing pulses is approximately constant as well. Therefore, θ_b can be detected when the peak of two consecutive pulses are equal. In this manner, the position when the inductance reaches its minimum value L_u can be detected regardless of the specific inductance profile by making use of the flatness of the inductance profile at unaligned position $(\theta_b - \theta_o)$. The method is illustrated in Fig.4.12. Once θ_b is detected, the phase is commutated and testing pulses are injected to the next phase in the sequence. The current in the energised phase is regulated by hysteresis current control. In this manner the motor is accelerated up to the take-over speed where CGPE pulses can be detected.

4.4.4 Summary

It has been stated that it is possible to start-up the motor using the basic principle of *CGSM*, however there is an uncertainty of rotor position estimation θ_o in the first two cycles which may cause an erratic start-up. Hence, it is not feasible to use it. Alternatively, a feedforward method can be applied to the SRM in similar manner as stepper motor. The motor is accelerated linearly up to the take-over speed where CGPE pulses can be estimated. This method assures robust start-up from standstill even under load that is reliable and smooth but neither efficient nor optimal. Optionally probing pulses method for start-up is explained. The position θ_b at minimum inductance is detected and used for phase commutation. Using this method the motor is accelerated up to the take-over speed where CGPE pulses can be estimated. In this method the start-up sequence may be more efficient, however the implementation is more complicated than feedforward. In this circumstances, the feedforward method is preferred to start-up the motor due to its easy implementation and smooth and robust start-up from standstill up to the take-over speed.

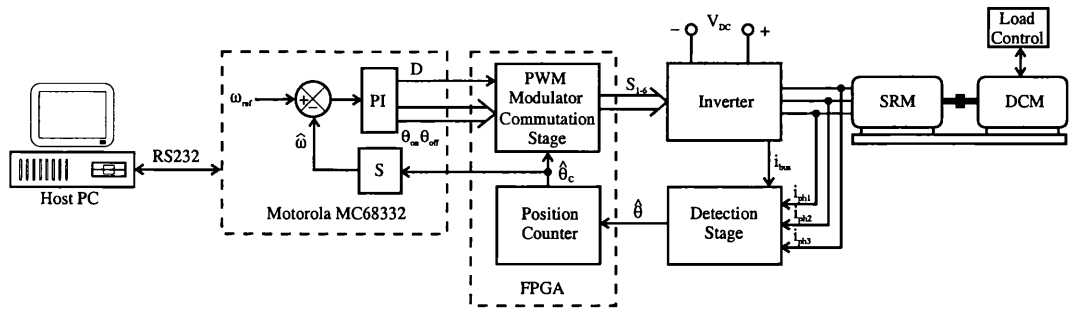

Figure 4.13: Block diagram of set-up.

4.5 Implementation of Current Gradient Sensorless Method

The fully sensorless closed-loop speed control system has been implemented for a 3-phase 6/4 switched reluctance motor, see Table 4.2, based on the theory of *CGSM* described in section 4.2. Fig.4.13 depicts the block diagram for the complete set-up of the control structure. The system includes: detection stage, start-up sequence, commutation stage, speed closed-loop PI control and inverter. The hardware consist mainly of a microcontroller (MC) MC68332 from Motorola which has been used to implement the PI-controller and the start-up sequence, a fully analog circuit for the detection stage, a Field-Programable-Gate-Array (FPGA) which is used for the commutation stage and the PWM modulator.

4.5.1 Implementation of hardware controller

The controller includes four speed wire boards which are connected to the back-plane of a full size rack, see Fig.4.14 (a). A Motorola Business Computer Card was used for the microcontroller board which is shown in (b). On the front panel there are one reset bottom and two connectors, (9 pin D connector for RS232 serial communication with the Host PC and 10 pin IDC connector for background debug mode). The commutation board contains a FPGA Xilinx XC3195A where the commutation logic and the PWM modulator are implemented. Also includes comparators and operational

Phases	3
N_s	6
N_r	4
Stator pole-arc	33.12^o
Rotor pole-arc	37.8^o
Air-gap	0.15mm
Phase resistance	$4.79 \pm 0.10\Omega$
Stator OD	$71.7 \pm 0.01mm$
Stator ID	$61.0 \pm 0.01mm$
Rotor OD	$38.5 \pm 0.01mm$
Rotor ID	$25.4 \pm 0.01mm$
Stack length	$50.8 \pm 0.01mm$
Shaft dia.	$12.0 \pm 0.01mm$
Max. inductance L_a not saturated	$118.0 \pm 0.02mH$
Min. inductance L_u	$14.66 \pm 0.02mH$
Ratio L_a/L_u	8.049
Total motor weight	1.895 kg
Wire diameter	0.6 mm
I_{max}	6 A
I_{rms}	3.46 A
Rated torque	0.7 Nm
Rated speed	800 rpm
DC-link voltage	70 V

Table 4.2: 3 phase SR Motor rating.

amplifiers for delta current regulation. The picture of this board is shown in (c). On the front panel there is a 10 way screw lock connector used to receive the signal from a 1024-line encoder, which is used for comparison with the estimated position. The I/O board is formed by a FPGA Xilinx XC3068 where the combination of PWM and commutation signal take place. The 6 output drive signals for the transistors are made through 6 optical drives allocated on the front panel, it also has 6 optical drives for general I/O signals. (d) depicts a picture of the board. Four identical detections stages are implemented in the detection board, one for each phase and one for the lower transistor bus. The detection stage is fully analog and is made using operational amplifiers, resistors and capacitors. Its circuit diagram is shown in Appendix C Fig.C.5. A picture of the board is shown in Fig.4.15. On the front panel there is a 10 way screw lock connector where each analog current signal is received.

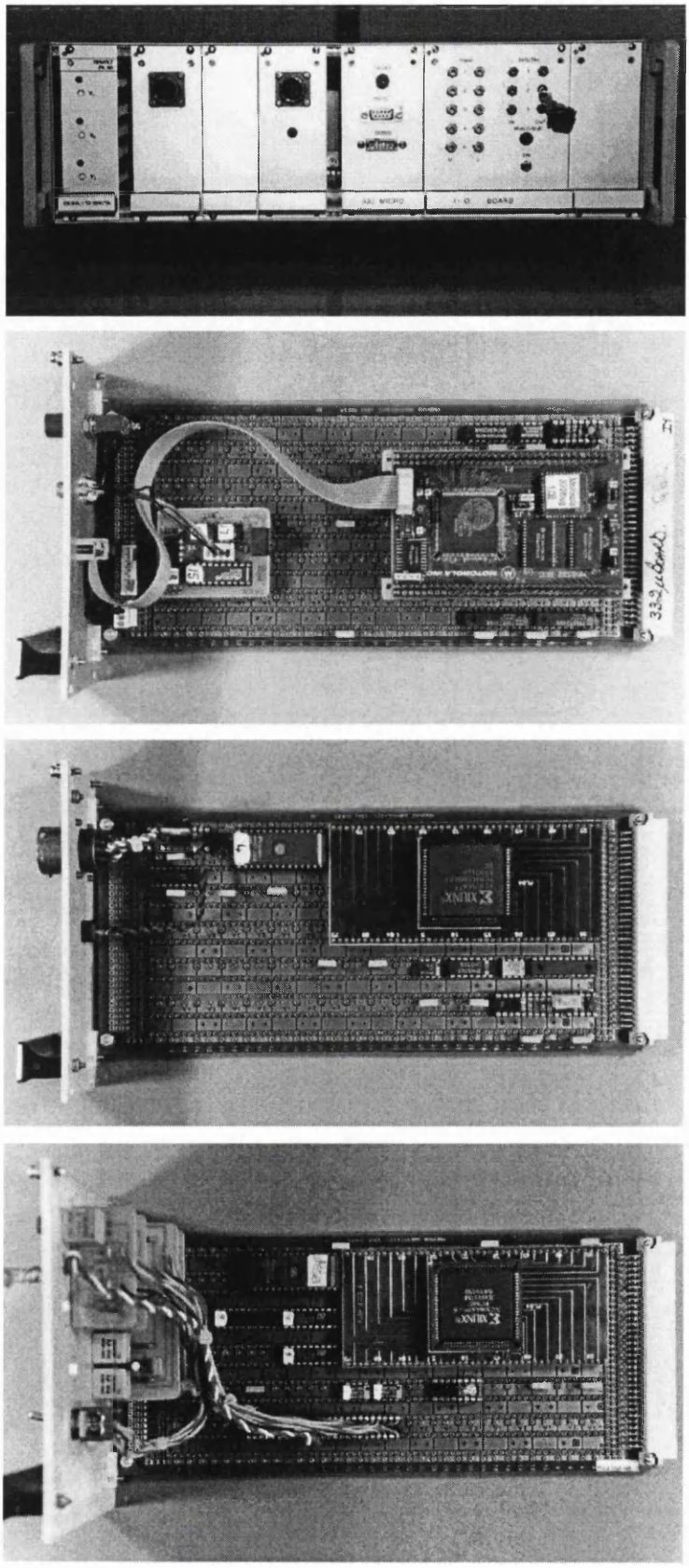

Figure 4.14: Controller pictures. a: Controller rack, b: Microcontroller board, c: Commutation board, d: I/O board.

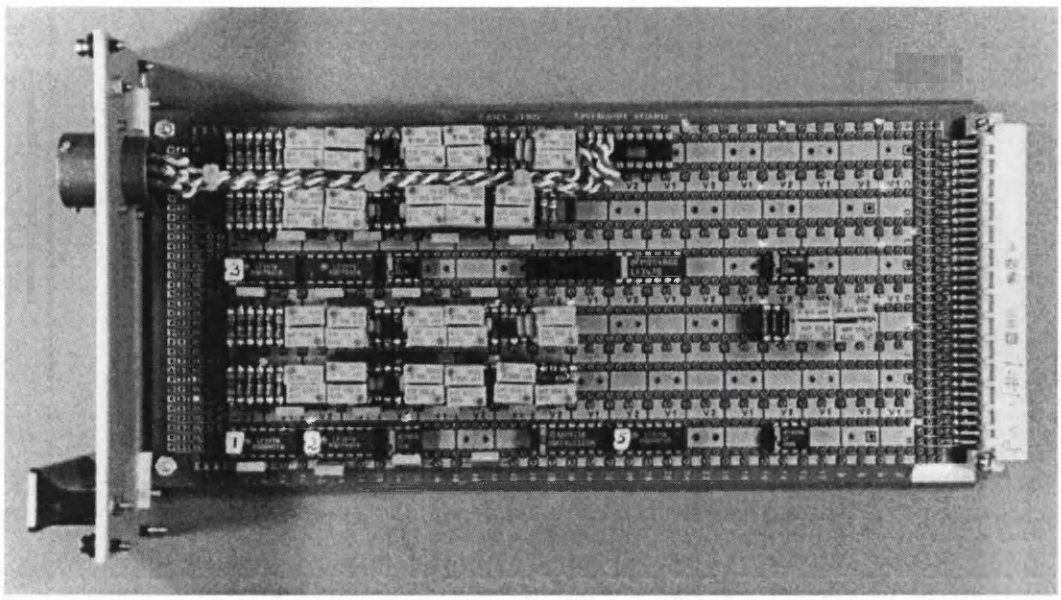

Figure 4.15: Picture of detection stage board.

4.5.2 Microcontroller MC68332

The microcontroller MC68332 was chosen to develop the *CGSM* due to its flexibility, however a less powerful microcontroller can be used. The MC68332 is fixed point and its main features are (for further information refer to [101]):

- 32-bit processor
- 24-bit address bus
- 16-bit external data bus
- 16-20 MHz clock
- 2 kB on-chip RAM
- 12 programmable chip selects
- 16 16-bit intelligent timer channels (TPU)
- 7 maskable interrupt lines

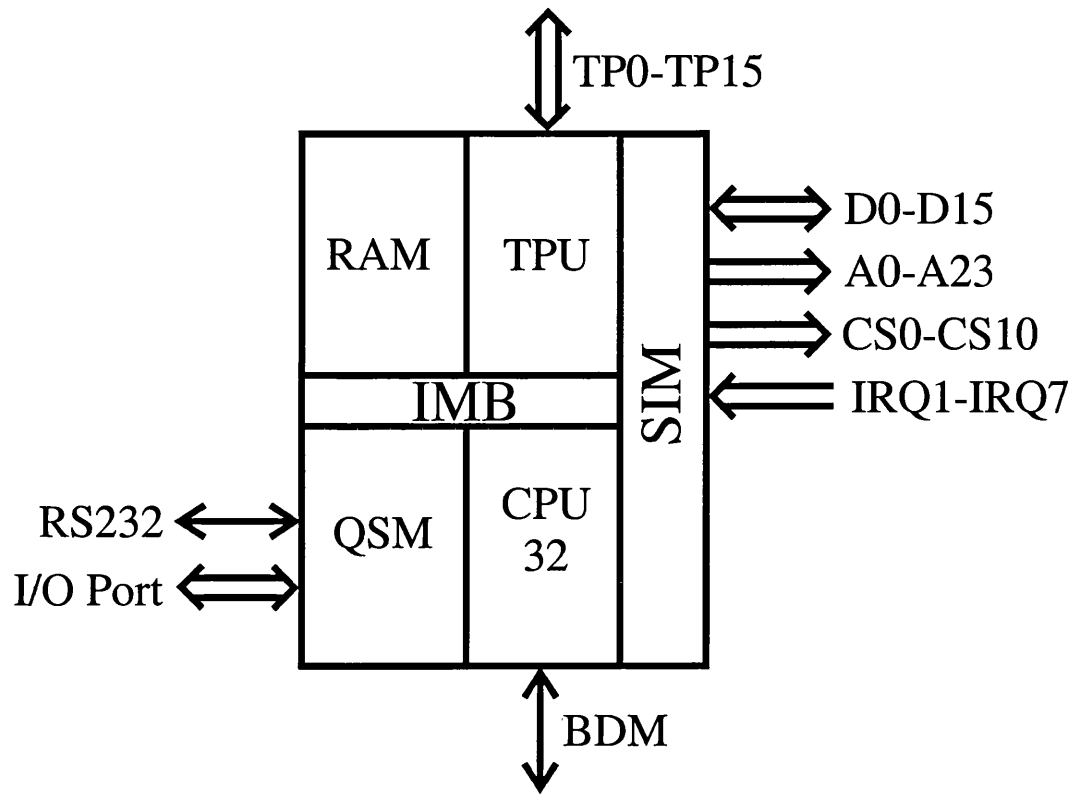

Figure 4.16: Block diagram of MC68332

- RS232 port on-board
- Up to 48 Discrete I/O pins

The block diagram is shown in Fig.4.16. The memory was mapped using the chip selects to access the external components like ROM, RAM, FPGA, etc. Each chip select is assigned to a user defined memory block. The read and write operations can be programmable from 0 to 13 wait states. The Periodic Interrupt Service Routine (PIT) is mainly used for the RS232 user interphase, data acquisition, start-up sequence and PI speed control. The interrupt was set at 1 kHz which was enough for speed control. The speed is estimated by counting the pulses from the position counter. The equation used follows:

$$w = (P_{new} - P_{old}) * F \tag{4.28}$$

where w = speed, P_{new} = new position, P_{old} = previous position and F = constant factor. This method is useful for medium and high speed and its resolution increases with speed. It was found to be suitable for the *CGSM* implemented here. The following variables can be set in the start-up sequence through the user's terminal interphase: initial and final (take-over speed) frequency, slope of the ramp and duty cycle step.

4.5.3 Start-up

Self-synchronisation and feedforward methods have been implemented for the start-up sequence and they are explained as follows.

Self-synchronisation

The implementation of self-synchronisation method does not require extra control or extra circuitry than the *CGSM* itself. The sequence for the self-synchronisation is as follows:

1. The rotor is aligned to either phase B or C depending to the desired direction of rotation, in order to place phase A in a position with enough torque to start-up.
2. Duty cycle is set to a value between 50% - 100% depending on the load.
3. Set commutation angles, $\theta_{on} = 45^o$ and $\theta_{off} = 75^o$.
4. Phase A is energised.
5. Commutation angles are generated directly from sensorless pulses of the detection stage.

Fig.4.17 depicts the speed and one phase current in the start-up procedure with no load, showing smooth acceleration from standstill to 2330 rpm ($\theta_{on} = 45^o, \theta_{off} = 75^o$). The phase current shows that synchronism is reached after three electrical cycles. Fig.4.18 is a zoom of the start-up procedure, also showing the CGPE pulses from all

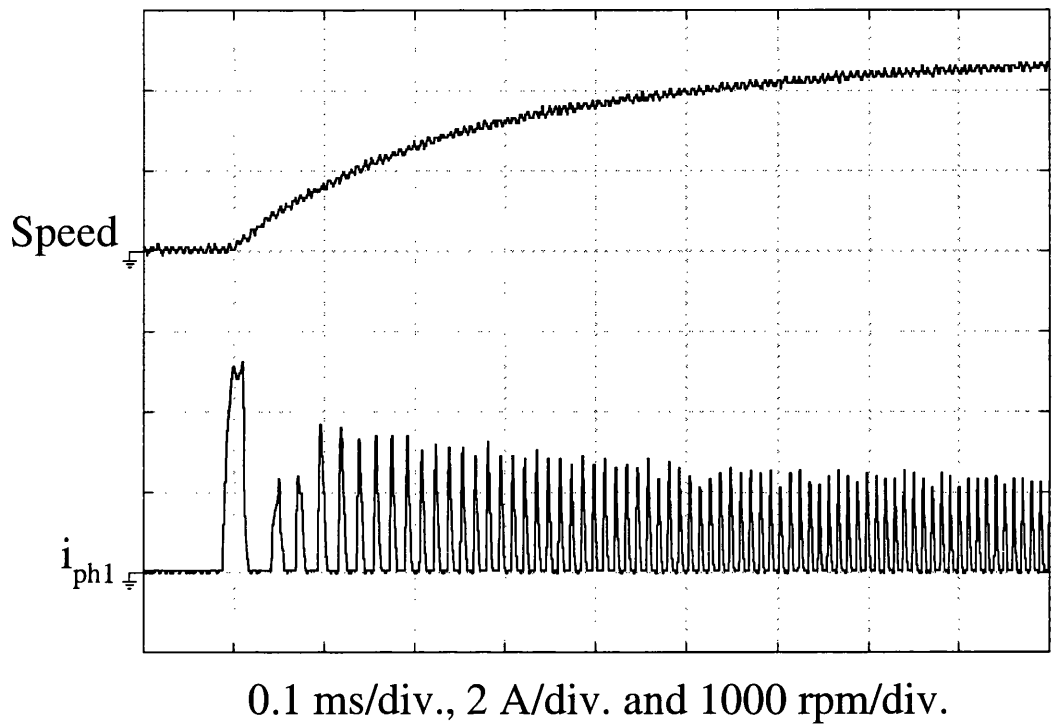

Figure 4.17: Self-synchronised start-up.

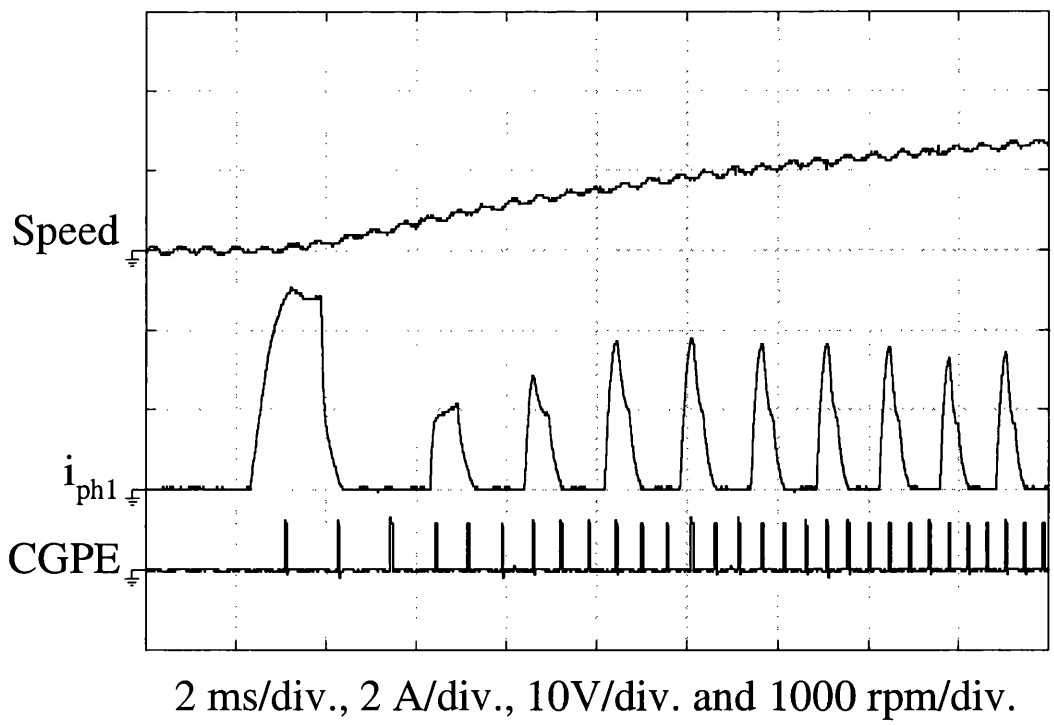

Figure 4.18: Zoom of self-synchronised start-up.

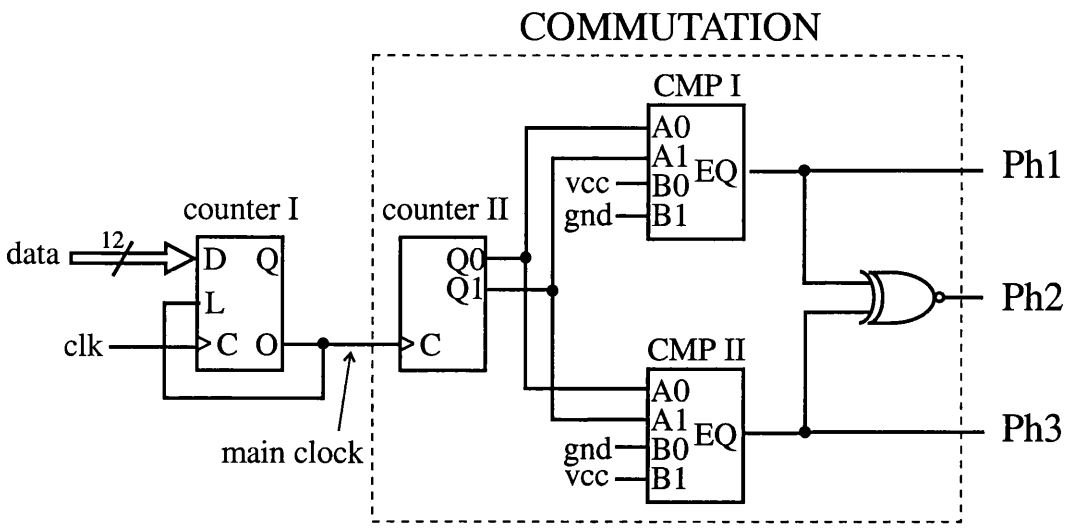

Figure 4.19: Digital circuit for generation of commutation in open loop.

three phases, starting with phase one (1-2-3-1...). Fig.4.18 demonstrates more clearly that synchronous operating is reached, after three electrical cycles.

This method allows a start-up of the motor even with load, however it may not start smoothly and therefore the method is erratic.

Feedforward

The implementation of the feedforward method requires the generation of a ramp of frequency. For this purpose, a 12-bit load counter is used to generate the main clock for commutation. Fig.4.19 depicts the digital circuit used. Counter I is clocked with fixed 5 MHz frequency. The pulse generated when it overflows is used as clock for commutation and to load the data value. The time that the counter overflow depends on the data value. The data ramp is generated by the microcontroller in the internal interrupt PIT and then sent to the commutation board (FPGA). The commutation is generated with 2-bits Counter II, two comparators and a XNOR-gate as shown.

Fig.4.20 depicts the experimental result during start-up, the signal is measured with a 1024-encoder line. First 76 Hz (380 rpm) excitation frequency is applied for a short period and then the frequency is increased linearly until 230 Hz where the take-over

speed of 1150 rpm is reached. The duty cycle is maintained at 100%. Once the take-over speed has been reached, the CGPE pulses can be used to commutate phases in closed-loop. Fig.4.21 shows i_{ph1}, i_{bus} and CGPE measured during transition from open-loop to closed-loop true sensorless at take-over speed of 1339 rpm, $\theta_{on} = 50°, \theta_{off} = 80°$.

Examples of the feedforward start-up are included. Fig.4.22 depicts a ramp of 0.5 s. with a take-over speed of 2100 rpm, the duty cycle is fixed at 100% and no load is coupled to the machine. Fig.4.23 shows a ramp of 0.65 s., the initial duty cycle is 100% and is reduced linearly down to 45% at the take-over speed of 1100 rpm. Fig.4.24 shows a ramp of 0.36 s with a take-over speed of 550 rpm, the duty cycle is decreased from 100% to 25%. An example of the start-up with load is depicted in Fig.4.25, the time ramp is 0.34 s with a take-over speed of 980 rpm, The load builds up from 0 to 0.42 Nm at the take-over speed.

Fig.4.26 shows i_{ph1} and i_{bus} measured during the start-up sequence. It can be seen that at the beginning the current is limited by a preset maximum current value, and as the speed goes up the peak current is reduced. Once the take-over speed has been reached, the CGPE pulses can be used for commutation.

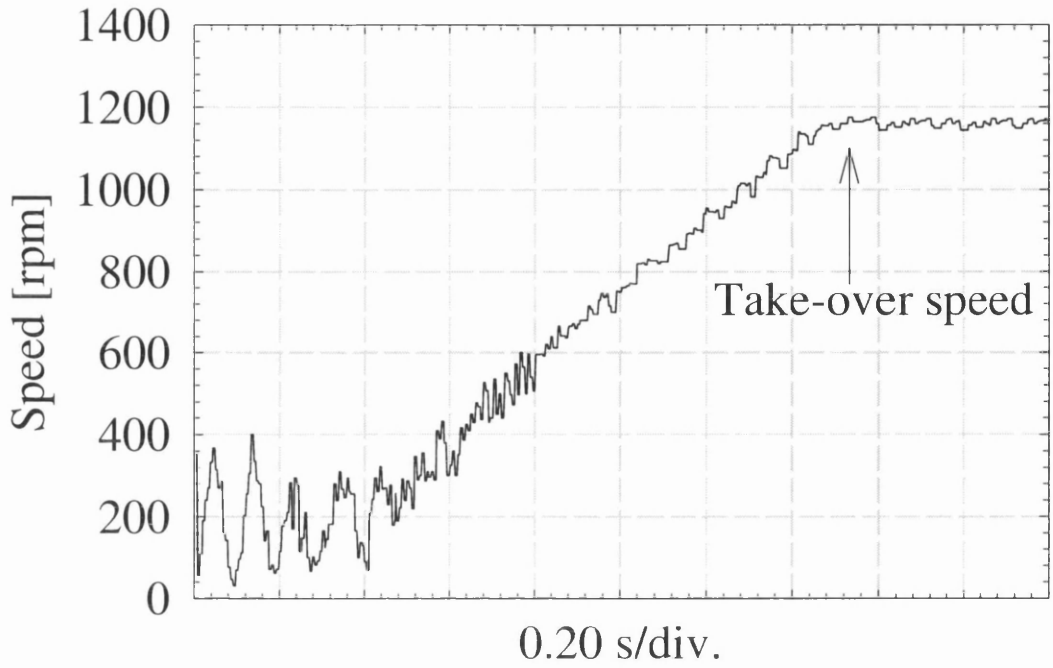

Figure 4.20: CGSM feedforward start-up (the signal is measured with a 1024-line encoder).

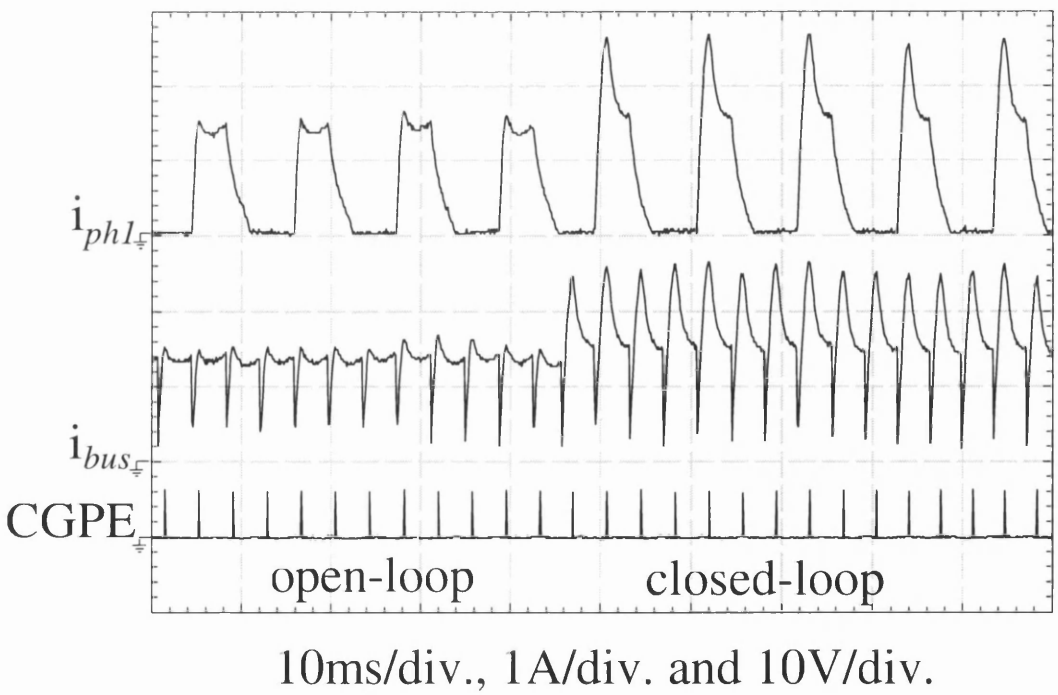

Figure 4.21: Take-over at a speed of 1339 rpm, $\theta_{on} = 50^o, \theta_{off} = 80^o$.

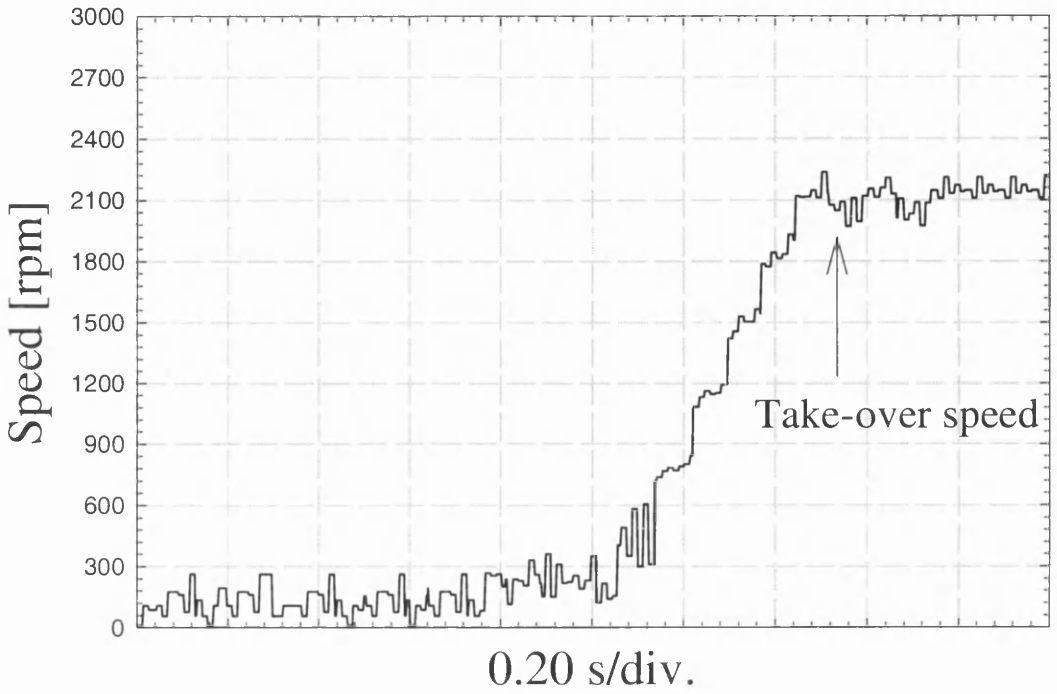

Figure 4.22: CGSM feedforward start-up, take-over speed at 2100 rpm with no load.

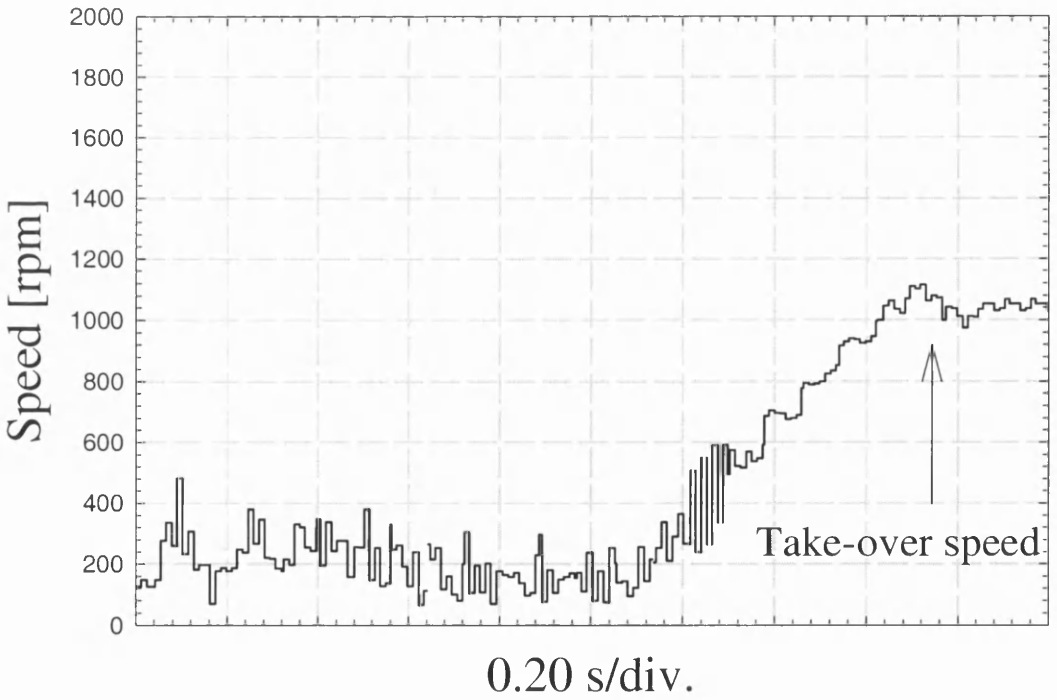

Figure 4.23: CGSM feedforward start-up, take-over speed at 1100 rpm with no load.

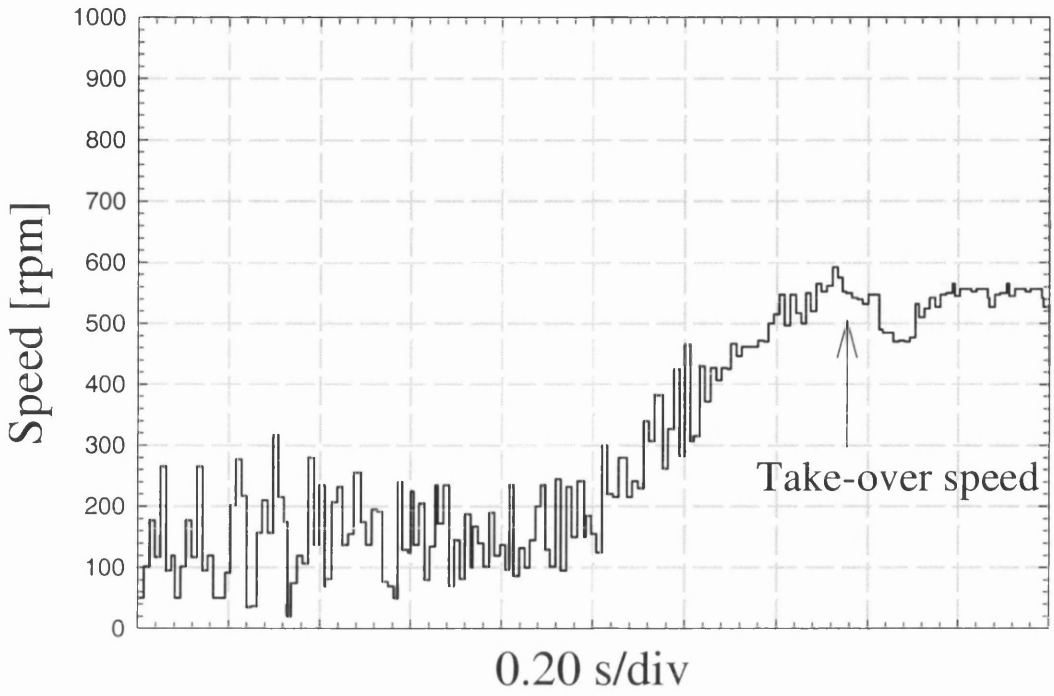

Figure 4.24: CGSM feedforward start-up, take-over speed at 550 rpm with no load.

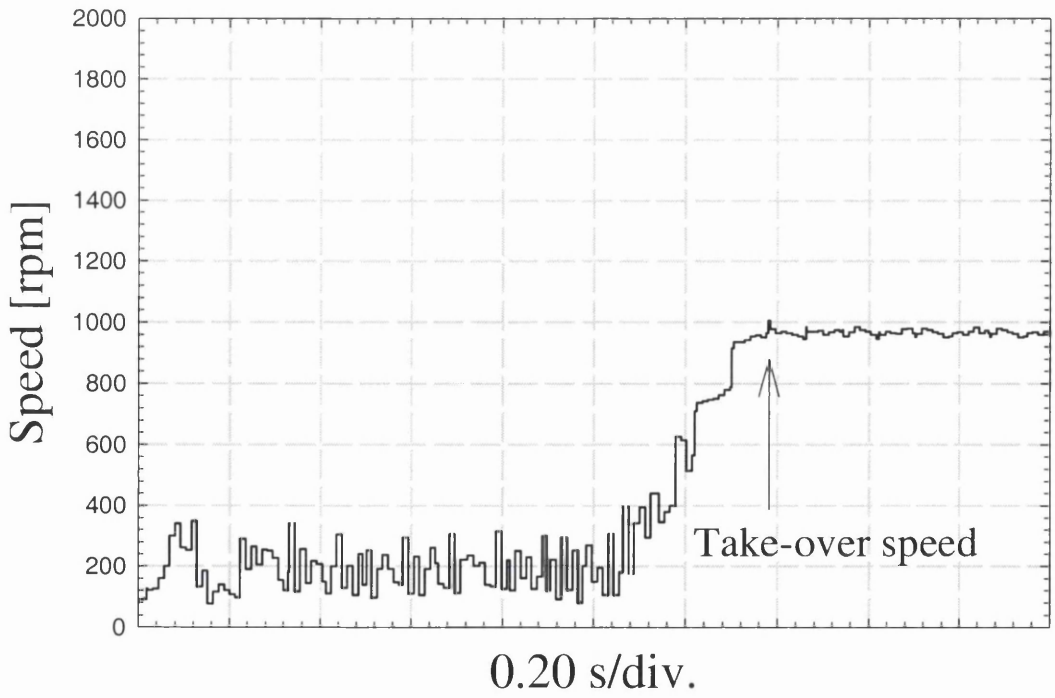

Figure 4.25: CGSM feedforward start-up, take-over speed at 980 rpm with load.

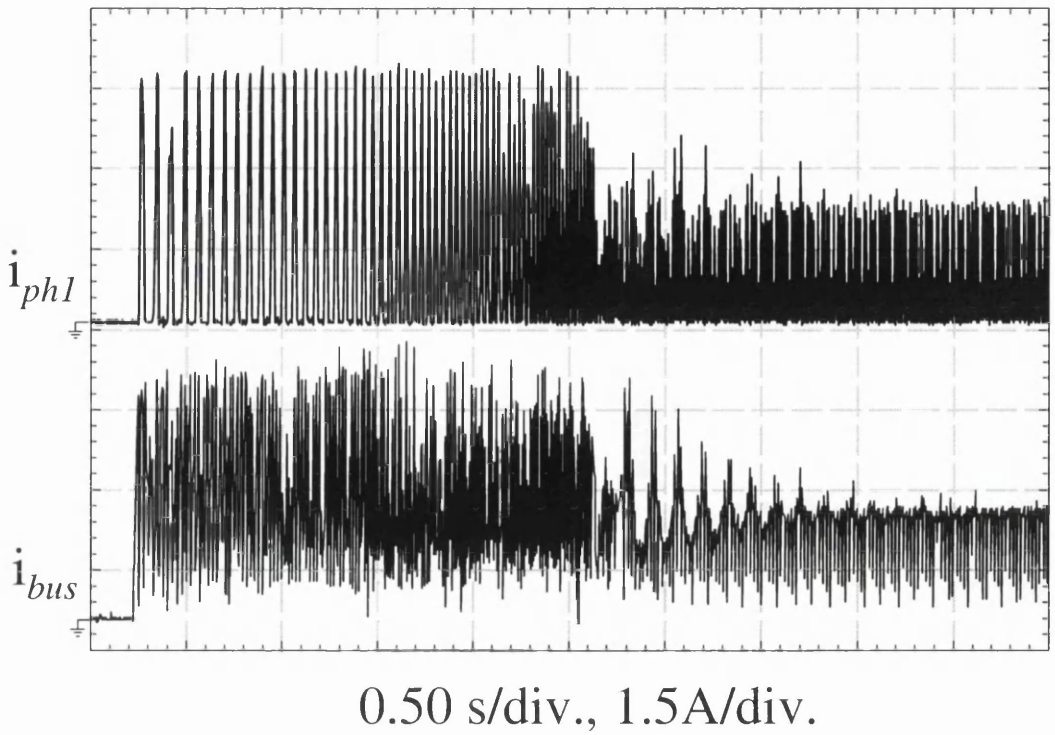

Figure 4.26: Current waveform measured during feedforward start-up.

4.5.4 Detection stage

According with the theory of *CGSM*, it is required to detect the change in $\frac{di}{dt}$ of the energised phase. An electric circuit that does the work is shown in Fig.4.27. The detection stage consists of a current sensor, two low-pass filters, a differentiator, a peak hold and a comparator.

The low-pass filters are used to eliminate the PWM switching frequency and possible noise. For each low-pass filter a second-order Butterworth filter is used, where the cut-off frequency is determined by the PWM switching frequency. In this case a cut-off frequency of 8 kHz was used for a switching frequency of 16 kHz. The differentiator is used to obtain the derivative of the current waveform $\frac{di}{dt}$, This signal goes to the peak hold, which keeps the maximum value of $\frac{di}{dt}$, and to the comparator that generates a pulse when $\frac{di}{dt}$ is smaller than the peak value. This pulse indicates θ_o.

Alternatively, $\frac{di}{dt} = 0$ can be detected which makes the detection stage more simple,

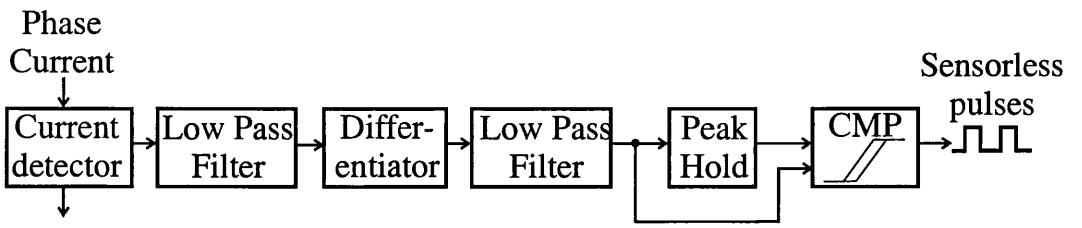

Figure 4.27: Detection stage.

however it puts constraint on the current waveform which should have at least one peak or flat current current waveform. In this case the peak hold is no longer required and the comparator produces a pulse when $\frac{di}{dt}$ is zero. The modified detection stage for the fully analogue electronic circuit is shown in Fig.4.28 (a). If the drive is going to be operated in single pulse mode (i.e. no PWM) the low-pass filters are not necessary and the number of component in the detection stage is reduced significantly as shown in Fig.4.28 (b).

As it has been stated before, the feedback signal can be either the current waveform of each phase or the current waveform of the lower transistor bus which contains the same information as the phase currents. The former requires one current sensor and detection stage per phase, in contrast, the latter requires only one current sensor and detection stage which reduces significantly the circuitry, thus it is preferable. A good example of current regulation with only one current sensor is presented in [102, 103]. A single pulse-train, which every pulse indicates θ_o, is obtained from a single detection circuit sensing i_{bus} or when combining (OR-gate) the sensorless pulses from each phase. Optionally, only one detection circuit may be used is all phase currents are multiplexed.

Four identical detection stages have been implemented on a board, one for each phase and the fourth one connected to i_{bus}. It can be selected from the controller which is used to generate commutation signals, i.e. either the three signals from each phase or the signal from i_{bus}. This was useful to compare the performance of both implementations. For a 3-phase 6/4 SRM the detection stage gives 12 pulses per revolution according with (4.15).

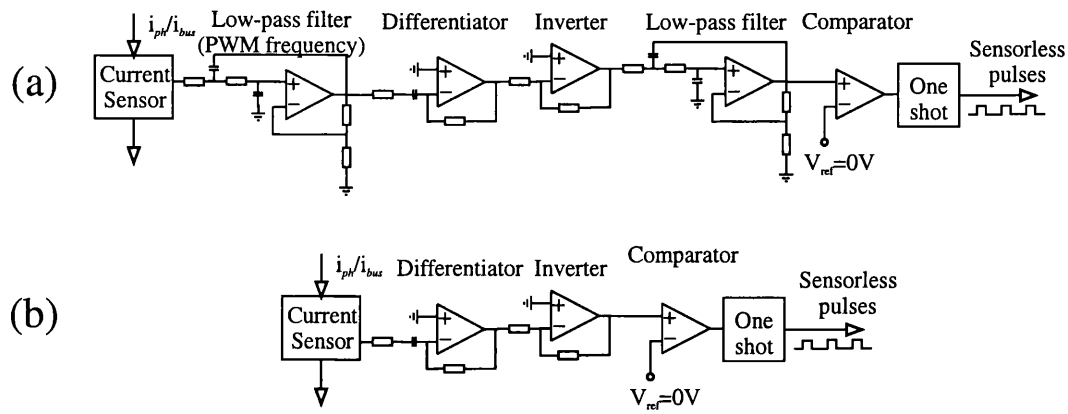

Figure 4.28: Detection stage for $di/dt = 0$ (a) for PWM voltage control, (b) for single pulse operation.

It should be noticed that the electronic circuitry required for the detection stage of *CGSM* is minimal (operational amplifiers, resistors and capacitors), with obvious scope for implementation as a single-chip solution.

4.5.5 Commutation stage

The objective of the commutation stage is to energise the phase windings in synchronism with rotor position. The pulses generated by the detection stage, which indicate θ_o, do not coincide with the desired commutation angles, i.e. the turn on angle must be before θ_o and the turn off may be in the range $\theta_o - \theta_a$. Therefore, extrapolation between pulses is required to obtain the instantaneous rotor position and commutate the phases. Some options of how the sensorless pulses can be used for commutation are explained below.

To use the sensorless pulses as commutation it is necessary to delay them by certain angles, (in the case of 3-phase machine may be 25° mech.). For this purpose a circuit including low-pass filters can be used. This method has been used by [99] in back-EMF sensorless method for brushless DC motors. The commutation signal may be generated from the rising edge of the delay pulses. When one phase is turned off the next in the sequence is turned on. This implementation restricts the commutation to a fixed dwell

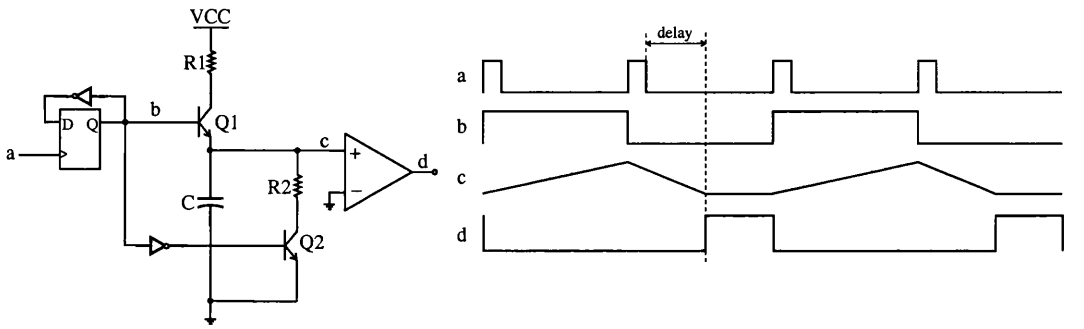

Figure 4.29: RC circuit for delay.

angle, and adjustment of commutation is not flexible.

Alternatively, a specific delay can be introduced by controlling the charging of a RC circuit. Fig.4.29 depicts the circuit proposed. The sensorless pulses from the detection stage clock a D-flip-flop (signal "a"), signal "b" is obtained and used to trigger transistor Q1, the inverted signal "b" triggers transistor Q2. The charge time in node "c", is determined by R1 and C when Q1 is on, and the discharge time is determined by R2 and C when Q2 is on. In this manner, if R2 is chosen for instance equal to R1/2 the discharge time will also be half of the charge time. The signal from node "c" is compared with zero to obtain the train of pulses "d". Two identical circuit are necessary but the input signal to control Q1 is "b" inverted. Therefore the signal d from the second circuit is shifted one electrical cycle. Again, the commutation signal may be generated from the rising edge of the delay pulses. This implementation is not very flexible, as the delay time depends on the RC value, however permits to set the firing angles to a pre-determined values.

Optionally, the commutation stage can be implemented entirely in a microcontroller using its timer. Capturing the values of the timer register every time that a sensorless pulse appears, speed w can be calculated as:

$$w = \frac{\Delta\theta}{t_1 - t_2} \tag{4.29}$$

where, t_1 = previous read timer value, t_2 = latest read timer value, $\Delta\theta$ = calculated according with (4.15).

The commutation angles of a phase winding (turn on θ_{on} and turn off θ_{off}), can be calculated to the desired values as a time function ΔT from the last sensorless pulse.

$$\Delta T_{on/off} = \frac{\theta_{on/off} - \theta_o}{w} \tag{4.30}$$

the subscript "on/off" means that both angles are calculated in the same way.

From the aforementioned, the necessary control for commutation can be provided by simple timer operations. One important feature that can also be implemented is the use of a watchdog-timer which will avoid the use of wrong sensorless pulses generated by an overcurrent. The time where a sensorless pulse should appear can be predicted from the previous speed calculation. Therefore in case of an overcurrent the sensorless pulses are disabled and commutation is determined from previous calculations. This implementation allows full flexibility in control of commutation angles.

Another simple method to generate commutation is interpolating linearly intermediate rotor position between two consecutive pulses by means of Phase-Locked-Loop (PLL) methods. These methods can be implemented using a microcontroller, a specific IC or even in discrete digital components. The research carried out in this thesis makes use of a PLL method implemented in a FPGA as follows.

FPGA implementation

The commutation stage has been implemented with a Field-Programmable-Gate-Array (FPGA, Xilinx XC3195A) in the demonstrator set-up, for flexibility in the development stage. This implementation also offers full flexibility to control commutation angles. The input signal for the commutation logic are the pulses from the detection stage connected to each phase winding and the lower transistor bus. The use of only one detection stage or three of them is selectable from the user interface.

The sensorless pulses are used to generate a position counter, which represents the instantaneous rotor position, as follows. The train of sensorless pulses spaced 30° (according to (4.15)), obtained from the detection circuit is used to generate a pulse

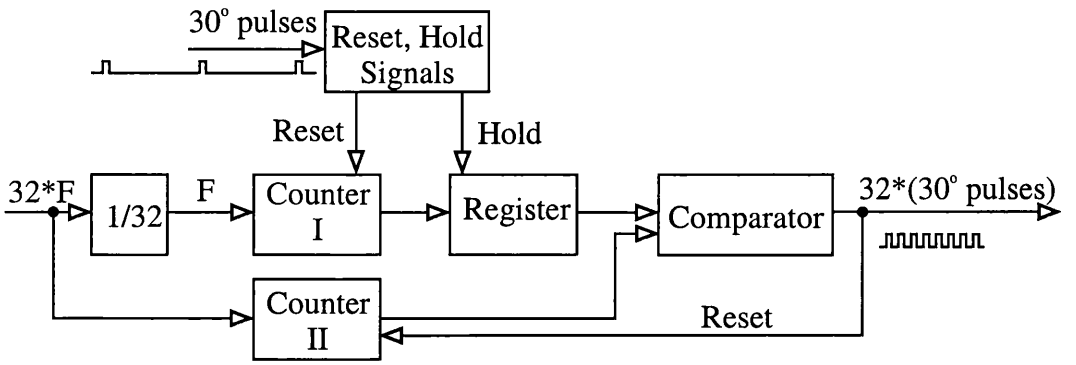

Figure 4.30: Block diagram of (PLL) position interpolation.

train with 32 pulses per 30^o. In other words, the frequency of the sensorless pulses is multiplied by 32 using a PLL. Fig.4.30 shows the block diagram of the implemented logic circuitry. There are two counters, counter I running at frequency F and counter II running at frequency $32 * F$. Upon arrival of a sensorless pulse, the value of counter I is held first and then the counter is reset. The value of the counter II builds up to the value in the register. When equal the comparator generates a pulse and resets counter II. So a resolution of 384 pulses per revolution is obtained which is enough to generate commutation pulses with adequate resolution.

The frequency "F" is chosen according to the maximum speed at which the motor is going to be operated. In this case, the maximum speed was taken as 5000 rpm. At this speed the frequency of the sensorless pulses is 1000 Hz (for a 3-phase 6/4 machine), and the count in the counters is 156 having $F = 156.25$ kHz. This count gives a margin in case that the speed goes above 5000 rpm. In the other hand, at low speed the counters may overflow if the number of bits of the counters are not enough. Therefore it must be taken into account the minimum speed to determine the number of bits. The minimum speed was considered 200 rpm which gives a frequency of sensorless pulses of 40 Hz. With a $F = 156.25$ kHz it gives a count of 3906, thus a 12-bit counters are used. To cover a large speed range and not use an excessive number of bits, F can be variable in stead of fixed. i.e. two or more values of F can be used according to the speed range, for instance there could be one value of F for low speed and other for high speed.

When i_{bus} is used and there is excitation overlap, i.e. two phases are on simultaneously, the current waveform has two peaks and therefore the detection stage generates two pulses, one when the previous phase is turned off and the other one for the peak corresponding to θ_o. In other words, a wrong pulse appears when the previous phase is turned off. Thus a logic is implemented to neglect the wrong pulses and to allow the pulse that indicates θ_o. This is illustrated in section next section.

4.5.6 Control strategy

The torque produced by the SRM drive is a function of the turn on, turn off angle and the phase current which are controlled according with the desired performance and cost of the drive.

In PWM voltage control the following strategies can be implemented.

1. Variable θ_{on}, constant θ_{off} or vice-versa with fixed duty cycle (D).
2. Variable D with variable θ_{on} and fixed θ_{off} or vice-versa.
3. Variable D with both fixed θ_{on} and θ_{off} .
4. Both θ_{on} and θ_{off} variables with fixed D.
5. Variable advance angle and D with fixed dwell angle.
6. Variable advance angle with fixed D and dwell angle.
7. All variables, θ_{on}, θ_{off} and D.

All this control strategies can be implemented using *CGSM*. The only operating constraint is to assure $\theta_{on} < \theta_o$ which is not an onerous restriction at any operating speed or torque. However, it should be noticed that exists a limit in updating the control variables (commutation angles, duty cycle), and also a limit in the maximum load torque transient. This is due to the low resolution in rotor position estimation. The

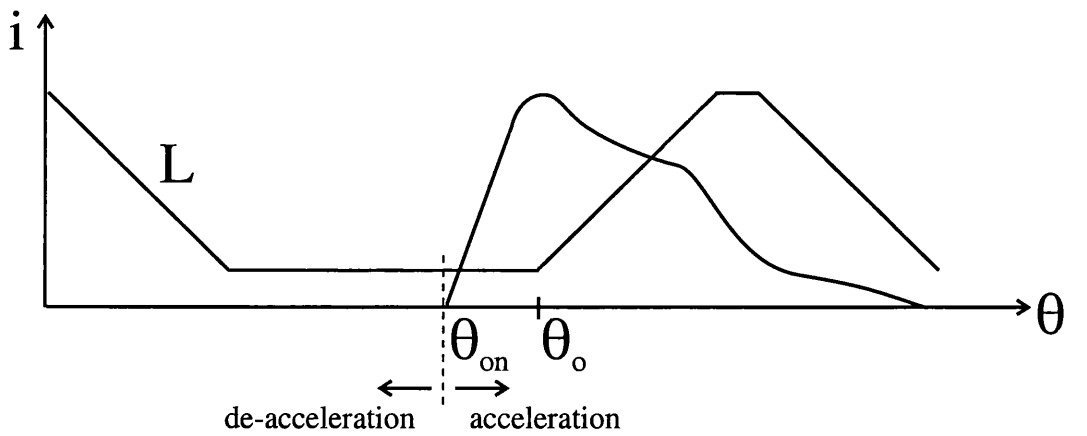

Figure 4.31: Changes of commutation angles in speed transients.

condition $\theta_{on} < \theta_o$ may not be true in a speed transient, i.e. the special characteristic of the current waveform may be lost.

CGSM is stable at any update of control variables or in a load torque transient that reduces the speed. Nevertheless, when the update accelerates the motor the turn on angle may not be before θ_o. For better understanding, let us first consider that the motor is rotating at constant speed, and the phase is commutated at the desired commutation angles. Now consider that the speed decreases due to a change in either the control variables or the load, in this transient the phase is commutated in advance because the rotor advances less than the estimated rotor position calculated from the previous speed. However the desired condition $\theta_{on} < \theta_o$ still valid. On the other hand, in the transient when the motor accelerates, the phase commutation is delayed because the rotor advances more than the estimated rotor position calculated from the previous speed. Here, the desired condition $\theta_{on} < \theta_o$ may be lost. It was found in practice that there is not limitation for updates in control variables or load torque transients when the motor de-accelerates, however in the other way around, there may be limitation. Therefore, the control variables should be updated smoothly when acceleration is expected. Fig.4.31 depicts how θ_{on} moves in speed transient.

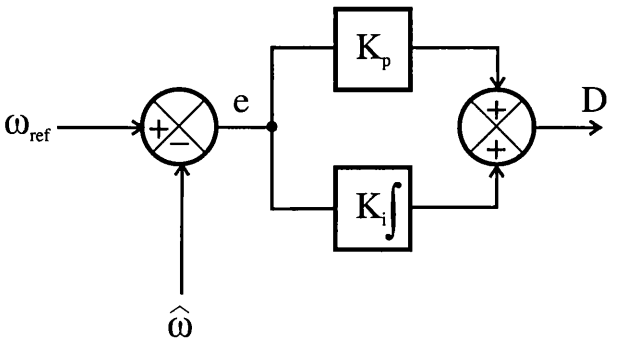

Figure 4.32: Speed controller.

4.5.7 Speed control

A standard PI closed-loop speed controller has been implemented as indicated in Fig.4.32. The variable to control for load torque compensation is the duty cycle. The commutation angles normally remain fixed but they are programmable and can easily be varied in the user interface to help to control the motor torque. The input signal for the controller are the speed reference and the estimated speed. The difference is an error signal which is multiplied by a fixed gain K_p and is also integrated with a gain K_i. Then the proportional and integral signals are added to produce the duty cycle according with the speed demand.

The microcontroller MC68332 is used to close the speed loop. The program written in "C" consists of the main interrupt (PIT) control loop executed every 1ms. The transfer function of the continuous system is,

$$\frac{D}{e} = K\left(\frac{s+a}{s}\right) \tag{4.31}$$

For the discrete plane z,

$$s = \frac{1-z^{-1}}{T_s} \tag{4.32}$$

$$e_n = z^{-1} \cdot e_{n+1} \tag{4.33}$$

where T_s = sampling period. Substituting (4.32) and (4.33) in (4.31) and rearranging

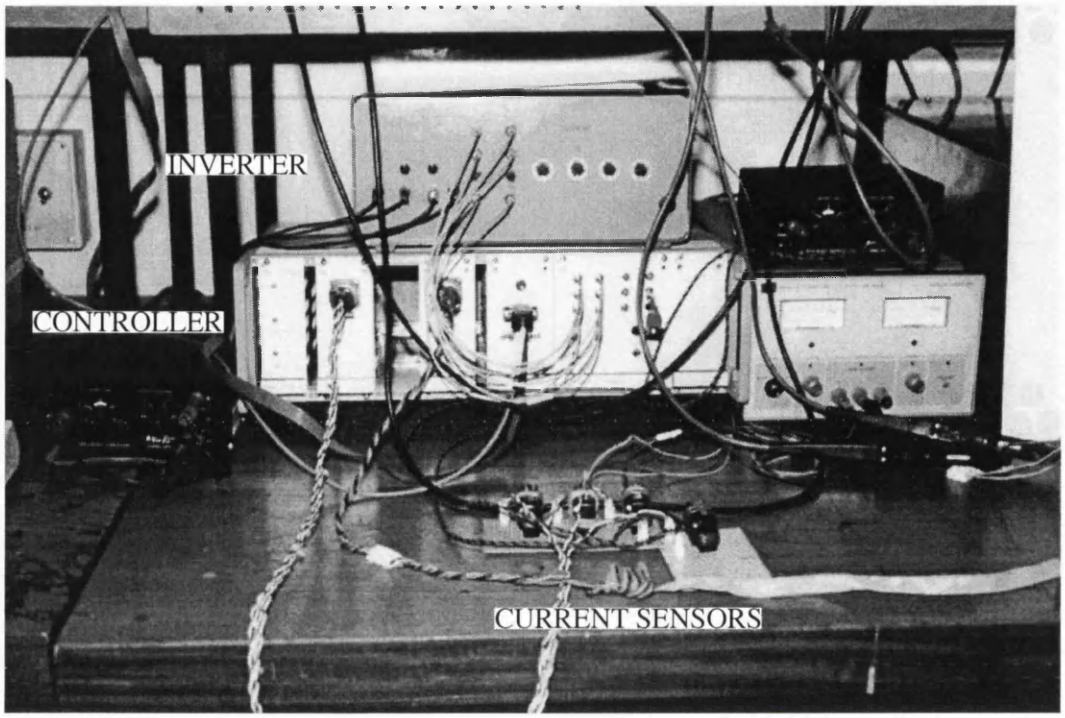

Figure 4.33: Controller and inverter overview.

it is obtained,

$$D_n = D_{n-1} + (K_1 \cdot e_n) - (K_2 \cdot e_{n-1}) \tag{4.34}$$

where, $K_1 = K(1 + a \cdot h)$, $K_2 = K$.

Careful tuning of the K_1 and K_2 gains resulted in a stable speed control. The control and user interface is done by and RS232 serial link. Using a simple terminal the commands to control the operation of the motor are sent to the controller. A picture or the controller and inverter overview is shown in Fig.4.33.

4.5.8 Summary

The hardware used for the implementation of *CGSM* has been described and also alternative options for implementation of phase commutation. The detection stage has been implemented in a fully analog circuit. The electronics required are simple i.e. operational amplifiers, resistors and capacitors, and it seems promising for implementation

as a single-chip solution.

CGSM has been implemented for a 3-phase 6/4 SRM with only one detection stage connected to i_{bus}. It has been stated that it is required a logic which neglects the wrong pulses when there is excitation overlap. Two methods of start-up have been implemented, self-synchronisation and feedforward, being the latter the most reliable.

There are several ways to obtain commutation angles from the sensorless pulses. The use of a microcontroller by itself or in combination with a FPGA are the most flexible architectures. *CGSM* does not compromise the SRM drive performance, is very stable and offers all the flexibility to control commutation angles and duty cycle. The only condition is that $\theta_{on} < \theta_o$, which is necessary anyway to produce adequate torque at high efficiency [34].

It is worthy to note that there may be a limit to update the control variables and to the maximum load torque transient allowed, for instance in a speed transient where the motor accelerates, the current waveform may be lost ($\theta_{on} < \theta_o$ may not be true).

A standard Proportional Integral (PI) speed controller is implemented in a microcontroller Motorola MC68332. The control variable to compensate speed is the duty cycle while the angles remain fixed. The commutation angles are programmable and may be varied to help to control the motor torque. The complete system resulted in a fully sensorless closed-loop speed control drive system for a 3-phase 6/4 switched reluctance motor.

4.6 Experimental results

To investigate the performance and limitations of *current gradient sensorless method* experimental tests were carried out The test motor and the load machine are coupled with flexible rubber couplings. The load machine is a PM motor connected in series with a resistance and a current controlled power supply. The complete set-up is shown

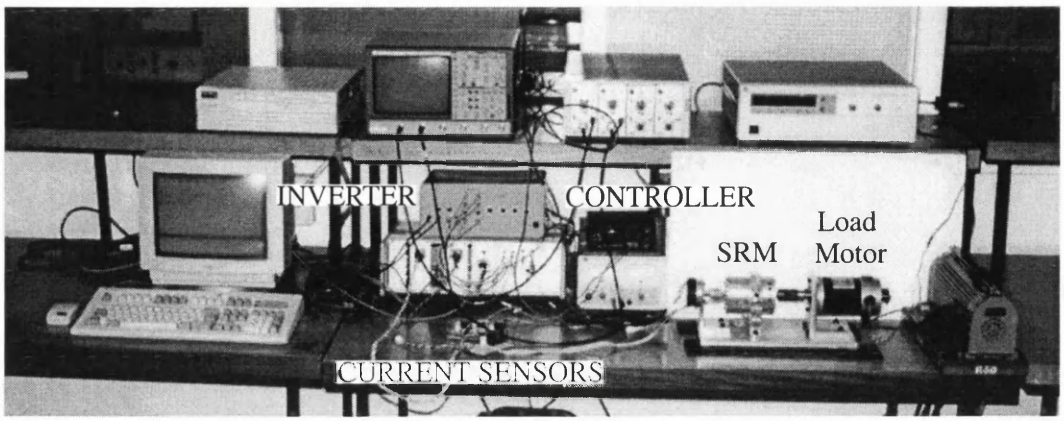

Figure 4.34: Hardware overview.

in Fig.4.34.

The experiments include: detection of sensorless pulses, accuracy in rotor position estimation, speed transients, torque transients and measurement of the torque-speed range where the motor can be operated with *CGSM*.

4.6.1 Sensorless pulses

Fig.4.35 shows one phase current (i_{ph1}), phase lower transistor bus current (i_{bus}), the *current gradient position estimation* (CGPE) pulses obtained from i_{bus}, and the decoded pulses (DP) for phase one measured at 1763 rpm with $\theta_{on} = 50^o, \theta_{off} = 80^o$. Clearly, the correct rotor position θ_o is detected. Fig.4.36 depicts i_{ph1}, i_{bus}, CGPE and DP for phase one measured at 1820 rpm, with $\theta_{on} = 50^o, \theta_{off} = 84^o$, but now there is excitation overlap, i.e. two phases are on simultaneously for a short (4^o) time. In this case, i_{bus} shows two peaks, note this time that two sensorless pulses appear per stroke, the first one is erroneous (when the previous phase is turned off) and the second one gives θ_o. A simple logic neglects the first pulse when there is excitation overlap, so DP becomes the decoded signal for phase one. From these results, it is proved that it is easy to estimate θ_o from only one detection stage connected to i_{bus}. Furthermore, the motor performance is not compromised in any way.

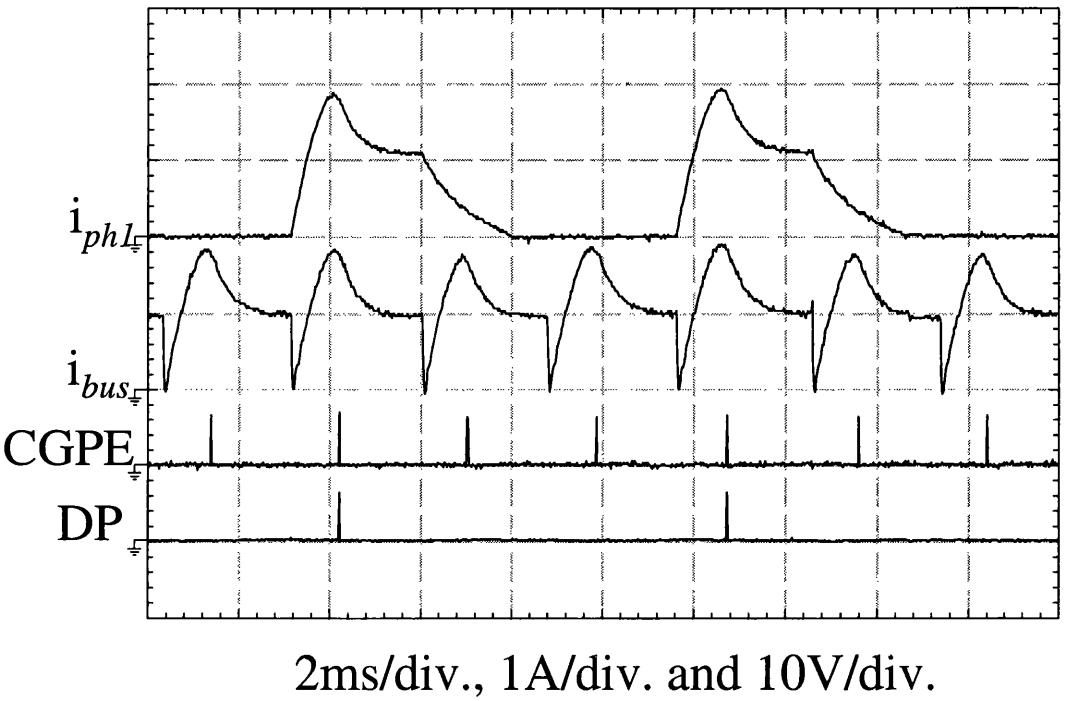

Figure 4.35: Single pulse current waveforms, $\theta_{on} = 50^o$, $\theta_{off} = 80^o$ (no excitation overlap)

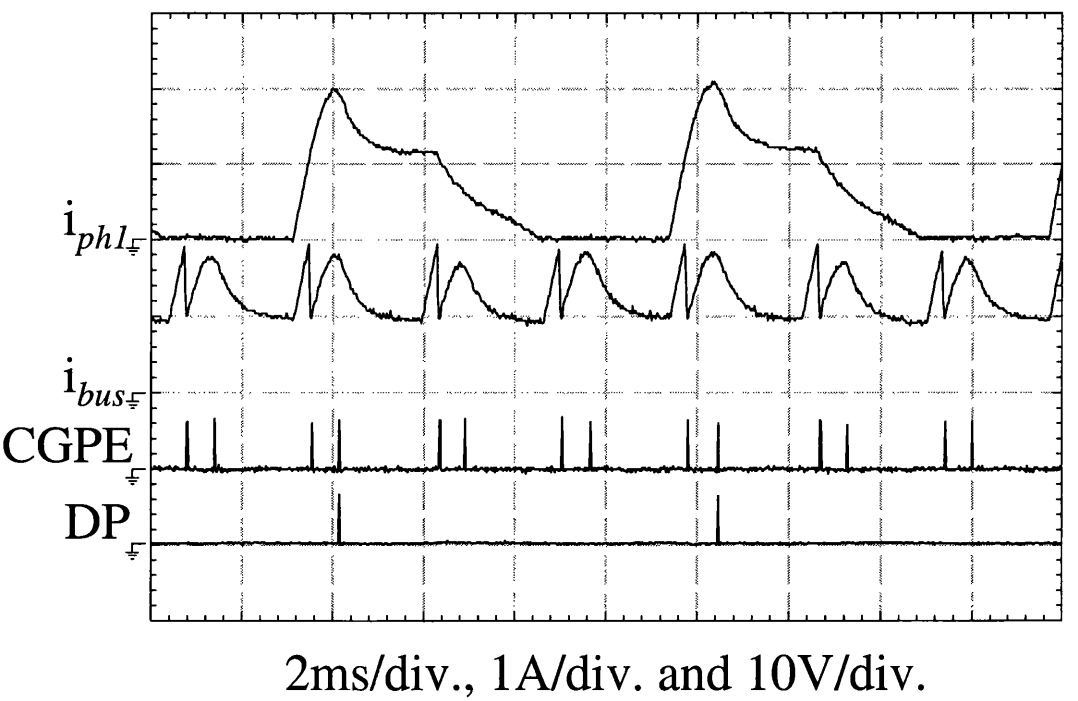

Figure 4.36: Single pulse current waveforms, $\theta_{on} = 50^o$, $\theta_{off} = 84^o$ (excitation overlap).

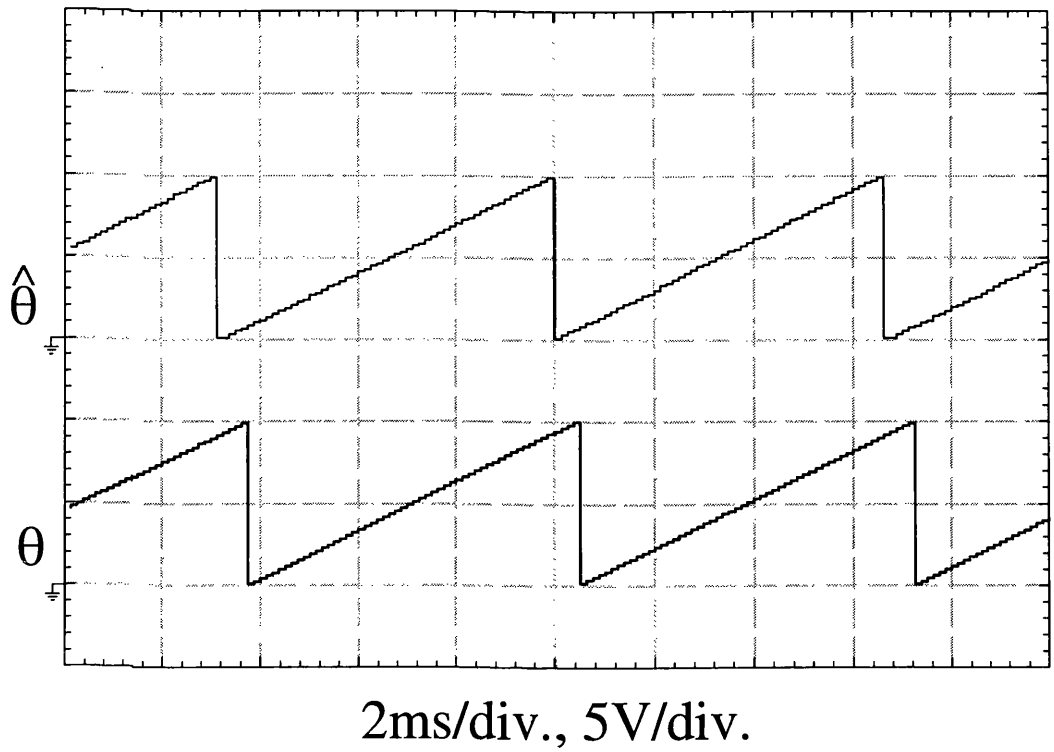

Figure 4.37: *CGSM* Position estimation at 2304 rpm, single pulse, $\theta_{on} = 45^o, \theta_{off} = 80^o$.

4.6.2 Accuracy

The accuracy on the rotor position estimation should be taken into account, because it influences strongly the performance of the drive. The measurements carried out were done in steady state with and without load. Fig.4.37 depicts the estimated position $\hat{\theta}$ and the position given by the 1024-line encoder θ in steady-state with no load measured at 2304 rpm, with $\theta_{on} = 45^o, \theta_{off} = 80^o$ and no load. Clearly the position signals show good agreement, we can observe that the estimated position is leading by approximately $2.4^o mech.$. However it should be noted that at higher speed the estimated position may be lagging because the the low-pass filters in the detection stage may impose a delay.

Fig.4.38 (bottom) shows $\hat{\theta}_{om}$, θ_{on}, $\Delta\theta_g$ and $\Delta\theta_m$, where $\Delta\theta_g = \hat{\theta}_{om} - \theta_{og}$ and $\Delta\theta_m = \hat{\theta}_{om} - \theta_{om}$. $\theta_{og} = 52.2^o$ is defined as the position where the mechanical overlap occurs, i.e. where the rotor and stator poles start to overlap and it is calculated from the stator and rotor pole arcs. θ_{om} is defined as the position where the magnetic

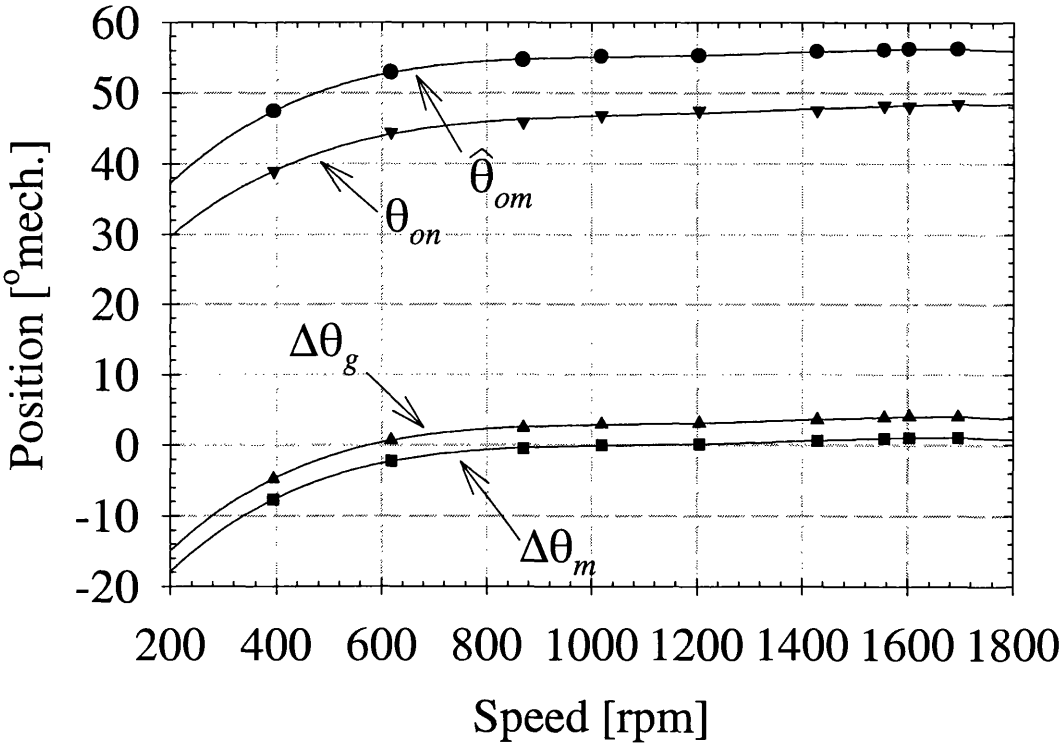

Figure 4.38: Measured accuracy of *CGSM* in steady-state.

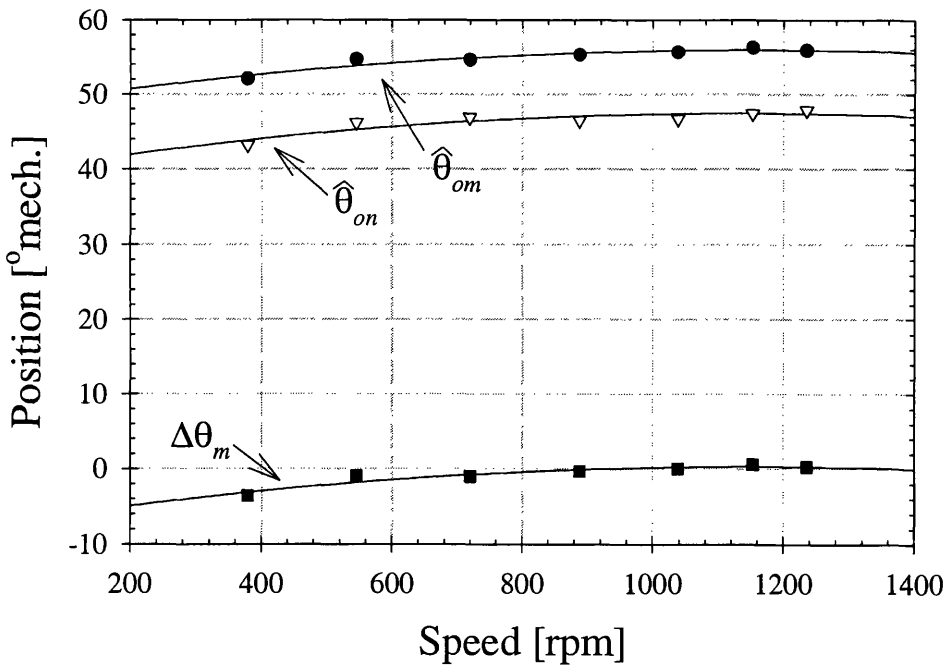

Figure 4.39: Measured accuracy of *CGSM* in steady-state driving 0.21 Nm.

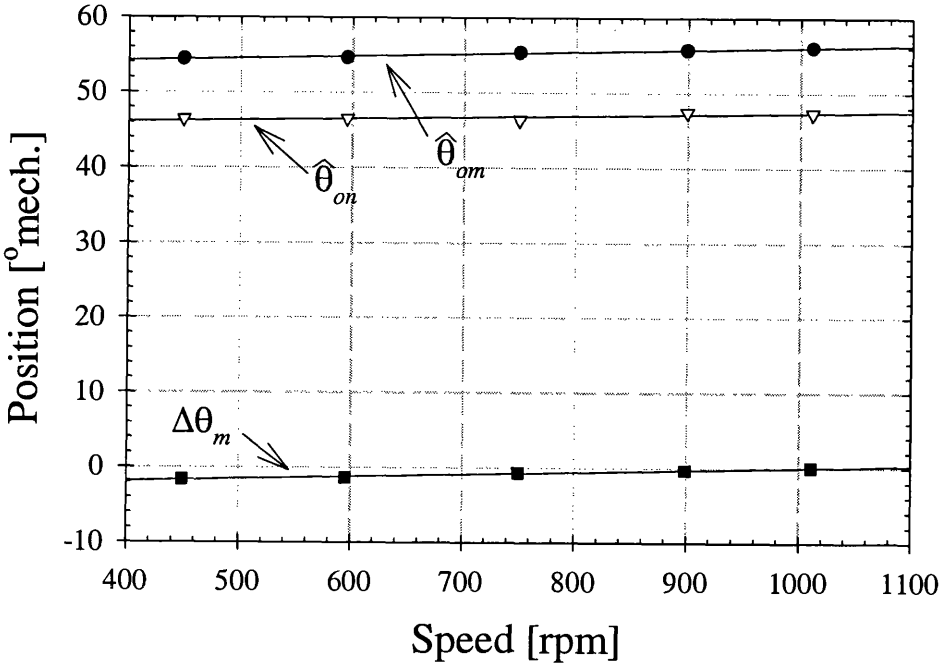

Figure 4.40: Measured accuracy of *CGSM* in steady-state driving 0.42 Nm.

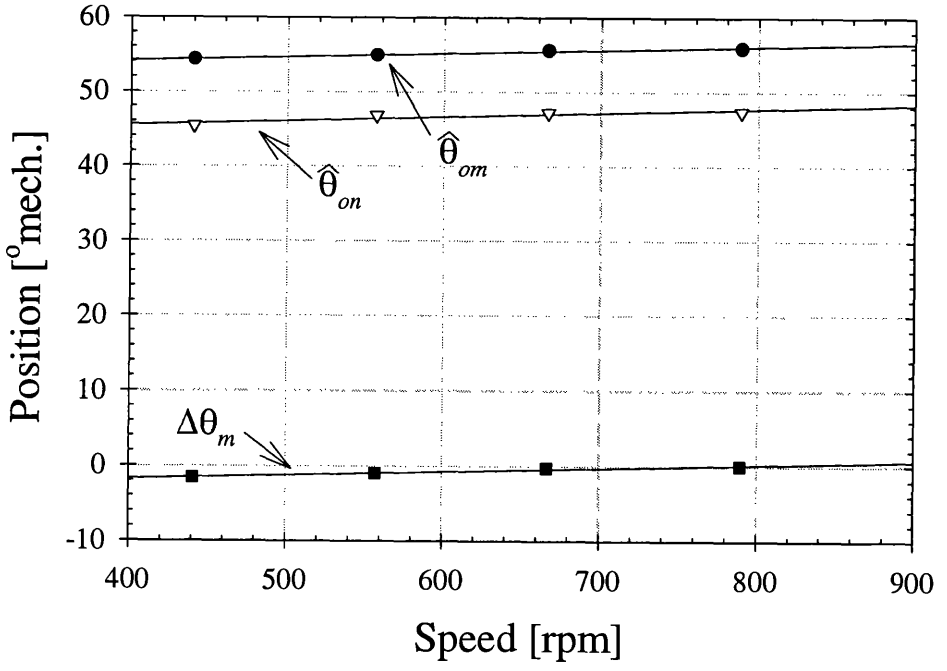

Figure 4.41: Measured accuracy of *CGSM* in steady-state driving 0.63 Nm.

overlap occurs obtained from experimental results. It can be observed that for speeds above 800 rpm, $\Delta\theta_g$ is quite constant and around 3^o. This difference shows us that the magnetic overlap differs from the mechanical overlap by 3^o, which gives,

$$\theta_{om} = \theta_{og} + 3^o = 55.2^o. \tag{4.35}$$

θ_{om} represents the real position. Hence, the firing angles are shifted 3^o (only θ_{on} is shown). Also, we observed that above 800 rpm $\Delta\theta_m$ is close to zero which means that the position estimation hardly differs from the real position. In contrast, at low speed there is a deviation of position estimation. This deviation in position estimation is caused by the accuracy in detecting $\frac{di}{dt} = 0$ and most important due to the effect of torque pulsation. More explicity, the speed is changing significantly in an electrical cycle at low speed due to the inherent torque ripple of the machine, therefore the linear extrapolation by PLL of rotor position in an electrical cycle starts to differ from the correct position. In other words, the most important factor determining the lowest feasible speed in *CGSM* is the torque ripple.

Other factors influencing the detection of rotor position are: the gain of the differentiator is sensitive to frequency, and the comparator amplifier may be offset i.e. $V_{ref} \neq 0$. At low speed the torque ripple causes the speed to change significantly in an electrical cycle, thus the error in rotor position estimation is increased. This imposes the minimum speed limit where *CGSM* can be used. On the other hand, at high speed the pulses may be delayed by the phase-lag of the low-pass filters. It should be noted that these factors can be solved electronically, or they can be corrected in the commutation angle controller as a function of speed.

The accuracy obtained when the motor is driving 0.21 Nm (30% of the maximum torque), is shown in Fig.4.39. This graph shows again that the major deviation occurs at speeds lower than 800 rpm. When driving a load of 0.42 Nm (60% of the maximum torque), the accuracy obtained is shown in Fig.4.40. Fig.4.41 depicts the error in rotor position estimation when a load of 0.63 Nm is coupled to the motor. It is clear that in all cases the largest error occurs at low speed.

4.6.3 Dynamic performance

Examples of sensorless closed-loop speed control are included. The minimum speed achieved was 200 rpm. A PI-controller acts on the PWM duty cycle for dynamic compensation. The firing angles remain fixed at $\theta_{on} = 48^o, \theta_{off} = 78^o$. An example of the drive's response to steps in speed reference is shown in Fig.4.42 for *CGSM* and Fig.4.43 with a 1024-line encoder, and clearly the performances with and without encoder feedback are comparable. Fig.4.44 and Fig.4.45 depict a series of speed transients with *CGSM* and encoder respectively, it is clear that both graphs show good agreement. Fig.4.46 shows i_{ph1} and i_{bus} measured during transition from open-loop to *CGSM* sensorless mode with closed-loop speed control with a reference speed of 1092 rpm. Fig.4.47 shows the sensorless drive's response to steps in load torque. The duty cycle is increased to compensate the load transient, demonstrating that *CGSM* could be acceptable closed-loop dynamic performance in many low-cost variable-speed applications.

A torque step of 0.42 Nm (0.60 p.u.), is applied when the motor is running sensorless, having $\theta_{on} = 50^o$ and $\theta_{off} = 79^o$. The results are shown in Fig.4.48 and Fig.4.49. In Fig.4.48, the feedback signal for rotor position estimation is i_{bus}, in contrast, in Fig.4.49, the sensorless pulses come from the three detection stages connected to each phase. This shows that the performance of the switched reluctance drive is not compromised when using only one detection stage connected to i_{bus}.

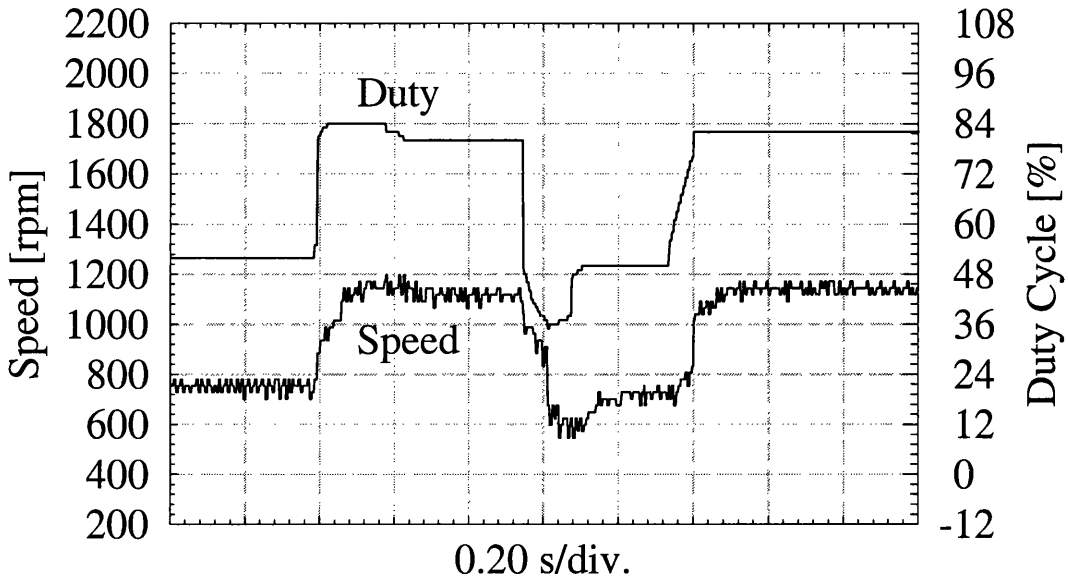

Figure 4.42: Zoom of speed transients. sensorless *CGSM* $\theta_{on} = 48^o, \theta_{off} = 78^o$.

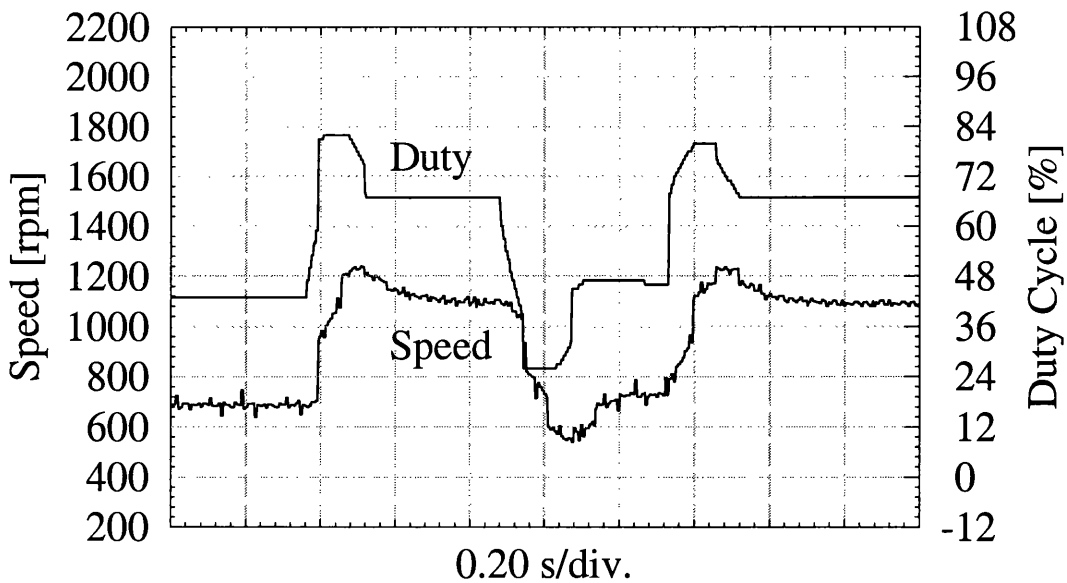

Figure 4.43: Zoom of speed transients. with sensor $\theta_{on} = 42^o, \theta_{off} = 72^o$.

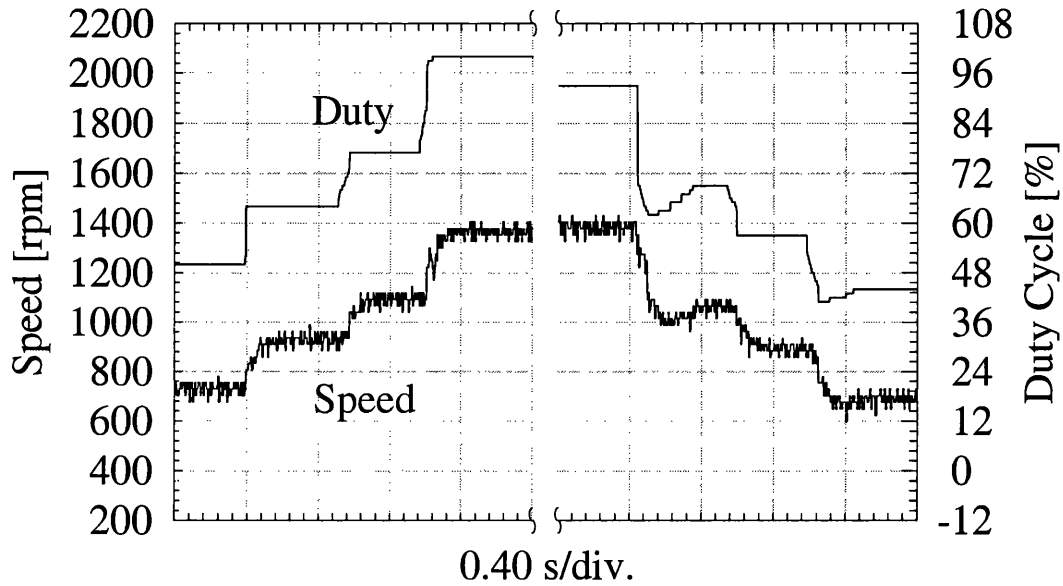

Figure 4.44: Measured sensorless speed transients.

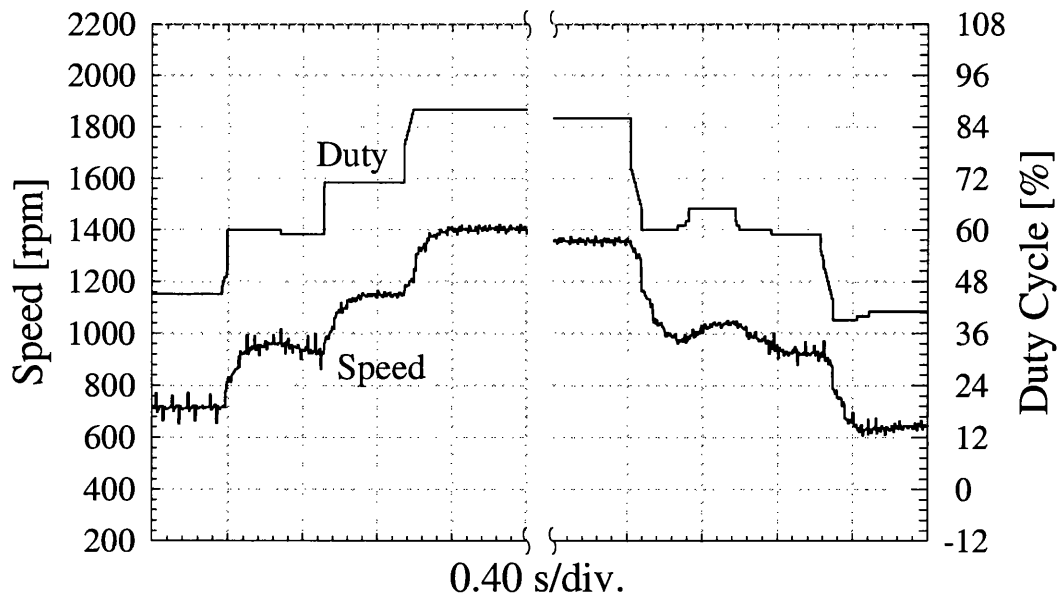

Figure 4.45: Measured sensor speed transients.

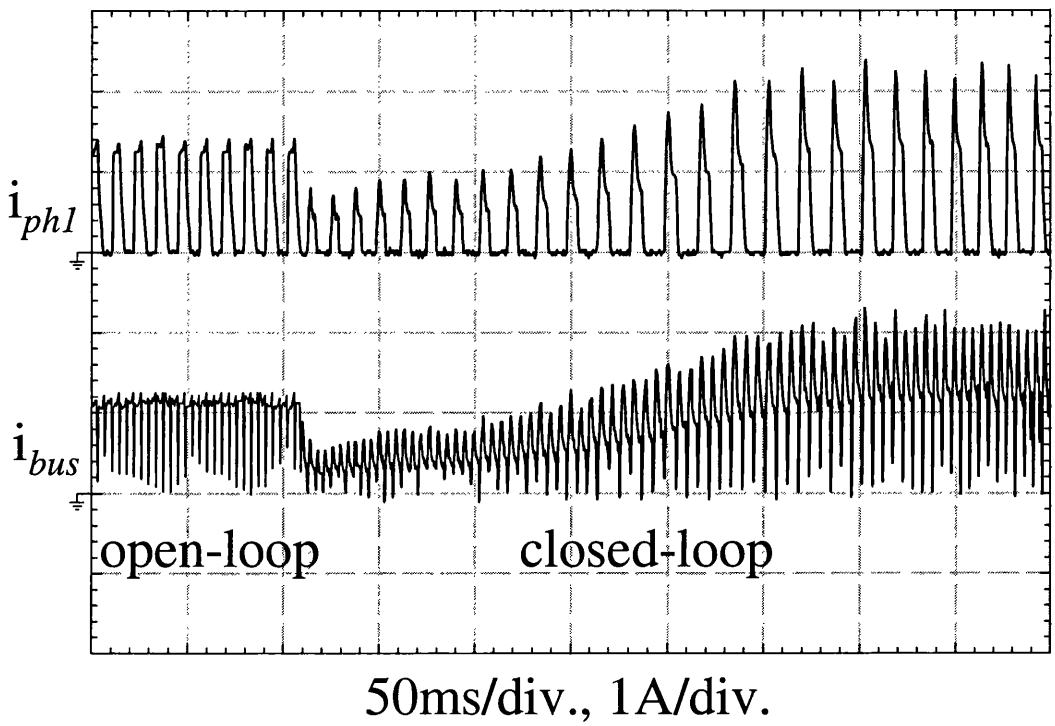

Figure 4.46: Take-over measured at speed=1339 rpm, $\theta_{on} = 50^o, \theta_{off} = 80^o$, swapping to closed-loop speed control with a speed reference of 1092 rpm.

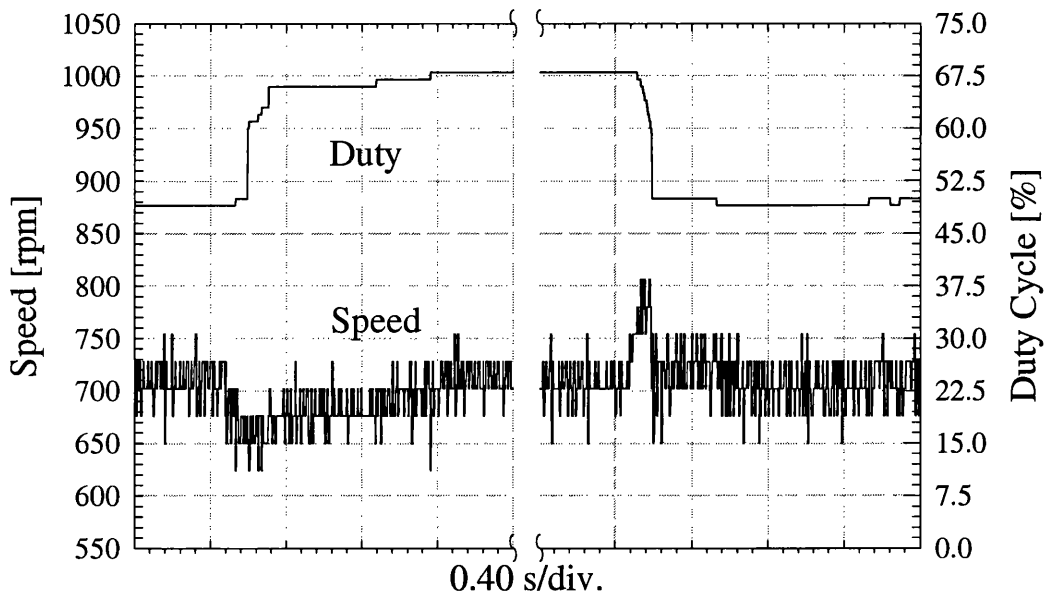

Figure 4.47: Transient response to steps in load torque.

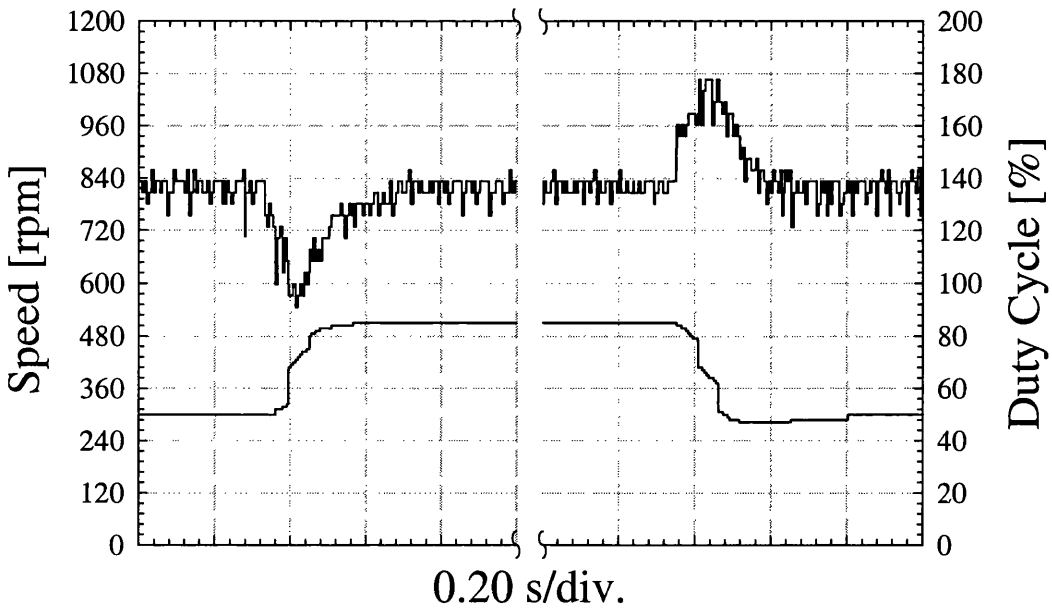

Figure 4.48: Transient response to a step of 0.42 Nm, (One detection stage connected to i_{bus}).

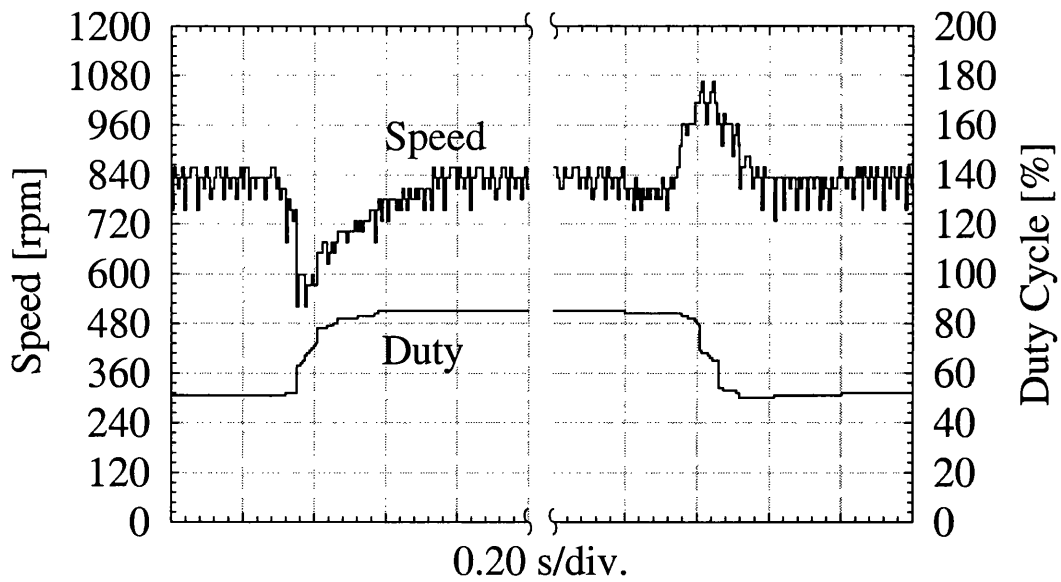

Figure 4.49: Transient response to a step of 0.42 Nm, (Three detection stages connected to each phase).

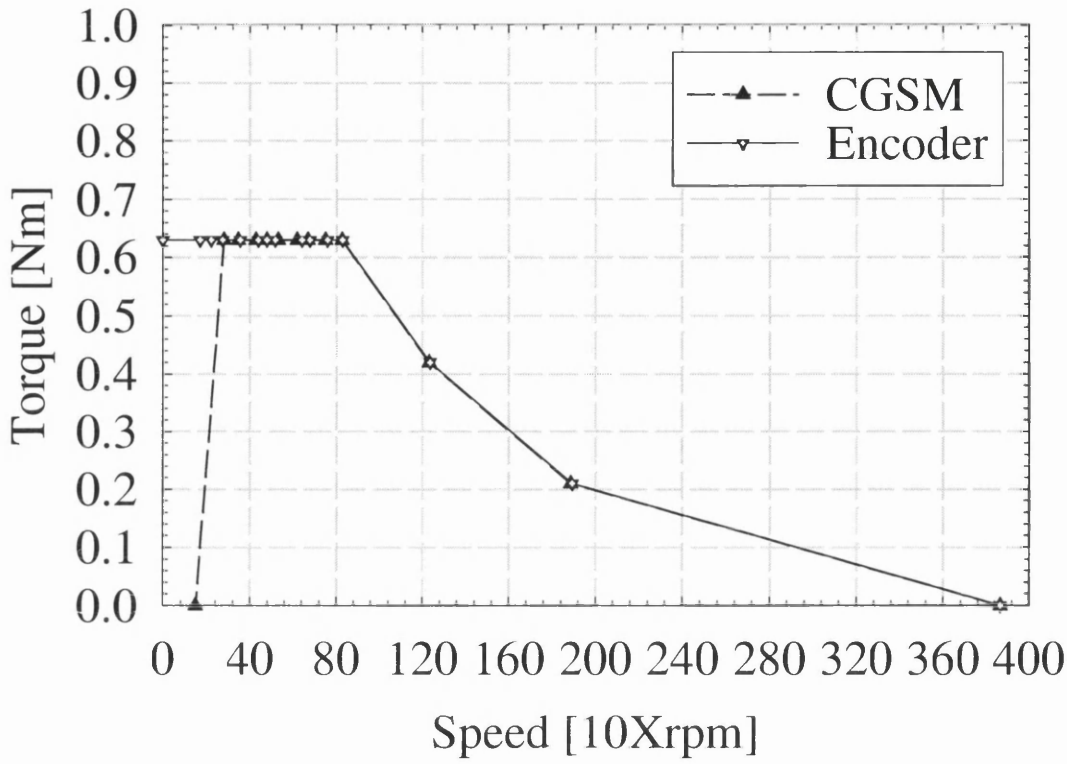

Figure 4.50: Torque-speed characteristic using *CGSM*.

Torque-speed characteristic

An important characteristic of any motor is the torque versus speed relation, where the torque is normally represented by the ordinate and the speed by the abscissa. This curve indicates where the motor can be operated safetly. Fig.4.50 depicts the torque-speed characteristic of the 3-phase 6/4 SRM used. And it also shows in which region *CGSM* can be applicable. It is clear that in the range from 0 to approximately 200 rpm estimation of rotor position is not possible. However above such speed, practically all the motor capability is covered. Based on this results we may generalised that *CGSM* is applicable in the whole constant power region of any motor. This argument is justified based on that for any SRM at medium and, in particular, at high speed (constant power region), the SRM has a peaky current waveform because it is operated in single pulse. As the current waveform is peakier the detection of rotor position with *CGSM* is easier and more robust.

On the other hand, the limit at low speed for the motor studied here was 25%

of the based speed, however, this will vary for other motors depending on the motor configuration and its characteristics.

4.6.4 Summary

The performance of *CGSM* has been investigated experimentally and proved that sensorless pulses can be obtained from every current waveform or from current in the lower transistor bus i_{bus} which is preferable because only one detection stage is required. The results show that the position estimation hardly differs from the real position at medium and high speed. However, at low speed there is deviation caused mainly by the torque ripple. At high speed there may be a delay caused by the cut-off frequency of the low-pass filters, this effect is reduced if the PWM frequency is increased. The error at low speed may be compensated as a function of speed.

The data obtained from the sensorless closed-loop speed control shows that *CGSM* is reasonably stable in speed and torque transients. The drive performance with and without sensor is comparable, furthermore the performance is not compromised in any way when using only i_{bus}. The torque-speed characteristic of the motor is limited when the motor is operated sensorless. At low speed *CGSM* is not applicable being the minimum limit in this case around 200 rpm. However at medium and high speed, all the motor capability can be used.

4.7 Conclusion

The basic principle of the new *current gradient* and *voltage magnitude sensorless method* has been discussed. Their theory, claims, advantages and limitations were given. It was stated that the sensitivity of these sensorless methods depends on the sharp change of phase inductance at (θ_o) and (θ_b).

For the first time the functionality of the new *current gradient sensorless method* for

SRM operated in PWM voltage control has been experimentally demonstrated. A brief discussion of how to use *CGSM* with one current sensor in the most common inverter topologies was given. The method detects one rotor position per phase per electrical cycle (stroke), with no *a priori* knowledge of motor parameters. The method is comparable in performance and complexity to the back-EMF sensing method of position estimation for brushless DC motors. Self-synchronisation and feedforward methods have been investigated as start-up procedures, being the latter the most reliable which assures robust start-up from standstill up to the predefined take-over speed even under load.

Experimental results confirm the theory and prove the concept of the new *current gradient sensorless method.* The position estimation can be detected with either one detection circuit per phase or with just one for the lower transistor bus current, which contains the same information as the phase currents, even with excitation overlap. The performance of the drive is not compromised in any way when using i_{bus} and most important it is used only one detection stage reducing significantly the implementation cost. It should be noticed that the only cost added by this scheme is the detection circuit which uses few and low-cost components with obvious scope for implementation as a single-chip solution. The results show that there is an error in rotor position estimation at low speed, the reasons are: offset in components of the detection stage and torque ripple which causes that the speed changes significantly in an electrical cycle. At high speed the cut-off frequency of the low-pass filters may introduce a delay in the sensorless pulses.

The firing angles may be varied freely with the one constraint that $\theta_{on} < \theta_o$, which is necessary anyway to produce adequate torque at high efficiency [34]. Feedforward (open-loop) is used to accelerate the motor smoothly from zero speed up to a maximum frequency and duty cycle determined by the desired take-over speed. A closed-loop speed PI-controller was implemented in sensorless mode and a series of speed and torque transients demonstrate the feasibility to close the speed loop by controlling the

PWM duty cycle. The results show that *CGSM* is reasonably stable for speed and torque transients.

In summary, it is concluded that the current gradient position estimation allows estimation of one rotor position per stroke with no *a priori* knowledge of the motor parameters except from the pole configuration. It is therefore applicable to most SRM topologies in a wide power and speed range and for most inverter topologies. The method allows to control the switched reluctance motor drive in two quadrants by controlling the commutation angles and PWM duty cycle, but could be expanded to four-quadrant operation, or continuous generator operation. This scheme is mainly suitable for medium and high speed applications. Also it should be noticed that this simple and low-cost implementation may allow the SRM technology into a range of air-moving and pump applications and even domestic appliances.

Chapter 5

High resolution Position Estimation For SRM Drives Using Flux linkage/Current Correction Model

This Chapter presents the research carried out on the study of position estimation algorithm for switched reluctance motors based on flux linkage and current observer. The theory, advantages and disadvantages of the algorithm are explained and discussed in detail, followed by the description of the simulation model together with results. The flux observer position estimation algorithm is implemented in real-time and the experimental results are presented which confirm the concept.

5.1 Introduction

One main reason why an electronic rotor position estimator is desired rather than a mechanical sensor is that mechanical sensors may be less tolerant of harsh environments than the motor itself leading to reliability problems and imposing limitations on the drive's application range. Furthermore, the overall physical envelope of the motor drive and the number of extra wires are increased. It should be noted that high resolution mechanical sensors, well protected to work under harsh environments are expensive.

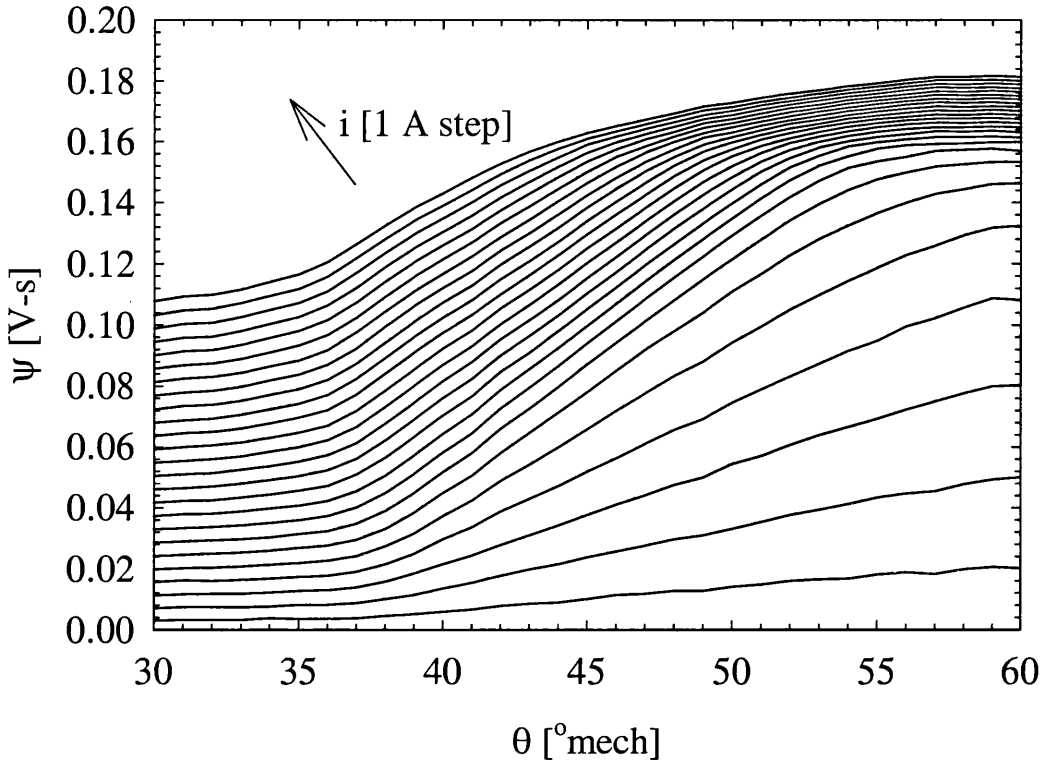

Figure 5.1: Measured magnetisation curves.

This chapter describes the principle of *High-grade* sensorless position estimation for a switched reluctance motor drive, using either flux linkage or current to correct for errors in rotor position. *High-grade* means that the algorithm is capable of estimating the rotor position accurately with fine resolution comparable to the position obtained from a resolver or encoder, i.e. typically 10000 pulses per revolution (ppr).

The estimation algorithm makes full use of the non-linear magnetic characteristics of the SRM through correlation of flux linkage (ψ), current (i) and rotor position (θ). The estimation model is simple, but with no loss in accuracy, leading to few real-time computations. Furthermore, a criterion is proposed to choose the phase most suited for position estimation when more than one phase conducts. The algorithm can also predict flux linkage, which in turn may be used to further correct the position estimate, and the features hereof are discussed.

An interesting approach for instantaneous rotor position estimation using current

correction model has been proposed recently by Acarnley *et al* [70, 71]. Its fundamental principle is based on the magnetic characteristics of the SRM (Fig.5.1); therefore all the non-linearities of $\theta = \theta(i, \psi)$ are taken into account. In [70] it is demonstrated that the algorithm works for the whole speed and conduction angles. However, simpler equations could be used in the algorithm for the same job without reducing its accuracy.

This work extends and discusses the position estimation technique presented in [70], and presents a simpler variation which requires fewer real-time computations. Furthermore, a criterion of how to choose the best phase for position estimation is given.

5.2 Theory

In this section, the proposed algorithm's principle is explained as a function of ψ, i and θ. The general flow diagram is shown in Fig.5.2. The block called *Position prediction* calculates the initial predicted position θ_p, which is obtained by extrapolation of the last updated and previous estimated positions. θ_p together with the predicted flux linkage ψ_p and the measured current i_m are used for the calculation of the rotor position error in each phase $\Delta\theta$ in the block named *Stage I*. This is the block where the current and flux linkage observer model are implemented. The block called *Position correction* calculates the final estimated position θ_e, which is obtained from θ_p and the contribution $\Delta\theta$ of the conducting phases. Finally, the block called *Stage II* obtains the corrected flux linkage ψ_c using θ_e, i_m and ψ_p. ψ_c can be used as the initial value for the next integration step in the *integrator* block for flux linkage correction. Different options can be used to represent each of these blocks which are now explained.

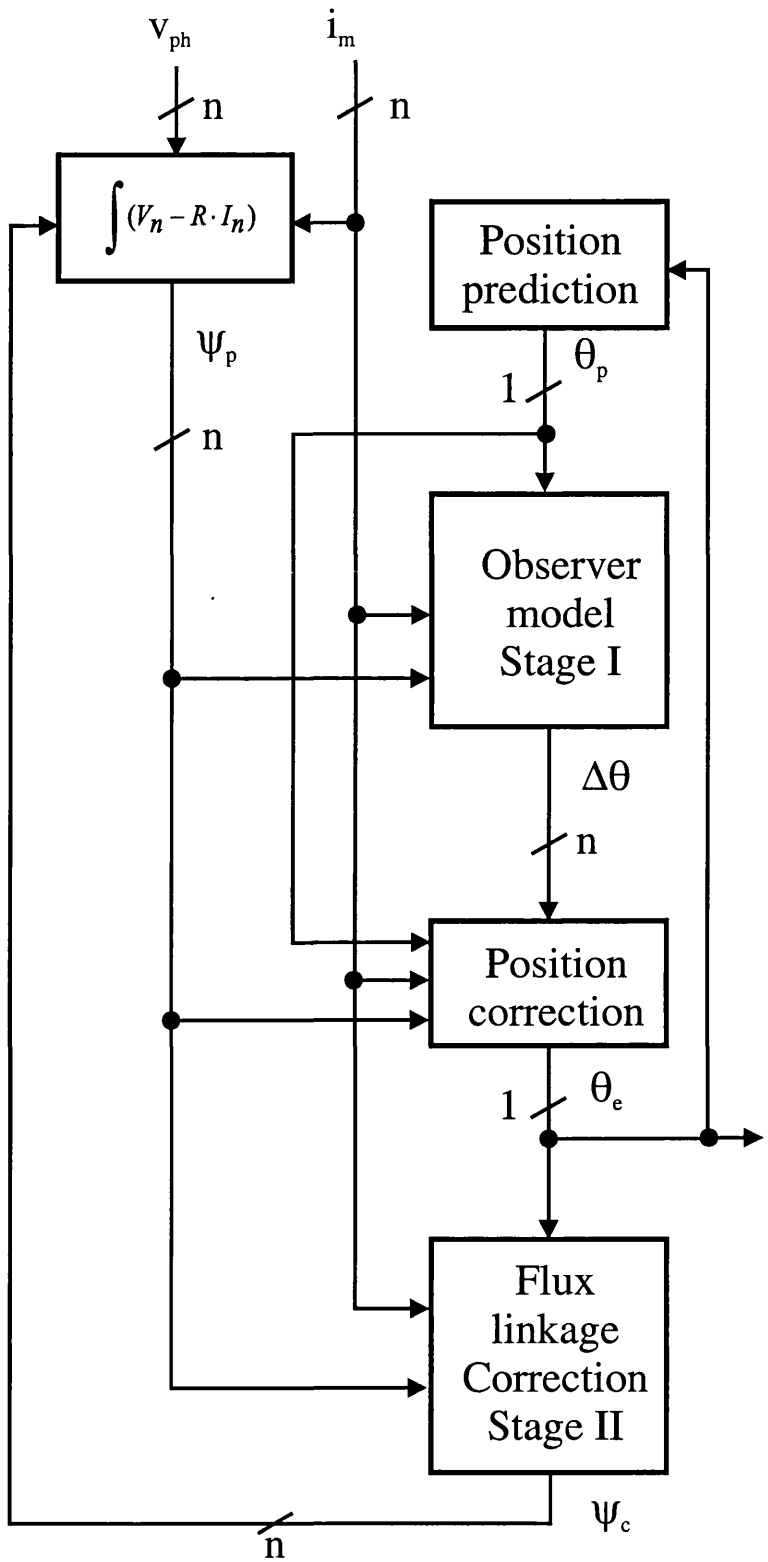

Figure 5.2: General flow diagram of position estimation algorithm. v_{ph} = Phase voltage, i_m = Current measured, θ_p = Predicted position, $\Delta\theta$ = Position error, θ_e = Estimated position, ψ_p = Predicted flux linkage, ψ_c = Corrected flux linkage for the next integration step.

5.2.1 Stage I

The flux linkage, current and position in each phase can be alternatively expressed as,

$$\psi = \psi(i, \theta), \tag{5.1}$$

$$i = i(\psi, \theta), \tag{5.2}$$

$$\theta = \theta(i, \psi). \tag{5.3}$$

Therefore, a small perturbation in ψ, i and θ can be expressed as follows,

$$\Delta\psi = \left[\frac{\partial\psi}{\partial i}\right]_{\theta=cst} \cdot \Delta i + \left[\frac{\partial\psi}{\partial\theta}\right]_{i=cst} \cdot \Delta\theta, \tag{5.4}$$

$$\Delta i = \left[\frac{\partial i}{\partial\psi}\right]_{\theta=cst} \cdot \Delta\psi + \left[\frac{\partial i}{\partial\theta}\right]_{\psi=cst} \cdot \Delta\theta, \tag{5.5}$$

$$\Delta\theta = \left[\frac{\partial\theta}{\partial i}\right]_{\psi=cst} \cdot \Delta i + \left[\frac{\partial\theta}{\partial\psi}\right]_{i=cst} \cdot \Delta\psi. \tag{5.6}$$

We define,

$$\theta_e = \theta_p + \Delta\theta, \tag{5.7}$$

where, θ_p = predicted position and θ_e = estimated position.

$$\Delta\psi = \psi_p - \psi_e, \tag{5.8}$$

where, ψ_p = predicted flux linkage and ψ_e = estimated flux linkage.

$$\Delta i = i_m - i_e, \tag{5.9}$$

where, i_m = measured current and i_e = estimated current.

θ_p is extrapolated linearly (assuming that the motor speed is constant in the calculation interval) by using previous and actual position values. The flux linkage for each phase can be predicted by applying Faraday's law,

$$\psi_p = \int (v_{ph} - R \cdot i)dt, \tag{5.10}$$

where, v_{ph} = phase voltage $(D \cdot V_{DC} - v_{drop})$[1] and i = phase current.

In this stage we have to assume that there is no error either in flux linkage ($\Delta\psi = 0$) or current ($\Delta i = 0$).

Case I

From (5.4), (5.5) and (5.6), six equations can be obtained which represent $\Delta\theta$. If we assume $\Delta i = 0$, the first three equations are:

$$\Delta\theta = \frac{1}{\left[\frac{\partial\psi}{\partial\theta}\right]_{i=cst}} \cdot \Delta\psi, \tag{5.11}$$

$$\Delta\theta = -\frac{\left[\frac{\partial i}{\partial\psi}\right]_{\theta=cst}}{\left[\frac{\partial i}{\partial\theta}\right]_{\psi=cst}} \cdot \Delta\psi, \tag{5.12}$$

$$\Delta\theta = \left[\frac{\partial\theta}{\partial\psi}\right]_{i=cst} \cdot \Delta\psi. \tag{5.13}$$

Case II

The rest are obtained when $\Delta\psi = 0$, giving,

$$\Delta\theta = -\frac{\left[\frac{\partial\psi}{\partial i}\right]_{\theta=cst}}{\left[\frac{\partial\psi}{\partial\theta}\right]_{i=cst}} \cdot \Delta i, \tag{5.14}$$

$$\Delta\theta = \frac{1}{\left[\frac{\partial i}{\partial\theta}\right]_{\psi=cst}} \cdot \Delta i, \tag{5.15}$$

$$\Delta\theta = \left[\frac{\partial\theta}{\partial i}\right]_{\psi=cst} \cdot \Delta i. \tag{5.16}$$

It can be observed that (5.11) is equal to (5.13), and (5.15) is equal to the negative value of (5.16). Hence, the options available for *Stage I* are reduced to four equations, (5.12), (5.13), (5.14) and (5.16). We define the partial derivatives as a conversion factors from either $\Delta\psi$ or Δi to error in position $\Delta\theta$.

[1] D, V_{dc} and v_{drop} correspond to the Duty cycle of the PWM modulation, DC link voltage and the voltage drop in inverter's devices respectively.

5.2.2 Stage II

For *Stage II*, we consider that the initial predicted position has been corrected and therefore $\Delta\theta = 0$.

Case I

When $\Delta i = 0$ and assuming $\Delta\theta = 0$, we obtain from (5.4), (5.5) and (5.6) that $\Delta\psi = 0$. Therefore we have from (5.8),

$$\psi_e = \psi_p. \tag{5.17}$$

Case II

On the other hand, if $\Delta i <> 0$, we obtain from (5.4), (5.5) and (5.6) the following equations,

$$\Delta\psi = \left[\frac{\partial\psi}{\partial i}\right]_{\theta=cst} \cdot \Delta i, \tag{5.18}$$

$$\Delta\psi = \frac{1}{\left[\frac{\partial i}{\partial\psi}\right]_{\theta=cst}} \cdot \Delta i, \tag{5.19}$$

$$\Delta\psi = -\frac{\left[\frac{\partial\theta}{\partial i}\right]_{\psi=cst}}{\left[\frac{\partial\theta}{\partial\psi}\right]_{i=cst}} \cdot \Delta i. \tag{5.20}$$

We can observe that (5.18) is equal to (5.19). Hence, the options available are reduced to two equations (5.18) and (5.20). In this case, the partial derivatives are considered as correction factors from Δi to $\Delta\psi$. From (5.8) the estimated flux linkage becomes,

$$\psi_e = \psi_p - \Delta\psi. \tag{5.21}$$

It should be noted that Case I does not have any correction factors in order to obtain the estimated flux linkage, therefore requires less operations than Case II. Now the

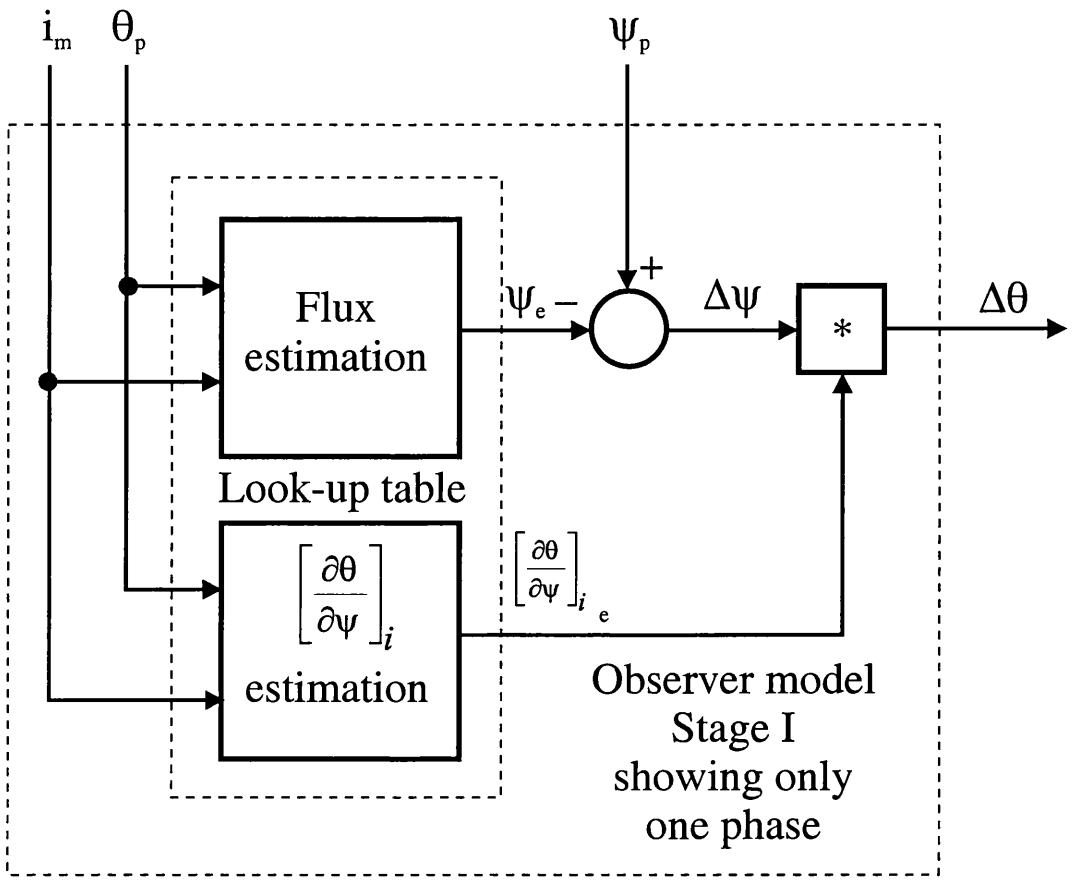

Figure 5.3: Block diagram of *Stage I*.

question raised is which model representing *Stage I* and *Stage II* is the best for real-time implementation. In real implementation, the current is more likely to have less error than the flux linkage which is predicted by the integration of the phase voltage. Therefore, the first impression is to go for the model that assumes $\Delta i = 0$. Simulations were carried out with (5.13) and (5.14) introducing an error in the prediction of flux linkage (shown in the next section (Fig.5.8)). The results demonstrate that both approaches are equally sensitive to error in the predicted flux linkage. Then the only criterion left for choosing the model is to take the simpler one, i.e. the model that requires minimum computation in order to reduce the number of operations made in real-time. It is worthy to note that the correction factors (partial derivatives) could be stored in a look-up table, however this option has the disadvantages of increasing the amount of stored data and also the calculation time.

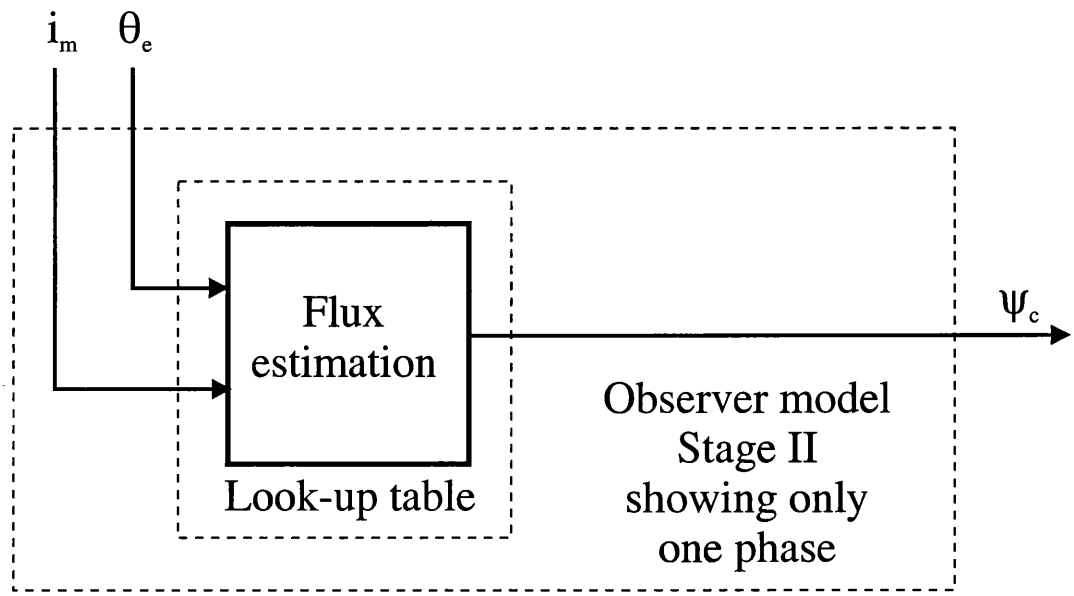

Figure 5.4: Block diagram of *Stage II*.

This thesis proposes the use of either (5.13) or (5.16) for *Stage I* and (5.17) for *Stage II*. Fig.5.3 and Fig.5.4 depict the block diagrams of *Stage I* (only for (5.13)) and *Stage II* respectively. It is important to note that the calculation of the correction factors is not significant. Furthermore, it can be reduced by having the magnetisation curves stored with 1A current step.

5.2.3 Position Correction

After obtaining the error in position $\Delta\theta_n$ for each phase in *Stage I*, the initial predicted position θ_p can be corrected by using one of the following options:

1. The errors in position for each phase ($\Delta\theta_n$) are averaged in order to obtain a single error position value ($\Delta\theta$), it gives,

$$\Delta\theta = \frac{[\Delta\theta_1 + \Delta\theta_2 + \Delta\theta_3 + \cdots + \Delta\theta_n]}{n}, \tag{5.22}$$

2. The errors in position for each phase ($\Delta\theta_n$) are weighed to obtain $\Delta\theta$, it results in,

$$\Delta\theta = [k_1 \cdot \Delta\theta_1 + k_2 \cdot \Delta\theta_2 + k_3 \cdot \Delta\theta_3 + \cdots + k_n \cdot \Delta\theta_n], \tag{5.23}$$

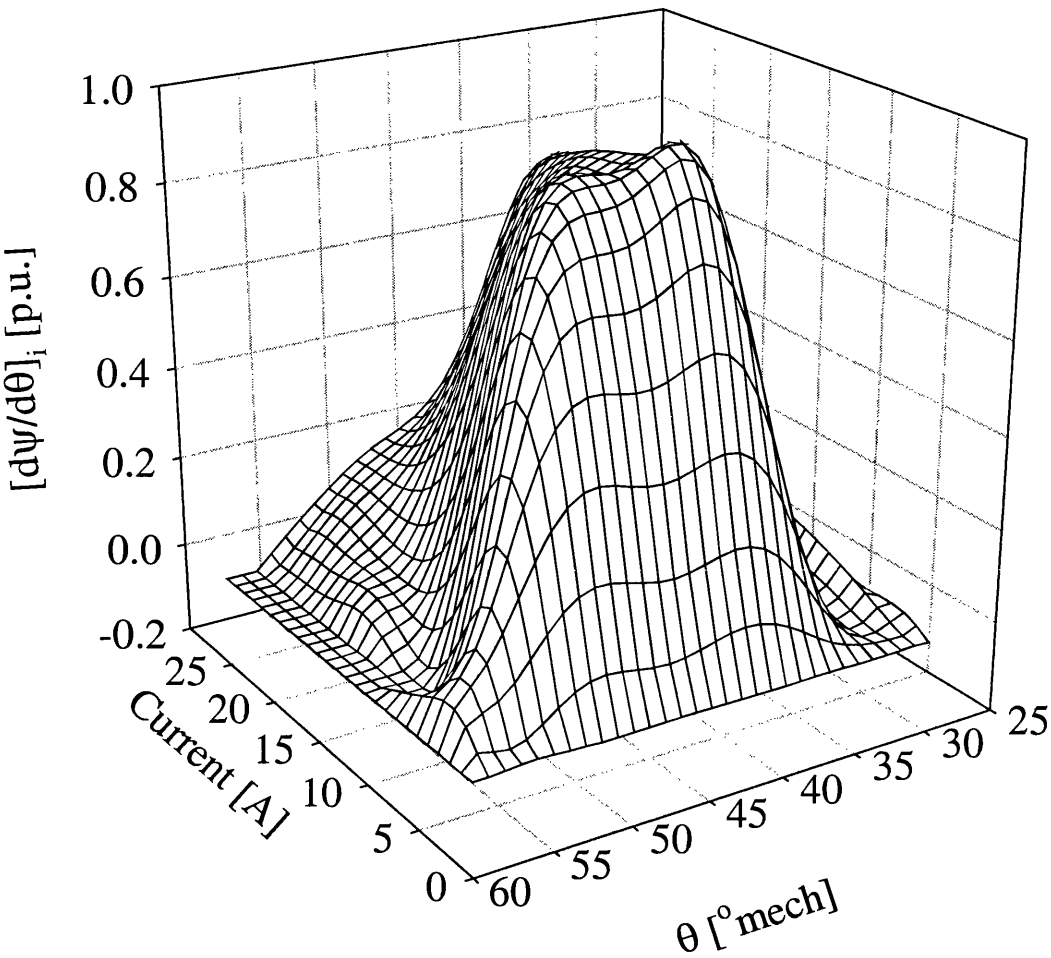

Figure 5.5: $\left[\frac{\partial\psi}{\partial\theta}\right]_{i=cst}$ normalised. $\theta_u = 30^o$, $\theta_a = 60^o$.

3. $\Delta\theta$ is equal to $\Delta\theta_b$, i.e. the position is corrected from the phase which can give more precise position information.

$$\Delta\theta = \Delta\theta_b, \tag{5.24}$$

where, n = number of phases which have current, k = weighting factor and b = *the best phase.*

The first two methods combine the error of all phases that have current into a single position correction factor. It is known that the position estimation is less accurate ($\Delta\theta$ is bigger) in the region close to unaligned (θ_u) and aligned (θ_a) position due to the small changes in $\left[\frac{\partial\psi}{\partial\theta}\right]_{i=cst}$ (Fig.5.1). Therefore, it is clear that (5.22) is more likely to

obtain a wrong $\Delta\theta$ when one phase, among all, is close to either θ_u or θ_a. In contrast, (5.23) will obtain a more precise $\Delta\theta$ when one of the phases is close to θ_u or θ_a. The third option estimates the position from *the best phase* among all conducting phases using (5.24). Therefore it avoids errors around θ_u and θ_a. Note that option two is the most general because options one and three can be obtained from two if the weight factors are chosen appropriately.

This thesis proposes the use of option 3 and its implementation is explained as follows. The criterion is to minimise the error $\Delta\theta$. Hence $\left[\frac{\partial\theta}{\partial\psi}\right]_{i=cst}$ should be minimum, or its inverse $\left[\frac{\partial\psi}{\partial\theta}\right]_{i=cst}$ maximum for the specific model chosen (5.13). Fig.5.5 depicts the normalised version of $\left[\frac{\partial\psi}{\partial\theta}\right]_{i=cst}$, which shows that the maximum resolution (minimum error $\Delta\theta$) is obtained around 40^o and 18A for the specific 8/6 4-phase SRM used. The minimum resolution is around θ_u and θ_a. Close to θ_a the resolution decreases as the current increases. One phase will be in a region with higher resolution than the other conducting phases. Therefore this information indicates which is *the best phase* to give effective position error. Furthermore, it may be used to represent the k_n factors for option 2.

5.2.4 Advantages and Disadvantages

The main advantage of the observer algorithm is that instantaneous position can be estimated because the algorithm is based in the model of the machine, which is run simultaneously with the actual motor.

Advantages

- High resolution of position estimation.
- It is applicable to any switched reluctance motor.
- It is applicable to true dynamic four-quadrants operation of the drive.
- The algorithm leads to minimum mathematical operation.

- The algorithm chooses the most accurate phase for position estimation from all conducting phases.
- It does not compromise the performance of the motor.
- It allows closed-loop speed control.
- It allows closed-loop position control.
- It allows current control and PWM voltage control.
- It permits soft, hard chopping and single pulse operation.
- It allows current profiling.
- Commutation angles can be set freely.
- It permits load torque transients.
- It is suitable for low and medium speed.
- It is applicable at stand-still with having an initialisation routine.
- It is applicable either using current and voltage in energised phase or unenergised phase (injecting probing pulses).

Disadvantages

The main disadvantage is the calculation of the predicted flux linkage.

- At high speed is limited by the speed of the DSP to cope with mathematical operations.
- Pre-stored data of magnetisation curves is needed.
- The electronics needed may be a significant part of the total cost of the drive.
- Difficult to obtain precise flux linkage by integration of phase voltage

5.2.5 Summary

The theory has been introduced and shows that there are four equations to represent the error in rotor position. Two of them translate the error in flux linkage into an error in position (flux linkage observer), while the other two translate the error in current into an error in position (current observer). It is recommended to use (5.13) and (5.16) which lead to fewer operations. An open loop method to correct the flux linkage is suggested in a second stage of the algorithm (5.17). Furthermore, how to chose *the best phase* for position estimation, from all conducting phases, is proposed and discussed with other options. The whole algorithm is illustrated in a block diagram.

5.3 Simulink^R model

The observer model was built in Simulink^R and the position is estimated at rate of 5kHz. Fig.5.6 depicts the block diagram of the complete model, which is formed mainly by 9 blocks. In order to analyse the different blocks of the algorithm, the actual position is used for commutation in this model, i.e. the estimated position is not fed back for commutation. Each block of the model is described as follows.

4 phase commutator: This block has as inputs the position, turn on and turn off angle, current reference, torque and speed. Commutation for each phase is generated simply by comparison of the position signal and firing angles.

Hybrid PI and Bang-Bang current controller: The detail of this block is shown in Fig.5.7 which contains 5 sub-blocks; current sampling, bang-bang controller, digital PI controller, PWM modulator, voltage calculation. The reference current and the actual current of all phases are sampled in the sampling sub-block at 5 kHz synchronised with the PWM modulator. For simplicity, the current is regulated in two ways depending on the speed. Bang-bang is used at high speed, and a PI control is used for low and medium speed. The reason is that at high

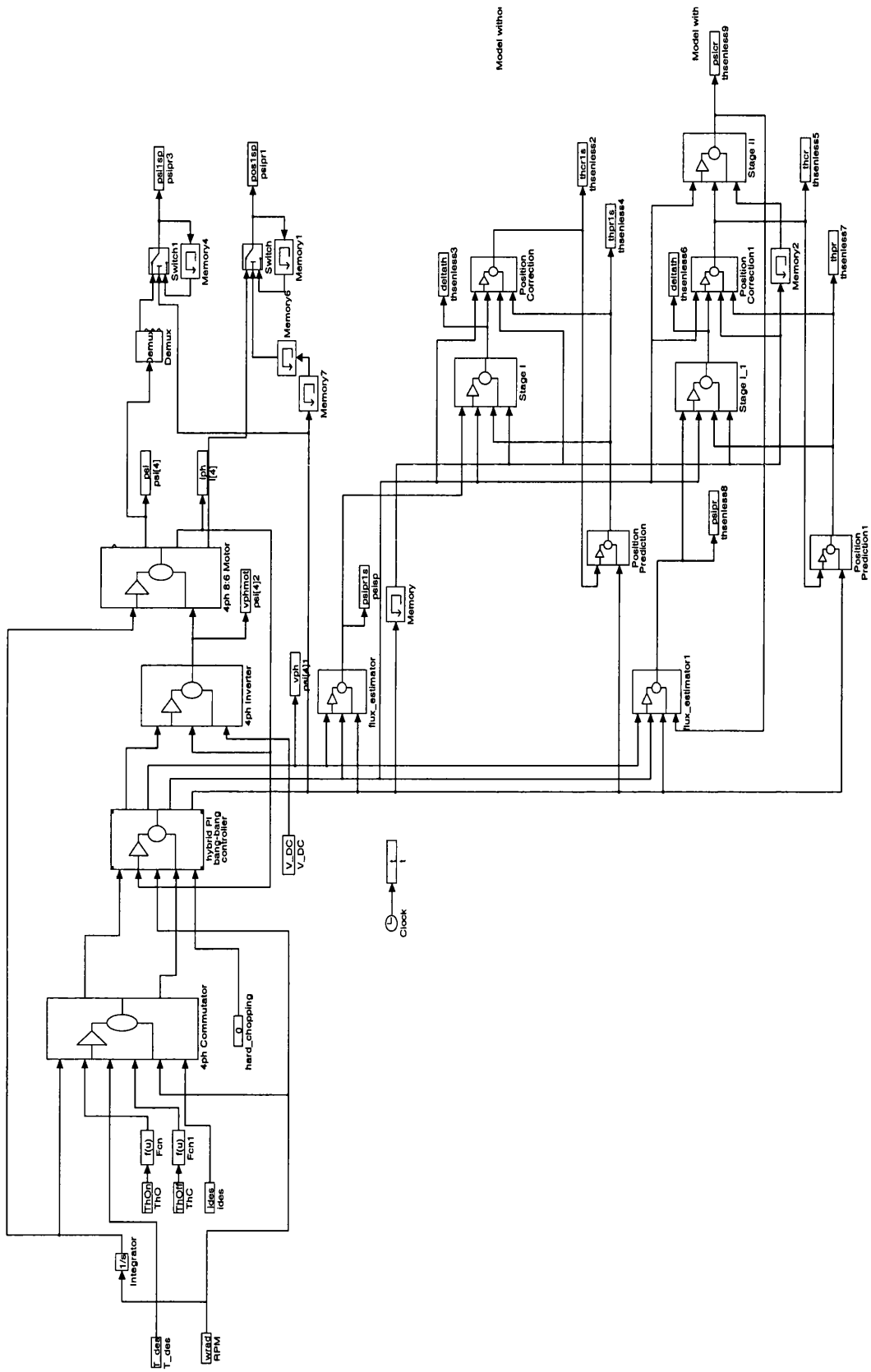

Figure 5.6: Simulink® model of the flux observer.

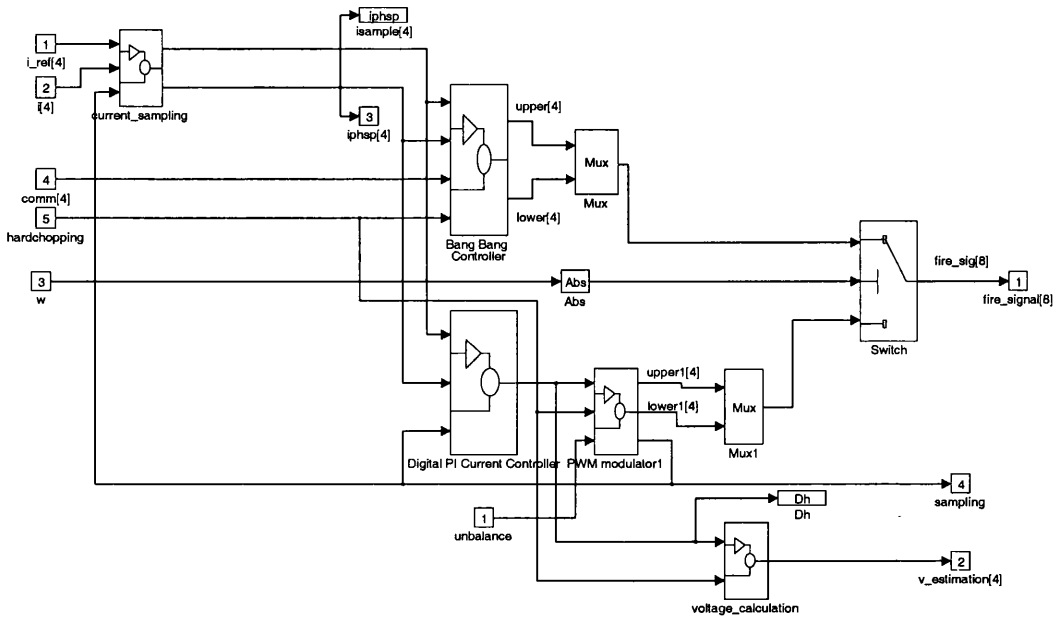

Figure 5.7: Block diagram of current regulator

speeds, the PI control with fixed gain needs several sample intervals to bring the current to the reference due to the large variation of the incremental inductance. In contrast, bang-bang response basically takes one sample interval to bring the current to the reference, although with a higher current ripple. The PI regulator calculates the required duty cycle to control the current. This duty cycle is used by the PWM modulator for generation of the switching signals for the inverter. The voltage estimation takes place in the voltage calculation block. The voltage is estimated depending if the drive is operated in hard chopping or soft chopping. The following equations are used:

For Hard chopping,

$$v_{ph} = 2 \cdot D_h \cdot [v_{dc} + v_d - v_t] - v_{dc} - 2 \cdot v_d, \tag{5.25}$$

For Soft chopping if $D_h \geq 50\%$, one transistor is always on and the other one is modulated, yielding,

$$v_{ph} = D_s \cdot [v_{dc} + v_d - v_t] - v_t - v_d, \tag{5.26}$$

For Soft chopping if $D_h \leq 50\%$, one transistor is always off and the other one is modulated, we obtain,

$$v_{ph} = D_s \cdot [v_{dc} + v_d - v_t] - v_{dc} - 2 \cdot v_d, \tag{5.27}$$

The relation between the hard duty cycle and soft duty cycle is as follows,

$$D_s = 2 \cdot [D_h - 0.5] \tag{5.28}$$

where v_{dc} = dc-link voltage, v_{ph} = phase voltage, v_d = voltage drop in the diode, v_t = voltage drop in the transistor, D_h and D_s are the hard and soft duty cycle respectively. The estimated voltage is used to estimate the flux linkage in the flux estimator block.

4 phase inverter: In this block the ideal leg of the classic inverter with two switches and two diodes per phase is modelled, only the voltage drop in the transistor and diode is taken into account.

4 phase 8/6 Motor: Each phase of the motor is modelled independently using a look-up table of a set of magnetisation curves and a look-up table of static torque data. The inputs are the rotor position and phase voltage. The flux linkage is calculated by integration of $(v_{ph} - R \cdot i_{ph})$. The current is obtained from the look-up table using flux linkage and rotor position. Once the current is calculated, it is used to obtain the instantaneous torque from a second look-up table.

Position prediction: The extrapolation of the next position takes place in this block. Linear extrapolation has been used for simplicity and reduction of calculation time. Simulation results shown that it was enough. It yields in

$$\theta_p = 2 \cdot \theta_{e(k)} - \theta_{e(k-1)} \tag{5.29}$$

where $\theta_{e(k)}$ = the actual estimated position and $\theta_{e(k-1)}$ = the previous estimated position. This predicted position is corrected in the block position correction.

Flux estimator: The discrete flux linkage of each phase is predicted by,

$$\psi_p = (v_{ph} - R \cdot i_{ph}) \cdot T_s + \psi_{old} \tag{5.30}$$

where ψ_p = predicted flux linkage, v_{ph} = phase voltage, R = phase resistance, i_{ph} = phase current, $T_s = 1/f_s$ = sampling period ($200\mu s$) and ψ_{old} = previous flux linkage. When *Stage II* is used, ψ_{old} is equal to the corrected flux linkage calculated in such stage.

Stage I: Either the flux observer or current observer is implemented here, i.e. equation from (5.11) to (5.16). For the flux observer, $\Delta\psi$ is translated to $\Delta\theta$, and for the current observer Δi is translated to $\Delta\theta$ which is used to correct the predicted position in the next block.

Position correction: The equation (5.7) is evaluated in this block which obtains the estimated position. The estimated position is fed back to the position prediction block. The selection of *the best phase* also takes place in this block using a loop-up table with the $\left[\frac{\partial\psi}{\partial\theta}\right]_{i=cst}$ data. The phase with highest $\left[\frac{\partial\psi}{\partial\theta}\right]_{i=cst}$ is chosen for position estimation.

Stage II: Any equation from (5.17) to (5.20) can be implemented here. For the case of (5.17), a simple look-up table is used for flux linkage correction as shown in Fig.5.4.

The model was implemented with two position estimators, *with Stage II* and *without Stage II*, in order to analyse the contribution of *Stage II* which is discussed in subsection 5.4.3.

5.4 Simulation results

The motor used is a 8/6 4-phase SRM. All the angles and $\Delta\theta$ are in mechanical degrees. Unaligned and aligned position are at 30° and 60° respectively. In order to analyse the algorithm, all simulations were carried out with commutation made from θ_{actual} [2]. i.e. position estimate not used for closed loop control at this stage.

5.4.1 Flux linkage and current observer models

The SR machine, in contrast with the AC and brushless DC systems, does not need continuous current flow in each phase. In other words, the current only flows in part of the whole electrical cycle (positive slope of the phase inductance for motoring). This is of great advantage for the calculation of the flux linkage because it means that the flux linkage is reset every electrical cycle in the period where there the current is zero. However, the calculation of flux linkage can end up with large errors, specially at low speed where the integration time is long.

We can assume that in real implementation, the measured current is more reliable than the predicted flux linkage. Therefore simulations were carried out introducing an error in the flux linkage prediction. The error consisted in neglecting the voltage drop of the inverter in the integration of the phase voltage.

Fig.5.8 depicts the results obtained when models (5.13) and (5.14) are used. The position is corrected using option 3. The motor is operated at 716 rpm and 8 A with $\theta_{on} = 30°$, $\theta_{off} = 55°$. (a) and (b) show the error in estimated position when the current observer and flux observer are used respectively ($\Delta\theta = \theta_{actual} - \theta_{e}$.), we observe that both observers behave the same and the position error oscillates between -1° and -0.2°. Note that the ripple in the position error is caused by swapping the position estimation from phase to phase. The graphs from (c) to (f) were obtained from the flux observer model (the results from current observer model are identical). (c) shows

[2]subscript *actual* refers to the true value, i.e. no error.

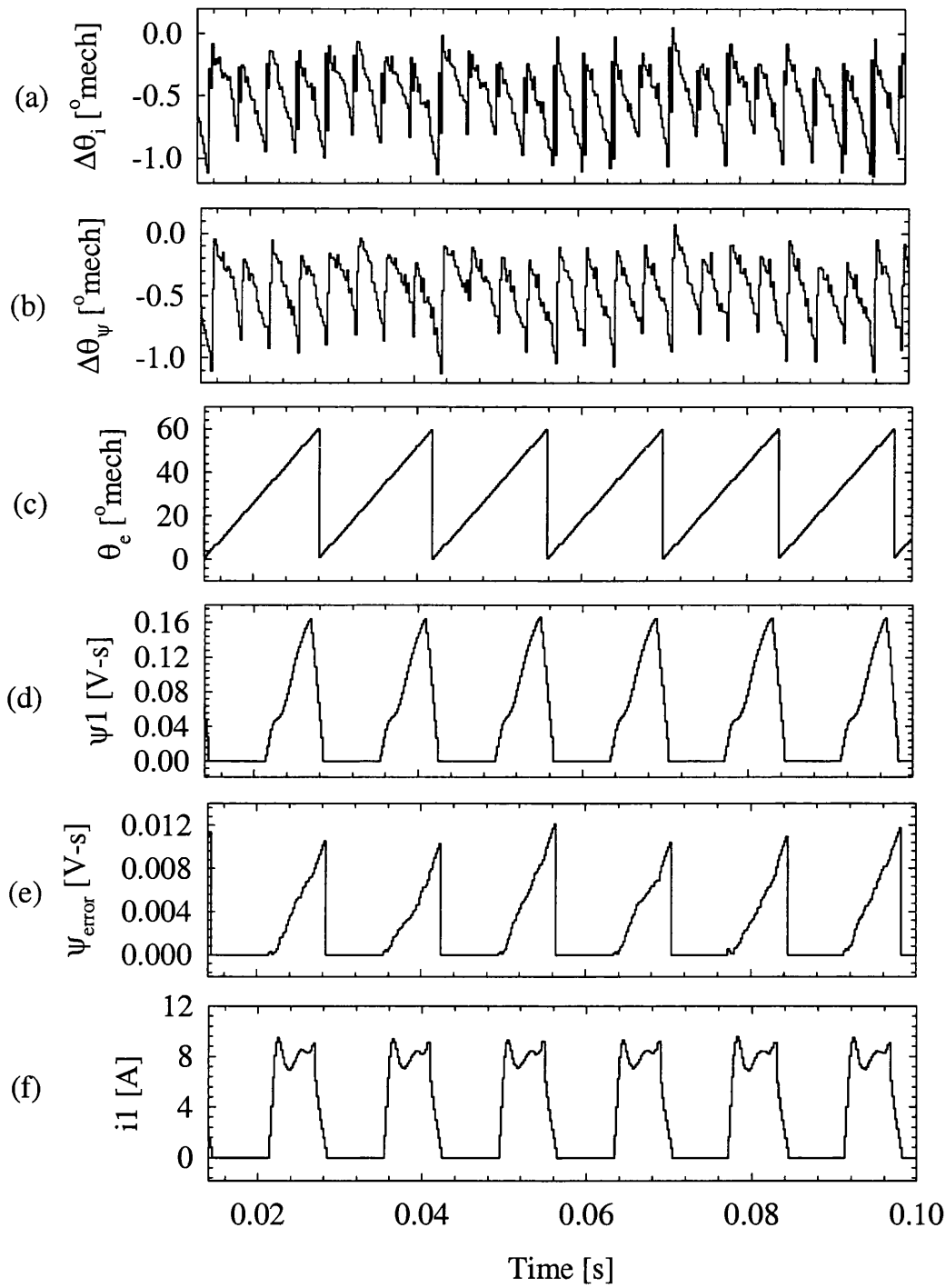

Figure 5.8: Sensitivity to flux linkage error of current and flux linkage observer model. Current observer model, a: Error in estimated position. Flux observer model, b: Error in estimated position, c: Position estimated, d: Flux linkage for phase 1, e: Error in flux linkage, f: Current in phase 1.

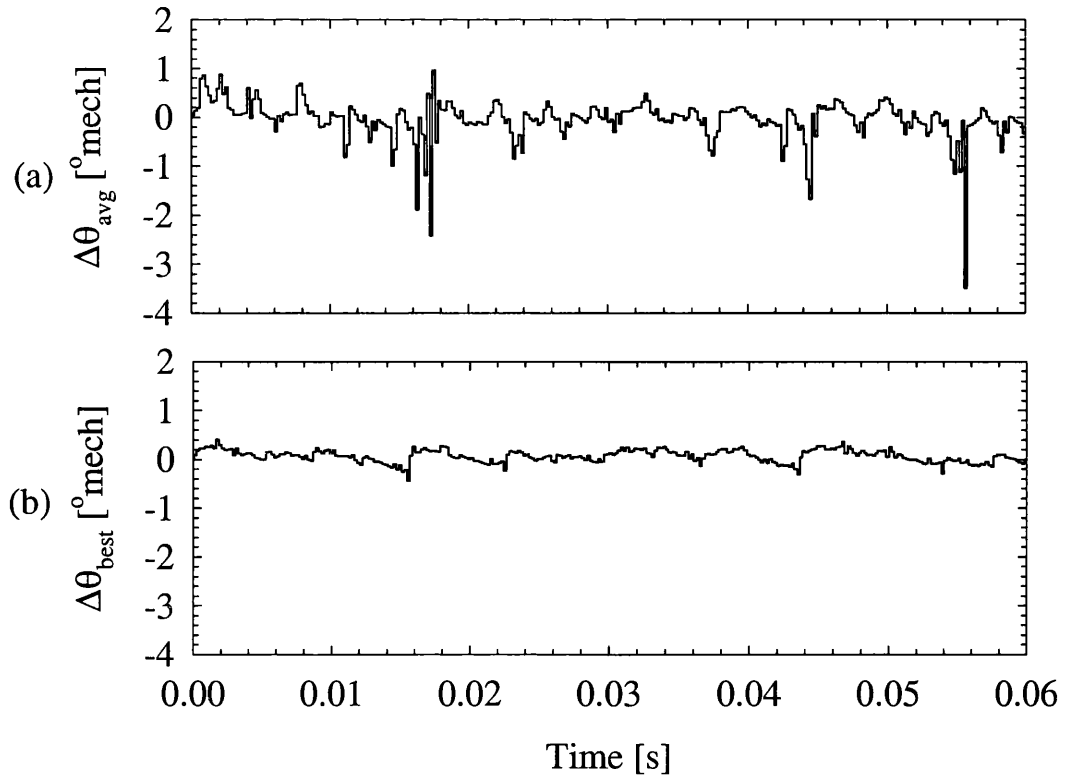

Figure 5.9: Comparison between error using the average and best phase method. a: $\Delta\theta_{avg}$, b: $\Delta\theta_{best}$.

the estimated position (θ_e), (d) shows the predicted flux linkage for phase one ($\psi 1$), (e) depicts $\psi_{error} = \psi_p - \psi_{actual}$ [3], note that ψ_{error} is increasing respect to time as expected and it is clear that the flux linkage is reset when the current is zero. (f) depicts the current flowing through phase 1. The result confirm that the current and flux linkage observer are equally sensitive to errors in flux linkage, therefore, we can conclude that there is not any advantage in using either the current or flux linkage observer. The work presented here is using the flux linkage observer.

5.4.2 Position correction

The normalised values of $\left[\frac{\partial\psi}{\partial\theta}\right]_{i=cst}$ were stored in a look-up table at every $1°mech$ (Fig.5.5). This table is read in each sampling cycle for all phases which have current. The phase with the maximum value is the one used to estimate the position.

[3]Note that this $\Delta\theta$ is different from the one defined in section 5.2

The results of Fig.5.9 were obtained using (5.13) with $\theta_{on} = 30^o$, $\theta_{off} = 55^o$, at 716 rpm and 8A. (a) and (b) depict the error in estimated position for option 1 and option 3 respectively. It should be noted that for option 1, the position range has to be limited i.e. the whole electrical cycle is not used for position estimation. Otherwise the errors around θ_u and θ_a make the algorithm to diverge from the actual position. It was found that eliminating the range $30^o \pm 2^o$ and $60^o \pm 2^o$ was enough. From the results, it can be observed that option 3 leads to a smaller position error than option 1.

Fig.5.10 clearly shows that the error in estimated position close to the aligned and unaligned positions is bigger than in the middle region, the simulation is carried out with $\theta_{on} = 30^o$ and $\theta_{off} = 55^o$. (a) shows the estimated position, (b) depicts the predicted flux linkage calculated by (5.30), (c) shows the estimated flux linkage calculated from the look-up table, (d) depicts the flux linkage error $\Delta\psi$ which oscillates between ± 0.002 V-s, (e) shows that $\left[\frac{\partial\theta}{\partial\psi}\right]_{i=cst}$ tends to ∞ close to aligned and unaligned position which makes large error around these positions (f) depicts the correction position factor $\Delta\theta$ which is obtained by the multiplication of (d) by (e) according to (5.13), also the *the best phase* from which the position is estimated is shown, note that the large correction factor $\Delta\theta$ close to aligned and unaligned position are avoided when choosing *the best phase* for position estimation. Moreover, it is observed that the correction factor $\Delta\theta$ is around zero in the region where position is estimated from phase one, which means a very good position estimation. (g) shows the current for phase one.

Fig.5.11 (a) depicts the normalised version of $\left[\frac{\partial\psi}{\partial\theta}\right]_{i=cst}$ for phase 1 (solid line) and phase 4 (dashed line), note that their intersection indicates that the position estimation should be swapped from phase 1 to phase 4, which results in graph (b) showing *the best phase* for position estimation. Here is clear that the resolution of position estimation is not only a function of current level but a function of rotor position. (c) depicts the current for phase 1 and phase 4, which have an excitation overlap of 10^o, (d) depicts the flux linkage for phase 1 and (e) shows the estimated position.

This thesis proposes the implementation of option 3, which has the advantage of

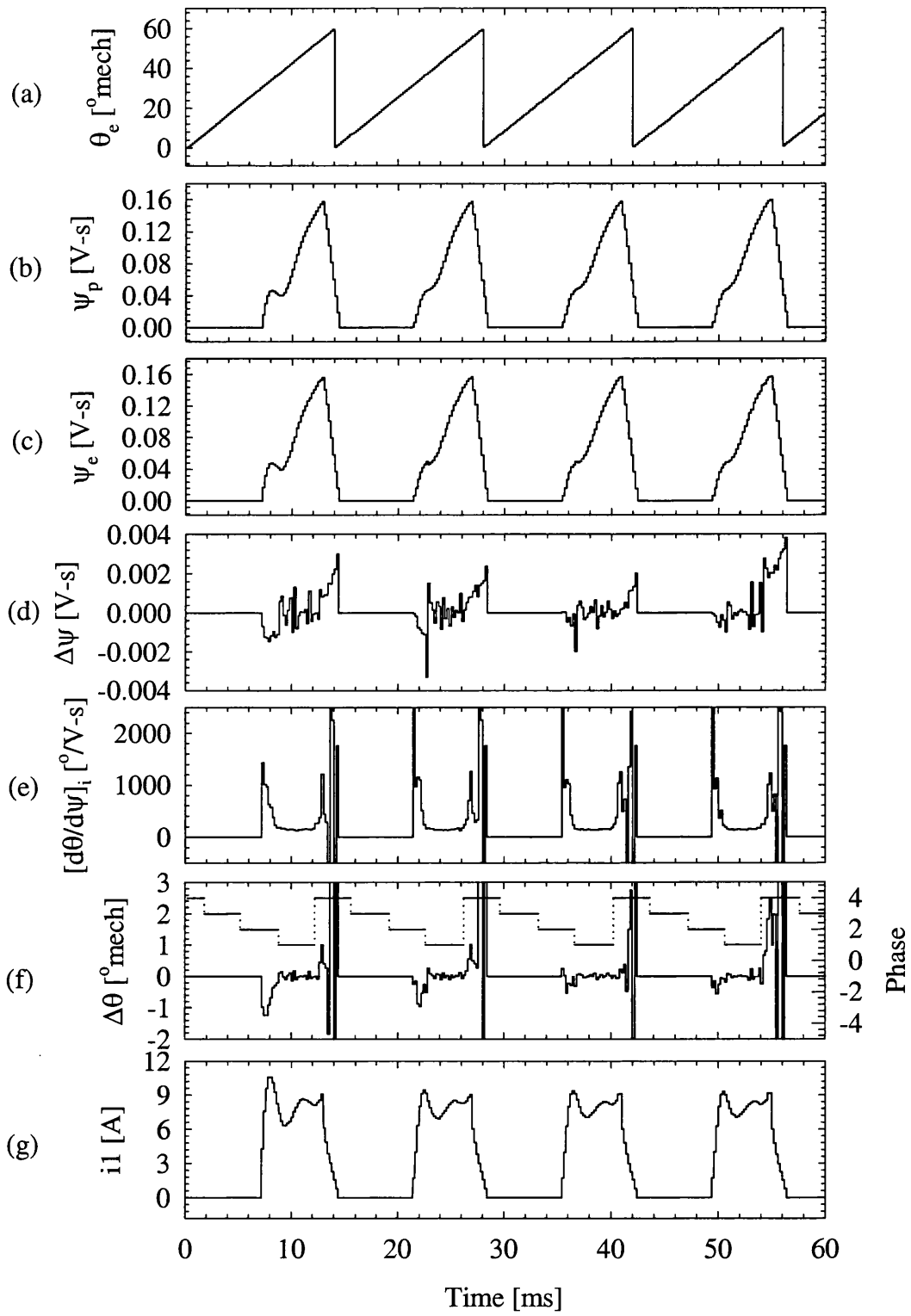

Figure 5.10: Estimated position at 716 rpm. a: Estimated position, b: Predicted flux linkage, c: Estimated flux linkage, d: $\Delta\psi$, e: $\left[\frac{\partial\theta}{\partial\psi}\right]_{i=cst}$ for phase 1, f: $\Delta\theta$, g: Current in phase 1.

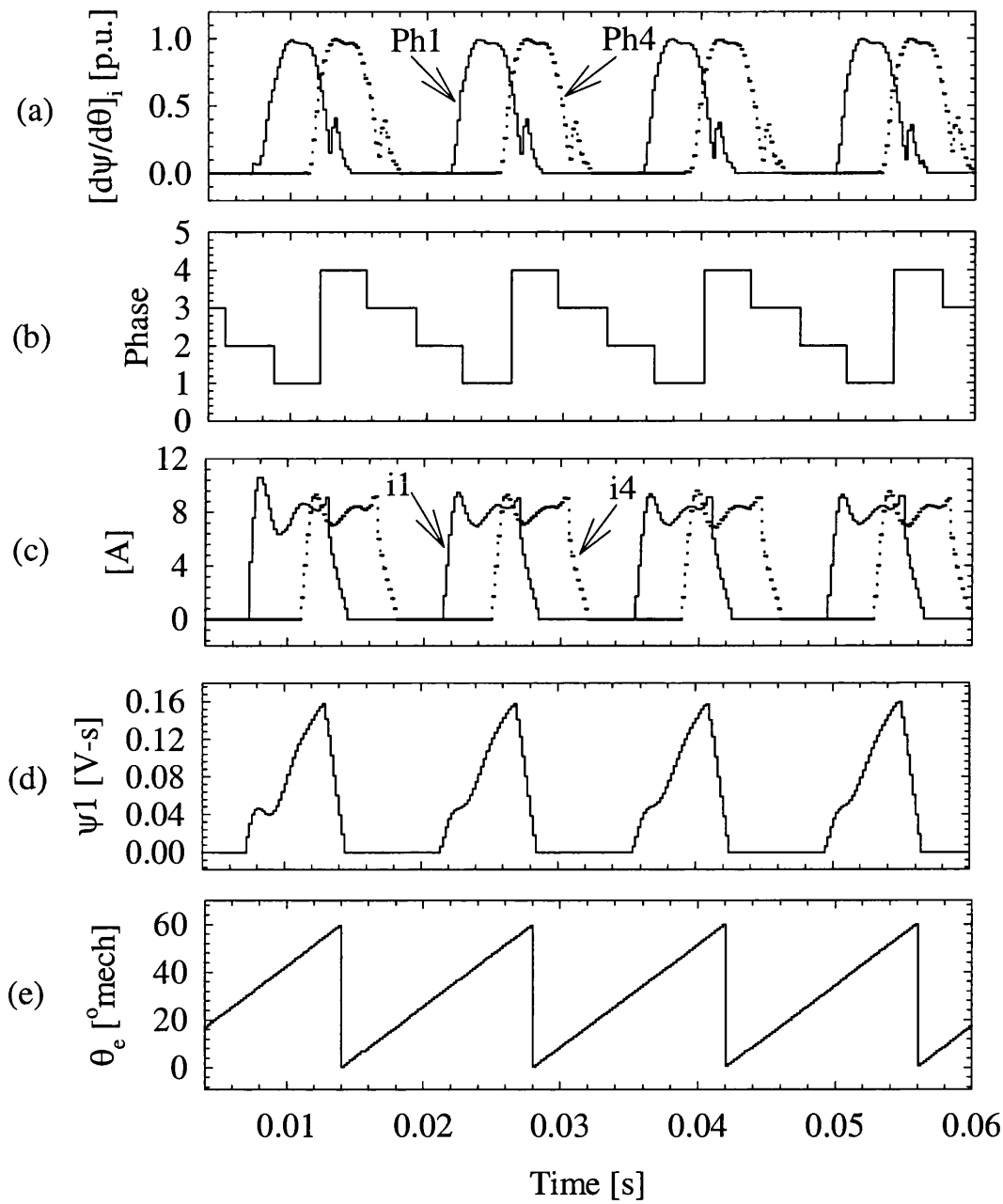

Figure 5.11: Flux observer model using the best phase for position estimation. a: $\left[\frac{\partial \psi}{\partial \theta}\right]_{i=cst}$ for phase 1 and 4, b: Phase from which the position is estimated, c: Current in phase 1 (solid line) and 4 (dashed line), d: Flux linkage for phase 1, e: Estimated position.

leading to the most precise position estimation when there is current flowing in more than one phase, doing so, the calculation of *Stage I* is reduced just for *the best phase* instead of all conducting phases.

5.4.3 Flux linkage correction

In this section the performance of *Stage II* is discussed. Again an error was introduced in the flux linkage prediction as before. It is well known that at low current, low speed the prediction of flux linkage (using the integration of phase voltage) is likely to have more errors. Therefore, to assess the performance of *Stage II*, simulations were carried out both *with* and *without Stage II.* with $\theta_{on} = 20^o$, $\theta_{off} = 55^o$, at 716 rpm and 5A. The solid line and dashed line correspond to simulations *without Stage II* and *with Stage II* respectively.

Fig.5.12 (a) depicts the current for phase 1, (b) shows the flux linkage for phase 1, the gray line represents the actual flux linkage ψ_{actual}. The error in flux linkage is plotted in (c), it is clear that *Stage II* is compensating the error in flux linkage when the flux linkage is not changing rapidly. In contrast, the flux linkage predicted *without Stage II* diverge all the time. However, when the actual flux is changing rapidly, the predicted flux linkage obtained *with* and *without Stage II* are very similar and this is the region where the phase in question is *the best phase* for position estimation, see (d) which shows the phase from which the position is estimated. As a result we observe that the error in estimated position, shown in (e), is quite similar for both cases. It is clear that the two errors are compareble and diverge from the actual position. (f) depicts the estimated position. It is clear that the estimated position both *with* and *without Stage II* are quite similar that make difficult to distinguish easily. From this result it is clear that the contribution of *Stage II* depends how fast the flux linkage is changing, which is a function of the current level, rotor position and the speed at which the motor is operated. Hence, in some cases *with Stage II* may compensate more than others, however the reduction in flux linkage error was found not to be significant. Therefore,

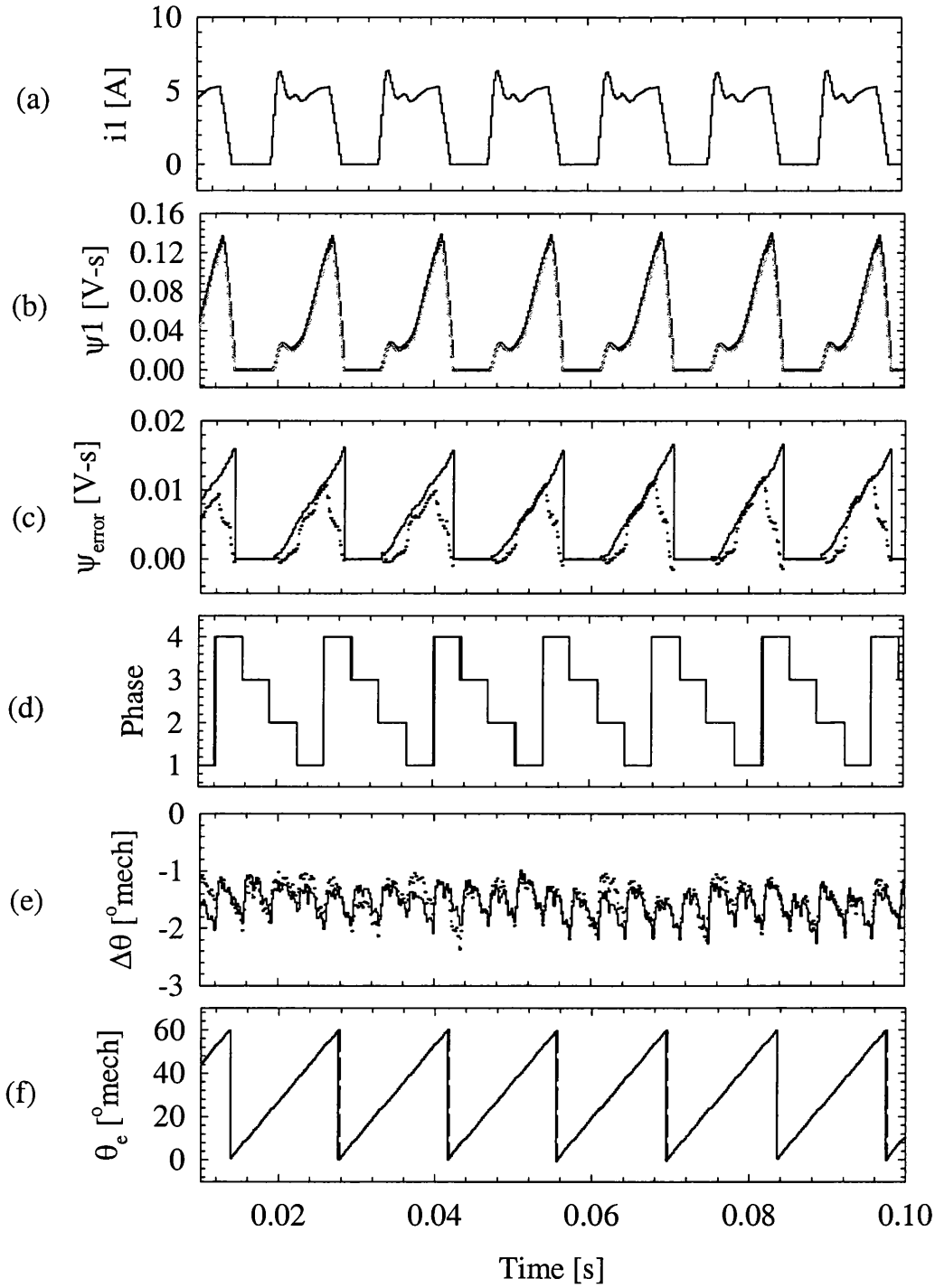

Figure 5.12: Effect of *Stage II*, solid line *without Stage II*, dashed line *with Stage II*. a: Current for phase 1, b: Flux linkage for phase 1, gray line is the actual flux linkage, c: Error in flux linkage, d: Phase from which the position is estimated, e: Error in estimated position, f: Estimated position.

it was decided not to used *Stage II*, with the advantage of decreasing significantly the calculations made in real-time.

5.4.4 Probing pulses for high-grade position estimation algorithm

At low motor speed, the main problem of this algorithm is the prediction of the flux linkage by (5.30). There are three reasons:

- The effect of the change in phase resistance is significant.
- Uncertainties in v_{ph}.
- Long integration period.

The fact that the phase resistance changes in function of the temperature and the uncertainties in the phase voltage introduce an error in the integration of $(v_{ph} - R \cdot i)$. This error is increased in every integration step, therefore the error in the predicted flux linkage in an electrical cycle becomes bigger with long integration period i.e. at low speed. This effect is known as drifting. In order to minimise this effect, the unenergised phases can be used instead of the energised phases. More explicit, using the energised phase, the integration time is from the turn on angle until the current extinguishes. In contrast, if high frequency pulses are injected in unenergised phases, the integration time is reduced significantly to just the probing pulse period. The current and flux linkage of the probing pulses can be used with the position estimation algorithm explained before in the same manner as when the energised phase is used. Fortunately, at low speed there is enough room where no current is flowing in a phase per electrical cycle for injecting probing pulses. There are two ways to inject probing pulses.

Constant flux linkage probing pulses: High fixed frequency probing pulses are injected in all unenergised phases. The duty cycle should be fixed less than 50%

in order to assure that the current returns to zero. In this mode, the flux linkage generated by the probing pulses is constant. In contrast the peak current changes as a function of rotor position.

Constant current level probing pulses: The transistor legs of all unenergised phases are on until the peak of the current pulse reaches a fixed reference value, normally around 10% of the rated current. In this mode, the peak current of the probing pulses is constant but not the flux linkage which changes as a function of rotor position. Note that the frequency of the probing pulses also changes as function of rotor position and must be measured for calculation of the flux linkage.

In both cases the probing pulses are injected through the switches of the inverter, i.e. no extra circuitry is added. The first option offers a fixed frequency sampling period in which the position can be estimated, in contrast in the second option the position will be estimated at variable frequency. It should be noticed that from the real-time implementation point of view, the second is more complicated because it requires the measuring of the time period of the probing pulse which means that a counter for each phase is required. Keeping the flux linkage constant is preferable because the main problem is the prediction of flux linkage, so the errors in flux linkage prediction can be minimised. Hence option one is more suitable for real-time implementation.

Option one has been implemented in the Simulink^{R} model with 10 kHz switching frequency. Simulations were carried out using the estimated position for commutation. Fig.5.13 shows the results of the start-up sequence. (a) and (b) depict the estimated position using the energised phase and the unenergised phase respectively. (c) shows the error in position for both methods, the solid line represents the energised phase method and we observe that the error is around $\pm 1^{o}$ degrees, in contrast, the dotted line representing the probing method is in the range of $\pm 2^{o}$. We can observe that the estimated position using energised phases is smooth, in contrast with the estimated position using unenergised phases which has a ripple. This is more clear looking at the error in position plotted in (c). However it should be taken into account that for both

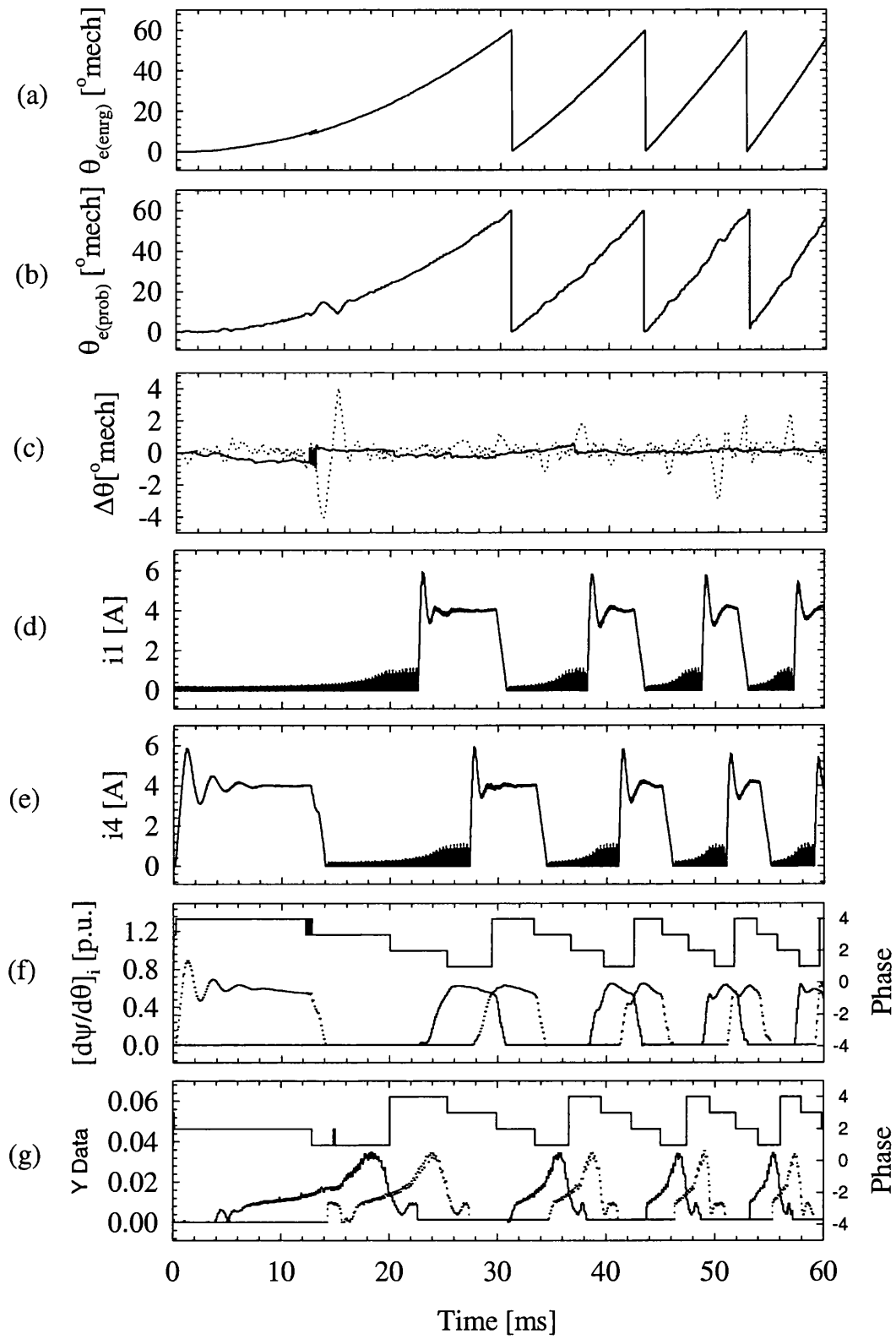

Figure 5.13: Estimated position using energised and unenergised phases while motor is accelerating. a: θ_e by energised, b: θ_e by unenergised, c: Error in estimated position for both energised (solid) and unenergised (dotted), d: Current in phase 1, e: Current in phase 4, f: $\left[\frac{\partial\psi}{\partial\theta}\right]_{i=cst}$ for phases 1 and 4 by energised, g: $\left[\frac{\partial\psi}{\partial\theta}\right]_{i=cst}$ for phases 1 and 4 by unenergised.

models the look-up table of the magnetisation curves is the same which contains 25 at 1 A step. This is the reason of the ripple in the estimated position with probing pulses. To reduce it, a different look-up table must be used with a smaller current step. If we assume that the maximum peak current of the probing pulses is 2 A, then a look-up table with a step of $\frac{2}{25}$ A will be enough. (d) and (e) show the current of phase 1 and 4 respectively, we can observe the change in the peak of the probing pulses as a function of the rotor position. Close to unaligned position the peak current is higher due to the small phase inductance. It should be noticed that the window, where probing pulses can be injected, is reduced as the speed goes up. $\left[\frac{\partial\psi}{\partial\theta}\right]_{i=cst}$ is around 60% when the energised phase is used, refer to (f), the solid line and the dotted line represent phase 1 and phase 4 respectively, also *the best phase* for position estimation is shown. (g) depicts $\left[\frac{\partial\psi}{\partial\theta}\right]_{i=cst}$ but this time when the unenergised phase is used, it is clear that the resolution is lower than when using the energised phase and has a peak around 4%. *The best phase* for position estimation is also shown. Comparing *the best phase* from (f) and (g) we observe that they are shifted by 90° Elec. which means that when the best phase using energised phase is one *the best phase* using unenergised phase is three which is its opposite.

5.4.5 Summary

Both flux linkage and current observer were implemented in Simulink^{R}. The simulation results showed that there is no difference in their performance when there is an error in flux linkage. The new option proposed of choosing *the best phase* for position estimation was investigated and found that it leads to a more accurate position estimation than averaging the contribution of all conducting phases. The effect of a second stage to correct the flux linkage was also analysed. The results show that its contribution was not significant and it is a function of the motor operating point. The problem of the prediction of flux linkage was stated which may be minimised at low speed by using probing pulses in unenergised phases.

5.5 Real Time Implementation

This section describes the real-time implementation of the *High-grade* sensorless method discussed in this chapter. It discusses the advantage of using a floating point digital processor against a fixed point processor. Also the structure of the DSP TMS320C31 used and the the real-time software developed. The Hardware of the full controller is explained in detail.

5.5.1 Philosophy of DSP platform

The most flexible way to develop new algorithms is using a digital processor. The reason is that the transition between the simulation stage and the real-time implementation is smooth and straightforward. Nowadays digital signal processors (DSP) are becoming much faster and powerful which have high level language compilers. Most of the DSP have C compilers which convert the C code to the assembler code. The great advantage is the saving of time in programming and debugging.

The easiest way to make calculations in real time is using a floating point processor which has the advantage that one does not have to worry about scaling factors and variable ranges. In floating point processors all variables may be represented in their physical values and every mathematical operation is directly calculated. On the other hand calculations in floating point tends to be slow. Fortunately, this is no longer a real limitation with fast digital processors like the TMS320C31 which is able to make 50 million floating point instructions per second with 40 ns single-cycle instruction execution time. In contrast for fixed point DSP all variables are represented by integers in the range of ± 32768, which means that each variable has to be converted to fit this range and make sure that the result of every mathematical operation is also in this range without reducing the accuracy. This is the reason why the development process is longer and more difficult with fixed point DSP. With floating point processors one can implement complex control algorithms easier and faster which will work more

accurately than with fixed point processors.

It was found that the most suitable DSP used for this project is the TMS320C31 from Texas Instruments, which offers high programming and debugging flexibility and a very powerful set of instructions.

5.5.2 DSP TMS320C31

The flux observer model (5.13) *without Stage II* was implemented on the Texas Instruments floating point DSP TMS320C31-50 platform for a four phase SR motor. The TMS320C31-50 is the highest-speed version of the TMS320C31 floating point digital signal processor [104]. Its most important features are:

- 40 ns, single-cycle instruction execution time
- 50 MFLOPS
- 25 MIPS
- One synchronous serial port to support 8-/16-/24-/32-bit transfer
- Floating point/integer multiplier
- 24-bit Program address bus
- 32-bit Program data bus
- Two 24-bit data address buses
- 32-bit data data bus
- 24-bit address bus of the Direct Memory Access (DMA) controller
- 32-bit data bus of the DMA controller
- 16 million 32-bit memory space

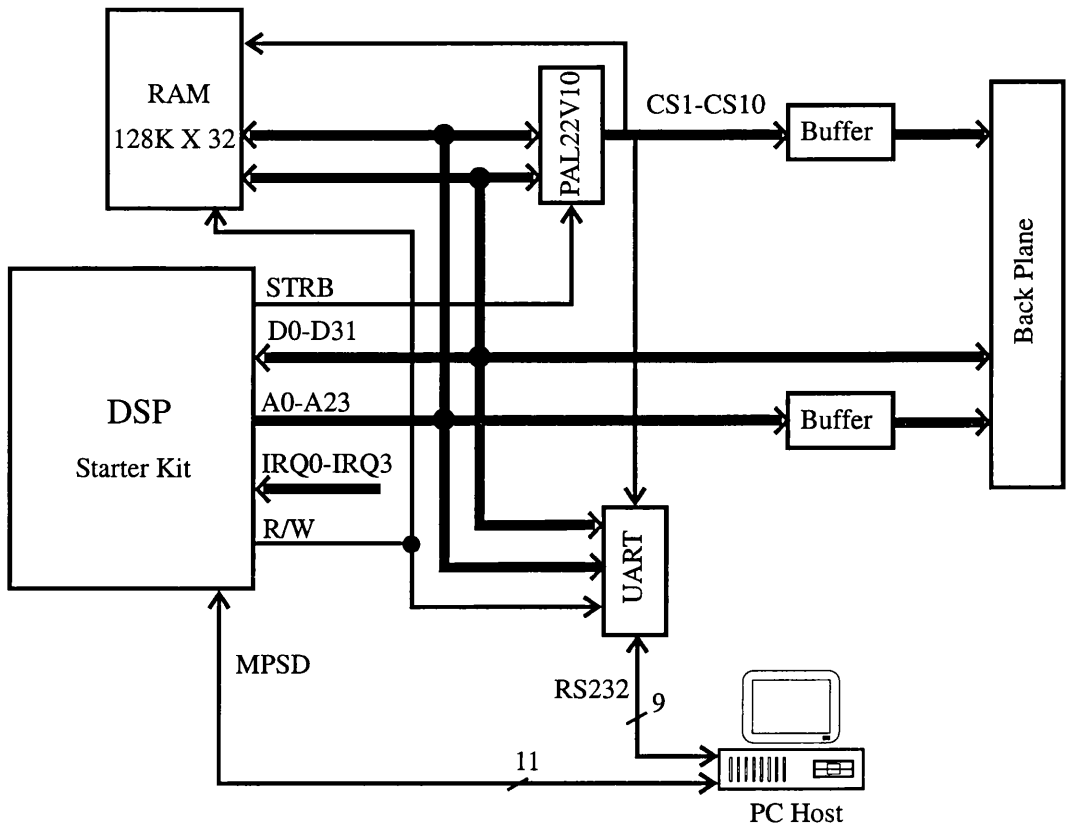

Figure 5.14: Block diagram of the TMS320C31-50 platform

- 64 32-bit CACHE
- 2K internal RAM
- 2 32-bit timer/event counters
- 4 external interrupt

Fig.5.14 shows the block diagram of the TMS320C31-50 platform. The memory map is decoded through 10 chip selects in a PAL22V10, the chip selects are used to access the 64Kx32-bit RAM and the rest of peripherals. Asynchronous serial communication is used to transfer data from the PC Host to the DSP and viceversa, the DSP does not have asynchronous serial port, therefore the UART TL16C450 from Texas Instruments was used running at 9600 baud rate with 8 bit word length. A windows terminal is used to send the control variables for instance current reference, firing angles, gains

of the current control, hard/soft chopping. The PC host is also used to download the program and debug it through the MPSD debugger cable.

5.5.3 Program structure

The external interrupt INT0 is used to execute the position estimation and current control routine. The routine is executed synchronised upon the arrive of interrupt request pulse from the PWM modulator in order to avoid switching noise. The PWM switching frequency is 5 KHz which means that all the position estimation plus the current control algorithm calculations should be made in a 200 μs window. The flow diagram is shown is Fig.5.15

The INT0 interrupt executes 9 tasks:

1. Read Current in each phase from Analog/Digital Converters
2. Read Commutation from FPGA board
3. Calculate the Best phase for position estimation
4. Predict the position
5. Execute closed-loop current control
6. Predict Flux linkage
7. Calculate Position error
8. Correct Position resulting in the final estimated position
9. Write to Digital/Analog Converter.

At the beginning of the routine, the current in each phase is measured from the 12-bit A/D Converters with a conversion ratio of 25A/4096. After, the commutation signals are read from the FPGA board to predict the flux linkage and set the current

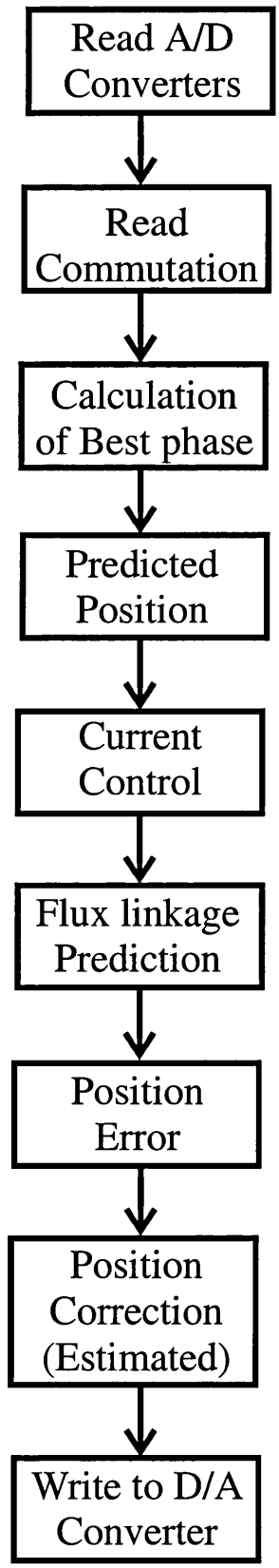

Figure 5.15: Flow diagram of the position estimation algorithm

reference. Following the calculation of the *best phase* for position estimation in function of the last estimated position. After the position prediction is made using the two previous position estimation. When the commutation of a phase is on, the current control calculates the necessary duty cycle to bring the current to the set current reference. Having the duty cycle, the prediction of the flux linkage is carried out according with (5.30). In the next block the position error is calculated (*Stage I*), following the block which deals with the correction of the initial predicted position, resulting in the final estimated position. This estimated position is fed back to the FPGA board for the calculation of commutation. Finally, internal variables are sent to the D/A Converter to observe them on the oscilloscope.

The magnetic machine characteristic and the normalised version of $\left[\frac{\partial \psi}{\partial \theta}\right]_{i=cst}$ data, are stored as two look-up table in the range of 30^o to 60^o every mechanical degree and current values in the range of 0 A to 25 A with steps of 1 A. Intermediate values are calculated by linear interpolation.

At stand-still the algorithm requires the initial rotor position, there are two options to obtain it. The first one needs to energise one phase in order to bring the rotor to aligned position, for the second option, probing pulses are injected in all phases and using a simple look-up table of the magnetisation curves the position can be estimated. The results presented here make use of the first option.

5.5.4 Controller

The block diagram of the real-time implementation is shown in Fig.5.16. The DSP TMS320C31 controller was built compatible to the Microcontroller MC68332 controller used in the *CGSM* discussed in the previous chapter. Therefore the same full size rack, the I/O board and the FPGA board were used. This was possible due to the programmable flexibility that FPGA offers. Also part of the C code was used, for instance generation of commutation angles. All this contributed to being able to build the new DSP controller faster.

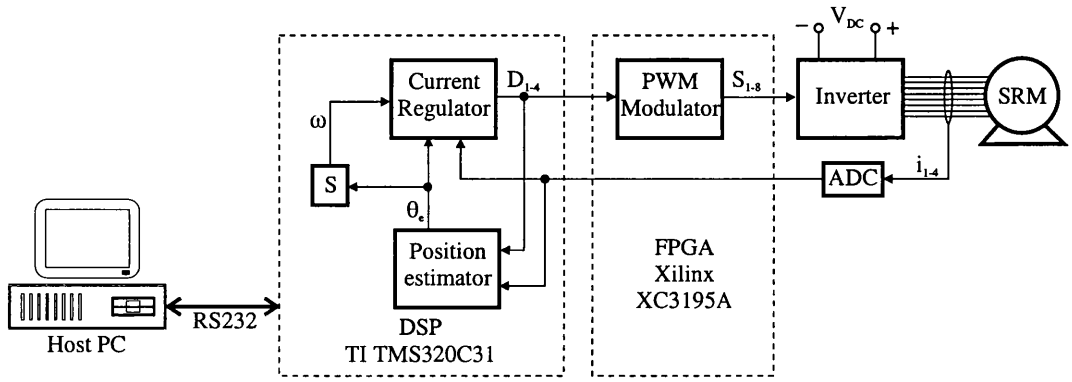

Figure 5.16: Block diagram of real-time implementation based on DSP TI TMS320C31.

The controller includes five speed wire boards inserted in the rack, see Fig.5.17 (a). The DSP board is shown in (b) which includes the Starter Kit with a TMS320C31-50 on board, the UART TL16C450 with the RS232 driver used for asynchronous serial communication, the PAL22V10 which decodes the chip selects and buffers to drive the back plane. The debugger cable MPSD is connected directly to the Starter Kit and the serial cable thought a 9 pin connector.

The A/D converter board is depicted in Fig.5.17 (c). It includes six AD678 A/D converters from Analog Devices with 200k conversions per second. The converters measure the current from each phase, and current and voltage signals from the DC-link for general protection. On the front panel there is a 10 way screw lock connector for phase current signal and two BNC connectors for current and voltage signals from the DC-link.

Fig.5.17 (d) shows the picture of the Encoder/Resolver board, which is used to measure the actual position for comparison with the estimated position. This includes a FPGA XC3020A and it is able to receive a position signal either from a encoder or resolver. On the front panel there are two 10 way screw lock connectors for the Encoder and Resolver signal. A 10-bit resolver was used to measure the actual position for comparison with the estimated position.

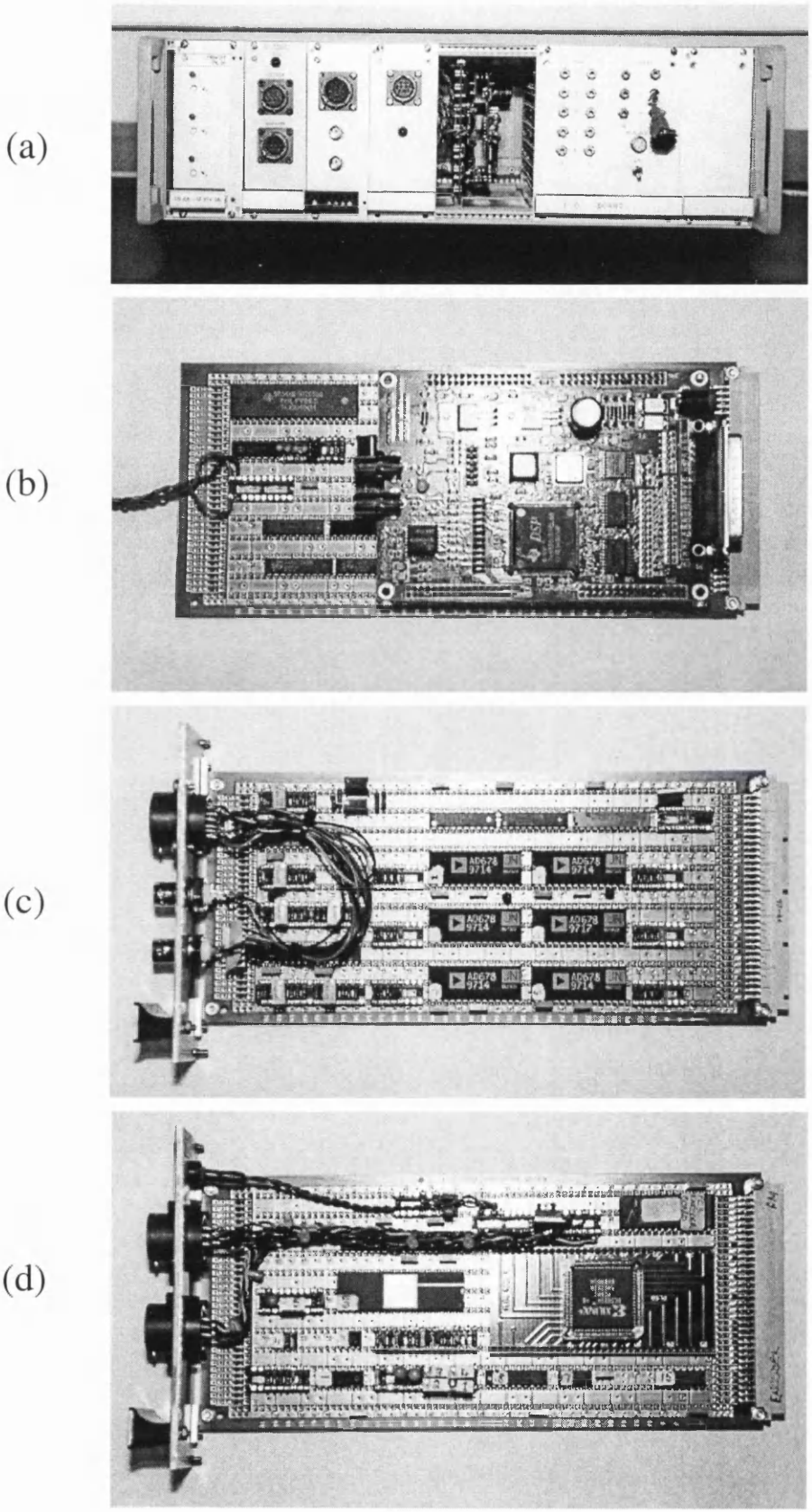

Figure 5.17: Pictures of the DSP controller boards. a: DSP controller rack, b: DSP TMS320C31 board, c: A/D Converter board, d: Encoder/Resolver board.

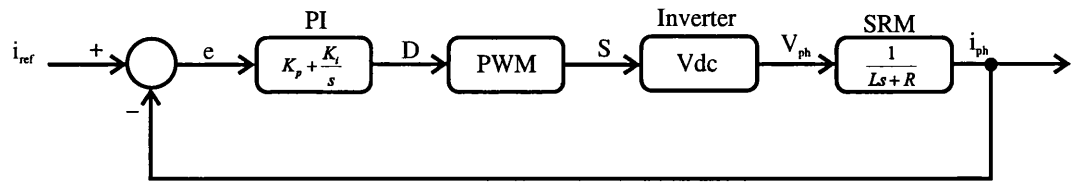

Figure 5.18: Small signal model of the closed-loop current controller

In order to reduce the calculation time in the DSP, the PWM modulator was implemented in a Field-Programmable-Gate-Array (FPGA, Xilinx XC3195A) board which is the same used in the Microprocessor controller shown in Fig.4.14 (c). Double sided PWM modulation was used to reduce noise in the system [105]. The current is sampled and synchronised with the PWM switching frequency which is 5 kHz. The position is estimated at the same rate.

The I/O board is the same discussed in subsection 4.5.1 and is shown in Fig.4.14 (d).

5.5.5 Current control

It is important to have a high bandwidth current controller to control very accurately the torque generated by the motor. The current regulator implemented here was a classical linear Proportional-Integral (PI) Pulse Width Modulation (PWM) control. The small signal model of the closed-loop current controller is shown in Fig.5.18, the error e is processed by the PI controller which calculates the duty cycle D required to bring the current to the desired reference. The PWM modulator produces the switching state for the inverter and the inverter block gives the phase voltage. Finally the SRM model produces the phase current.

The linear PI compensator has the form:

$$\frac{D(s)}{e(s)} = K_p + \frac{K_i}{s} \tag{5.31}$$

We consider the two terms of the PI controller separately. To translate the integral

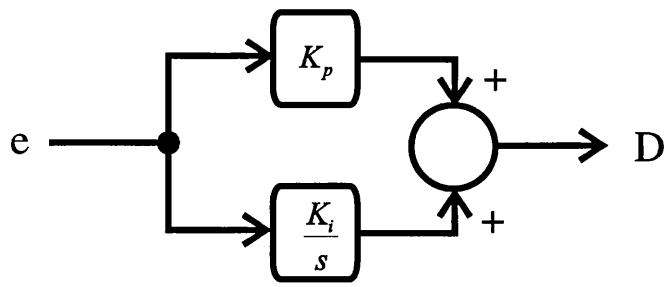

Figure 5.19: Block diagram of the PI controller

controller into the discrete-time representation, we applied Euler transformation,

$$s = \frac{1 - z^{-1}}{T_s} \tag{5.32}$$

Hence, the integral controller in the z domain is,

$$\frac{D(z)}{e(z)} = \frac{K_i}{\left[\frac{1-z^{-1}}{T_s}\right]} = K_i \cdot \frac{T_s}{1 - z^{-1}} \tag{5.33}$$

given that the z^{-1} represents a delay of one sample period, we can represent the I controller equation as follows,

$$D_{k(i)} - D_{k-1(i)} = K_i \cdot T_s \cdot e_k \tag{5.34}$$

and therefore,

$$D_{k(i)} = K_I \cdot e_k + D_{k-1(i)} \tag{5.35}$$

where $K_I = K_i \cdot T_s$ = integral gain, T_s= the sampling period, D= Duty cycle and e= current error (current reference - actual current).

The proportional controller equation is represented as,

$$D_{k(p)} = K_p \cdot e_k \tag{5.36}$$

The contribution of each controller is added which results in the final equation,

$$D_k = D_{k(p)} + D_{k(i)} \tag{5.37}$$

as shown in Fig5.19.

The current is measured using Hall current sensors and then converter to digital values through the A/D converters. The PI current regulator software was implemented in "C" language.

5.5.6 Summary

The advantages of using a floating point processor have been briefly discussed. The sensorless controller has been built based on a DSP TMS320C31 platform which is described in detail. The structure of the sensorless algorithm, implemented in "C", is presented and explained together with the theory behind the PI current regulator.

5.6 Experimental Results

In order to study the performance and limitations of the proposed algorithm, an experimental setup was used. Fig.5.20 shows a picture of the experimental setup. The test 8/6 4-phase SR motor was coupled to the PM load machine through a gear box with a 7:1 ratio. The ratings of the SRM are shown in Table 5.1. All the experimental results presented have been obtained when the SRM Drive is running truly sensorless, ie. the estimated position is fed back and used for commutation. A 10-bit resolver was used to measure the actual position for comparison with the estimated position. The experiments include: Start-up, steady state with PWM voltage control, steady state with current regulation, speed transient.

Fig.5.21 shows the start-up sequence with a duty cycle of 60%, $\theta_{on} = 30^o$ and $\theta_{off} = 55^o$, the estimated position is depicted in (a), a repetitive ripple around 3% is observed due to the swapping of position estimation from phase to phase. (b) shows the phase from which the position is estimated, (c) and (d) depict $\left[\frac{\partial \psi}{\partial \theta}\right]_{i=cst}$ and current for phase 1 respectively. Note that $\left[\frac{\partial \psi}{\partial \theta}\right]_{i=cst}$ is proportional to the phase current.

Fig.5.22 depicts again the start-up sequence but this time we can observe the error

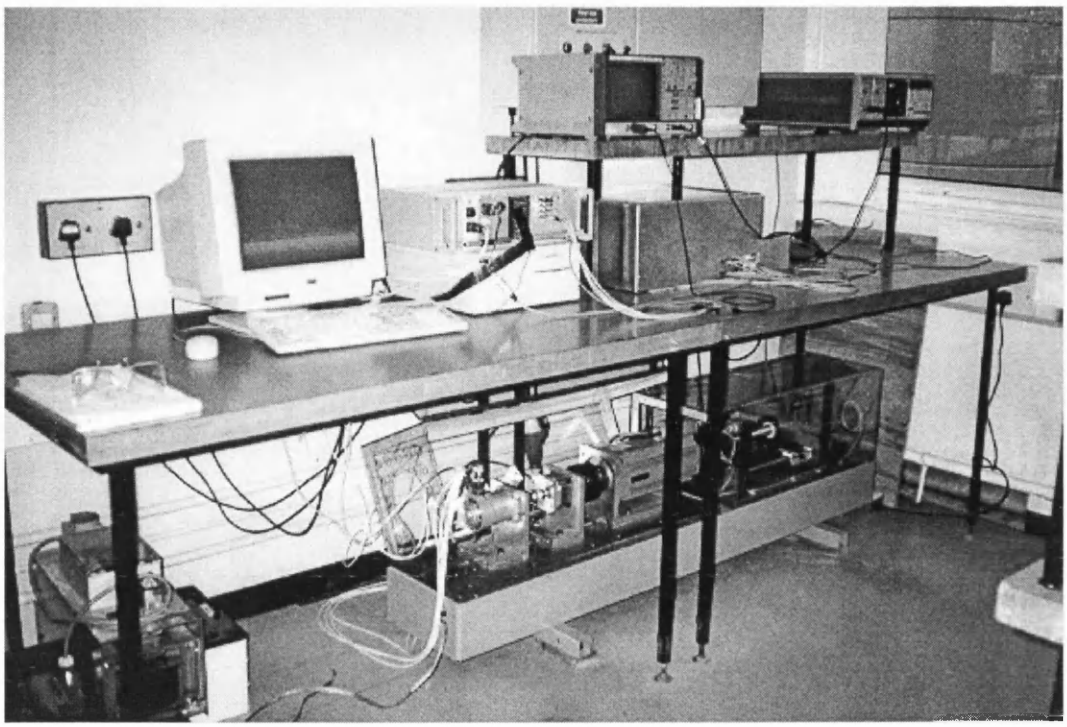

Figure 5.20: Hardware overview of the DSP controller.

in the estimated position in (c), initially the error is around 0 and 3 degrees however as the speed goes up the errors moves in the range of -2 to 1 degrees. (a) and (b) show the estimated and actual position respectively, and it is clear that they are close to each other by 1 or 2 degrees error. *The best phase* where the position is estimated is shown in (d), (e) depicts the current in phase 1.

In Fig.5.23 we can see clear how the best phase is chosen at 893 rpm with $\theta_{on} = 30^{o}$ and $\theta_{off} = 50^{o}$ and $D = 60\%$. (c) shows $\left[\frac{\partial \psi}{\partial \theta}\right]_{i=cst}$ for phase 1 and 4 with a peak value around 4%. When the value of phase one is higher than phase four the position is estimated from that phase, the intersection indicates that the position estimation should be swapped to phase 4. This can be seen clear in (b) which shows *the best phase* for position estimation. (a) depicts the estimated position, we observe a ripple due to the swapping from phase to phase, however the position would still be accurate enough to be used to drive the motor.

An example of higher speed is shown in Fig.5.24 at 2053 rpm, $\theta_{on} = 30^{o}$, $\theta_{off} = 50^{o}$

Phases	4
N_s	8
N_r	6
Stator pole-arc	21^o
Rotor pole-arc	22^o
Air-gap	$0.2 \pm 0.01mm$
Phase resistance	$1.28 \pm 0.10\Omega$
Stator OD	$80.0 \pm 0.01mm$
Stator ID	$70.0 \pm 0.01mm$
Rotor OD	$43.6 \pm 0.01mm$
Rotor ID	$30.0 \pm 0.01mm$
Stack length	$70.0 \pm 0.01mm$
Max. inductance not saturated L_{ao}	$27.0 \pm 0.02mH$
Min. inductance L_u	$4.30 \pm 0.02mH$
I_{max}	17 A
Rated Power	5 kW
DC-link voltage	100 V

Table 5.1: 4 phase SR motor ratings

and $D = 70\%$. (a) shows the estimated position, we observe that the resolution is 24 pulses per electrical cycle (146 ppr) which is less in this case than a slower speed. This is due to the ratio (estimation frequency/speed) is reduced. However the position estimation has enough accuracy for phase commutation. (b) depicts *the best phase* and (c) $[\frac{\partial \psi}{\partial \theta}]_{i=cst}$ for phase 1 with a peak around 4%. (d) shows the phase current for phase 1.

Fig.5.25 is an example when the motor is running under load at 165 rpm, $\theta_{on} = 30^o$ and $\theta_{off} = 55^o$, the peak current is 17 A which is in the saturation region. Again the estimated position has a approximatly 4% ripple and the peak of $[\frac{\partial \psi}{\partial \theta}]_{i=cst}$ is around 98%.

Fig.5.26, 5.27 and 5.28 depict the position error at two different speeds. In Fig.5.26, the motor is running at 866 rpm, (a) and (b) show the estimated position and the actual position respectively which compare well, however the error in the estimated position oscillates in the range of $\pm 3^o mech..$ and is shown in (c). (d) depicts the *best phase* and

(e) the current in phase 1. Fig.5.27 depicts a zoom of the estimated position at 926 rpm. (a) and (b) show the estimated and actual position, it is clear that both match very well however in the estimated position one can observe 5% ripple. This is more clear in (c) which depicts the error in the estimated position, the error is in the range from $-2^o mech.$ to $+1^o mech.$. (d) shows the current in phase 1. Fig.5.28 depicts the result when the motor is running at 1886 rpm, $\theta_{on} = 30^o$, $\theta_{off} = 55^o$ and $D = 70\%$. The estimated and actual position are shown in (a) and (b) respectively. (c) shows the error in estimated position which oscillated between -2 and 1 degree.

Fig.5.29 and 5.30 show examples of different speed when the motor is running under load. The results when the motor is running at 272 rpm with $\theta_{on} = 30^o$, $\theta_{off} = 55^o$ and $D = 63\%$ are depicted in Fig.5.29. (a) and (b) show the estimated and actual position and we can observe the good agreement between them. (c) depict the error of the estimated position which is in the range of +3 to 0 degrees. (d) shows the current in phase one, the peak is around 11 A which in in the saturation region of the machine. Fig.5.30 depict the results obtained when the machine is running at 794 rpm with the same firing angles but with $D = 70\%$. Again (a) and (b) show the estimated and actual position respectively, the error between them is around -2 degrees. (c) shows the error of the estimated position which oscillates between -2 and 0 degrees. The motor is running in the saturation region as the peak current in phase 1 is around 9 A.

Fig.5.31 (a) shows the estimated position at 840 rpm, $\theta_{on} = 30^o$, $\theta_{off} = 55^o$ and $D = 60\%$, (b) depicts the predicted flux linkage (ψ_p), (c) shows the estimated flux linkage (ψ_e) obtained from the look-up table, (d) shows the the error in flux linkage ($\Delta\psi$) which is used to calculate the position error in *Stage I.* The current in phase 1 is depicted in (e).

Fig.5.32 is an example when the motor is running under load at 833 rpm with the same firing angles but $D = 70\%$. (a) shows the estimated position which has 3% ripple. (b) and (c) depict the predicted and estimated flux linkage, we should expect that the flux linkage is a straight line with a constant slope, however we can observe that it has

a ripple mainly around ± 0.003 V-s caused by the uncertainty in the phase resistance and voltage drop in the transistors. This ripple shows up in the estimated position. $\Delta\psi$ is shown in (d), we can observe that a bigger error (-0.04 V-s) appears when the phase is been de-fluxed. (e) shows the current in phase 1 which is in the saturation region of the machine.

Steady state of the PI current regulator is shown in Fig.5.33, the motor is running at 226 rpm with $\theta_{on} = 30^o$ and $\theta_{off} = 55^o$ and current regulated at 2.1 A. (a) depicts the estimated position, (b) shows $\left[\frac{\partial\psi}{\partial\theta}\right]_{i=cst}$ for phase 1 (solid line) and 4 (dashed line) and (c) depicts the current in phase 1. Example of the PI current regulator is shown in Fig.5.34 when a step in current reference is applied. (a) shows the estimated position and is observed when the motor is accelerated. (b) depicts $\left[\frac{\partial\psi}{\partial\theta}\right]_{i=cst}$ for phase 1 (solid line) and 4 (dashed line), note that its value is increased proportional to the phase current which is depicted in (c) for phase 1. Steady state of the PI current regulator is presented in Fig.5.35. (a) and (b) shows the estimated and actual position respectively, It is observed that the estimated position has a ripple, this is more clear in (c). In this case the error in the estimated position is oscillating around -3 and 0 degrees. (d) depicts the best phase that is used for position estimation and (e) shows the current in phase 1.

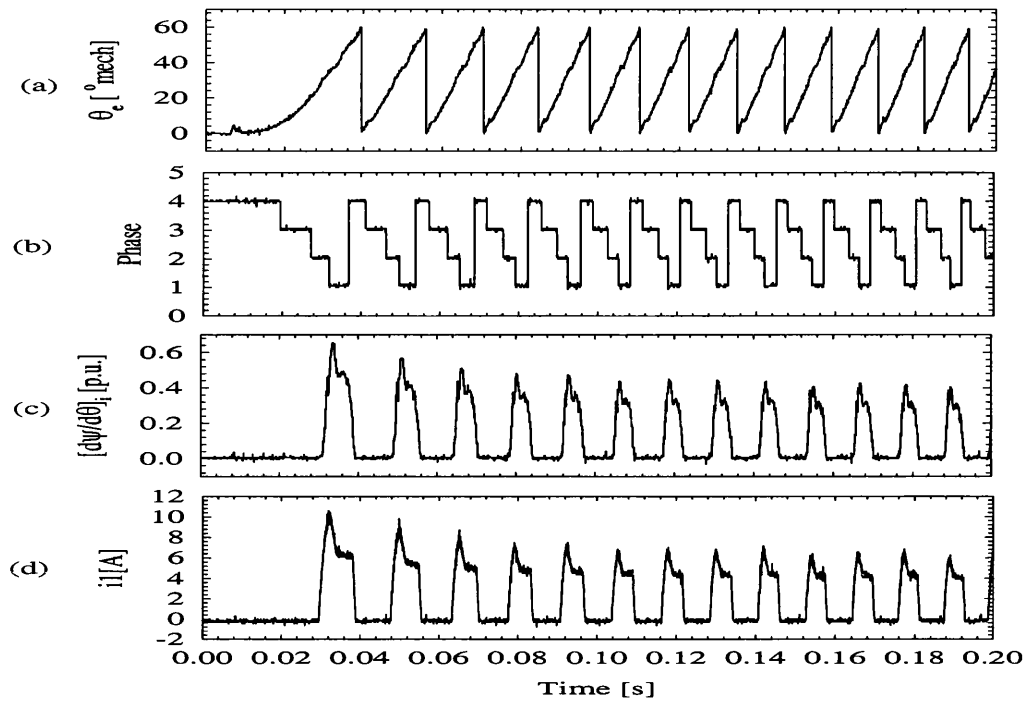

Figure 5.21: Start-up, $\theta_{on} = 30°$, $\theta_{off} = 55°$, $D = 60\%$. a: Estimated position, b: Phase from which the position is estimated, c: $\left[\frac{\partial \psi}{\partial \theta}\right]_{i=cst}$ for phase 1, d: Current in phase 1.

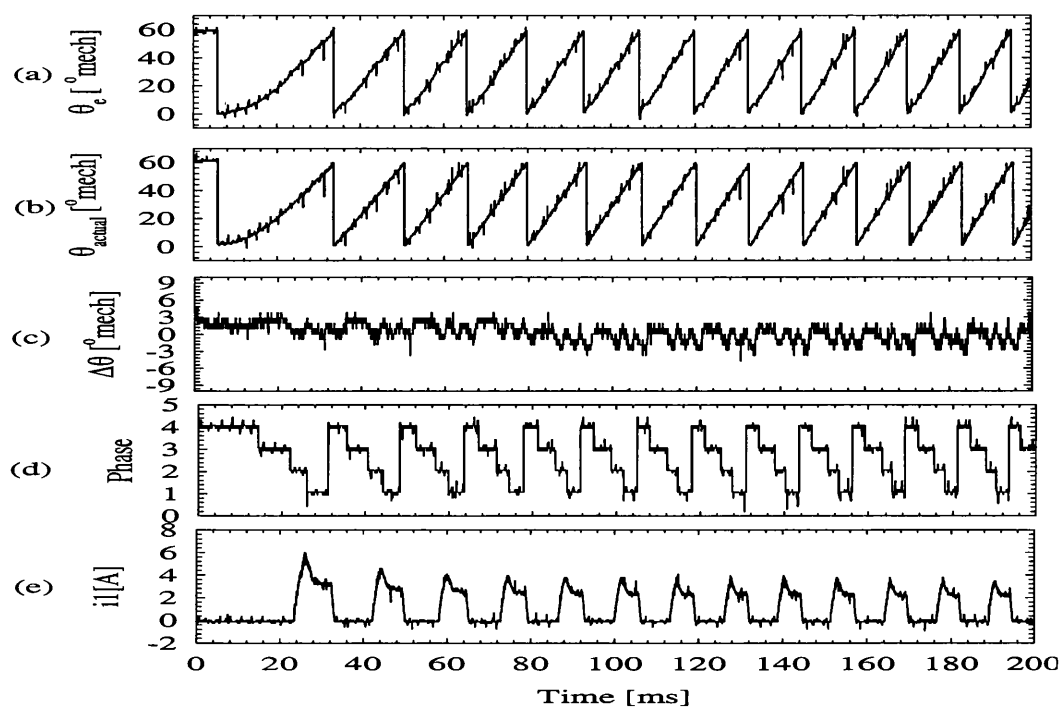

Figure 5.22: Position error in start-up, $\theta_{on} = 30°$, $\theta_{off} = 55°$, $D = 60\%$. a: Estimated position, b: Actual position, c: Error in estimated position, d: Phase from which the position is estimated, e: Current in phase 1.

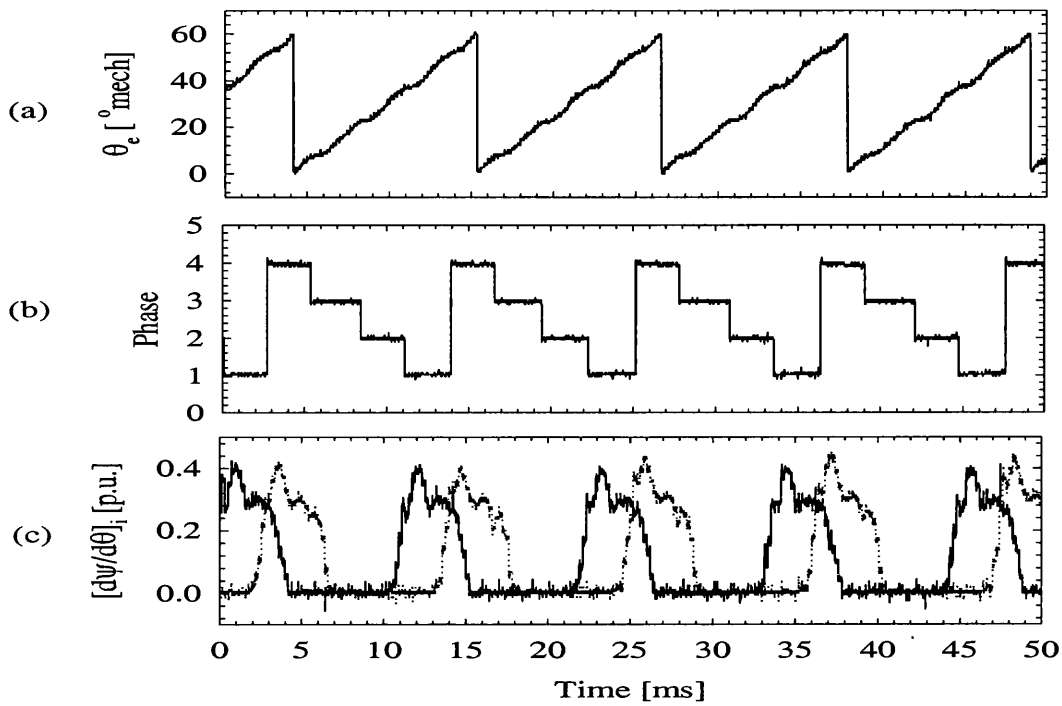

Figure 5.23: Estimated position at 893 rpm, $\theta_{on} = 30^o$, $\theta_{off} = 55^o$, $D = 60\%$. a: Estimated position, b: Phase from which the position is estimated, c: $\left[\frac{\partial \psi}{\partial \theta}\right]_{i=cst}$ for phase 1 and 4.

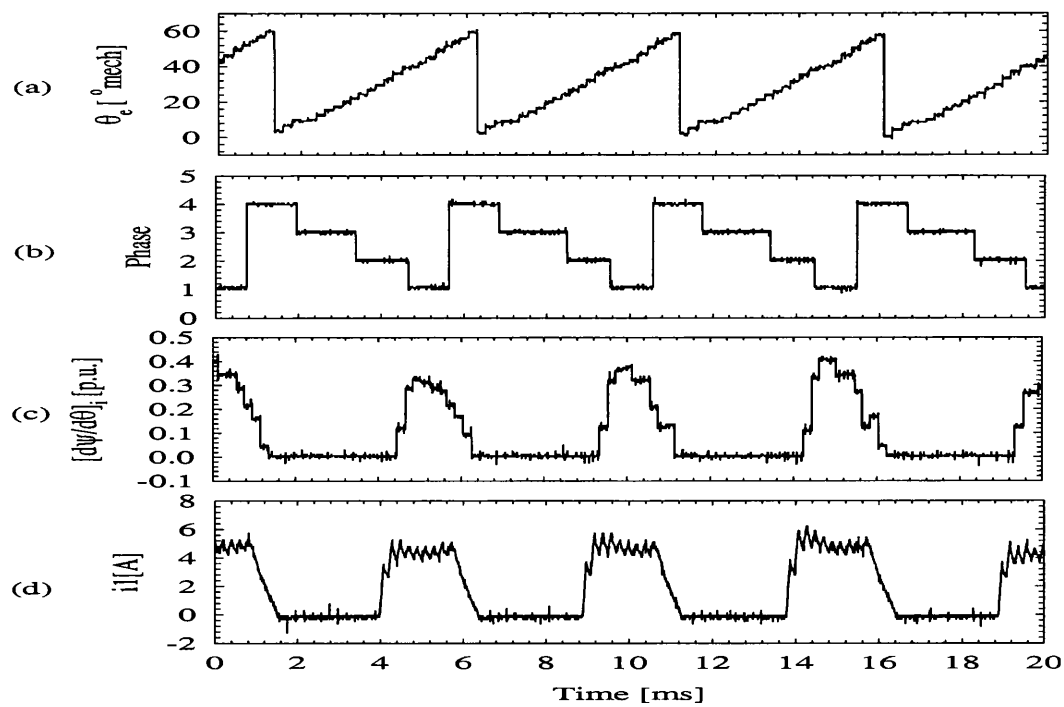

Figure 5.24: Estimated position at 2053 rpm, $\theta_{on} = 30^o$, $\theta_{off} = 55^o$ and $D = 70\%$. a: Estimated position, b: Phase from which the position is estimated, c: $\left[\frac{\partial \psi}{\partial \theta}\right]_{i=cst}$ for phase 1, d: Current in phase 1.

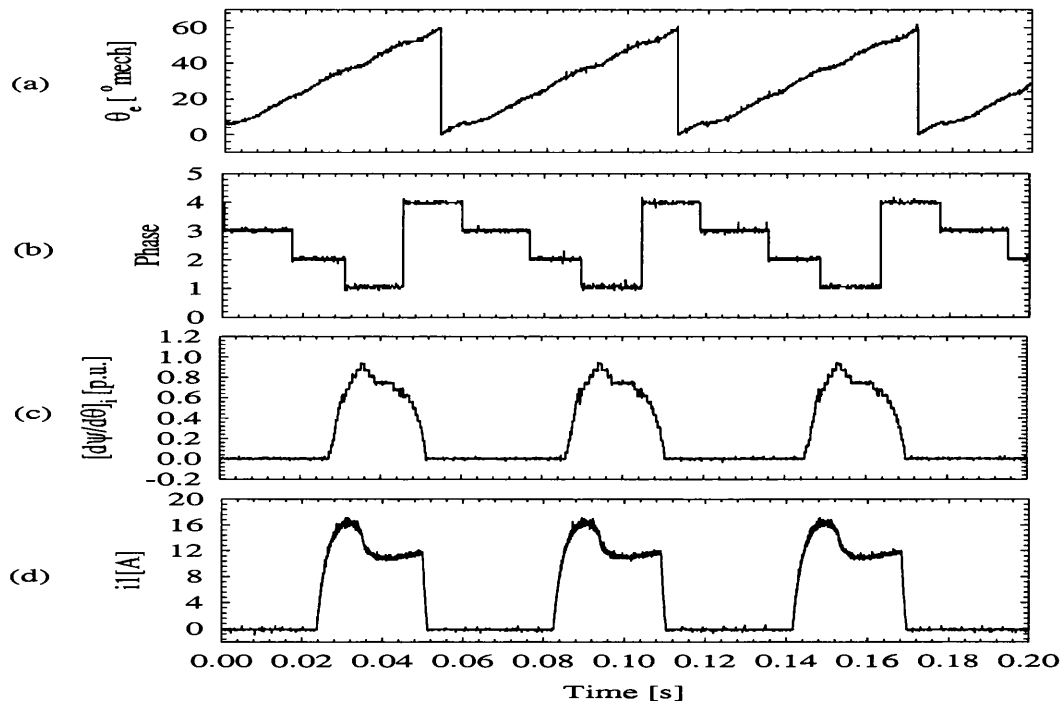

Figure 5.25: Estimated position at 165 rpm, $\theta_{on} = 30^o$, $\theta_{off} = 55^o$ and $D = 60\%$. a: Estimated position, b: Phase from which the position is estimated, c: $\left[\frac{\partial \psi}{\partial \theta}\right]_{i=cst}$ for phase 1, d: Current in phase 1.

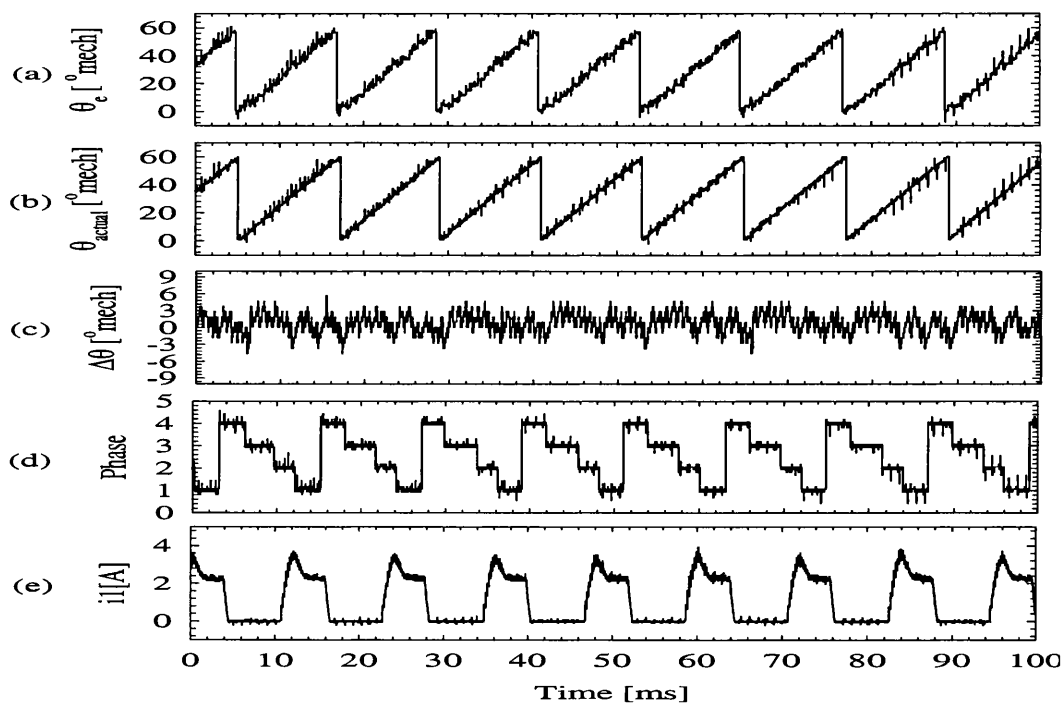

Figure 5.26: Estimated position at 866 rpm, $\theta_{on} = 30^o$, $\theta_{off} = 55^o$ and $D = 60\%$. a: Estimated position, b: Actual position, c: Error in position estimation, d: $\left[\frac{\partial \psi}{\partial \theta}\right]_{i=cst}$ for phase 1, e: Current in phase 1.

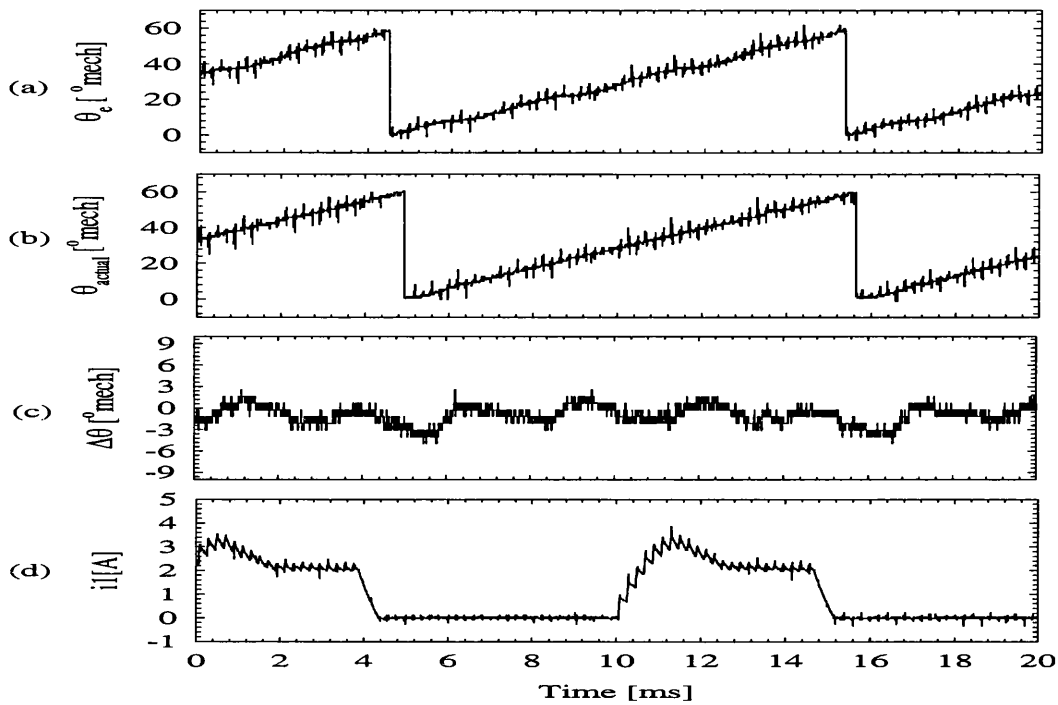

Figure 5.27: Zoom of estimated position at 926 rpm, $\theta_{on} = 30^o$, $\theta_{off} = 55^o$ and $D = 60\%$. a: Estimated position, b: Actual position, c: Error in position estimation, d: Current in phase 1.

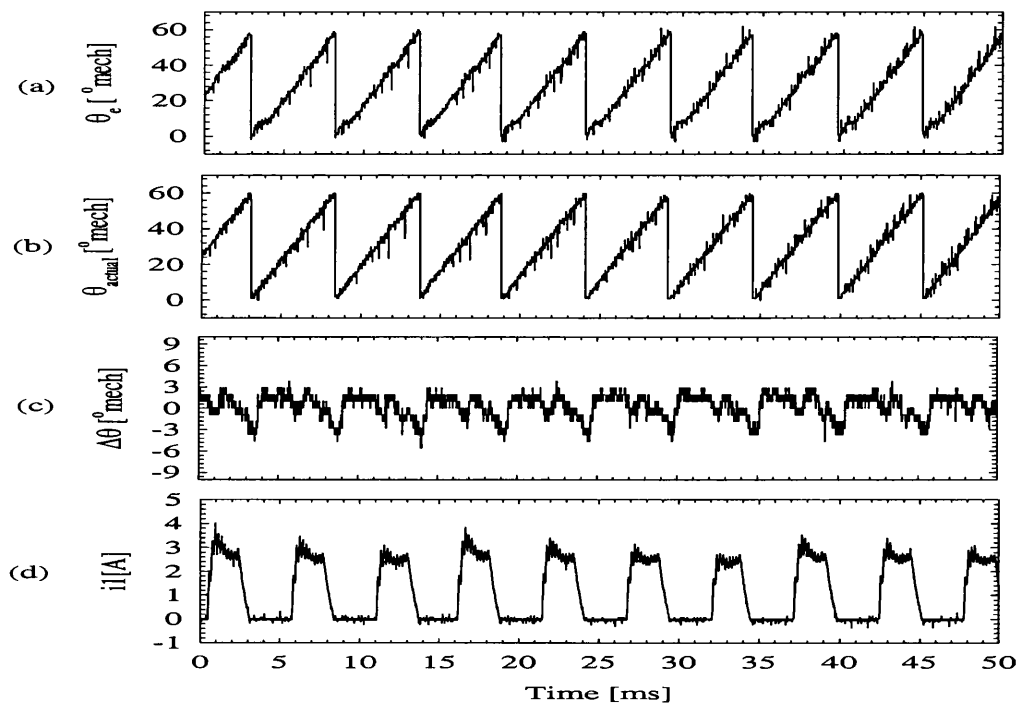

Figure 5.28: Estimated position at 1886 rpm, $\theta_{on} = 30^o$, $\theta_{off} = 55^o$ and $D = 70\%$. a: Estimated position, b: Actual position, c: Error in position estimation, d: Current in phase 1.

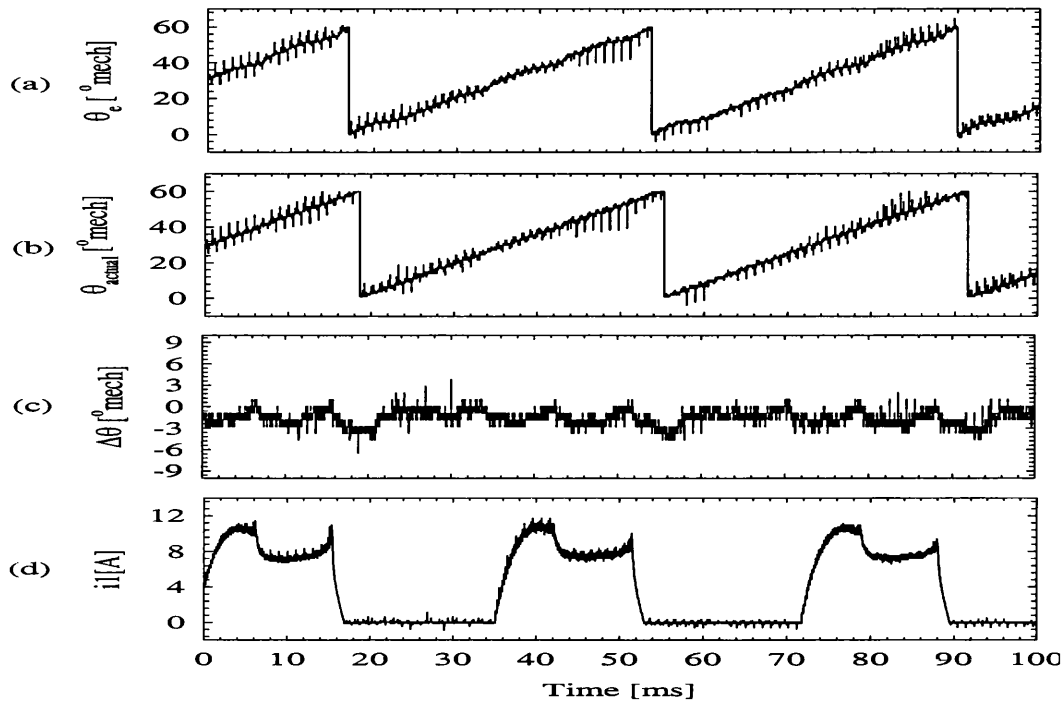

Figure 5.29: Estimated position at 272 rpm in the saturation region, $\theta_{on} = 30^o$, $\theta_{off} = 55^o$ and $D = 63\%$. a: Estimated position, b: Actual position, c: Error in position estimation, d: Current in phase 1.

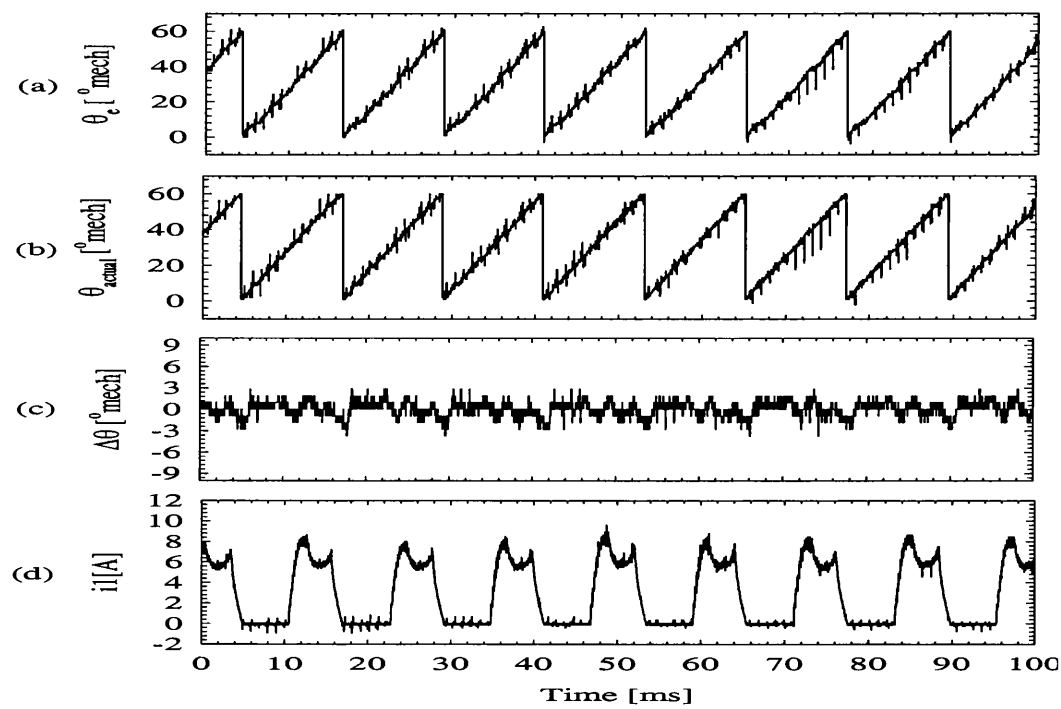

Figure 5.30: Estimated position at 794 rpm in the saturation region, $\theta_{on} = 30^o$, $\theta_{off} = 55^o$ and $D = 70\%$. a: Estimated position, b: Actual position, c: Error in position estimation, d: Current in phase 1.

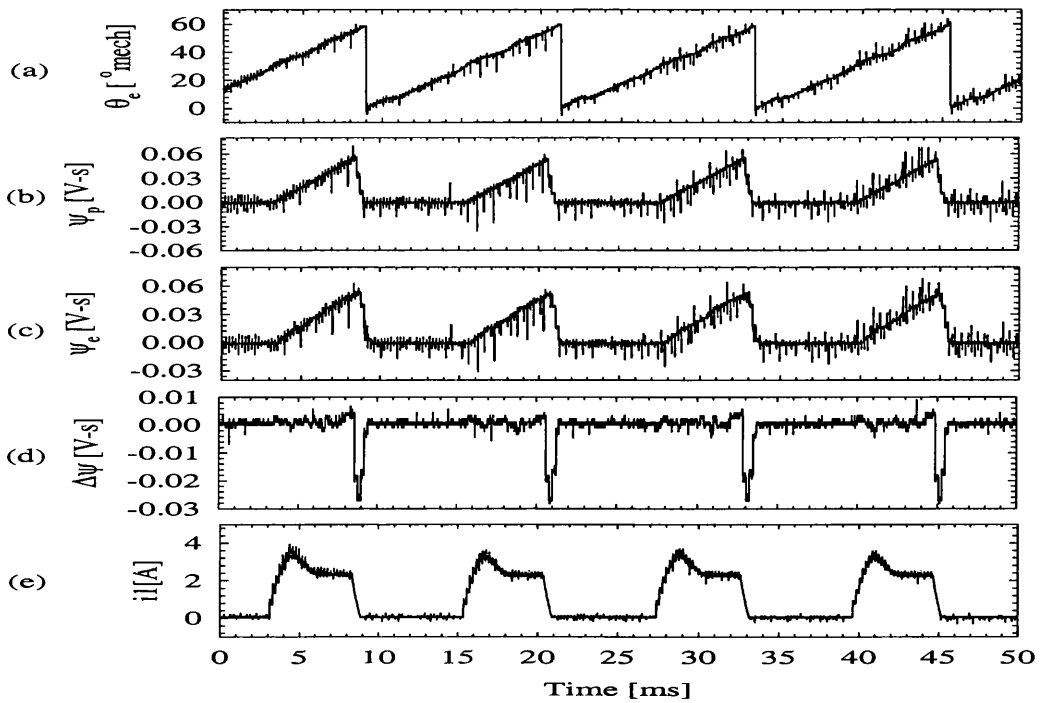

Figure 5.31: Estimated position at 840 rpm, $\theta_{on} = 30^o$, $\theta_{off} = 55^o$ and $D = 60\%$. a: Estimated position, b: Predicted flux linkage, c: Estimated flux linkage, d: $\Delta\psi$, e: Current in phase 1.

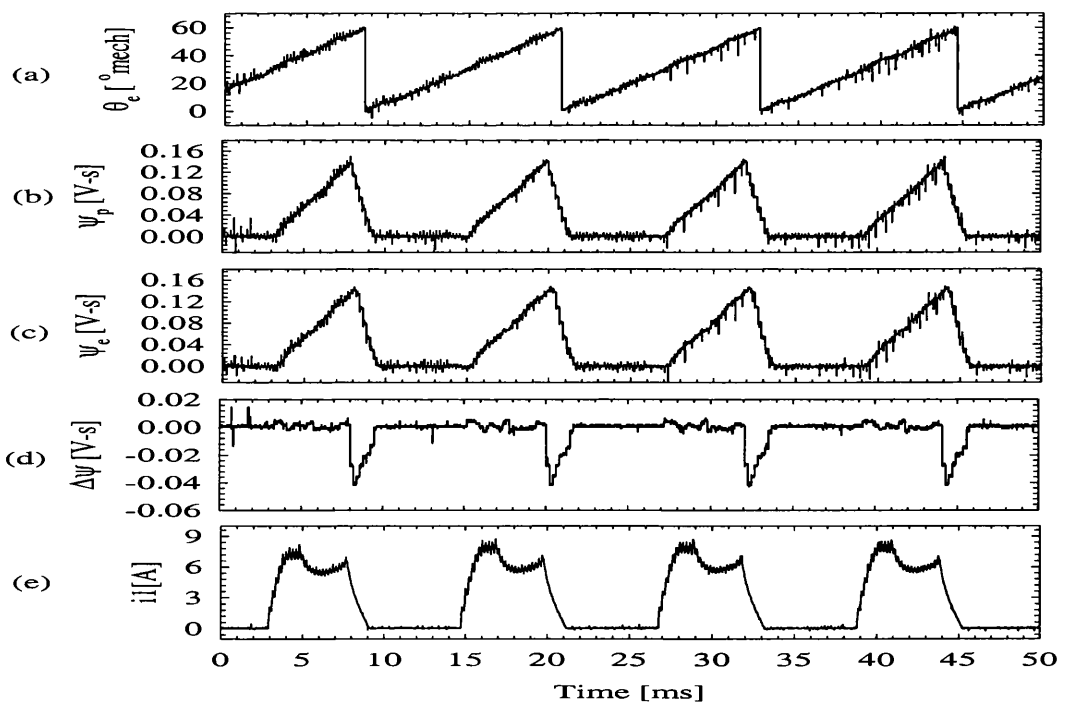

Figure 5.32: Estimated position at 840 rpm, $\theta_{on} = 30^o$, $\theta_{off} = 55^o$ and $D = 60\%$. a: Estimated position, b: Predicted flux linkage, c: Estimated flux linkage, d: $\Delta\psi$, e: Current in phase 1.

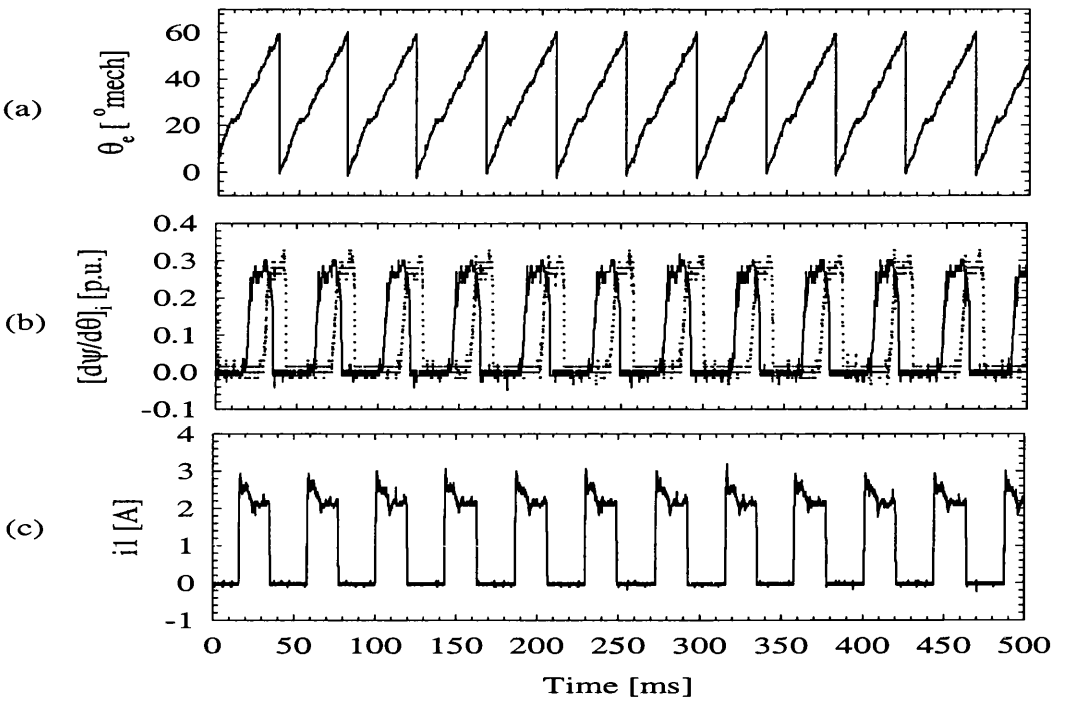

Figure 5.33: Current controlled, $\theta_{on} = 30°$, $\theta_{off} = 55°$. a: Estimated position, b: $\left[\frac{\partial \psi}{\partial \theta}\right]_{i=cst}$ for phase 1 and 4, c: Current in phase 1.

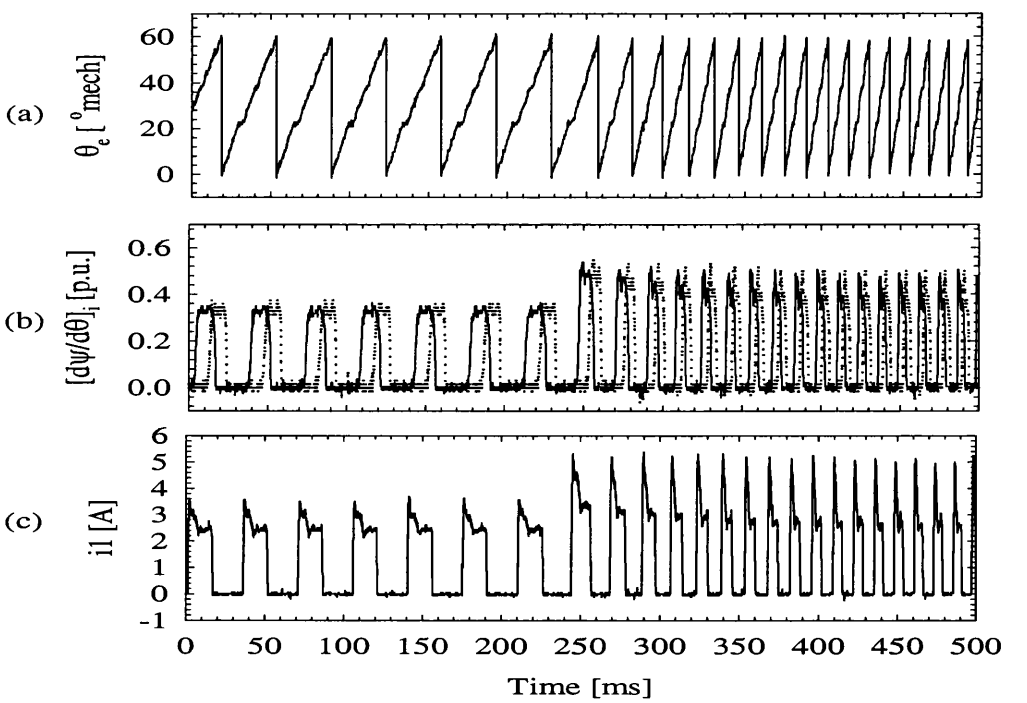

Figure 5.34: Step in current, $\theta_{on} = 30°$, $\theta_{off} = 55°$. a: Estimated position, b: $\left[\frac{\partial \psi}{\partial \theta}\right]_{i=cst}$ for phase 1 and 4, c: Current in phase 1.

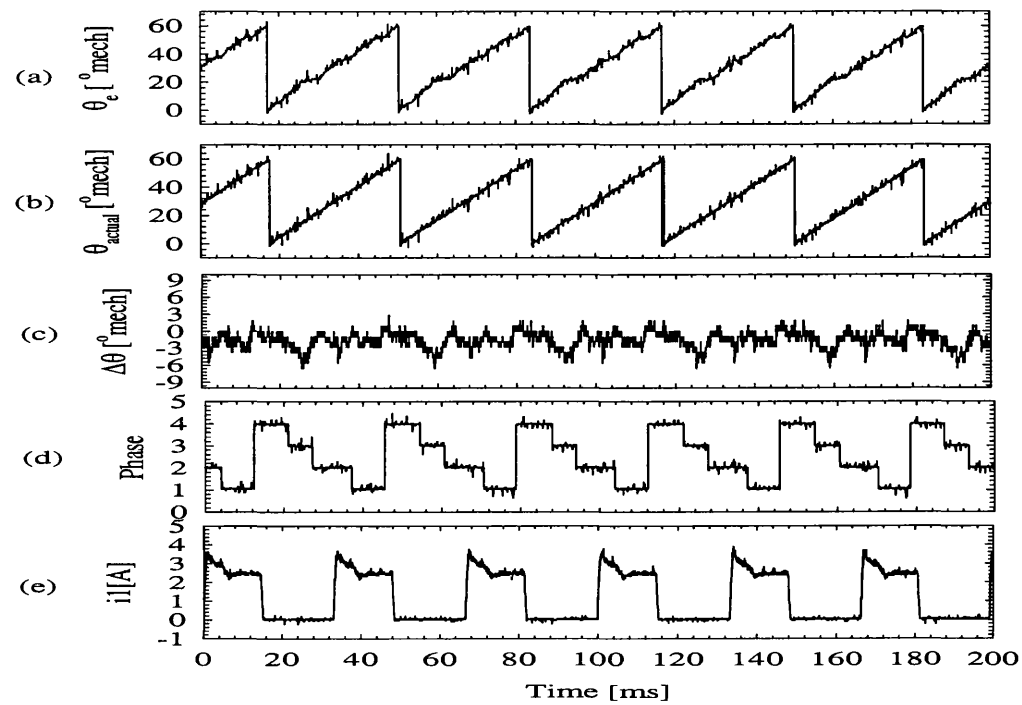

Figure 5.35: Current regulated at 2.5 A, $\theta_{on} = 30°$, $\theta_{off} = 55°$. a: Estimated position, b: Actual position, c: Error in estimated position, d: Phase from which the position is estimated, e: Current in phase 1.

5.6.1 Limitations

In assessing the performance of the position estimation algorithm, it is observed that the estimated position error lies mainly in the range from $-2°mech.$ to $1°mech.$. This is considered to be a reasonable performance as the motor does not lose synchronization. The most important sources of position error are:

- Prediction of the flux linkage
- Error in measured current
- Quantisation error

The most difficult problem of this algorithm is the prediction of the flux linkage by (5.30). The sources of error in the experiments carried out here are listed as follows:

- The voltage in the dc-link is assumed constant, however it may have a ripple due to the current demanded in the motor.
- The voltage in the phase is calculated ideally by multiplying the PWM duty cycle by the dc-link voltage, however in reality there is a drop in voltage due to the switching time.
- The phase resistance is assumed constant, but it is known that it changes as a function of temperature.
- The voltage drop in the IGBT is taken into account as constant, however it may vary as a function of current level and temperature.
- The voltage drop in the power leads is not taken into account.

All these should be taken into account in the calculation of the voltage in the phase.

The error introduced by the measured current is probably the smallest of these because of the double sided PWM used. However, the noise level in the system still may affect the measurement.

The quantisation error produces a lag in the estimated position. It can be reduced if the estimation frequency is increased. However, the main limitation is the DSP capability to deal with mathematical operations. Another limitation might be the maximum switching frequency allowed by the switches.

Usually the resolution of a mechanical position sensor like an encoder or resolver is measured by the number of pulses per revolution, in contrast, having a fixed estimation frequency the resolution of position estimation is a function of the speed which is expressed by,

$$\sigma = \frac{6 \cdot w}{f_s} \tag{5.38}$$

where σ = resolution [$^o mech.$], w = motor speed [rpm], and f_s = sampling frequency [Hz] at which the position is estimated.

Speed [rpm]	Resolution [$^{o}mech$]
500	0.6
1000	1.2
1500	1.8
2000	2.4

Table 5.2: Resolution in position estimation

Therefore it is desired that the estimation frequency is as high as possible. For the work carried out here the estimation frequency is 5 kHz, the resolution obtained at varies speeds is shown in Table 5.2.

5.6.2 Summary

The concept of the position estimation algorithm has been confirmed experimentally. Results for start-up sequence, PWM voltage control and PWM current regulation are presented when the drive is running truly sensorless. A ripple in the estimated position is observed and it is concluded that this ripple is a consequence of changing the position estimation from phase to phase, and errors in the predicted flux linkage. However the estimated position is still sufficient for phase commutation. Results when the motor is running under load show good stability of the algorithm. It should be noted that the results obtained with PWM voltage control present less ripple in the estimated position than results obtained with PWM current regulation.

5.7 Conclusion

This Chapter discussed the possible models for a high resolution position estimator algorithm based on the magnetic characteristics of the SRM. The simulation results show that the models assuming either $\Delta i = 0$ or $\Delta\psi = 0$ are equally sensitive to errors in flux linkage. This suggests that the only criterion to chose the best model for real-time implementation is that one which requires the minimum number of operations.

The models that satisfy this criterion are:

- Either (5.13) or (5.16) for *Stage I*,
- And only (5.17) for *Stage II*.

It has also been demonstrated that the method proposed in this thesis for position correction which is based on taking the *best phase* (option 3) for position estimation leads to a more precise position estimation than averaging the contribution of all conducting phases. The contribution of the *Stage II* is discussed and it is concluded that in general its contribution is not significant.

The real time implementation of the new sensorless algorithm based on the flux observer model *without Stage II* was built on a DSP TMS320C31 platform. The experimental results confirm the theory and prove the concept of the algorithm which leads to minimum calculations and choose the most accurate phase for rotor position estimation. This algorithm offers the advantage of a very good resolution of rotor position estimation in a wide speed range in dynamic 4 quadrants operation, hence, its main application can be servo drives.

On the other hand, it suffers in the prediction of flux linkage by (5.10), (5.30). One reason is because the phase resistance is changing as a function of motor temperature and the other is the drifting in the integration of the phase voltage. Unlike other motor technologies as AC or brushless DC machines, the switched reluctance motor has a zero current period every electrical cycle. Therefore, the flux linkage can be reset to zero when no current flows in a phase. However, at very low speed the integration time is long and the error in flux linkage can be significant in one electrical cycle. A method has been proposed to reduce this problem. It consist in using the same position estimation algorithm but the current and flux linkage are obtained from probing pulses injected in unenergised phases instead of the values in the energised phase. In other words, the current and flux linkage of the probing pulses are used as input of the position estimation algorithm in the same way as when using the energised phase. The probing

pulses can be of constant flux linkage or constant current, being the first preferable due to reduction of error in flux linkage. Using probing pulses, the integration time is constant and reduced significantly to the probing period, hence the reduction of error in the predicted flux linkage.

This algorithm at high motor speed operation is mainly limited by the speed of the DSP to cope with real-time calculations, however the fact that every day there are more powerful and cheaper DSP may open the window for very high speed applications.

Chapter 6

Conclusions

This thesis has focused on the investigation and development of two new sensorless methods for switched reluctance motors with the aim of covering the two criteria discussed in section 1.3, which are the reduction of the SRM drive cost and the operation of the SRM drive in a harsh environment. The first sensorless method, called *current gradient sensorless method*, identifies one rotor position per stroke using the phase current waveform and no magnetic motor parameters are required. It has been shown experimentally that this method is applicable to medium (in the high speed range below the rated speed) and high (above the rated motor speed) speed drives. The second method makes use of flux linkage and current observer, and the full magnetic information of the switched reluctance motor. This method allows a high resolution rotor position estimation which is mainly limited by the speed of the DSP to cope with real time calculations. General conclusions of the research carried out, and possible future work guide lines for further improvements and developments are given in this chapter as follows.

6.1 General conclusions

Note that most of the objectives discussed in section 1.4 were achieved through the development of this work.

6.1.1 Low cost/resolution sensorless methods for switched reluctance motor drives

The theory of two new sensorless methods have been discussed, which are *current gradient sensorless method* and *voltage magnitude sensorless method.* The theory of the former is also developed for the case of switched reluctance generators. The *current gradient sensorless method* using PWM voltage control has been successfully implemented in real-time for the first time. The method estimates the rotor position where the rotor and the stator pole start to overlap with *no a priori* knowledge of any magnetic motor parameters. The information required for this method is the phase current waveform from each phase, however it has been proposed to split in two the lower dc-link bus of the classic inverter, i.e. the transistor bus and the diode bus. This was with the aim of reducing the current sensors and detection stages required to just one placed in the lower transistor bus. The experimental results showed that using one single detection stage did not put any limitation in the drive performance as excitation overlap was possible. Following this idea of a single current sensor for this method, a series of suggested places of the current sensor and minor modifications for the most common inverter topologies were also presented.

Start-up methods were investigated experimentally. It was found that the self-synchronisation method may be used even under load conditions. However, this method was not reliable due to the high peak current in the initial electrical cycle and it may even start in the wrong direction. For this reason, feedforward was investigated as a second start-up method. It was found that this method offers the most reliable and robust start-up from standstill. The motor is accelerated up to a pre-defined take-over

speed in open loop, similar to a stepper motor. The experimental tests demonstrated that feedforward method works well with and without load at different take-over speeds.

The *current gradient sensorless method* was fully implemented using a hybrid platform. The detection stage was implemented in an analog manner, which is formed by simple components, such as, OPAMs, resistors, and capacitors. The commutation stage and PWM modulator was implemented in FPGA technology, and the speed controller in the microcontroller MC68332 from Motorola. The main reason for choosing this implementation was that it offers full control flexibility which was very important in the investigation of this sensorless method. However, simpler implementations of this method are possible, in particular, full analog, using a less powerful microcontroller or simple digital logic. Furthermore, it is worthy to emphasise that the additional components of this method are minimal with the obvious scope to implement it in a single chip solution similar to those ICs available for the back-EMF sensorless method for brushless DC motors.

It was found that the commutation angles may be selected freely, as it was confirmed experimentally that the condition of turning on the phase before the stator and rotor pole start to overlap ($\theta_{on} < \theta_o$), which is required by the *current gradient sensorless method*, did not introduced a limitation in the performance of the drive. It was shown that it is possible to perform closed-loop speed control using this sensorless method. For this purpose, a proportional-integral controller that acts in the PWM duty cycle[1] was used. The obtained experimental tests in speed and torque transient showed the reliability and robustness of this sensorless method.

The accuracy of the rotor position estimation obtained by *current gradient sensorless method* was investigated. The experimental measurements showed that this sensorless method is applicable at medium and high speed as the current waveform becomes peakier with increased speed. On the other hand, it was confirmed that this

[1]The angles may also be varied to help in the torque demand.

method is not applicable at low speed mainly because the torque pulsation causes significant speed variation. The region of the motor torque-speed characteristic, where *CGSM* can be applicable, was measured and compared with the region that was possible using the encoder. The results clearly showed that *CGSM* covers the medium and high speed region.

In summary, it can be concluded that *current gradient sensorless method* is a very simple and cheap but it is also robust and reliable. It offers one rotor position estimation per stroke in two quadrant operation but it could be extended to dynamic four quadrant operation or even continuous generation operation. Through the work carried out in this thesis, it has been proved that such resolution is good enough for reasonable speed and torque transients, and therefore, could be a serious sensorless method for applications such as pumps, fans, compressors and others. Furthermore, it should be noted that the *current gradient sensorless method* is applicable to any regular switched reluctance motor and for most inverter topologies, and is very similar in complexity and performance to the back-EMF sensorless method for brushless DC motors.

Finally, it is worthy to mention that the most important contributions to this method are:

- Real time implementation of the *current gradient sensorless method* for switched reluctance motors.
- Identification of the advantages and limitations of the *current gradient sensorless method.*
- Development of the *current gradient sensorless method*'s theory for switched reluctance generators.
- Experimental study of start-up procedures for the *current gradient sensorless method*, in particular self-synchronisation and feedforward.
- Experimental study of accuracy and dynamic performance of the *current gradient*

sensorless method.

- Reduction of current sensors and detection stages for rotor position information.
- Implementation of two-quadrant closed-loop speed sensorless control using *current gradient sensorless method.*
- Experimental test of speed and torque transients using *current gradient sensorless method.*

which were not done by previous researchers [98].

The work carried out in the *current gradient sensorless method* resulted in three publications [28, 29, 30], one of them being refereed journal article.

6.1.2 High resolution sensorless methods for switched reluctance motor drives

A new sensorless method for high resolution of rotor position estimation of switched reluctance motors has been investigated. The algorithm is based on flux linkage and current observer making use of the motor magnetic characteristic. The algorithm uses the energised phases for position estimation and its inputs are the measured phase current and the calculated phase voltage from the switching states. The algorithm is formed by four stages, which are: position prediction, observer model (*Stage I*), position correction, and flux linkage correction (*Stage II*). The general theory of each stage was developed and presented systematically.

For the *Stage I*, two models (one for flux linkage observer, and the other one for current observer), of the algorithm were identified which require simpler calculations. These models were implemented in Simulink, and the simulation results showed that the performance of both models is the same when an error in flux linkage is introduced. From these results, it can be concluded that there is no advantage in using the flux linkage observer or the current observer.

A novel method of position correction is introduced. The method consist in choosing *the best phase* for rotor position estimation from all conducting phases. This new method was investigated and compared with the method of averaging the position information from all conducting phases (a method proposed previously by [70]). The simulation results demonstrated that choosing *the best phase* significantly reduces errors in rotor position estimation. As a second method for position correction, it was suggested to weight the contribution of each conducting phase by using weighting factors.

The possible models for the *Stage II* were developed. The simplest model for this stage was identified and its contribution was investigated. The simulation results showed that the *Stage II* does not reduce significantly the error in flux linkage, furthermore, its contribution depends how fast the flux linkage is changing, and therefore, it is dependent of the motor operating point. For this reason, it was decided no to implement the *Stage II* in real time, with the additional advantages of reducing significantly the calculation time in the DSP.

The proposed high resolution sensorless algorithm based on flux linkage observer was successfully implemented using the Texas Instrument DSP TMS320C31 platform in combination with a FPGA Xilinx XC3195A. The rotor position was estimated at rate of 5 kHz, a limit imposed by the maximum speed of the DSP. Furthermore, the new method for position correction was demonstrated to be reliable and robust. The algorithm was tested in open-loop PWM voltage control and closed-loop PWM current regulation control. A series of experimental results were presented, including start-up, steady state, speed transient and operation under load. These results demonstrate that the proposed algorithm is robust, reliable and offers high resolution in a wide speed range. It is worthy to note that the estimated rotor position had a ripple, mainly caused by error in the predicted flux linkage and the swapping of the rotor position from phase to phase. However, the estimated rotor position was good enough for phase commutation. It should be also noted that the other factor that plays an important role in the

accuracy of the algorithm is the accuracy of the measured magnetisation characteristic of the machine because the algorithm is based entirely on this information.

It was found that the main difficulty of the method was the prediction of the flux linkage by the integration of the phase voltage, this problem was worse at low speed where the voltage drop in the phase resistance, which is a dependent variable of temperature, is a significant part compared to the applied voltage. This causes an uncertainty in the calculation of the phase voltage, and this is accentuated by the integration effect which yields in drifting errors in the flux linkage. Other source of errors in the phase voltage are the voltage drop in the switching transition due to the inherent turn on and turn off time of the switches, and the voltage drop in the conduction period of the switches and leads from the inverter to the motor. A solution to this problem has been proposed, which suggests the use of exactly the same algorithm but using the flux linkage and current obtained from injected high frequency pulses in the unexcited phases instead of the phase that is generating the main torque. Two types of probing pulses have been discussed for this purpose, i.e. constant peak current or constant flux linkage probing pulses. It is concluded that the latter is more suitable due to the low sensitivity to errors in flux linkage.

In summary, it can be concluded that the proposed sensorless algorithm for switched reluctance motors based on flux linkage or current observer is robust and suitable for high resolution position estimation of any switched reluctance motor. The algorithm does not put any limitation in the drive performance, and therefore, dynamic four quadrant operation is possible. The experimental results showed that the proposed method (*the best phase*) for position correction works well. Furthermore the whole position estimation algorithm is simple, but with no loss in accuracy and resolution, leading to few calculations in real-time. This algorithm is suitable for applications such as servo drives where high position resolution is required, however it should be noted that at high speed is limited by the processing time of the DSP. This limitation is becoming less important because every day there are available more powerful, cheaper

and faster DSPs. This means that the fast growing digital signal processing technology may allow the application of this sensorless algorithm to those applications considered cost-sensitive.

Finally, it is worthy to mention that the most important contributions to this method are:

- Development of the theory of sensorless control for switched reluctance motor based on flux linkage and current observer.
- A novel method of how to chose *the best phase* for position estimation among all conducting phases is introduced.
- Identification of advantages and drawbacks of the new sensorless method.
- Implementation of the flux linkage observer sensorless method in Simulink^{R}.
- Study of the flux linkage observer sensorless method using probing pulses in unenergised phases.
- Performance investigation of flux linkage and current observer.
- Performance investigation of a second stage for flux linkage correction.
- Real time implementation of the flux linkage observer for position estimation.
- Experimental test of PWM voltage control in sensorless mode.
- Experimental test of closed-loop current control in sensorless mode.

which were not done by previous researchers [70, 71]..

The results of this high resolution sensorless method have been published in [31].

6.2 Future work

The initial objectives of the project have been successfully reached through the development of this thesis. However, the results also open new questions and new possible improvements of the algorithms for further investigation. This possible future work is listed as follows.

Low cost sensorless methods

1. The theory indicates that the *current gradient sensorless method* is applicable to switched reluctance generators. Therefore, experimental validation of braking and continuous generation are necessary.

2. The *voltage magnitude sensorless method* may be useful for low speed applications where current regulation is possible. Full real implementation of this method needs further investigation.

3. An extensive test of the *current gradient sensorless method* in motors with different number of phases, topologies, and power levels is required for further validation of the method.

4. Investigation of the method in tracking the rotor position on the fly. The question is if the *current gradient sensorless method* is able to estimate the rotor position when the rotor is already rotating without been energised.

5. The results show that there is a scope for implementation of the *current gradient sensorless method* in a single-chip solution similar to those ICs available for position estimation of brushless DC motors, i.e. the *current gradient sensorless method* could be put on a single-chip. Hence, further development in this direction will be worthwhile.

6. There are some important niches in the industrial motor drives which could be satisfied with the *current gradient sensorless method*, for instance pumps, compressors, and fans. In other words, the simple and low-cost implementation of

current gradient sensorless method may allow the SRM technology into a range of air-moving, pump applications and even domestic appliances. Therefore, a detailed and extended study of these and others possible industrial applications require further investigation.

High resolution sensorless methods

1. Methods for compensation of errors in flux linkage need further investigation.
2. On-line self-identification of the magnetisation curves is the next important development step for this algorithm.
3. Implementation of the average and instantaneous torque and the position control loops.
4. Further investigation of the algorithm's performance at very low speed and standstill, and if the algorithm allows position estimation on the fly.
5. The motor torque-speed characteristic that can be covered with this algorithm need further investigation.
6. Real time implementation of the algorithm using probing pulses at constant flux linkage is necessary in order to investigate its limitations.

In order to have a sensorless switched reluctance motor drive that covers the motor's full torque-speed characteristic, and therefore, be a serious contender of the conventional drive driven by a mechanical sensor, it may be necessary to combine two or three sensorless methods. From the results obtained through this thesis, it seems that such a combination could be possible with the *current gradient sensorless method* for the high speed range, flux linkage or current observer sensorless algorithm using the energised phases for medium speed range, and the same observer algorithm but using probing pulses for low speed. This proposed combination looks promising, but further analysis, investigation and experimental testing will be required.

Appendix A

Soft-switching applied to Switched Reluctance Motor Drives

This Appendix presents the work carried out in Soft-Switching applied to SRMs. This work was carried out in the first year of my PhD studies as a side project in order to get good insight of the SRM technology and power electronics. The Appendix starts with a brief discussion of the origin of losses in switches and follows with a description of current methods available to reduce switches' losses, for instance, Snubbers and Soft-Switching topologies. The principle of operation of the well known Soft-Switching topologies, Resonant dc-link (RDCL), and Active Clamp Resonant dc-link (ACRDCL) already applied to AC technology, is discussed. A simple RDCL and ACRDCL front-end SR inverter is proposed, and investigated. Simulations are carried out in order to analyse the functionality of the proposed inverter, followed by the description of the real implementation of the ACRDCL-SR inverter using a Microcontroller-FPGA platform. Finally, experimental results are presented and discussed which confirm the functionality of the proposed ACRDCL-SR inverter.

A.1 Losses in switches

In most inverter applications, there is a demand to operate the power inverter at the highest possible switching frequency to improve the required inverter output waveforms. However the main limitation on raising the switching frequency is the switching losses. BJTs, IGBTs, and GTOs are usually used for medium and high power applications because of their high current and voltage capabilities, however they have worse switching characteristics than MOSFETs, especially the severe turn-off current tail under hard switching. The power converter determines the efficiency of the electric energy flow from the source to the load, the concern being the most efficient use of the electric energy. Ideally no loss should occur in the power stage, however in reality this is not the case and the waste of power should be minimised in the converter stage. The power converter is composed of a set of electrical components constituting a network that links the source and the load. The components are:

- Semiconductor electronic switches.
- Passive elements: capacitor, inductors, resistors, (note that these components may represent an important part of the size, weight and cost of the overall cost of the power converter).
- Sensors.

In the common Hard-Switched (HS) power converter, the switches are turned on and turned off while simultaneously experiencing voltage and current. This results in switching power losses proportional to the switching frequency: this is the major disadvantage of HS. The other source of inverter losses is conduction losses, which are generated by the internal resistance of the switch. A simple analysis of the dynamic switches' characteristics is necessary for better understanding of losses in power converters, which is explained as follows.

The ideal loss-less switch has the following characteristics [106]:

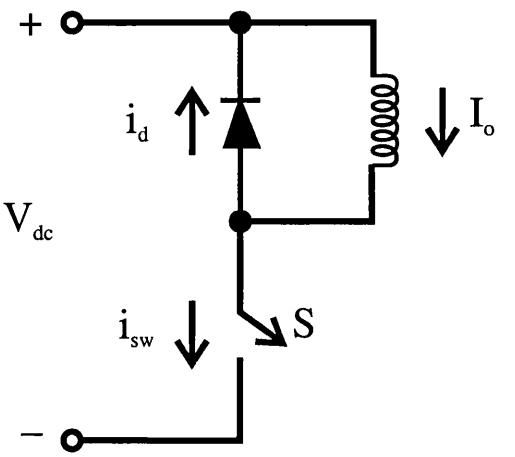

Figure A.1: Inductive Switching circuit

- When the switch is off: Blocks arbitrarily large forward and reverse voltages, and zero current flows.
- When the switch is on: Conducts arbitrarily large current, and zero voltage drop.
- When the switch is triggered: Switch from on to off or vice-versa instantaneously with minimum power required from control source.

Unfortunately, it is impossible to have all the ideal characteristics in a real switch, hence some electric power is dissipated in switches, which is the main challenge to reduce. A simple circuit, shown in Fig.A.1, is used to analyse the power dissipation in a controllable switch, a pure inductive load and an ideal diode are assumed. The energy dissipated in the switching time and in the on-state can be approximated as

$$W_{ton} = \frac{1}{2} \cdot V_{dc} \cdot I_o \cdot t_{ton} \quad \text{(A.1)}$$

$$W_{toff} = \frac{1}{2} \cdot V_{dc} \cdot I_o \cdot t_{toff} \quad \text{(A.2)}$$

$$W_{on} = V_{drp} \cdot I_o \cdot t_{on} \quad \text{(A.3)}$$

where W_{ton}, W_{toff}, W_{on}, V_{dc}, V_{drp}, I_o, t_{ton}, t_{toff}, and t_{on} are turn on energy losses, turn off energy losses, conduction losses, voltage supply, voltage drop across the switch when conducting, load current, crossover time on (transition turn on time), crossover

time off (transition turn off time), and time on, respectively. The switching power loss P_{sw} can be expressed as,

$$P_{sw} = (W_{ton} + W_{toff}) \cdot f_{sw} = \frac{1}{2} \cdot V_{dc} \cdot I_o \cdot [t_{ton} + t_{toff}] \cdot f_{sw} \tag{A.4}$$

and the conduction power losses P_c is the power dissipated during the on-state,

$$P_c = W_{on} \cdot t_{on} \cdot f_{sw} = V_{drp} \cdot I_o \cdot D \tag{A.5}$$

where f_{sw}, and D are the switching frequency, and the duty cycle respectively.

From (A.4), it is clear that switching power loss varies proportional to both switching frequency, and crossover times t_{ton} and t_{toff}. (A.5) shows that the conduction power loss varies proportional to the duty cycle and the voltage drop. The total average power semiconductor dissipation (P_t) is the addition of switching loss (P_{sw}) and conduction loss (P_c), i.e. $P_t = P_{sw} + P_c$. Now, the basic heat transfer equation has to be taken into account

$$T_J = T_A + R_{JA} \cdot P_t \tag{A.6}$$

where T_J, T_A, R_{JA}, and P_t are junction temperature, ambient temperature, thermal resistance from semiconductor junction to ambient, and average power semiconductor dissipation respectively. The switch has a maximum permissible junction temperature, therefore, the temperature in the switch has to be maintained below this maximum value. It can be seen from (A.6) that if P_t increases R_{JA} must decrease to maintain T_J constant, however a switch with small R_{JA} is expensive or impractical for most of the cases. Therefore, a big heatsink, or even the use of more complex heat transfer method such as watercooling, is necessary to reduce the temperature in the switches at high switching frequency. In other words, the main problem is how to get rid of, or avoid the generation of the heat from the power converter when it is operated at high frequency.

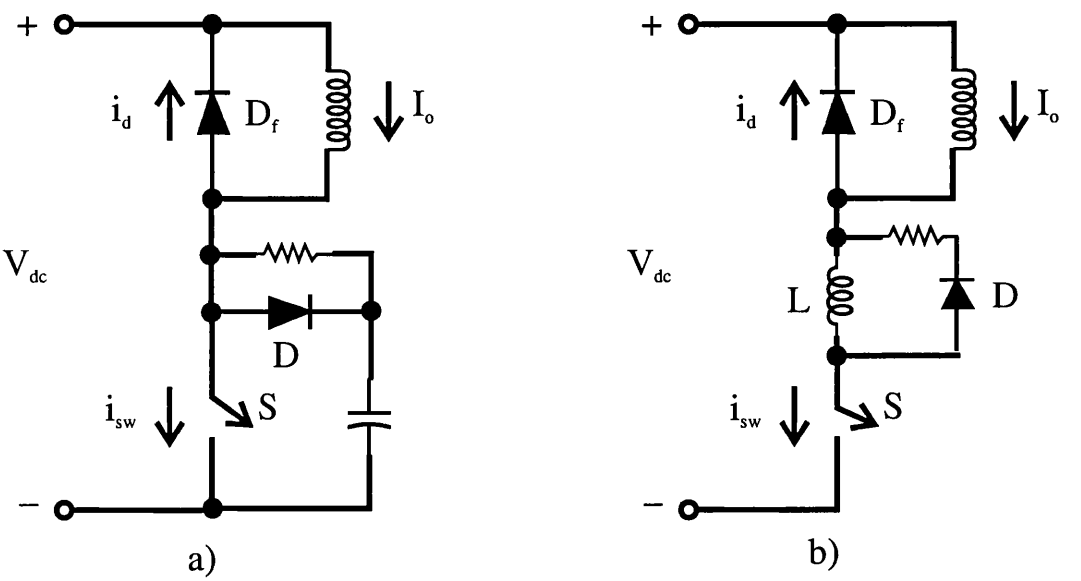

Figure A.2: Dissipative snubbers. a) turn-off snubber, b) turn-on snubber

A.1.1 Snubbers and Soft-Switching

Two sources of power dissipation in power converters have been identified in the foregoing analysis, i.e. switching power loss and conduction power loss. To reduce P_c it is necessary to make switches with a very low voltage drop on-state. From the point of view of the hardware designer, there is nothing to do in this case. On the other hand, to reduce P_{sw}, fast switches are needed i.e. switches with small t_{ton} and t_{toff}. Another option is to create an external protection of the switch. There are two ways to achieve such protection on the switch: using Snubbers or applying Soft-Switching to the converter.

Snubber circuits consisting of diodes and passive components in series and parallel with the switch as shown in Fig.A.2. The principle of turn-off snubber is as follows: The current i_{sw} is initially equal to I_o. When the switch is turned off, the current i_{sw} decreases linearly and the difference $(I_o - i_{sw})$ flows into the capacitor until the voltage in the capacitor reaches V_{dc}. At this point the freewheeling diode D_f starts conducting, hence the voltage across the switch S reaches V_{dc}. When the switch turns on the energy stored in the capacitor is dissipated in the resistor. On the other hand, the principle

of turn-on snubber is as follows: The voltage across the switch S is initially V_{dc}. When the switch is turned on, the current i_{sw} rises from zero to I_o and the voltage in the switch S is reduced by the voltage drop over the inductance L. During the on interval I_o flows through L. When the switch turns off, the energy stored in L is dissipated in the resistor.

Snubbers protect switches by decreasing the power stress at the commutation point. However, power is dissipated in the snubber resistor, hence the overall power loss in the power converter is not reduced. Furthermore, the number of components is increased with all its consequences such as weight, space, cost, reliability and packaging problems.

The alternative and interesting method to reduce switching losses is Soft-Switching (SS). The concept of SS is to provide zero voltage (ZVS) across the switch or zero current (ZCS) through the switch during the transition time, to the extend that switching losses can be neglected, thus permitting high switching frequency. SS topologies are extensively studied for reduction of switching losses, and may reduce significantly switching losses. More reliable and efficient operation of the devices is expected with SS, thus more efficient operation of the drive. Fig.A.3 depicts the $V\&i$ locus of the switch for HS converters with and without snubbers, and SS converters. It can be seen that SS minimises significantly the power dissipated in the switching transition.

The advantages of soft-switching are a consequence of the reduction of switching stress in the switch, which are:

1. Absence of switching losses: Because the switch does not experience simultaneously voltage and current during the switching interval.

2. Allows high switching frequency: The switches can be operated at their maximum switching frequency because the switching losses are reduced.

3. The need of snubbers disappears: Providing zero voltage across the or zero current through the switch during the switching transient, there is no reason to have snubbers to protect the switch.

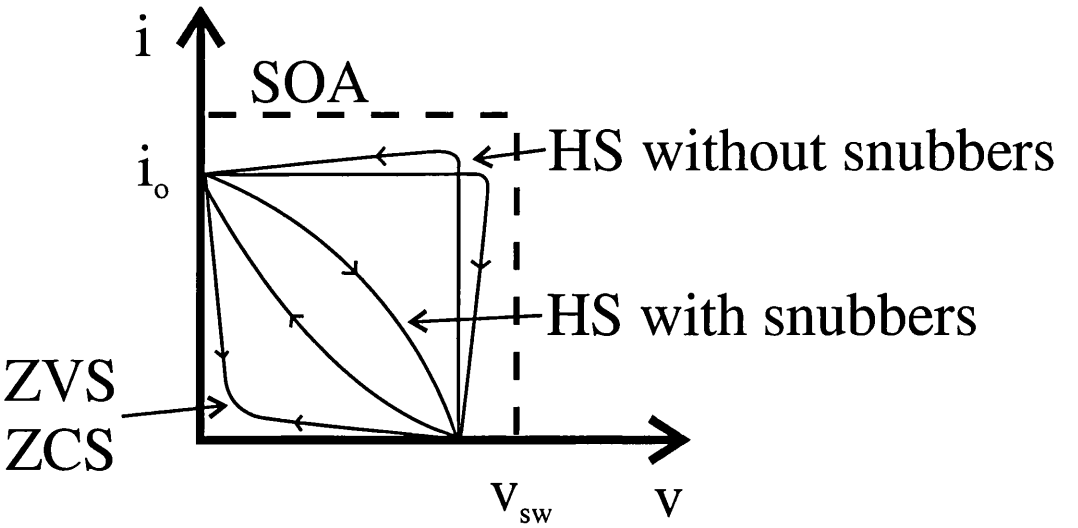

Figure A.3: Comparison of the loci curve for HS and SS.

4. Switch operating area (SOA) is no longer a limitation: A large SOA is no longer required because there is not simultaneously voltage over and current through the switch.

5. Heat in the inverter is reduced: This is directly related to the reduction of switching losses. As the switching losses are reduced, there is less electrical power dissipated, resulting in less heat in the converter. This is a great advantage, which means small heatsink, and therefore, a more compact converter.

6. Electromagnetic interference is reduced as a consequence of reduced of $\frac{dv}{dt}$: ZVS means no $\frac{dv}{dt}$ when transistor commutates.

7. Better quality of output waveforms: The external waveforms that the load demands can be more accurately generated due to the high switching frequency.

8. Acoustic noise is reduced: Another advantage of high frequency is that over 20 kHz the switching noise is not perceived by the human ear.

9. Better power density: Higher power per volume ratio in the inverter can be achieved because the size of heatsink is significantly reduced, and smaller switching devices may also be used.

The price to pay in order to achieve these benefits are the following drawbacks:

1. VA rating in the switch is higher than HS: Either the voltage over switches is higher than the power supply voltage or the current through switches is higher than the current load I_o. (more than $2 \cdot V_{dc}$ or $2 \cdot I_o$ in the worst case).

2. Extra active and passive components: In order to create zero voltage or zero current in the switching transition, resonant circuits (LC tank) are used in combination with extra switches. The additional cost of extra components must be justified by the energy saving and performance of inverter. These components have to be designed specially for the converter.

3. Control complexity: Extra control and sensors are necessary to control the resonant circuit LC.

4. Conduction losses: When high current flows through passive components or switches, the conduction losses can become significant. $R_{ESR} \cdot I^2$ and $R_{on} \cdot I^2$ are the power dissipated in passive components and in active components respectively.

Soft-Switching offers strong advantages and an efficient use of electrical power and devices, allowing the improvement of power converters. However, there are some characteristics that work against itself. The main problem with SS topologies is that they require higher VA ratings of the semiconductor devices than HS, and resonant LC components. It is worthy to note that the additional control required by SS may compromise the robustness of the converter.

ZVS Soft-Switching topology is preferable rather than ZCS at high switching frequencies due to the internal capacitances of the switch. If the transistor is turned on at zero current but at non-zero voltage level, the internal capacitances discharge into the switch. In contrast, no such loss occurs if the switch is turned on at zero voltage. The most popular ZVS topologies are the Resonant dc-Link (RDCL), and the Active

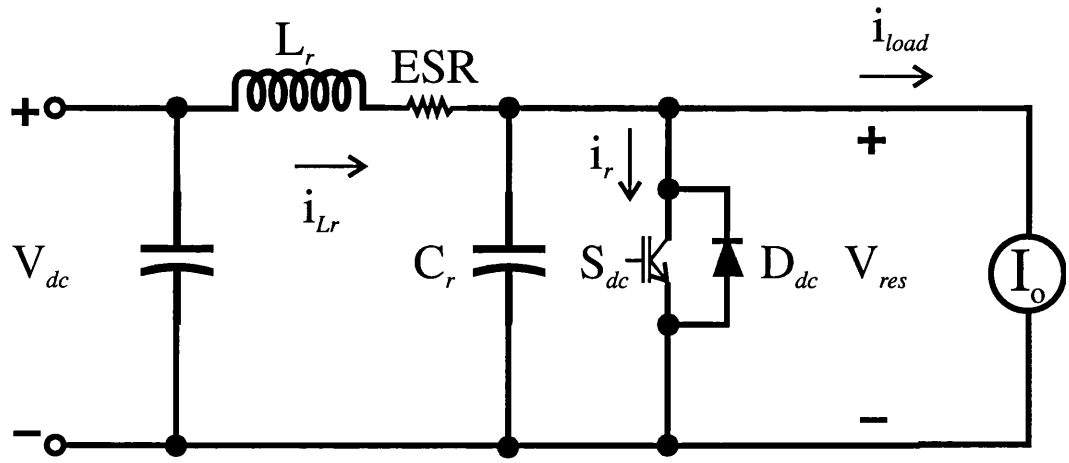

Figure A.4: Resonant dc-link inverter

Clamp Resonant dc-Link (ACRDCL) proposed by Divan which are explained in the next subsections.

A.1.2 Resonant dc-link (RDCL)

A resonant circuit is introduced between the dc input voltage source V_{dc} and the load, [107]. As a result, the input voltage to load V_{res} oscillates between 0 and approximately twice the dc input voltage. The basic circuit is shown in Fig.A.4. The extra components are: 1 Transistor, 1 Diode, 1 Inductor and 1 Capacitor.

The impedance and the resonant frequency are $Z_o = \sqrt{\frac{L_r}{C_r}}$, and $f_r = \frac{1}{2 \cdot \pi \cdot \sqrt{L_r \cdot C_r}}$ respectively. The principle of this circuit is as follow: First the switch S_{dc} is turned on, and the current i_{Lr} increases linearly with slope $\frac{V_{dc}}{L_r}$. S_{dc} remains on until enough energy is stored in L_r in order to make sure that V_{res} returns to zero in the resonant cycle. The difference between i_{Lr} and I_o ($I_m = i_{Lr} - i_{load}$) is monitored to control the turn off of S_{dc}. Once I_m reaches the positive current reference i_{ref}, S_{dc} is turned off. After S_{dc} is turned off the resonant cycle starts. V_{res} increases until its peak (approximately $2 \cdot V_{dc}$), and then returns to zero. V_{res} is clamped to zero by the diode D_{dc}. At this moment, S_{dc} is turn on to repeat the sequence. Steady and transient states of RDCL are depicted in Fig.A.5 for a $V_{dc} = 25V$.

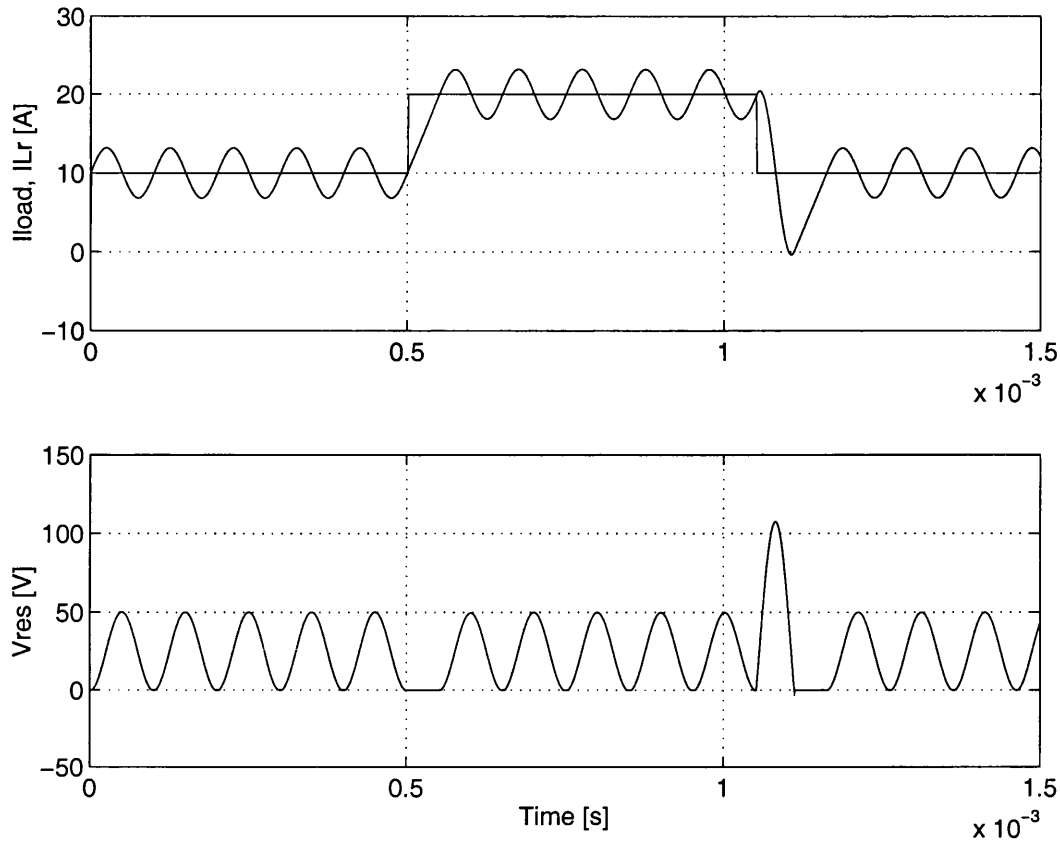

Figure A.5: Current and voltage waveforms of RDCL.

The following can be observed:

1. Load current constant: While the load current is constant, the zero voltage period and the maximum peak voltage are constant in every resonant cycles.

2. Positive load current transient: The stored energy in L_r is much lower than the necessary to make the system to resonate, i.e. $I_m \ll i_{ref}$. Therefore, the zero voltage period is extended because the switch S_{dc} remains on until I_m reaches the i_{ref}.

3. Negative load current transient: The stored energy in L_r is much higher than the necessary to make the system to resonate i.e. $I_m \gg i_{ref}$. In this case, more current is pumped into C_r, making the peak voltage much higher than $2 \cdot V_{dc}$. Note that the resonant voltage increases immediately and therefore the zero voltage

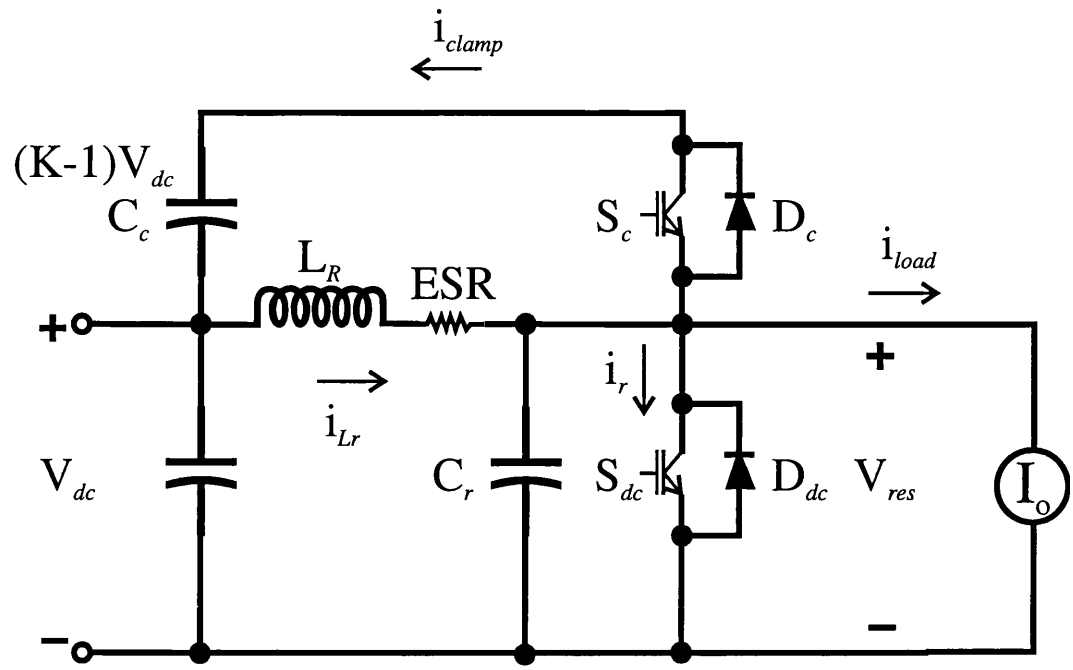

Figure A.6: Active Clamp RDCL inverter

period is very short. When the voltage returns to zero, the zero voltage period is extended before the next resonant cycle starts because the voltage is clamped by D_{dc}.

It can be seen that changes in the load current affect the peak voltage, and the zero voltage periods of the resonant cycle. The Quasi-Resonant dc-Link topology eliminates the voltage overshoot by controlling the energy stored in L_r [108]. During each negative load current transient, L_r is disconnected from V_{dc} and connected to a negative voltage to reduce its high current until i_m reaches i_{ref}: in this period the voltage in the bus is zero. The peak voltage is maintained at $2 \cdot V_{dc}$ during all the resonant cycles despite load current transients. This topology needs 3 extra transistors, 3 diodes and a secondary power supply which applies the negative voltage to L_r.

A.1.3 Active Clamp Resonant dc-Link (ACRDCL)

An interesting alternative to reduce the peak voltage of RDCL is clamping the voltage between V_{dc} and $2 \cdot V_{dc}$. This is possible by adding few components to the

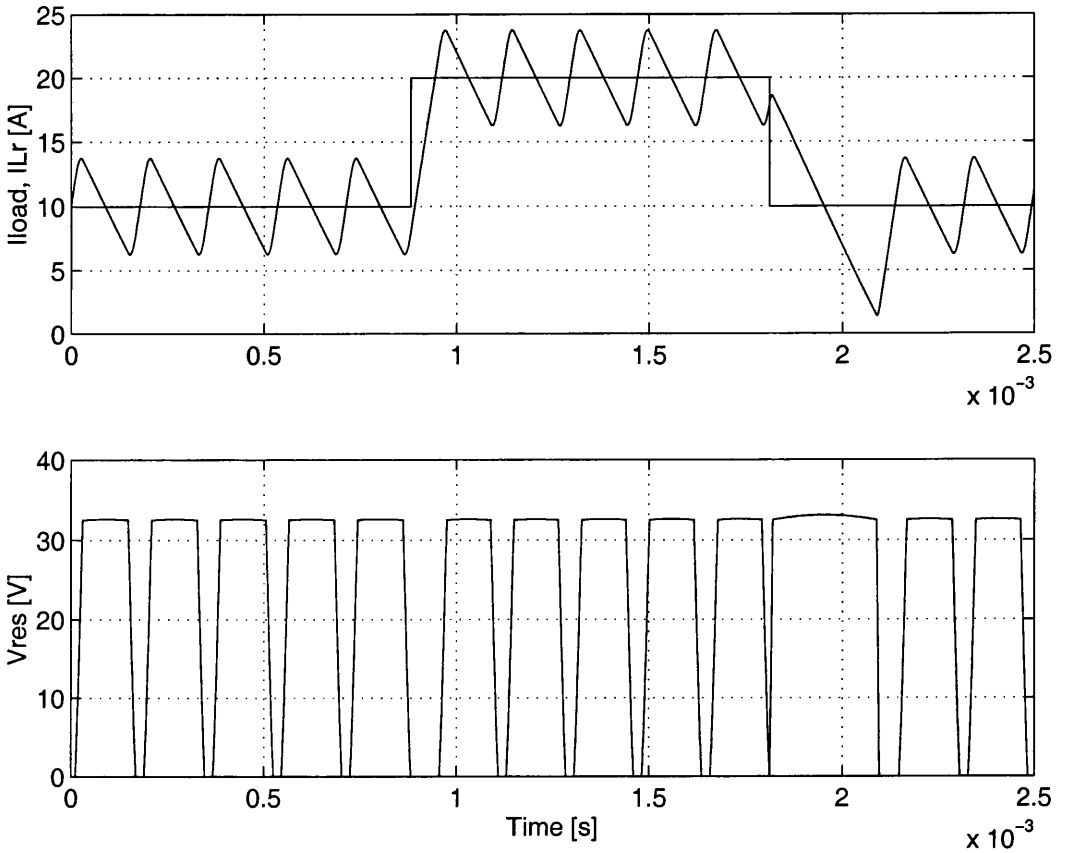

Figure A.7: Current and voltage waveforms of ACRDCL.

resonant circuit as shown in Fig.A.6. The total components are 2 Transistors, 2 Diodes, 2 Capacitors and 1 Inductor.

The resonant frequency is expressed as [109]:

$$f_r = \frac{1}{2 \cdot \sqrt{L_r \cdot C_r} \cdot \left[\cos^{-1}(1-K) + \frac{\sqrt{K \cdot (2-K)}}{K-1}\right]} \tag{A.7}$$

where K is the clamp constant (the clamp voltage is $K \cdot V_{dc}$). It can be seen from A.7 that if $K \geq 2$ the circuit degenerates into RDCL. The Resonant frequency f_r decreases as K is close to 1, when $K = 1$, f_r is zero. Hence, there is a limit where it is not practical to clamp the voltage. The clamp constant is usually 1.2 to 1.5. The impedance of this topology is the same as the RDCL.

The principle of this topology is as follow: The control of S_{dc} is equal as in RDCL. When the resonant cycle starts, V_{res} increases until reaches the clamp voltage $K \cdot V_{dc}$,

at this moment, D_c starts conducting and clamps the bus voltage. While D_c conducts, S_c can be turned on any time. The energy transferred to the clamp capacitor C_c by D_c conducting, is recovered when S_c conducts. S_c is turned off when the net energy transferred to C_c equals zero and the L_rC_r tank resonates until the dc bus reaches zero. At this time, V_{res} is clamped to zero by the diode D_{dc}, and then S_{dc} is turned on to repeat the sequence. The steady and transient states of ACRDCL are shown Fig.A.7 for $V_{dc} = 25V$ and $K = 1.3$.

The following can be observed:

1. Load current constant: Similar to RDCL, while the load current is constant, the zero voltage period and the clamp period are constant during the resonant cycles.

2. Positive load current transient: The stored energy in L_r is much lower than necessary to make the system to resonate and the zero voltage period is extended similar to the RDCL.

3. Negative load current transient: The stored energy in L_r is much higher than necessary to make the system to resonate. In this case, the resonant voltage increases immediately similar to the RDCL, however, the excess of energy is pumped into C_c rather than into C_r, hence extending the clamp voltage period. When the net exchange energy in C_c is zero, S_c is turned off and V_{res} decreases to zero. At this time, the zero voltage period is extended similar to the RDCL.

It is clear that the resonant frequency for both RDCL and ACRDCL is affected by transients in load current, however ACRDCL has the advantage of giving a fixed clamp voltage ($K \cdot V$) in every resonant cycle even under load transients. The aim of the next sections is the study of these two topologies applied to the SR drive.

A.1.4 Summary

The origin of losses in the switching devices has been discussed briefly. Snubbers and Soft switching methods to reduce the switching losses have been discussed, the latter being an attractive method. Soft switching allows switching to take place with no simultaneous voltage over and current through switches: however it adds some control requirements and components. RDCL and ACRDCL are well known topologies already applied to AC technology, however little work has been reported in the literature on these topologies applied to SRM. The basic principle of both RDCL and ACRDCL has discussed.

A.2 Resonant dc-link inverter for current controlled switched reluctance motor

For high efficiency of the SRM in a wide speed range, the phase current should be regulated and the commutation angles should be chosen according with speed. The current is regulated usually by Bang-Bang control or PWM duty-cycle control. In PWM the frequency is fixed in the order of 5-25 kHz and the duty cycle is varied to regulate the current, therefore the switching instant depends on the duty cycle and it is not repetitive. In Bang-Bang control, which is the simplest technique to control the current, the phase current is compared with a reference current, the comparison determines if the switch is on or off. To avoid excessively high switching frequency there are two options:

1. Hysteresis control: Use of a hysteresis band where the transistors are turn on or off in order to maintain the current within the band ($i_{rf} \pm \frac{\Delta I}{2}$). The switching frequency is variable.

2. Delta modulation: The switches are allowed to change their states only at certain instants, i.e. the output of the comparison between phase current and reference

current is synchronised to a fixed frequency clock. In this case the phase current varies with the inductance and is no longer contained within a fixed tolerance band around i_{rf}.

Soft-switching topologies are old news, and most of them are based on the Resonant dc-Link, Active Clamp Resonant dc-link proposed by Divan [107, 109, 110] and the Resonant Commutated Pole proposed by De Donker [111]. These topologies can replace traditional Hard-Switched control. However, for the former the resonant frequency is larger than the inverter switching frequency for good resolution in the output voltage due to discrete pulse modulation (DPM).

This section presents a functionality study of the Switched Reluctance Motor (SRM) inverter utilising a resonant dc-link or an active clamp resonant dc-link to provide current regulation with zero-voltage switching. By simply synchronising the switching instants in the SR inverter to the resonant link zero voltage periods, high bandwidth delta-modulated current regulation, necessary in high-performance SR drives, is performed with minimal inverter switching losses. The classic 2-switches-and-2-diodes-per-phase inverter configuration is maintained. The RDCL-SR and ACRDCL-SR inverters were simulated to study their functionality, and the ACRDCL-SR inverter was built in order to validate its operation experimentally. Comparisons between hard-switched and soft-switched waveforms are presented and it was found that the ACRDCL-SR inverter maintains all performance and robustness aspects of the hard-switched inverter drive, albeit the soft-switching adds some control requirements. The experimental results show that the presence of soft-switching does not compromise the functionality drive performance compared to hard-switching in any aspect. And applying the resonant link to the SRM inverter presents no difference compared to AC-drive applications.

There is a range of possible SRM inverter configurations [112] but most attention is paid to the "classic" configuration with two switches and two diodes per phase, as it offers easy and robust control with the capability of driving the phase voltage rail-to-rail, independent control of each phase current and high reliability.

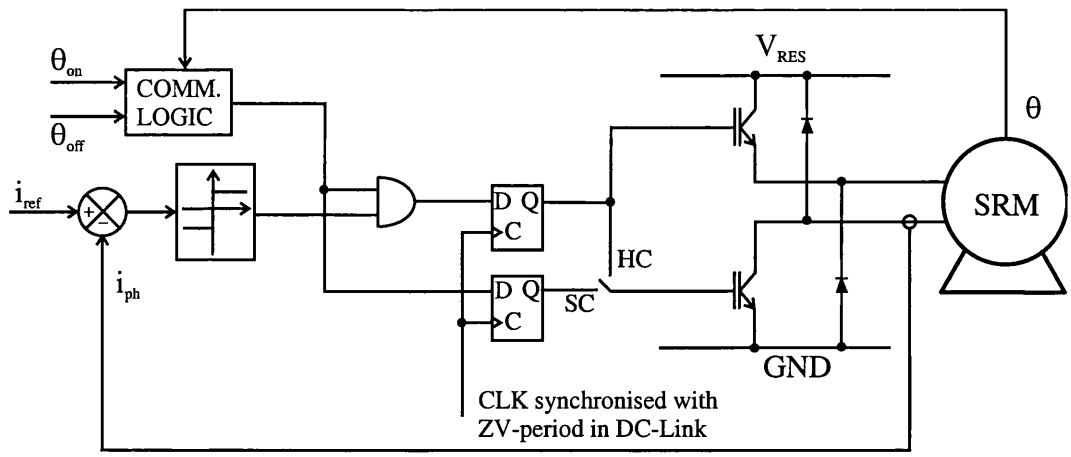

Figure A.8: Principle of the control scheme - one phase shown.

The SRM drive technology is not yet as established as AC and commutator DC drives, and has not undergone the same scrutiny as these. Many aspects of the 3 phase AC inverter have been improved, soft-switching being one of the more promising ones, effectively eliminating the switching losses and allowing increased switching frequencies, both features required in modern high-performance motor drives. However, progress in AC technology is not always directly applicable to SRM drives. Soft-switching SRM inverters with reduced number of switches have been proposed. In [113] and [114] were suggested unipolar, modified C-dump topologies using 2 thyristors per phase and one BJT/IGBT in the C-dump circuit. The C-dump inverter imposes increased control requirements and has reduced fault tolerance compared to the classic inverter [34]. Moreover, it could be argued that there is little incentive in using the reputedly "rugged and cheaper" SR motor instead of a more expensive motor type, only to compromise these advantages by using a complex and less reliable inverter topology.

Soft-switching in AC inverters has resulted in well known schemes such as the auxiliary resonant commutated pole converter [115] and the discrete pulse modulated (DPM) resonant dc link topology [107, 109] (or its many variants providing additional improvements, see for example [116]) which can replace traditional hard-switched PWM control. However, for good resolution in the output voltage, the resonant frequency is orders of magnitude larger than the inverter switching frequency, thus very high. DPM

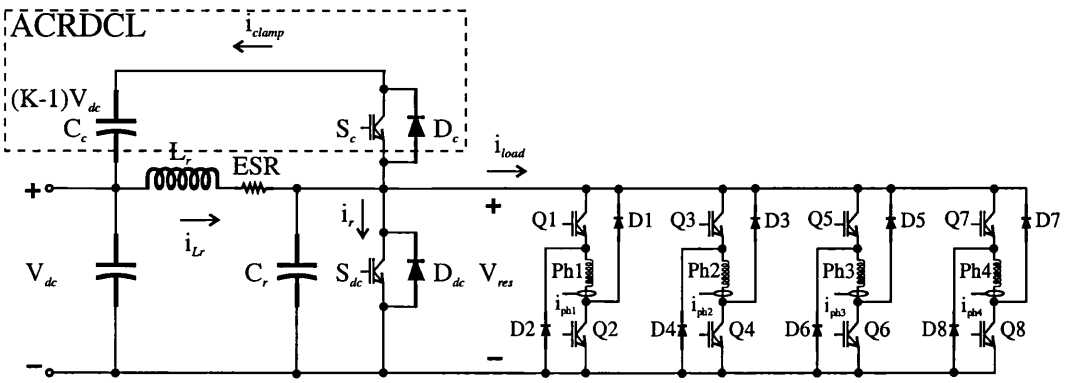

Figure A.9: Proposed 4 phase resonant dc-link SRM converter.

could be applied to delta-modulated current-regulated SRM drives. A quasi-resonant dc-link topology was proposed [111], employing a resonant commutated pole to collapse the dc-link voltage whenever switching takes place in an inverter phase-leg.

Here it is proposed a simpler and more robust approach, namely the resonant dc-link. The RDCL can be applied to SRM drives in combination with delta-modulation. As the current controller only takes action at discrete instants in delta-modulation, the dc-link voltage could vary over every switching period T_{sw} as long as the mean voltage in the dc-link is equal to the supply voltage, i.e. $\frac{1}{T_{sw}} \int_0^{T_{sw}} V_{res} = V_{dc}$ (this argument is neglecting stress on motor windings and power stage components). In this scheme, the dc-link is constantly resonating and the switching instants in the inverter are synchronised to the link zero-voltage periods as shown in Fig.A.8. The basic drive circuit is shown in Fig.A.9, and is amenable to the same variations found in AC drives. The circuit can operate with and without voltage clamp (ACRDCL and RDCL, respectively), the clamp circuit being shown in the dashed box of Fig.A.9. During the period where V_{res} is zero, the inverter phase switches are allowed to change state, similar to hard-switched constant frequency delta-modulation. Therefore, all control flexibility found in the hard-switched topology is maintained, while the switching losses are greatly reduced. In summary: the dc-link voltage resonates at f_r between 0 and $2 \cdot V_{dc}$ (or $K \cdot V_{dc}$ in ACRDCL). The inverter switching instants are synchronised to the zero voltage periods. The relation between the inverter switching frequency and the

resonant frequency is: $f_r = m \cdot f_{sw}$, where m is any integer, $m \geq 1$.

A.2.1 Simulation results

Simulations of an 3 phase SR motor model are conducted to verify the functionality of the resonant dc-link front-end SR drive. The circuit is shown in Fig.A.9 for a 4 phase inverter, however, the principle is the same for a 3 phase or other number of phases. The switches and diodes are assumed ideal. The resonant frequency (f_r) is 60 kHz. The switching frequency is equal to the resonant frequency.

RDCL

In Fig.A.10, A.11 and A.12, the speed of the rotor motor is constant at 1000 rpm, V_{dc}=150 V, the current reference is 5A, the commutation angles are $\theta_{on} = 45^o$ and $\theta_{off} = 82$. Fig.A.10 (top) shows the three phase currents and rotor position, (center) the load current and inductor current, and (bottom) the resonant capacitor voltage. The inverter is operated in "hard-chopping", i.e. both upper and lower switch in a phase-leg are used to regulate the phase current, therefore the phase voltage is switched between $+V_{res}$ and $-V_{res}$. Fig.A.11 shows results obtained with "soft chopping" i.e. only one switch regulates the current and the phase voltage is switched between $+V_{res}$ and 0, otherwise same conditions as in Fig.A.10. Fig.A.12 shows the phase currents obtained with a constant dc-link voltage for hard chopping (top graph) and soft chopping (bottom graph). The switching frequency is 60 kHz as RDCL. Clearly, there is little difference if any difference in the quality of the current control. It can be seen that the edges in the current waveforms are softer, which could help reduce the stator ovalisations, a well known source of noise [11]. The current of the inductor L_r oscillates in a band around $\pm$40A which is much bigger than the band where the load current is. It can be seen that there are some overshoots in the resonant link voltage upon a transient in the load current. For soft chopping the overshoots are less because the step of change of the load current is inferior.

Fig.A.13 shows the phase currents obtained at 5000 rpm, $\theta_{on} = 40^o$ and $\theta_{off} = 77^o$, and the reference current of 5A is never reached due to the increased speed. Single pulse operation is the result. Fig.A.14 shows the phase currents with the same conditions but with constant dc-link voltage. Comparing Fig.A.13 to Fig.A.14, it can be seen that there is not difference in the quality of the current waveform using RDCL. The only difference is the 60kHz ripple in the current waveform when using RDCL.

ACRDCL

To limit the peak resonant link voltage, the model was simulated with the Active Clamp Resonant dc-link. This topology makes use of the added circuit shown in the dashed box of Fig.A.9. Fig.A.15 and A.16 show the results for hard chopping and soft chopping respectively. They were obtained with same conditions as Fig.A.10 and A.11 but this time the resonant link voltage is clamped to 1.3 of V_{dc} i.e. $1.3 \cdot (150V) = 195V$. The resonant frequency is reduced from 60 kHz to 37.4 kHz due to clamping voltage according to (A.7). The current in L_r still oscillating in a band around $\pm$40A. Fig.A.17 shows the phase current at 5500 rpm, the current reference is not reached, resulting in single pulse operation. We can observe that the quality of the current waveform is the same as when using HS or RDCL.

The simulations verify the functionality of the simple and well-working inverter topology with a resonant dc-link front-end to the classic SRM inverter, applicable in the drive's entire torque-speed range. They also show that the presence of soft-switching does not compromise the drive performance compared to hard switching in any aspect, and adding the well-known benefits of soft-switching. Operation with or without overlap between conducting phases is possible, as well as soft or hard chopping and single-pulse operation.

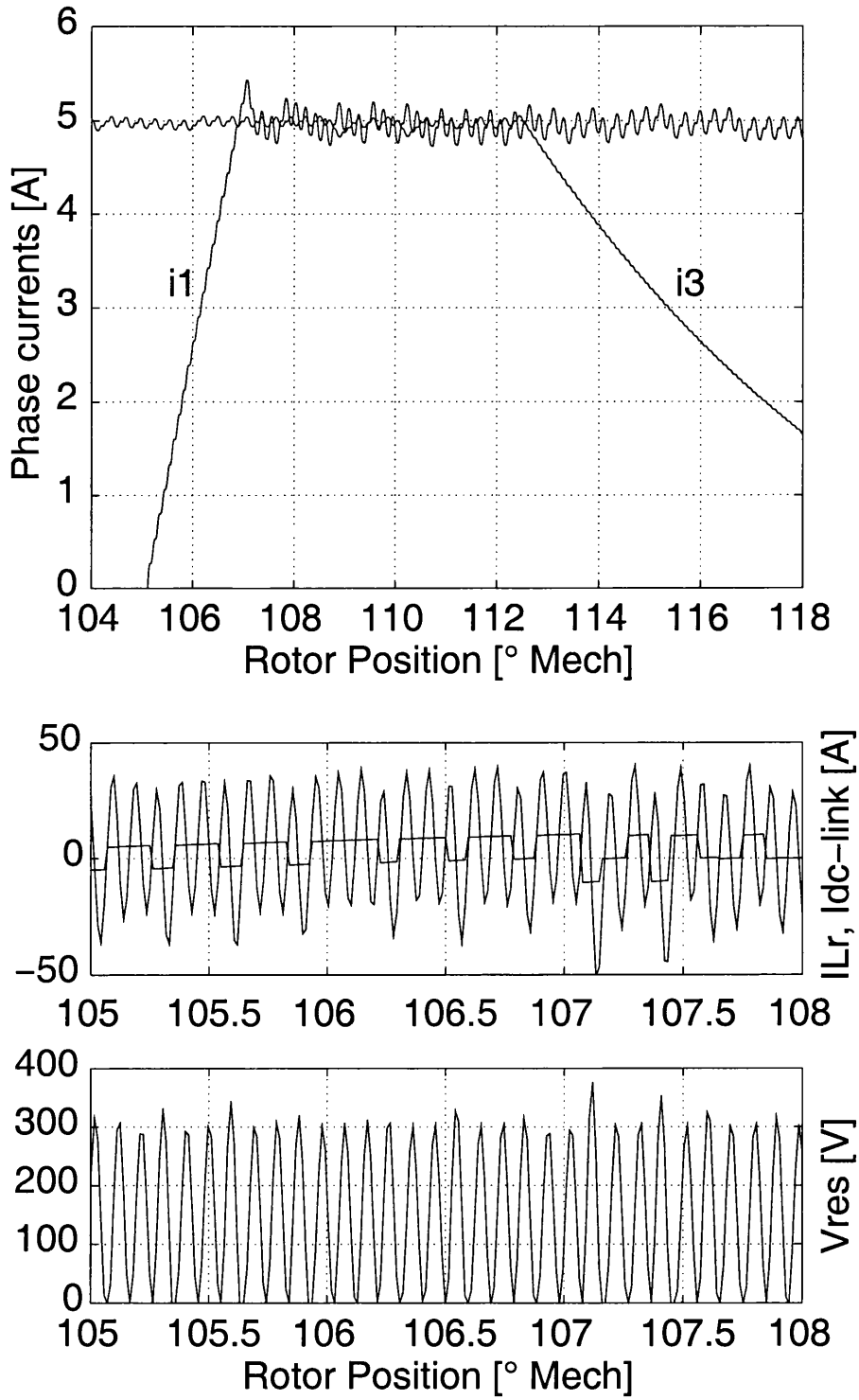

Figure A.10: Waveforms of RDCL with Hard chopping, (top) phase currents, (center) L_r and dc-link current, (bottom) resonant link voltage.

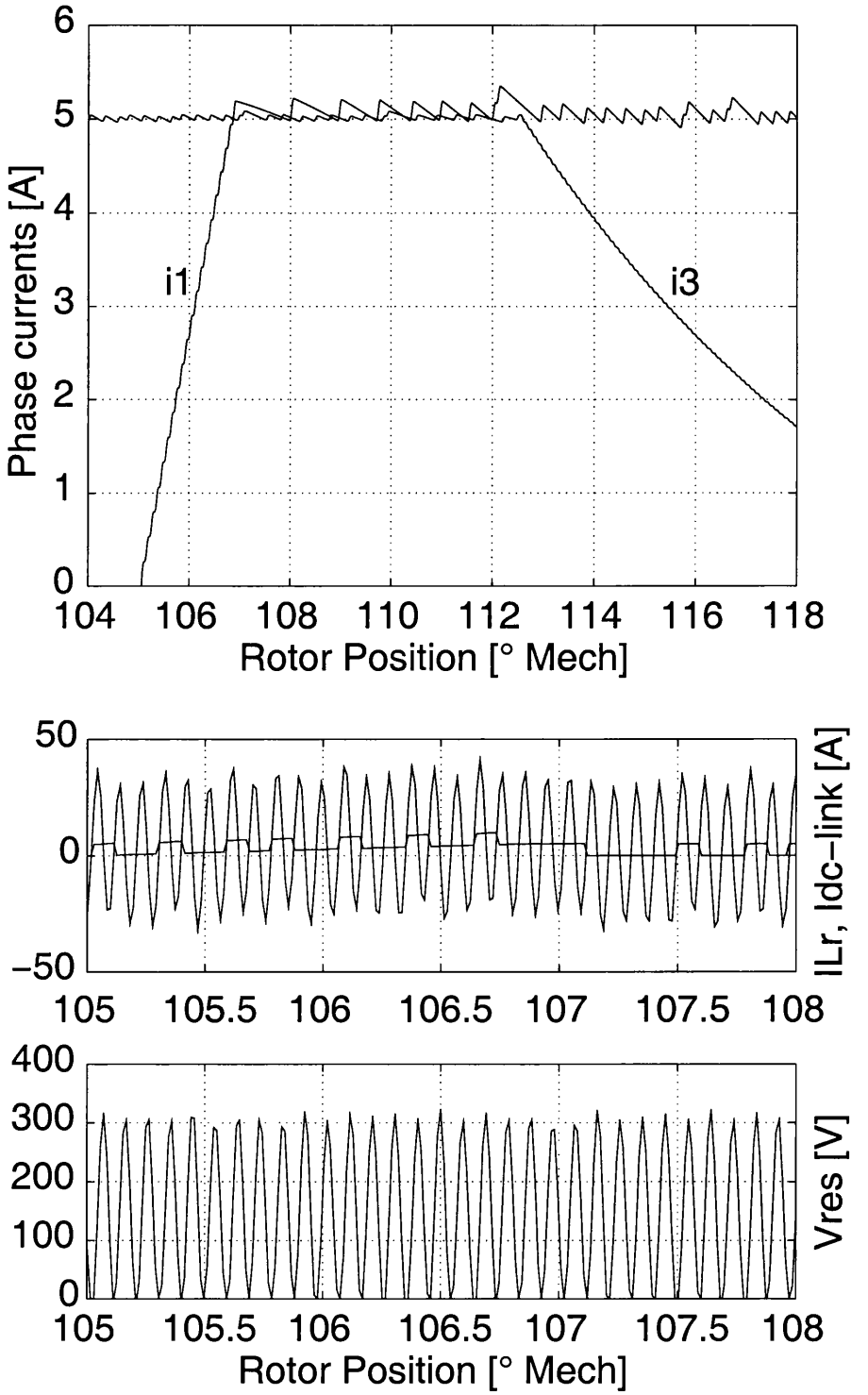

Figure A.11: Waveforms of RDCL with Soft chopping, (top) phase currents, (center) L_r and dc-link current, (bottom) resonant link voltage.

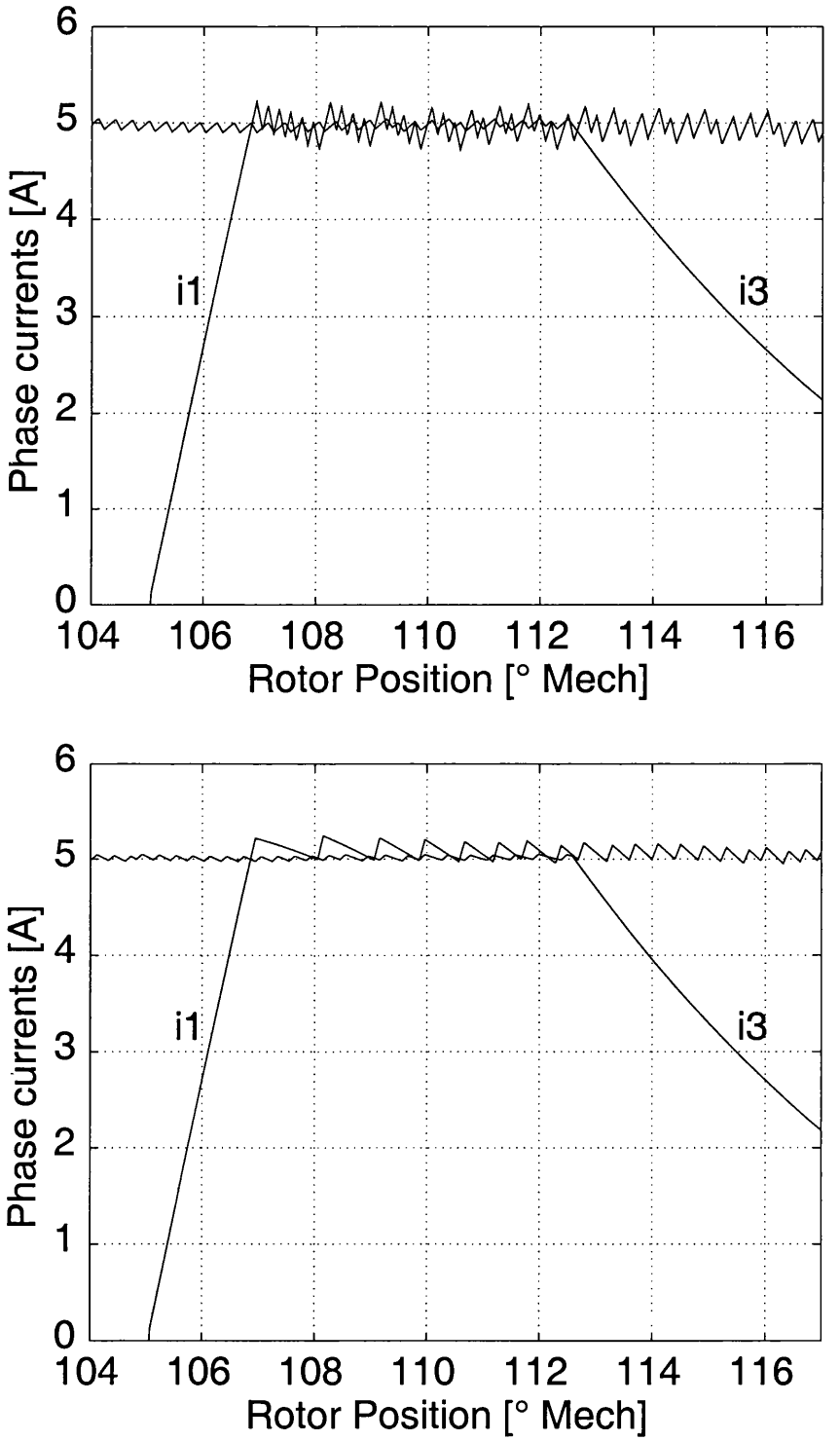

Figure A.12: Top: Waveforms of hard chopping with fixed dc-link voltage, Bottom: Waveforms of soft chopping with fixed dc-link voltage.

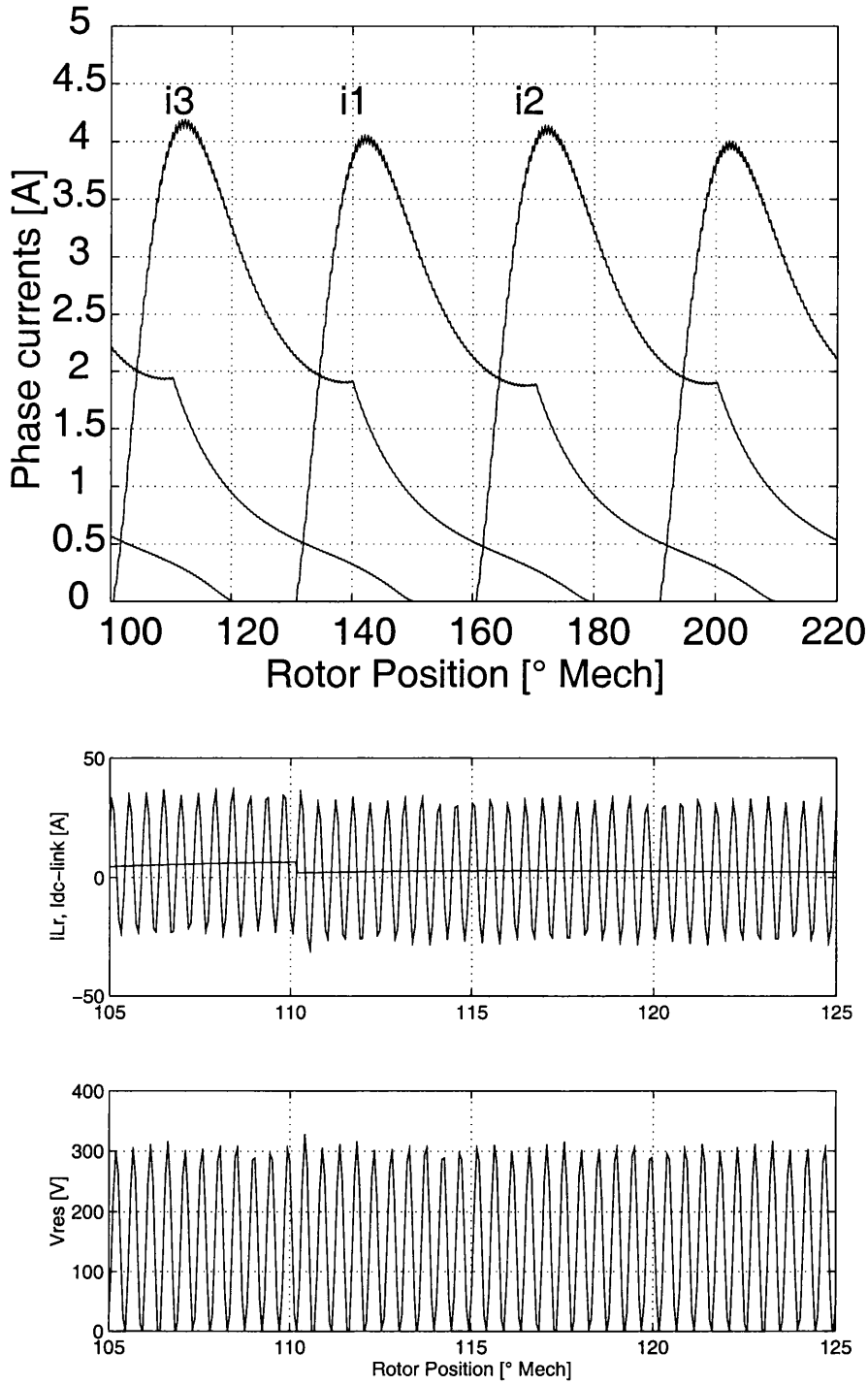

Figure A.13: Waveforms of RDCL with single pulse, (top) phase currents, (center) L_r and dc-link current, (bottom) resonant link voltage.

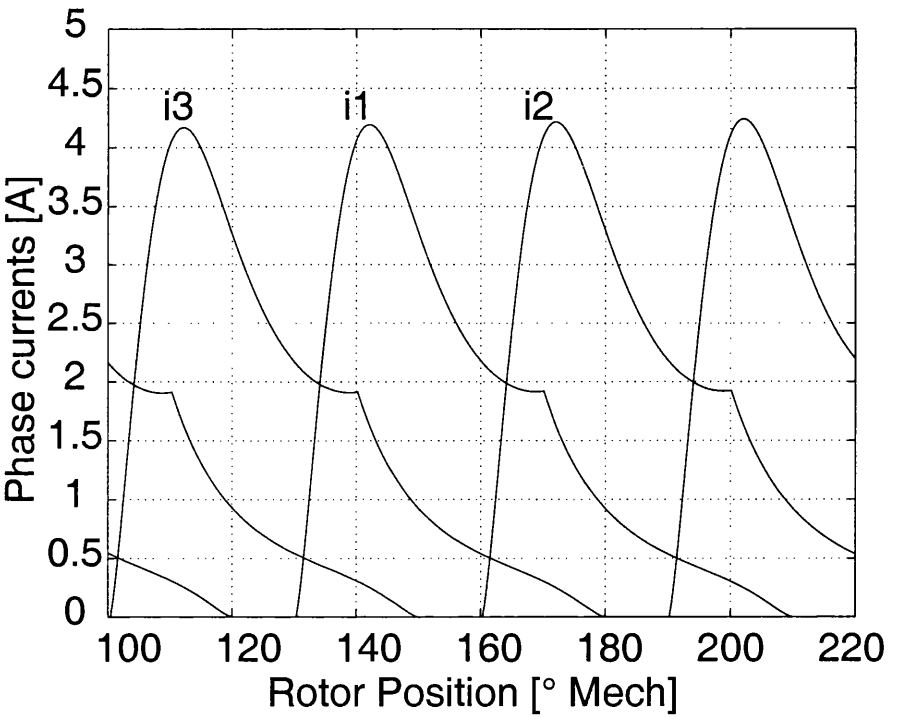

Figure A.14: Waveform of single pulse with constant dc-link voltage.

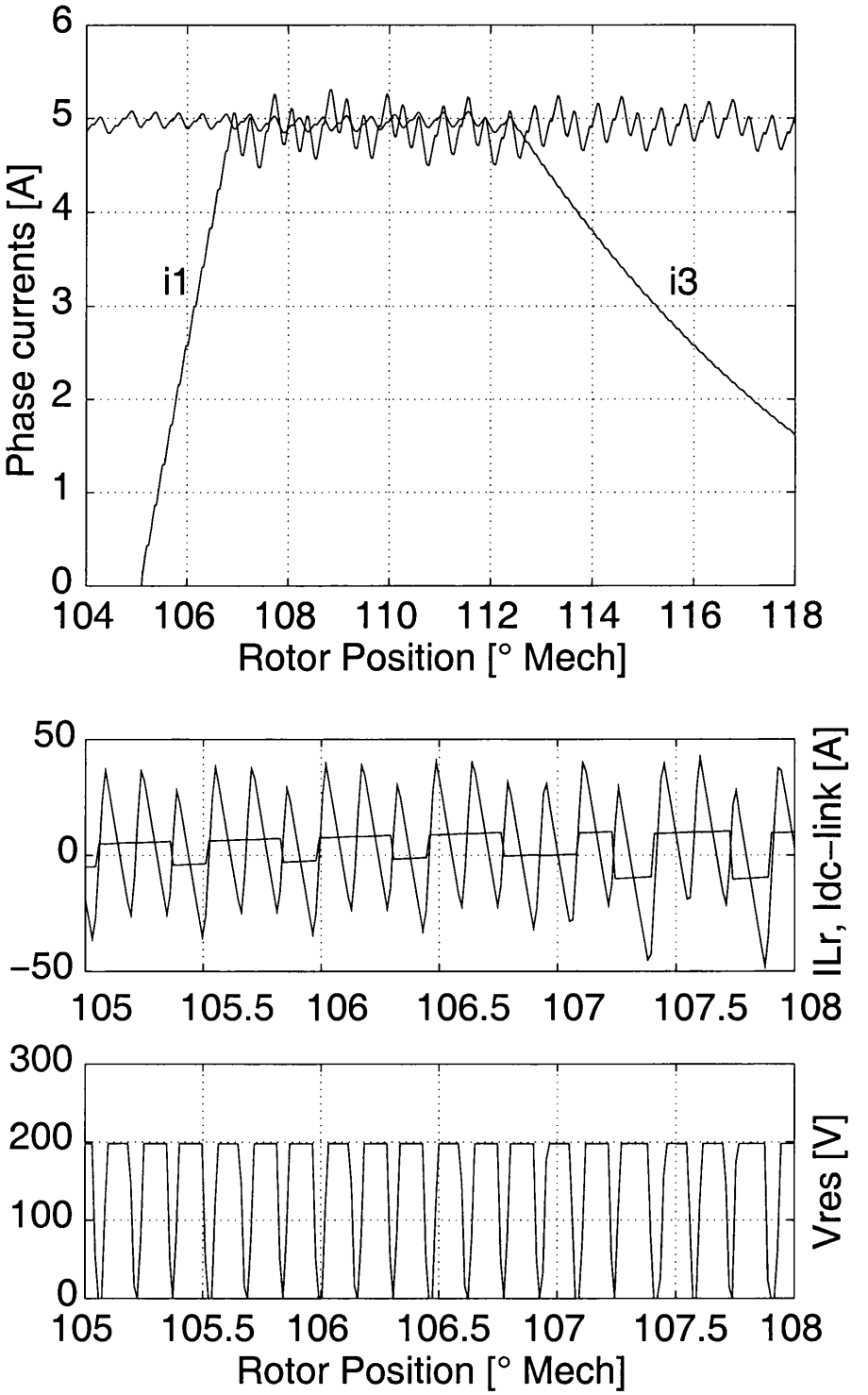

Figure A.15: Waveforms of ACRDCL with Hard chopping, (top) phase currents, (center) L_r and dc-link current, (bottom) resonant dc-link voltage.

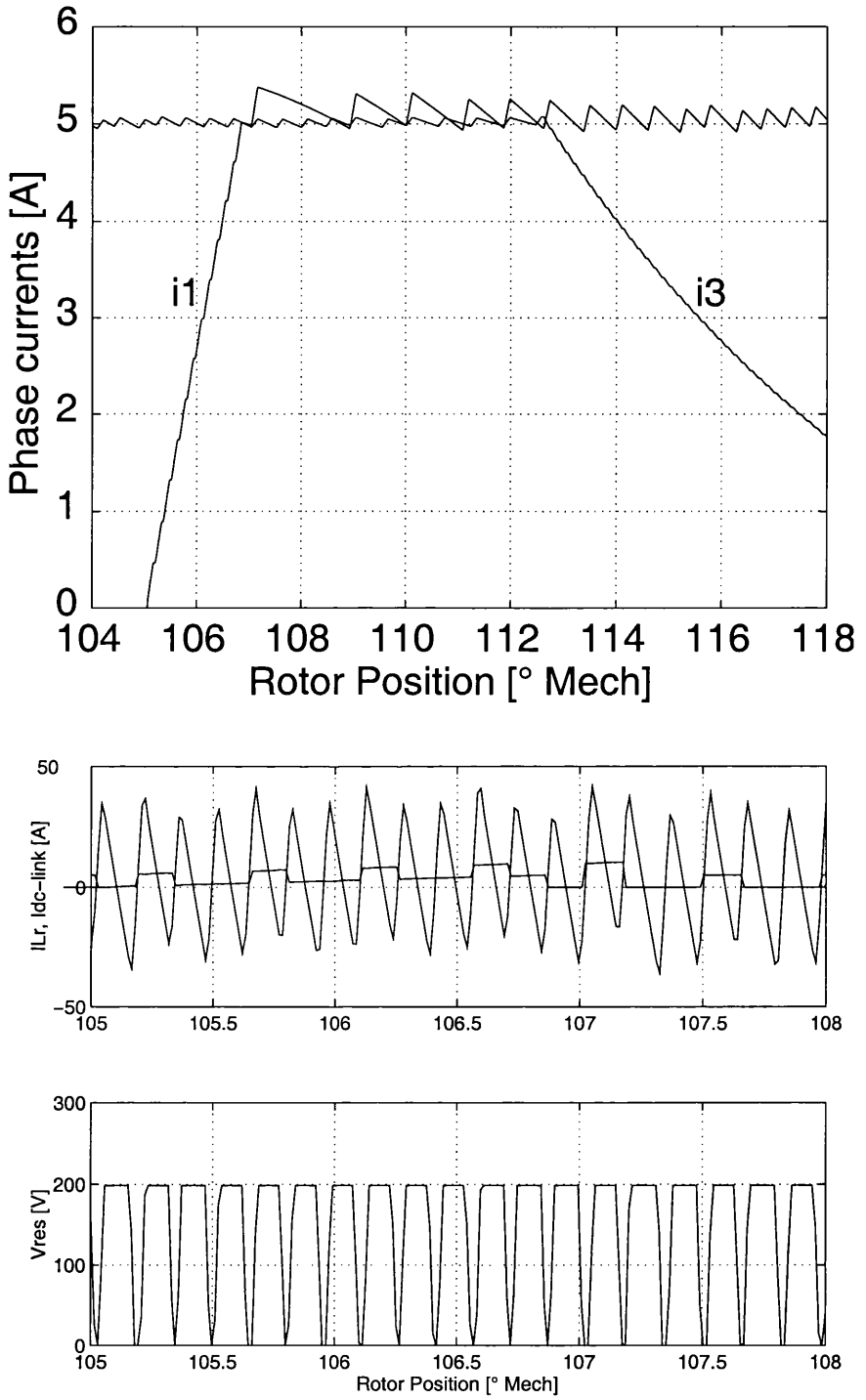

Figure A.16: Waveforms of ACRDCL with Soft chopping, (top) phase currents, (center) L_r and dc-link current, (bottom) resonant link voltage.

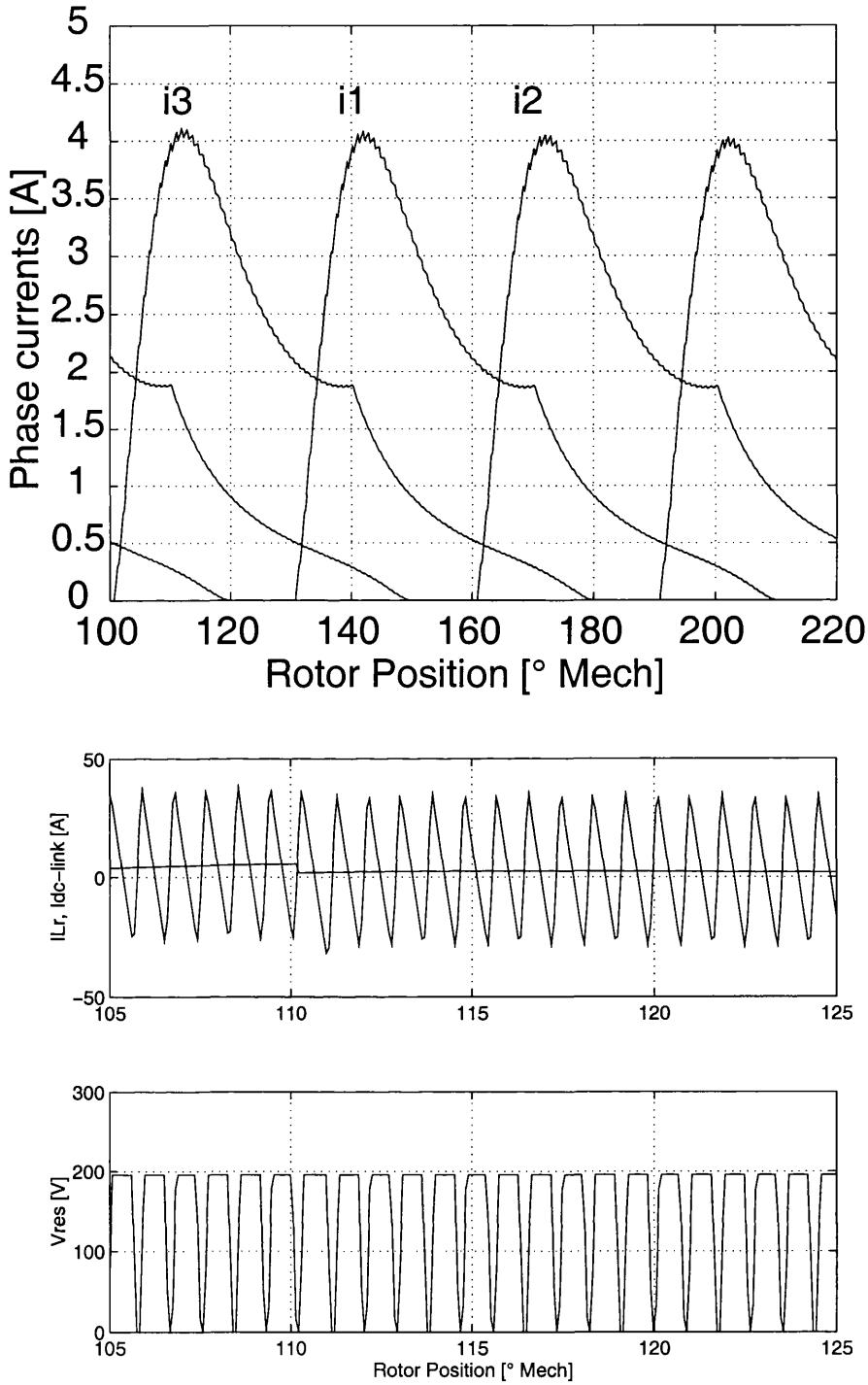

Figure A.17: Waveforms of ACRDCL with single pulse, (top) phase currents (center) L_R and dc-link current, (bottom) resonant link voltage.

Phases	4
N_s	8
N_r	6
Stator pole-arc	22.6^o
Rotor pole-arc	23^o
Air-gap	$0.3 \pm 0.01mm$
Phase resistance	$0.3 \pm 0.10\Omega$
Stator OD	$120.7 \pm 0.01mm$
Stator ID	$96.8 \pm 0.01mm$
Rotor OD	$60.0 \pm 0.01mm$
Rotor ID	$43.2 \pm 0.01mm$
Stack length	$75.0 \pm 0.01mm$
Max. inductance	9.15mH
Min. inductance	1.45mH
Rated voltage	270 V
Rated power	3 hp (2.2kW)

Table A.1: 4 phase 8/6 SR Motor ratings

A.2.2 Real time implementation

In order to verify the functionality of the proposed ACRDCL-SR inverter topology and confirm the simulation results, the ACRDCL-SR inverter was built to control a 4 phase 8/6 SRM. Table A.1 shows the motor rating, and the resonant circuit components are shown in Table A.2. The dc source voltage V_{dc} is 100V and the C_c is pre-charged up to 30V. The ACRDCL resonant frequency is 60 kHz with a clamp constant $K = 1.3$, i.e. 130V clamp voltage. Fig.A.18 is a picture of the ACRDCL and the inverter used.

The controller of the ACRDCL is made using a hybrid circuit, (i.e. analog and digital control), and the SRM control is based on the microcontroller MC68332-FPGA platform, basically the same hardware controller described in subsection 4.5.1. The required signals to be measured in the ACRDCL are:

- Voltage in the dc-link V_{res}.
- Current in the resonant inductor i_{Lr}.

Comp.	Value	Material
L_r	48μH	iron-powdered E-core, flat copper foil winding
C_r	50nF 600V	polyropylene
C_c	1500μF 385V	electrolyte
Toshiba IGBT	1200V 100A	MG100Q2YS40

Table A.2: Components of the ACRDCL.

- Current in the load i_{load}.
- Current in the clamp capacitor i_{clamp}.
- Voltage in the clamp capacitor V_{clamp}.

The control signal and the resonant waveforms are shown in Fig.A.19 under no load, i.e. $i_{load} = 0$. These signal are processed fully analog to control the ACRDCL as follows. When V_{res} is zero (or close to zero), the signal V_z goes high and S_{dc} is turned on with the rising edge, $G_{S_{dc}}$ is the gate signal for S_{dc}, this switch is on until the rising edge of the signal I_m, which goes high when $(i_{Lr} - i_{load}) > i_{ref}$ $(i_{ref} = 2.5A)$. At this time the tank resonates and the resonant voltage increases until reaches the clamp voltage, where the clamp diode D_c starts conducting, at this moment the I_c signal goes high and the PI signal goes low. While D_c is conducting, S_c can be turned on any time. S_c is turned off when the PI signal goes high. G_{S_c} is the gate signal for S_c.

The control signals V_z, I_m, I_c and PI are obtained through a fully analog circuit. The PI signal is the output of the Proportional-Integral control to regulate the voltage in the clamp capacitor. These signals are sent to the FPGA, where the switching signals are generated for S_{dc} and S_c. There are some protection signals to avoid noise from the resonant circuit. The protection signals enable the control signals as follows. After the rising edge of I_m, there is a fixed time t_1 where any glitches from I_c are neglected, the signal I_c is enabled by "*Enable on* S_c" signal. This signal is reset by the falling edge

of I_c. The enable signal "*Enable off* S_c" goes high after t_2 and enables the turn off of S_c by *PI*. "*Enable off* S_c" is reset when S_c is turned off. S_c is not allowed to be turned off in the period of t_2. This is to make sure that the resonant voltage reaches zero. Once S_c is turned off, it should pass a time t_3 until "*Enable on* S_{dc}" goes high which enables the control signal V_z. This flag is reset with the turn on of S_{dc}, where the cycle starts again.

Fig.A.20 (top) shows a period of the resonant voltage V_{res}, the current in S_{dc}, D_c, S_c, and the gate signal $G_{S_{dc}}$ for S_{dc} in steady state with no load connected. It is clear that when V_{res} is close to zero, the IGBT S_{dc} is turned on until there is enough energy in L_r and therefore there is a small peak current flowing through S_{dc}. After, the L_rC_r tank resonates and V_{res} increases until reaches the clamp voltage 130V. At this time the clamp diode D_c starts conducting, note that the current oscillates due to internal stray inductance of the diode, this oscillations show up in V_{res} as well. While D_c conducts, the IGBT S_c is turned on with zero voltage. At some point i_{clamp} reverses and S_c starts conducting. S_c is turned off until the net energy transferred to C_c is zero. Once S_c is turned off, the tank resonates and V_{res} decreases to zero, where the sequence starts again. The resonant current in L_r is depicted in the bottom graph, together with V_{res} and $G_{S_{dc}}$. It is clear that the current decreases with a constant slope when the voltage is clamped. Fig.A.21 shows several cycles of the resonant waveforms under the same conditions.

a)

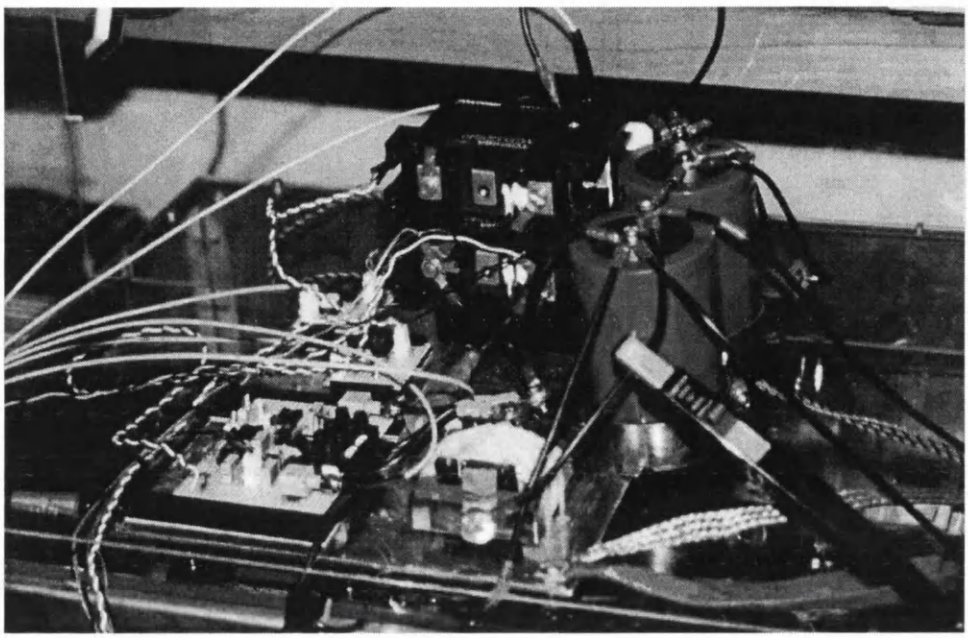

b)

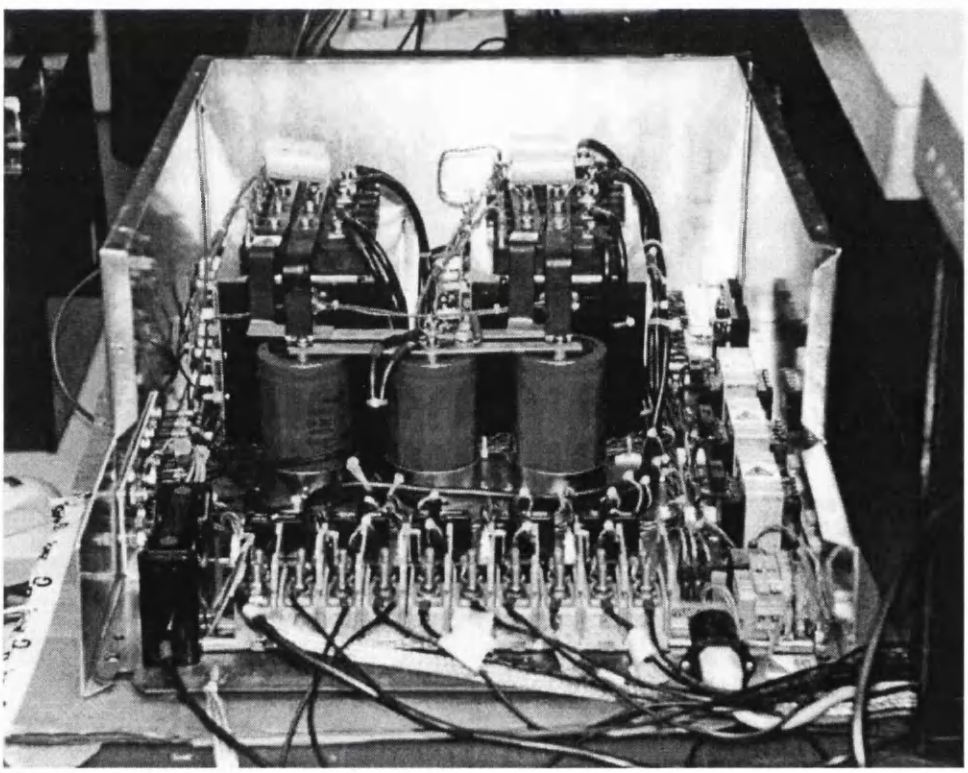

Figure A.18: Pictures of the active clamp resonant dc-link and inverter, a: ACRDCL circuit, b) 4 phase SR inverter.

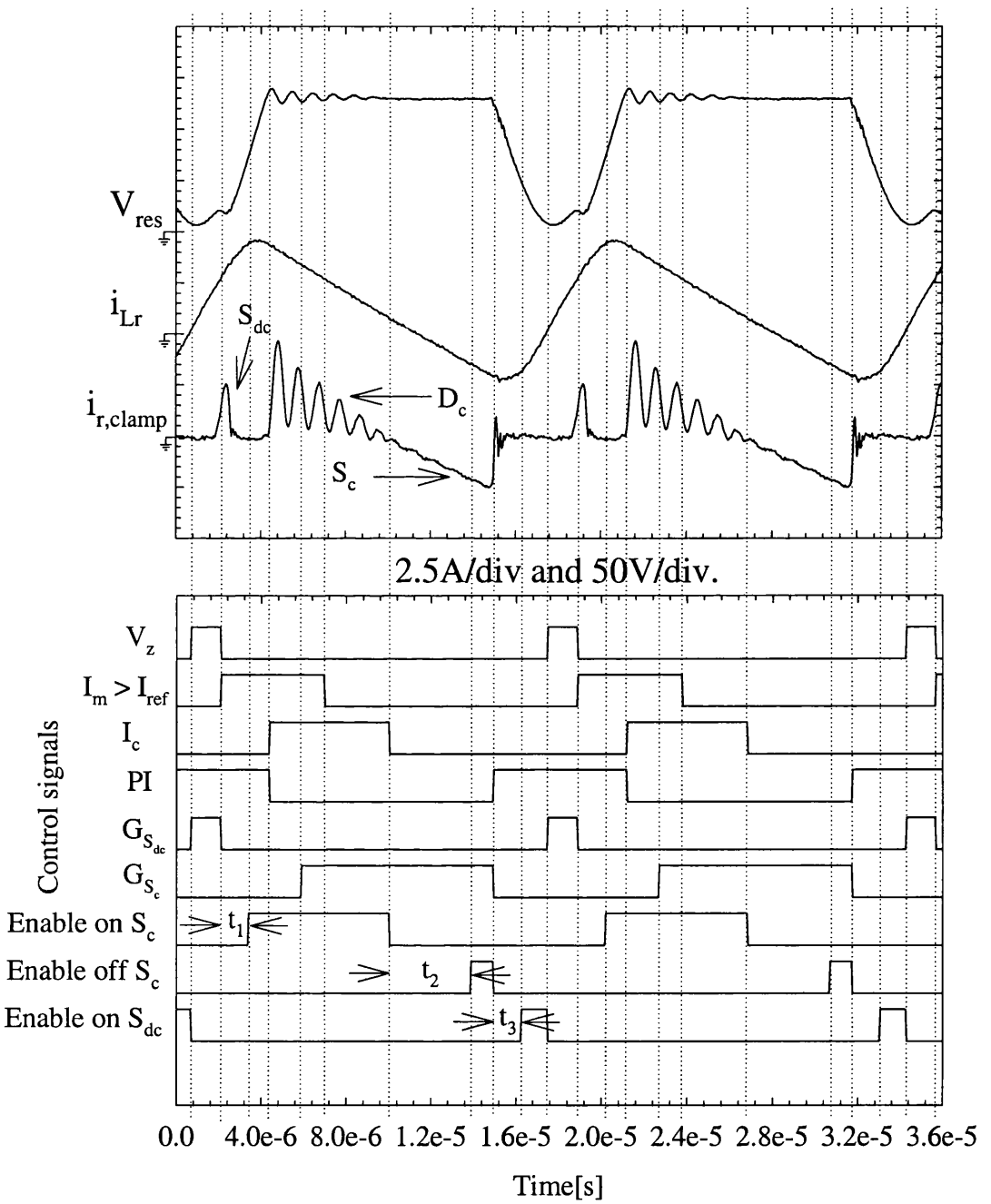

Figure A.19: Control signal of ACRDCL.

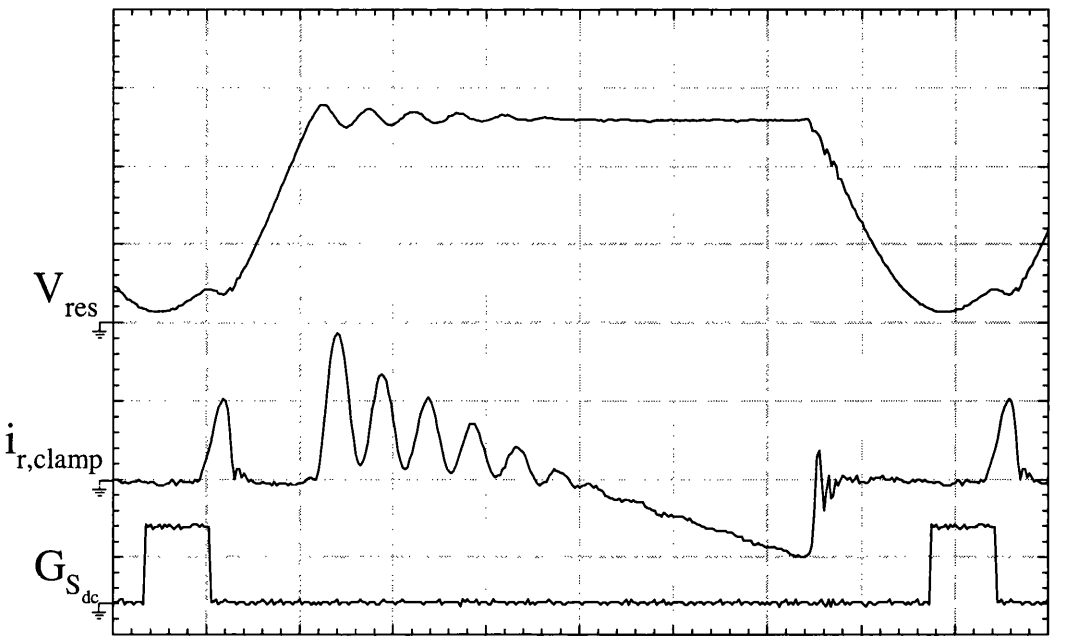

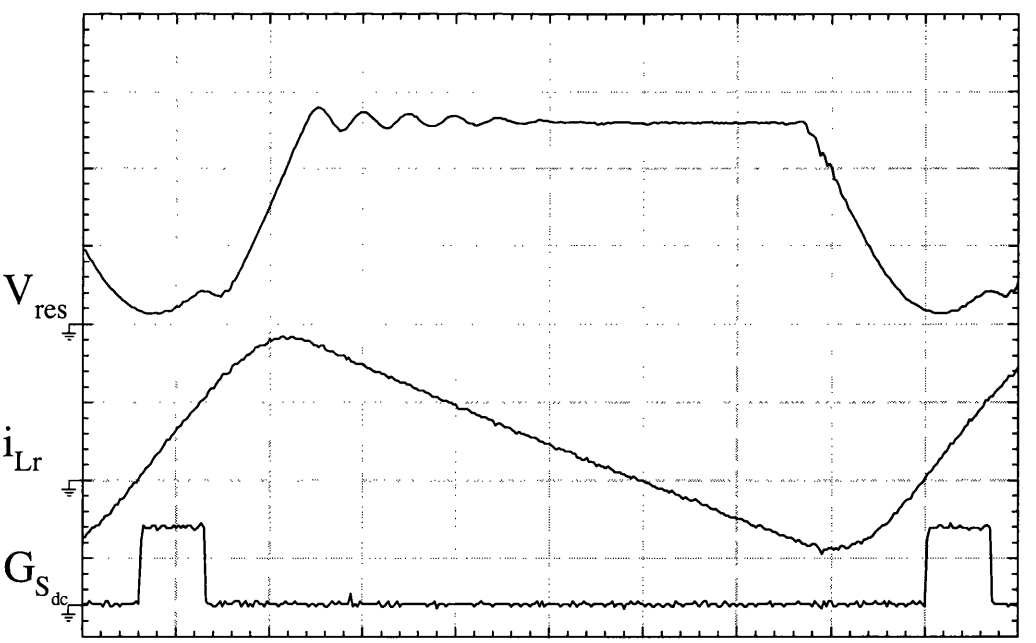

Figure A.20: Zoom in of the resonant waveforms, Top: Resonant voltage, current in L_r and gate signal for S_{dc}, Bottom: Resonant voltage, i_{clamp} and gate signal for S_{dc}.

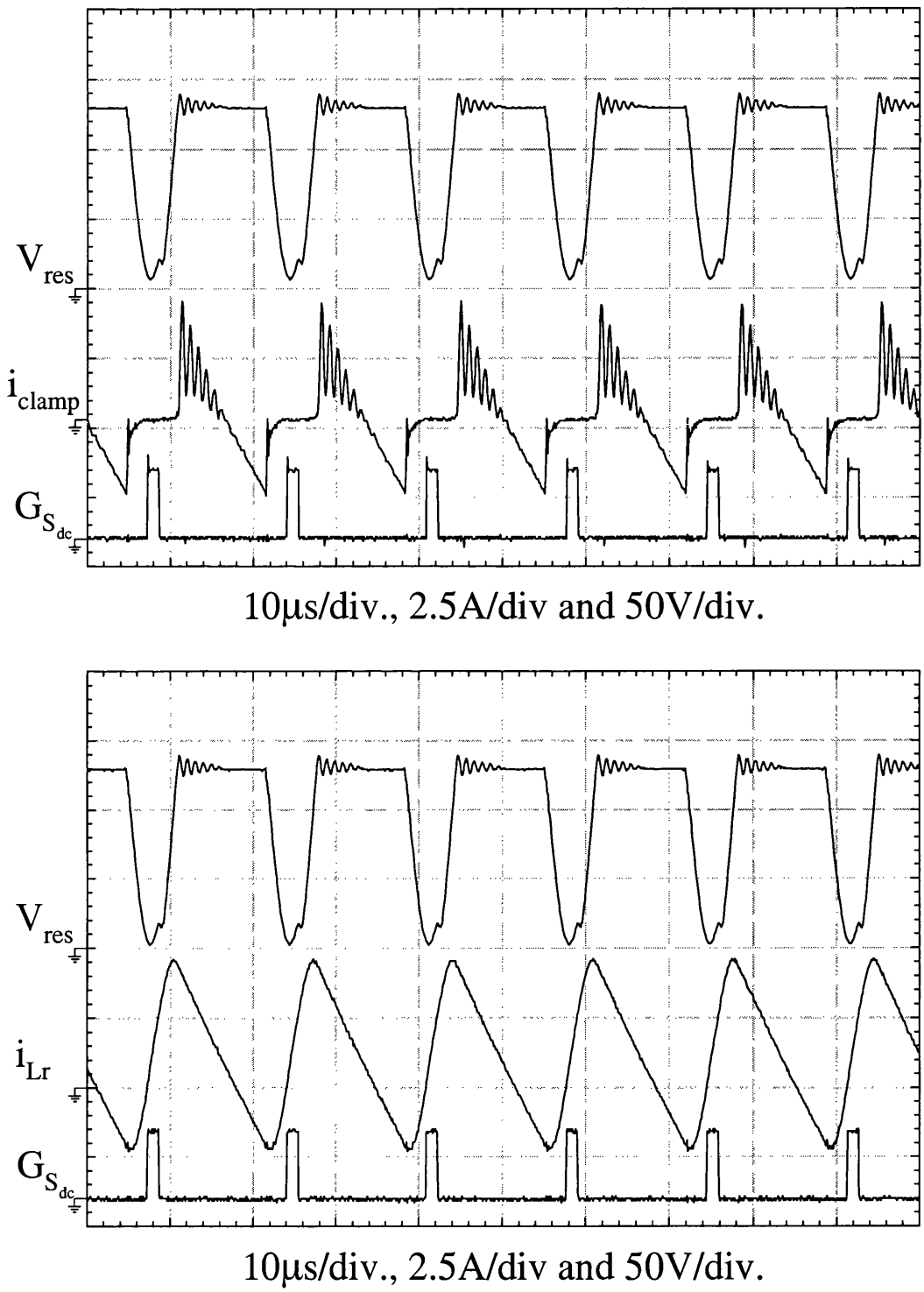

Figure A.21: Resonant waveforms Top: Resonant voltage, current in L_r and gate signal for S_{dc}, Bottom: Resonant voltage, i_{clamp} and gate signal for S_{dc}.

A.2.3 ACRDCL experimental results

A range of tests were carried out in order to investigate the performance of the ACRDCL-SR inverter. The tests include current regulation with soft chopping and hard chopping with no motion and different speeds, and single pulse operation. The picture of the experimental setup and test-rig are shown in Fig.A.22. The SR motor is loaded using a PM motor connected to a bank of resistors.

Experiments of current regulation with no motion were carried out initially. Only phase one is energised and the current is regulated at 15A with soft-chopping and hard-chopping. Fig.A.23 (top) depicts the results when using soft chopping. We observe that in the positive transient of the load current (from 0A to 15A), the zero voltage period is extended. On the other hand, the period of clamp voltage is increased in the negative transient of the load current (from 15A to 0A). Note that in this transient there is a large amount of current pumped into the clamp capacitor, and therefore D_c conducts for a long period of time. Ideally, the same conduction time of D_c should be for S_c in order to keep constant the voltage in the clamp capacitor over a resonant cycle, however, the conduction period of S_c can be controlled by a simple PI controller over several resonant cycles in order to maintain constant the voltage in the clamp capacitor. This is the way that ACRDCL has been implemented. Note that the period, where S_c conducts, varies in every resonant cycle. Fig.A.23 (bottom) depicts the results obtained using hard chopping when the current is regulated at 15A in phase one. In this case the transients are twice as big than when using soft chopping. Note that the load current changes from being positive to negative with a step of 30A. This bigger transient makes obviously the zero voltage period and the clamp voltage period longer, and therefore affecting the resonant frequency. It is note worthy that the current in L_r follows the current in the load and follows the same trend as the simulation result obtained in Fig.A.7.

Fig.A.24 shows soft-chopping (top) and hard-chopping (bottom) current regulation, respectively. The rotational speed of the 4-phase SR motor is kept constant at 1700

a)

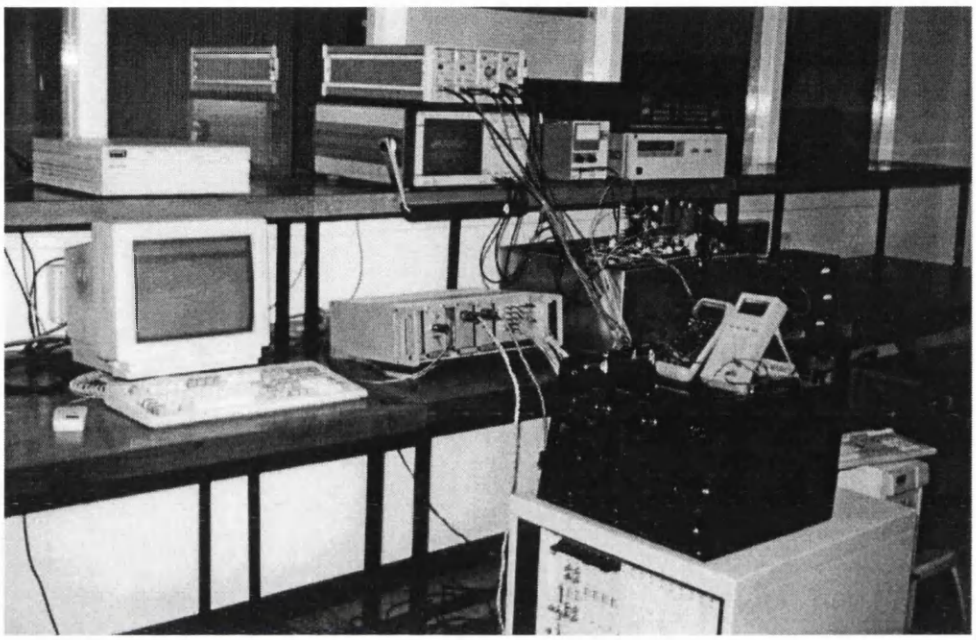

b)

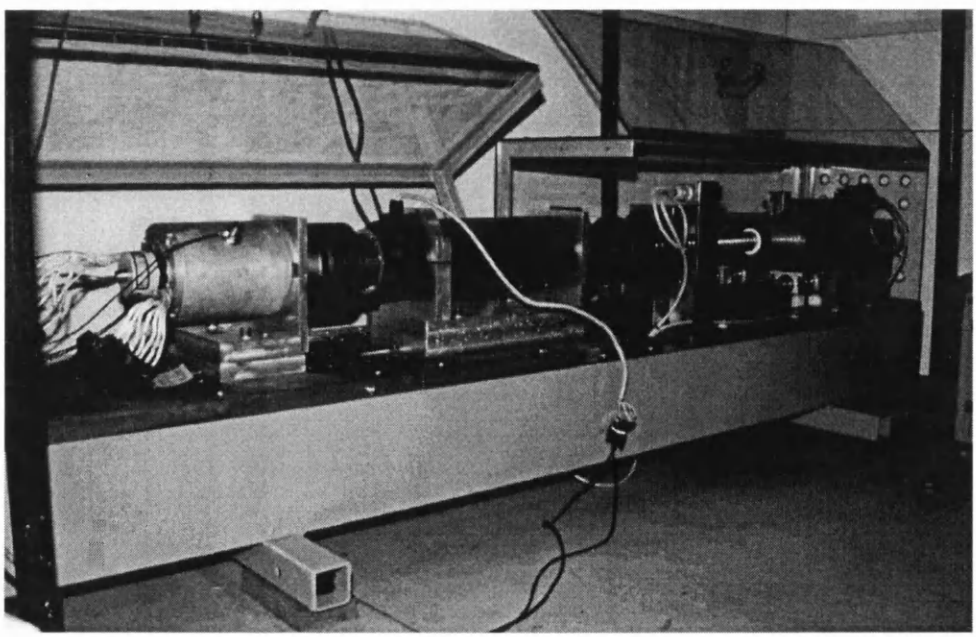

Figure A.22: Pictures of the hardware setup, a: Overview of controller and measurement equipment, b) Test-rig.

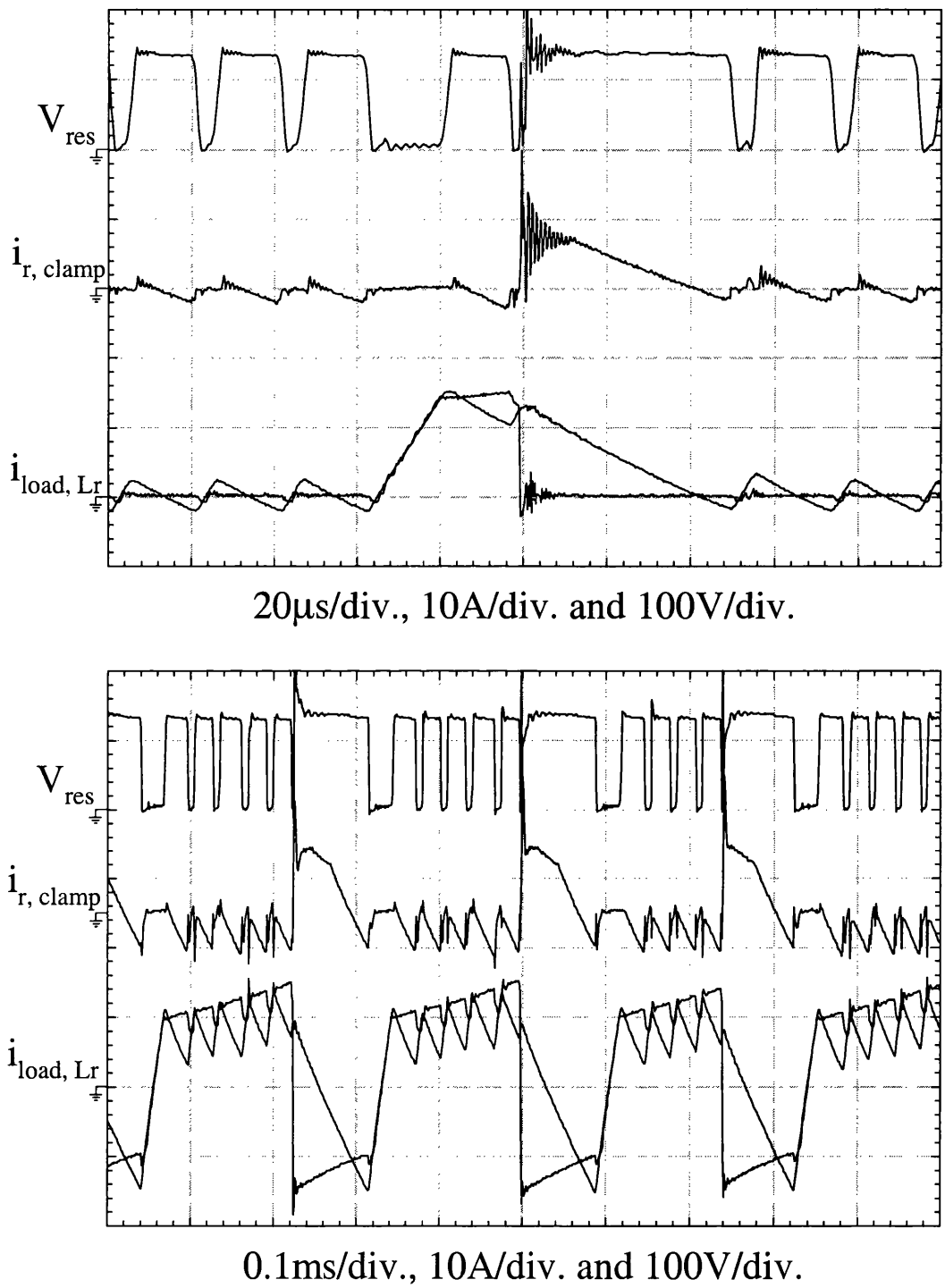

Figure A.23: Current regulation at 15A at standstill, Top: Soft chopping, Bottom: Hard chopping.

rpm, with a reference current level of 15A, the commutation angles are $\theta_{on} = 32^o$ and $\theta_{off} = 44^o$. Two phase currents and the voltage in phase 1 are shown. It can be observed that in soft-chopping when both transistors are conducting, one or more resonant periods appear in the phase voltage and when only one transistor is off, the (constant) zero-voltage loop is applied to the motor phases instead of the (negative) resonating voltage.

In hard-chopping, multiple resonant pulses appear in the phase voltage waveforms when both transistors conduct. However, when they are turned-off and the phase current freewheels back to the supply, the resonant period is extended, because the clamp-diode D_c conducts longer. This in turn causes increased current ripple as $-1.3 \cdot V_{dc}$ is applied to the winding and the effective current regulation band width (BW) is reduced. Soft-chopping has the advantage of reducing the reactive power exchanged between the supply and the motor windings, due to its zero-voltage loop. In other words, the load current in soft-chopping changes between $+i_{load}$ and 0 in contrast to hard-chopping that changes between $\pm i_{load}$. The effect may be reduced if the freewheeling diodes D1, D3, D5 and D7 are connected direct by the clamp capacitor. In this case, hard-chopping may behaves similar to soft-chopping. When the phase is turned off phase current freewheels through the diodes and the phase voltage is $-V_{res}$. Both graphs show that the first resonant cycle, after the turn off of the phase, is longer than the following ones, again because of the transient in load current. Clearly, soft-chopping results in "smoother" ripple currents.

A zoom of soft-chopping current-regulation with excitation overlap is shown in Fig.A.25 (top). The commutation angles are $\theta_{on} = 32^o$ and $\theta_{off} = 52^o$ with a reference current level of 15A at 1600 rpm. Here is clear that the clamp period (i.e. when $V_{res} = 1.3 \cdot V_{dc}$) is increased when the load current changes from $+i_{load}$ to $-i_{load}$ (a negative step in i_{load}). In contrast, after a positive step in load current the zero resonant voltage period is increased (this is a well know characteristic of the ACRDCL). The current in the resonant inductor i_{Lr} follows the load current within a band of $\pm$10A.

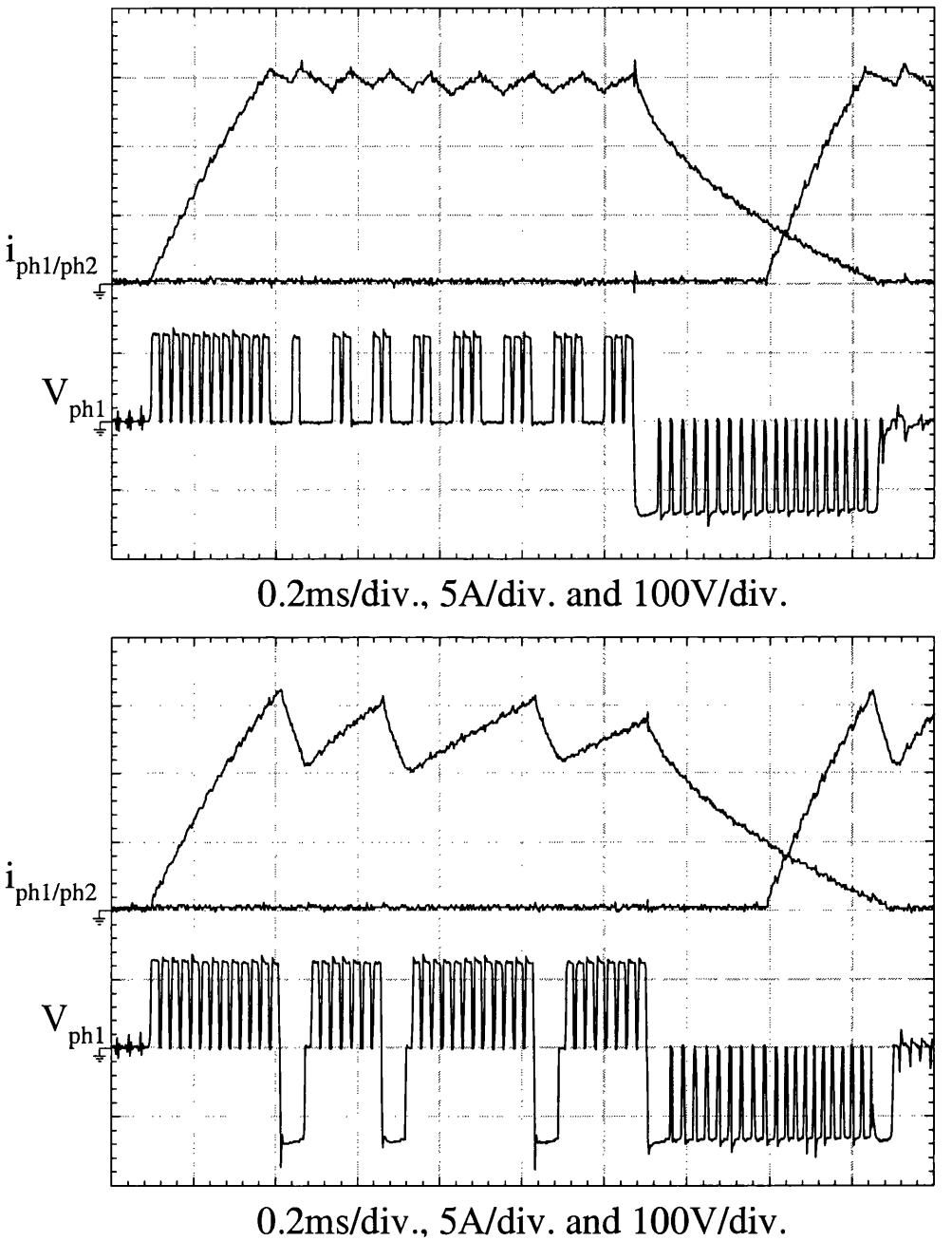

Figure A.24: Soft-chopping (top), hard-chopping (bottom) current regulation with soft-switching.

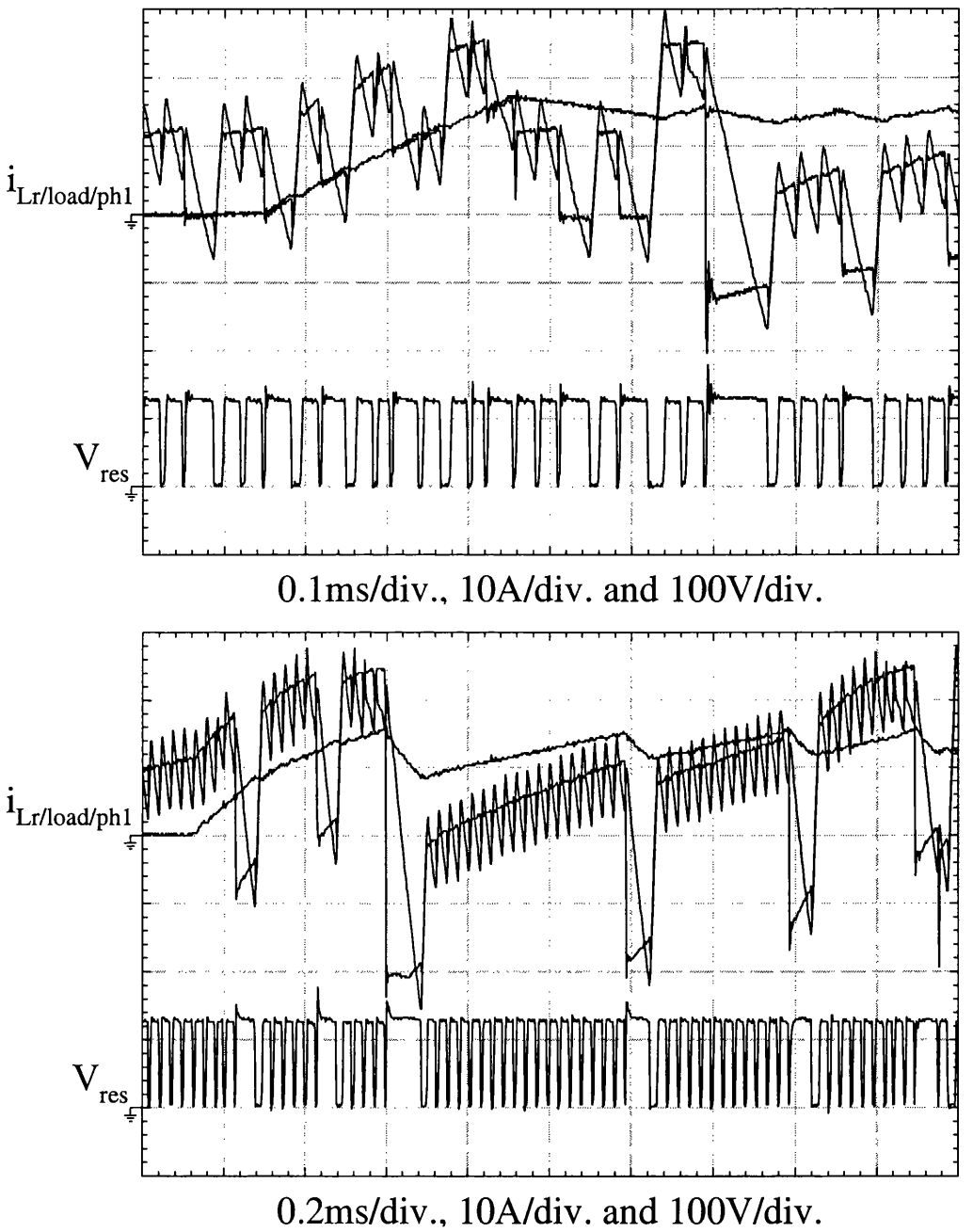

Figure A.25: Zoom of soft-chopping (top), hard-chopping (bottom) current regulation with soft-switching and excitation overlap.

This range depends on how much energy is stored in L_r when S_{dc} is on, the design of the L_rC_r tank, and the reactive power exchanged between the resonant circuit and the motor windings. The bottom graph of Fig.A.25 depicts a zoom of hard-chopping current-regulation with excitation overlap at 1700 rpm. Here the changes in load current are twice than of soft-chopping, making the resonant clamp periods longer. Also it can be observed that the current in the resonant inductor follows the load current in a band of $\pm$10A.

Fig.A.26 depicts soft-switching (top graph) and hard-switching (bottom graph), respectively, for soft-chopping. The commutation angles are $\theta_{on} = 32^o$ and $\theta_{off} = 44^o$ with a reference current level of 15A at 1700rpm. Clearly, there is no reduction in the quality of the current regulation, when applying soft-switching.

Soft-switching and hard-switching for hard-chopping are shown in Fig.A.27 top and bottom graph, respectively for the same commutation angles, reference current level and speed as before. It is observed that with soft-switching the current ripple is larger than in hard-switching due to the interchange of energy between the load and the resonant circuit. In other words, the effective inverter switching frequency is reduced by the long clamp period of the resonant voltage. The result is that hard-chopping operating with soft-switching gives a more peaky phase current waveform than when operating under hard-switching.

Phase current waveforms for single-pulse operation at 3150rpm (where the current regulator is running out of volts), with commutation angles $\theta_{on} = 30^o$ and $\theta_{off} = 50^o$, are depicted in Fig.A.28 top and bottom graph for soft-switching and hard-switching, respectively. The only noticeable difference is the high-frequency component in the soft-switched current waveform. An electrical cycle of phase current waveform and phase voltage for soft-switching with excitation overlap are shown in Fig.A.29 top and bottom graph for soft-chopping and hard-chopping, respectively. The commutation angles are $\theta_{on} = 32^o$ and $\theta_{off} = 52^o$ at 1000 rpm with a reference current level of 10A. These graphs demonstrate that ACRDCL-SR inverter behaves as the hard-switched

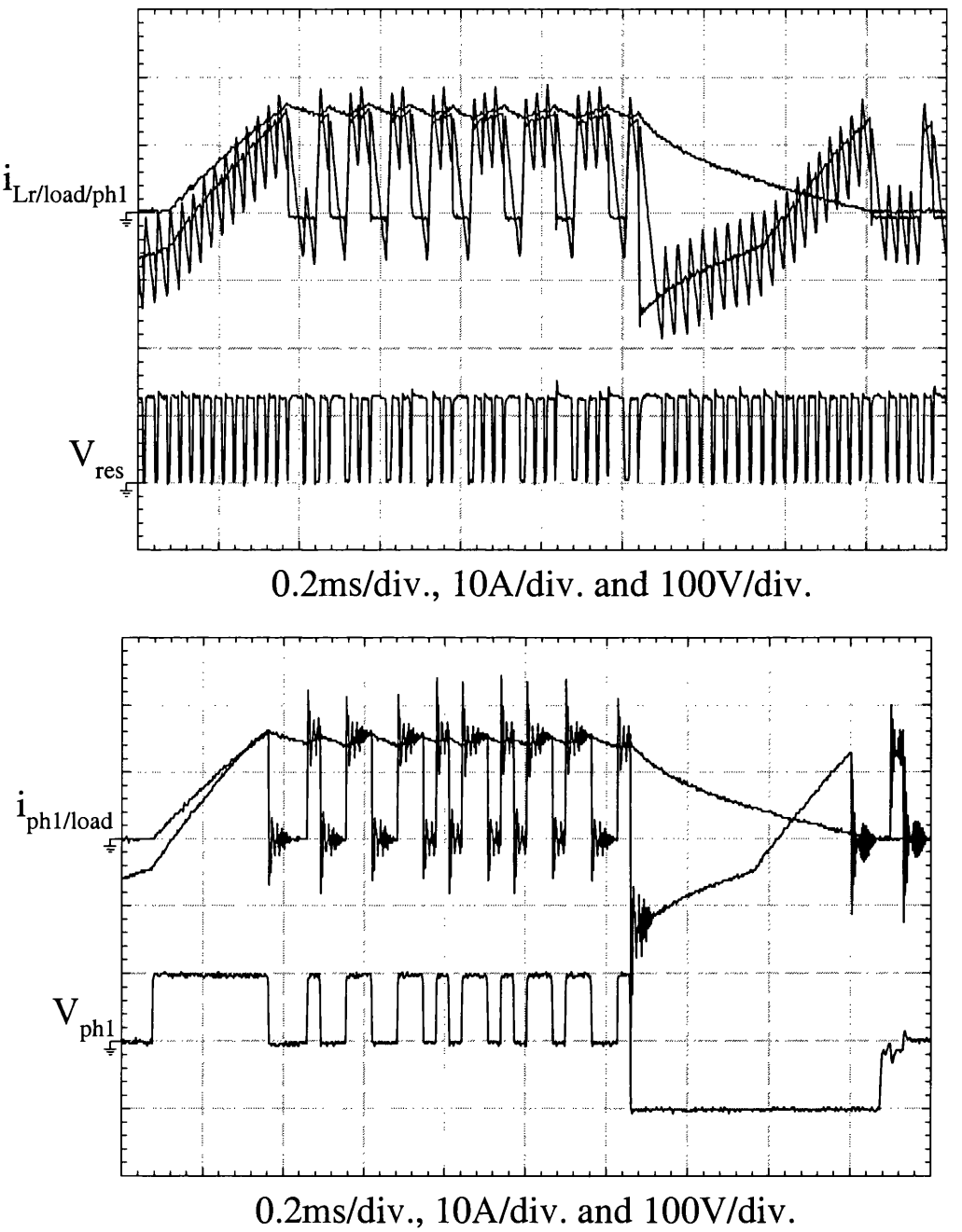

Figure A.26: Phase current with soft-chopping for soft-switching (top) and hard-switching (bottom).

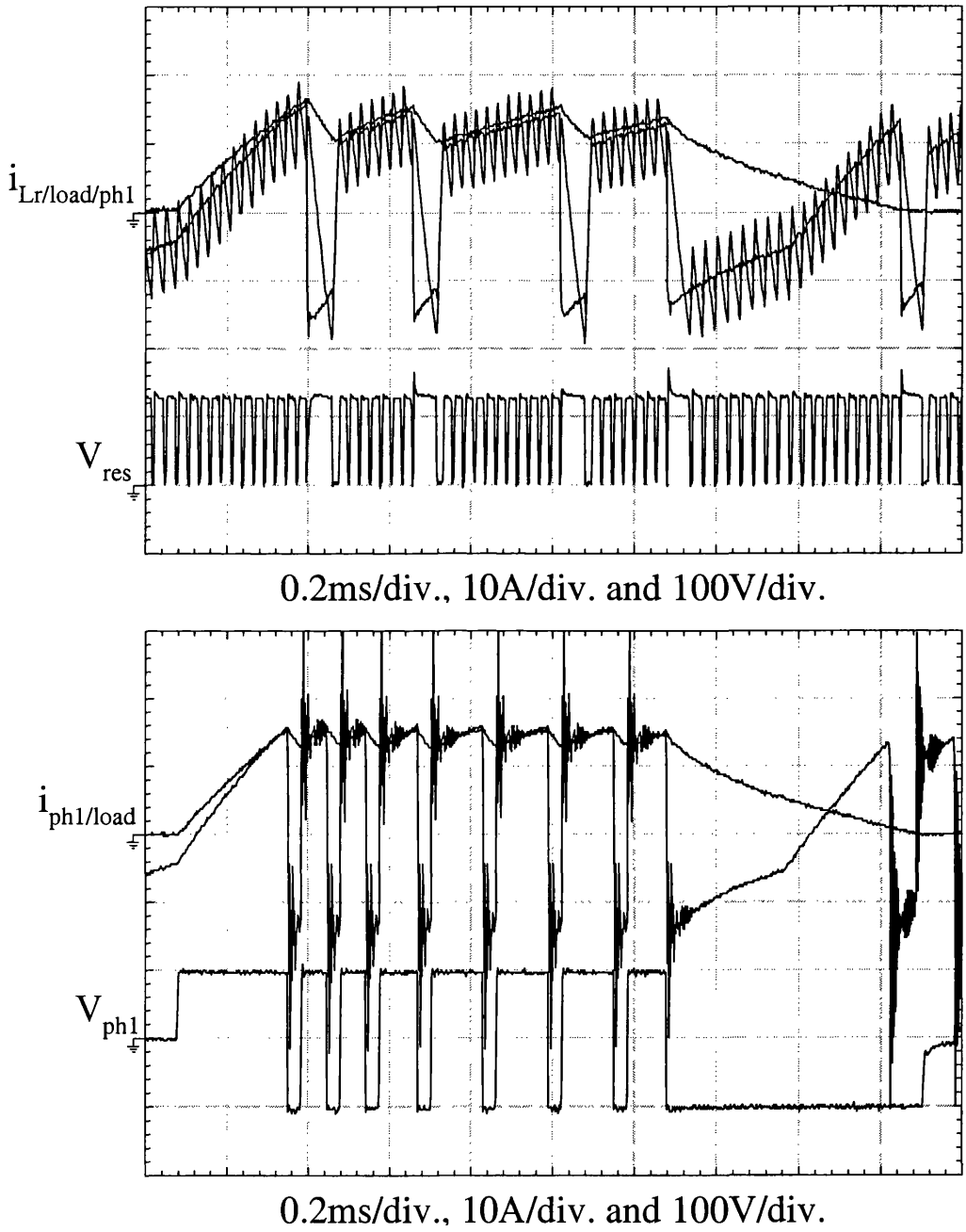

Figure A.27: Phase current with hard-chopping for soft-switching (top) and hard-switching (bottom).

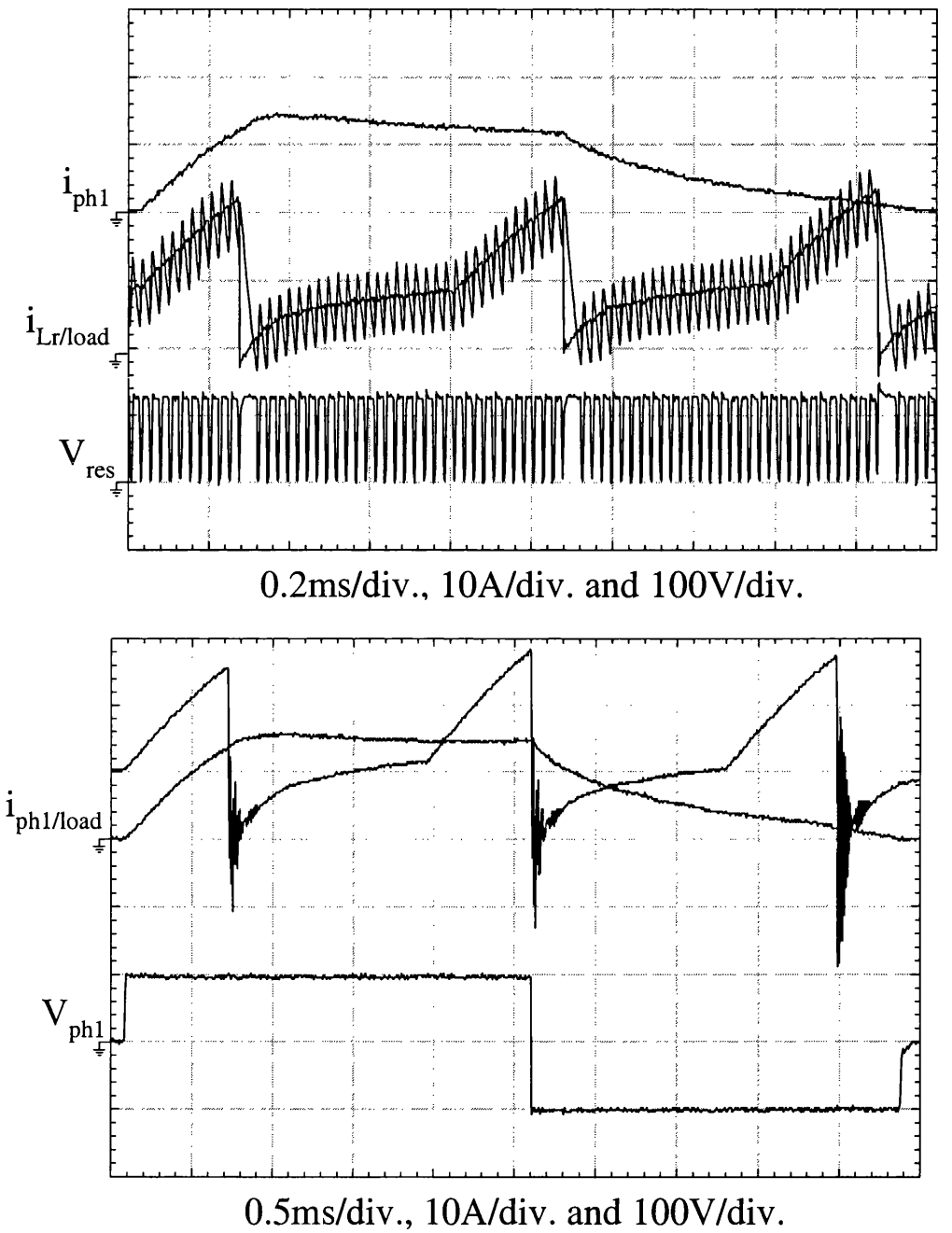

Figure A.28: Phase current in single pulse with soft-switching and hard-switching.

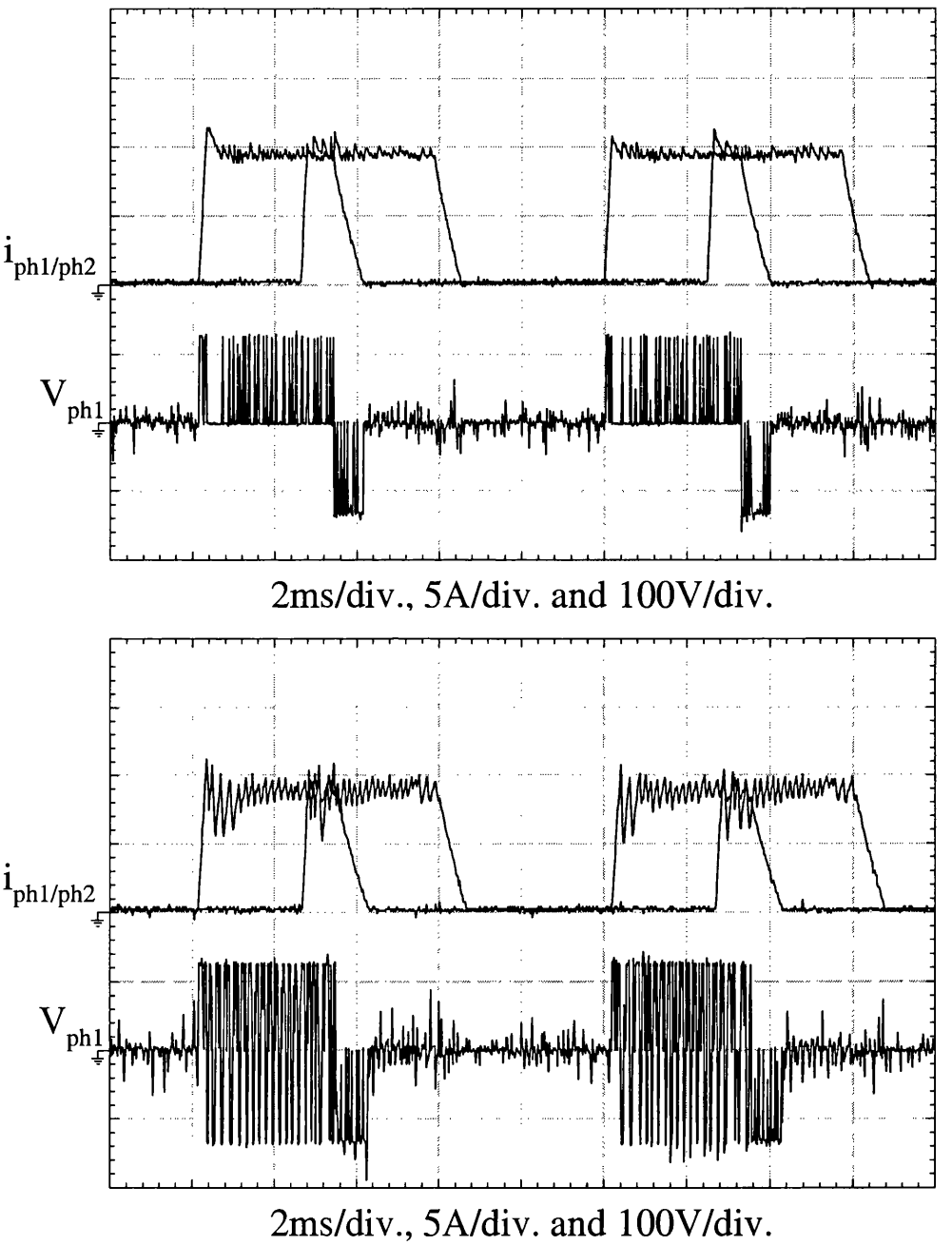

Figure A.29: Soft-chopping (top), hard-chopping (bottom), current regulation with soft-switching and excitation overlap.

inverter and that the ACRDCL does not compromise the performance of the SRM inverter.

Finally, the transient of the turn-on and turn-off in the IGBT of the inverter are shown in Fig.A.30 for soft-switching. The top graph depicts the $V_{IGBT} - i_{IGBT}$ locus, which shows very small switching losses. We observe that the turn-off transient has more losses than the turn-on transient, this is mainly due to the effect of long tail in the current at the turn-off. This is more clear in the bottom graph which shows the voltage and current waveform of the switch in the time domain. On the other hand, Fig.A.31 depicts the switching transient for hard-switching, the top graph shows the $V_{IGBT} - i_{IGBT}$ locus and we observe clearly that there is simultaneous voltage and current in both turn-on transient and turn-off transient which means high switching losses. The bottom graph shows the voltage and current waveform in the time domain, note that unlike the result of soft-switching, there is a spike in the current at turn-on, and a spike in the voltage at the turn-off, which produce high EMI.

From these results, it is clear that in soft-switching the stress on the transistor is much lower than in hard-switching. The result is that the switching losses are reduced significantly and therefore the overall efficiency may be expected to increase (assuming that the switching losses dominate the conduction losses). It should be noticed that the ACRDCL must be carefully designed and optimised together with the SR inverter so that the overall drive efficiency is increased.

A.2.4 Summary

A resonant dc-link front-end to the classic SRM inverter has been proposed. Simulations showed that the combination of RDCL or ACRDL with Delta modulation for SRM does not compromise the performance of current control for SRM drive, albeit the soft switching adds some control requirements.

The resonant dc-link front-end (ACRDCL) to the classic delta-modulated SRM

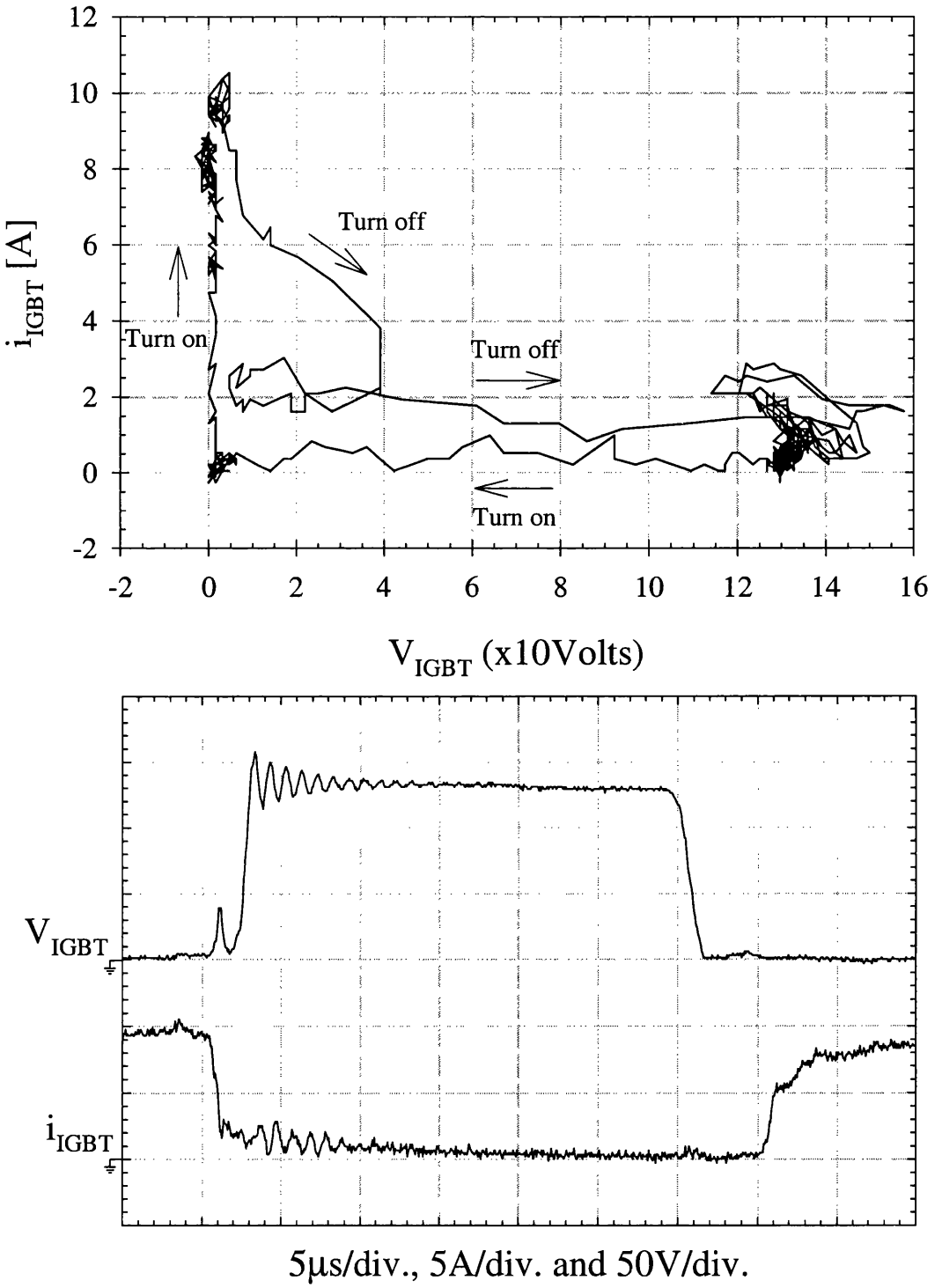

Figure A.30: Turn-on and turn-off with soft-switching, Top:$V_{IGBT} - i_{IGBT}$ switching locus for inverter's IGBT, Bottom: Voltage and current waveforms.

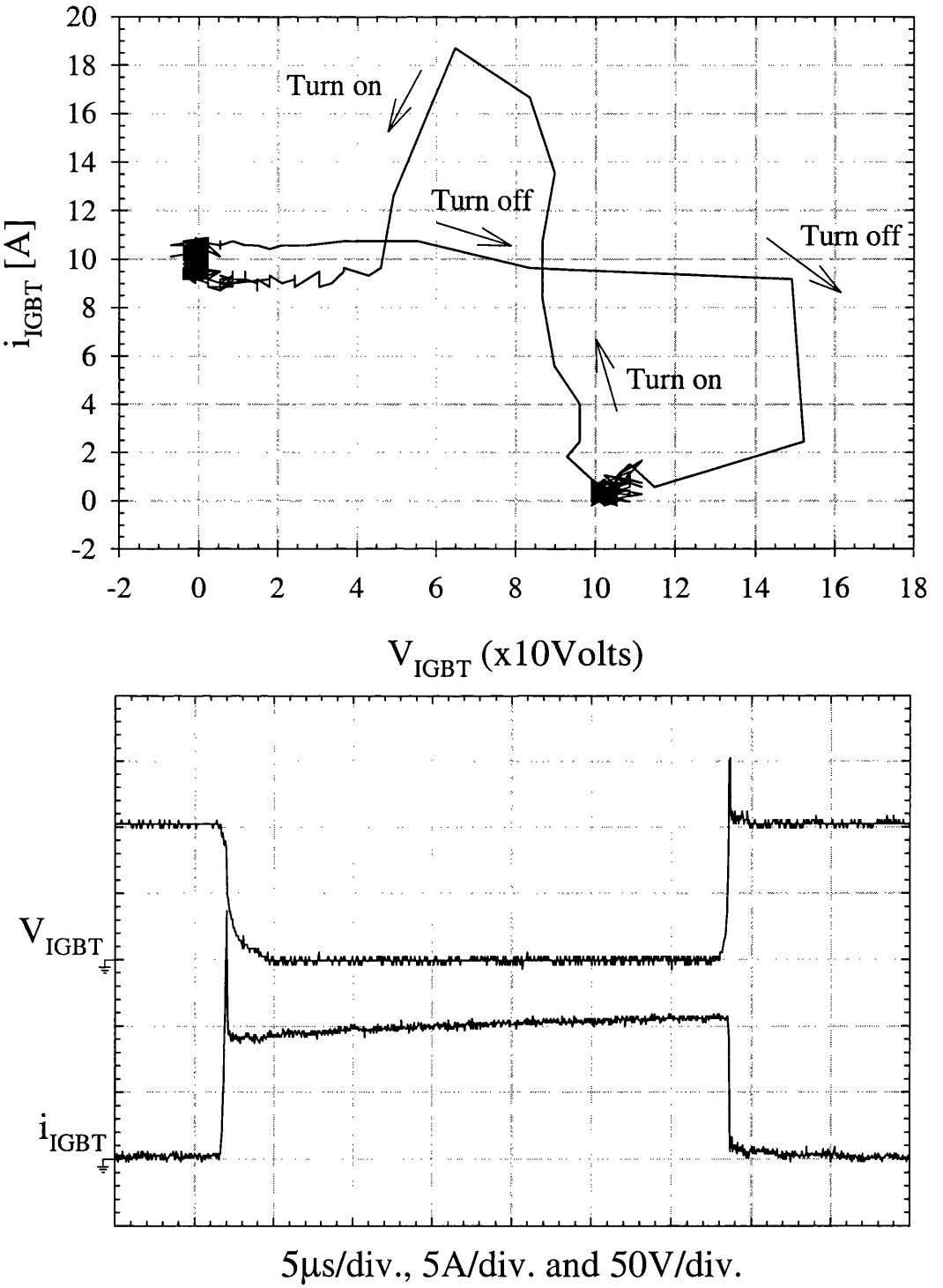

Figure A.31: Turn-on and turn-off with hard-switching, Top:$V_{IGBT} - i_{IGBT}$ switching locus for inverter's IGBT, Bottom: Voltage and current waveforms.

inverter with synchronisation between the resonant frequency and the inverter switching frequency has been built. The basic functionality of the circuit is described and proved experimentally. The experimental results show a simple and well-working soft-switching scheme, applicable in the drive's entire torque-speed range. Operation with or without excitation overlap between conducting phases is possible, as well as soft or hard chopping and single-pulse operation. The ACRDCL-SR inverter allows high bandwidth delta-modulated current regulation with minimal switching losses. The ACRDCL must be carefully designed and optimised together with the SR inverter in order to increase the overall drive efficiency.

The experimental results showed that the resonant frequency is affected by the reactive power exchanged between the supply and the motor windings. The worst case is when two phases go from $+V_{res}$ to $-V_{res}$. The clamp resonant period in load transients was found to be smaller for soft-chopping than for hard-chopping. For soft-chopping, the resonant frequency is not affected significantly and therefore the current ripple is similar for both soft-switching and hard-switching. In contrast, the resonant frequency deviation in hard-chopping has an affect on the current regulation, showing a higher ripple for soft-switching than hard-switching. It should be noticed that using this topology, a small error in the commutation angles is introduced as the commutation is synchronised with the zero voltage period. However, this topology can be controlled such that resonance occurs only when a change in the switching state of the inverter is required rather than continuously, as explained in [116]. Another topology which resonates only when necessary is the pole inverter [115, 110]

In summary, it can be concluded that the resonant dc-link and active clamp resonant dc-link front-ends behave no differently when applied to Switched Reluctance Motor Drives than when used in AC-drives. More importantly, it may also be concluded that the SRM delta-modulated current regulation is not compromised by the presence of soft-switching.

A.3 Conclusion

In addition to the investigation in the area of sensorless methods, research was carried out in soft switching applied to switched reluctance motors. In particular, the functionality study of the classic inverter with a front-end resonant dc-link was presented. The experimental results showed that the proposed ACRDCL-SR inverter maintains all the performance of the hard-switched inverter drive, but adds some control requirements, which should be compensated by the saving in switching losses of the inverter.

This Appendix proposed a resonant dc-link front-end switched reluctance drive for high bandwidth delta-modulated current control. The aim of this research was the reduction of the switching losses in the inverter in order to increase the overall efficiency of the drive. The classic inverter was used, and its switching instants were synchronised with the zero-resonant dc-link periods. The normal operating modes of current-regulated SRM drives were simulated, and the comparisons between hard-switched and soft-switched waveforms were presented. The active resonant dc-link switched reluctance drive was built and its control fully implemented in real time. The circuit resonates at rate of 60 kHz and the detail description of the hybrid implementation was presented.

A series of experimental tests were carried out, which included current regulation using hard chopping, soft chopping and single pulse operation. The tests where carried out at standstill and at different speeds. The experimental current waveforms with soft-switching and hard-switching are compared and the results demonstrated that the proposed inverter maintains all the robustness and performance aspects of the traditional hard-switched inverter drive. It is worthy to note that the resonant frequency was affected by the power exchange between the motor and the inverter. This yielded long zero-voltage and clamp voltage periods, the effect was worse for current regulation under hard chopping, where the power exchange is higher than soft chopping. It should be noted that the change in the resonant frequency also introduces a dither into the commutation angles, this may have some effects in the performance of the motor, in

particular, the generated torque.

In summary, the experimental results showed a simple and robust soft-switching switched reluctance drive, which works well in the whole torque-speed range with or with no excitation overlap between two neighbouring phases. The soft-switching reluctance drive yielded to minimum switching losses, this was clearly demonstrated in the comparison between the experimental voltage-current locus in the switching transition obtained from soft switching and hard switching. In the soft-switched inverter, the V-i locus is close to the ideal trajectory, however there are some minimum losses. These losses are the result of the long tail in the turn off transition of the IGBT. Furthermore, it should be noted that the current regulation is not compromised by the presence of soft switching, however, the soft switching adds some control requirements which may be compensated by the increase of the overall drive efficiency. This advantage of the the soft-switched inverters may be more evident in high power applications, however, it is worthy to note that the resonant components are very critical part of the circuit and should be carefully designed together with the SR inverter in order to obtained an increase of the overall drive efficiency. Finally, It can be concluded that there is a trade-off between efficiency and fault tolerance when using the resonant dc-link. In other words, the resonant dc-link may improve the SR inverter efficiency but on the other hand may compromise the SR inverter fault tolerance.

A.4 Future work

1. It was found that the power exchange between the motor and the resonant inverter affects the resonant frequency. A possible solution to this problem is to split the upper rail in two buses, one for the upper transistors and other one for the upper diodes, the latter being connected directly to the clamp capacitor. Doing so, it is expected a minimum disruption in the resonant frequency. Experimental validation is required for this topology.

2. The proposed active clamp resonant dc-link SR inverter introduces a dither in the commutation angles. One way to solve this problem is the use of a resonant topology that resonates only when necessary rather than resonating continuously. The possible topologies could be the modified active clamp resonant dc-link [116] and the resonant pole.

3. The optimisation of the resonant components (inductor and capacitor) for maximum efficiency require further investigation.

Appendix B

Motors and inverters used

This appendix presents the magnetic characteristic and picture of motors and inverters used through the development of this thesis. The lamination drawings of the motors and the PC-SRD output files are also included.

Low cost sensorless method

The magnetisation curves and the measured static torque are shown in Fig.B.1 and Fig.B.2 respectively, for the test three phase motor used in the *current gradient sensorless method.* Pictures of the test rig and load set-up are shown in Fig.B.3 and Fig.B.4. The load motor was a PM motor Sanyo Denki, 20V, 5.7A. The resistance connected in the motor terminal was 135 Ω. The classic inverter topology with two transistors and two diodes per phase is used with the variation of splitting the lower rail into two buses, the lower diode bus and the lower transistor bus, so that the current in the commutating transistors can be observed. The TableB.1 above shows the inverter characteristic. A picture of the inverter unit is shown in Fig.B.5.

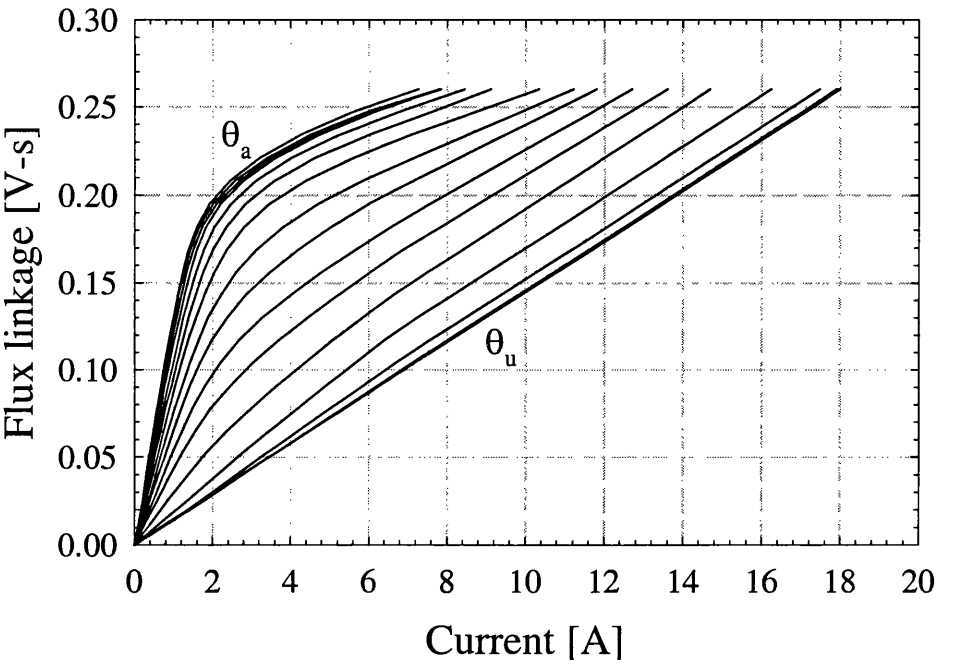

Figure B.1: Measured magnetisation curves for one phase.

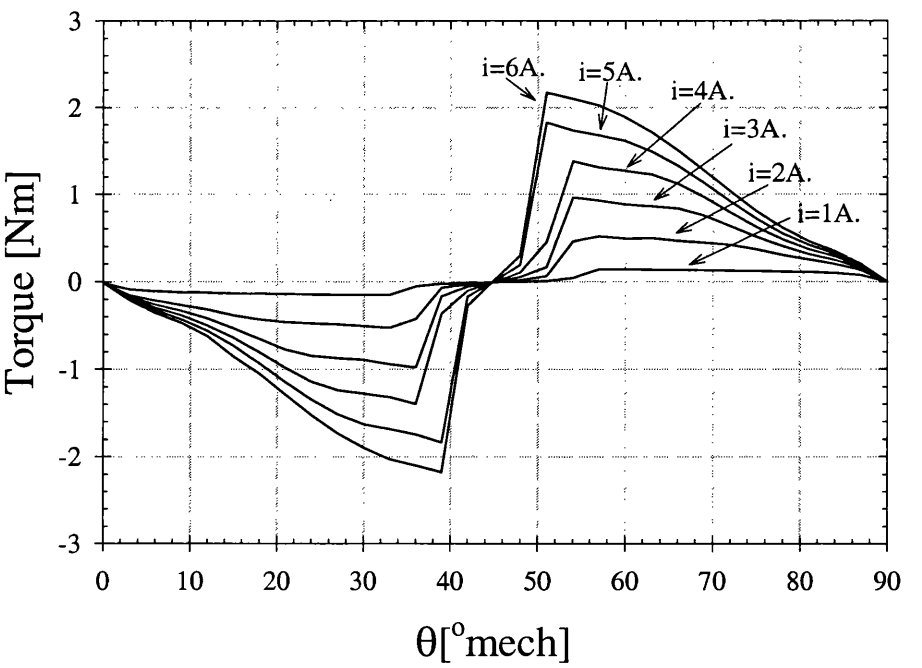

Figure B.2: Measured static torque for one phase.

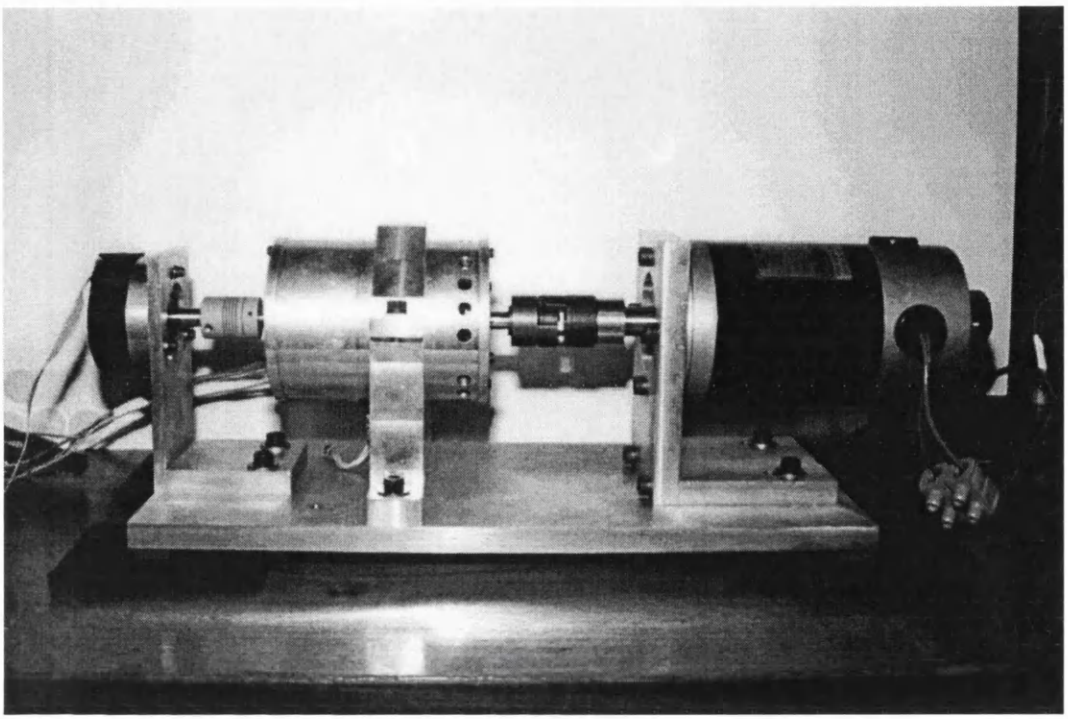

Figure B.3: Test rig with the 3-phase 6/4 SRM and the PM machine as a load.

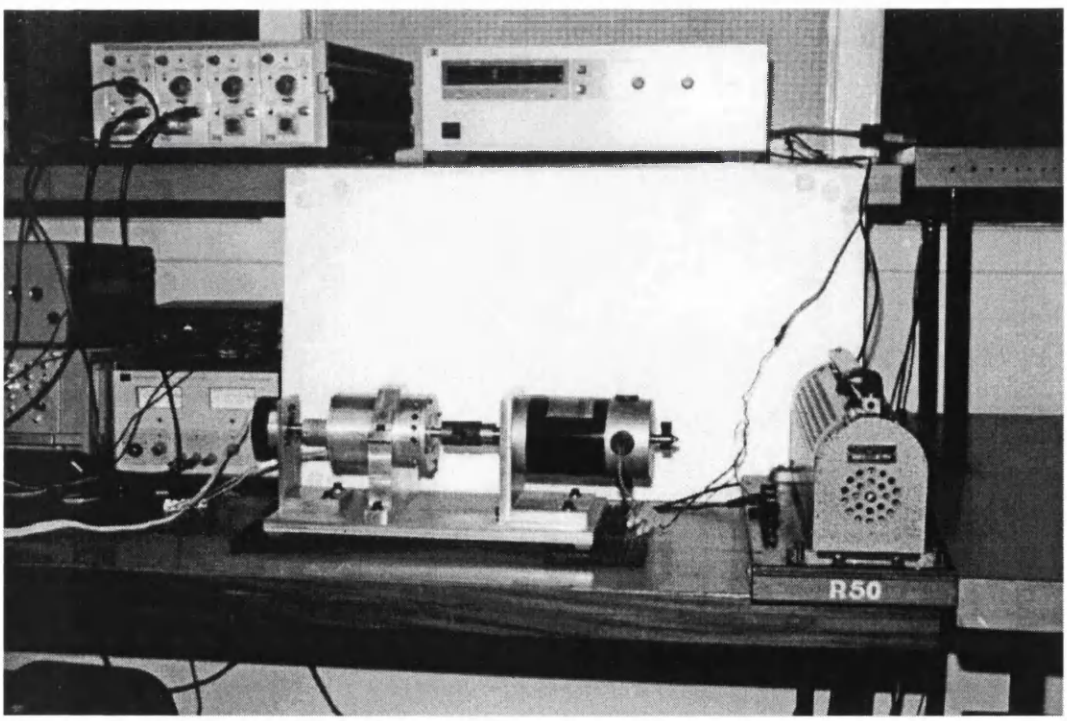

Figure B.4: Load setup overview.

Transistors	IRF 840, 500 V, 8 A continuous, 32 A peak, $R_{DS(on)} = 0.85\Omega$
Diodes	BY 229-600, 600 V, 8 A continuous, 16 A peak
DC-link capacitor	1000 μF, 250 V
Current sensors	LEM 100 1:1000
DC-link voltage used	60 V

Table B.1: Inverter components.

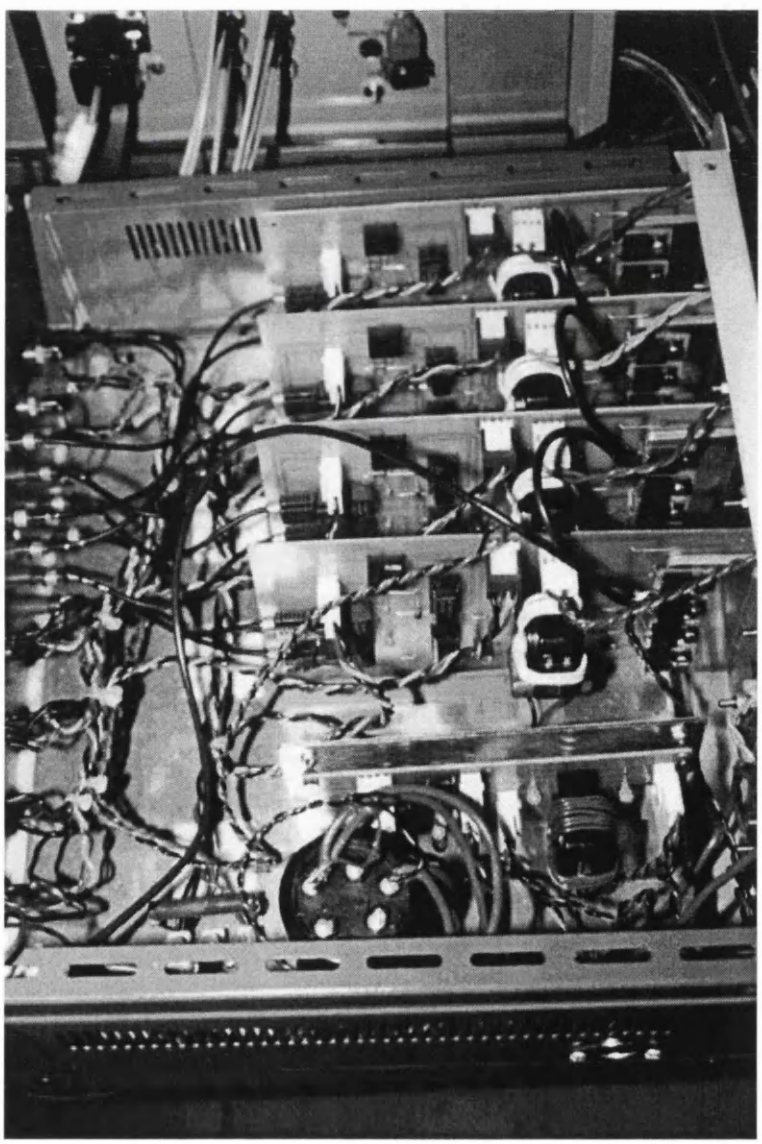

Figure B.5: Inverter unit.

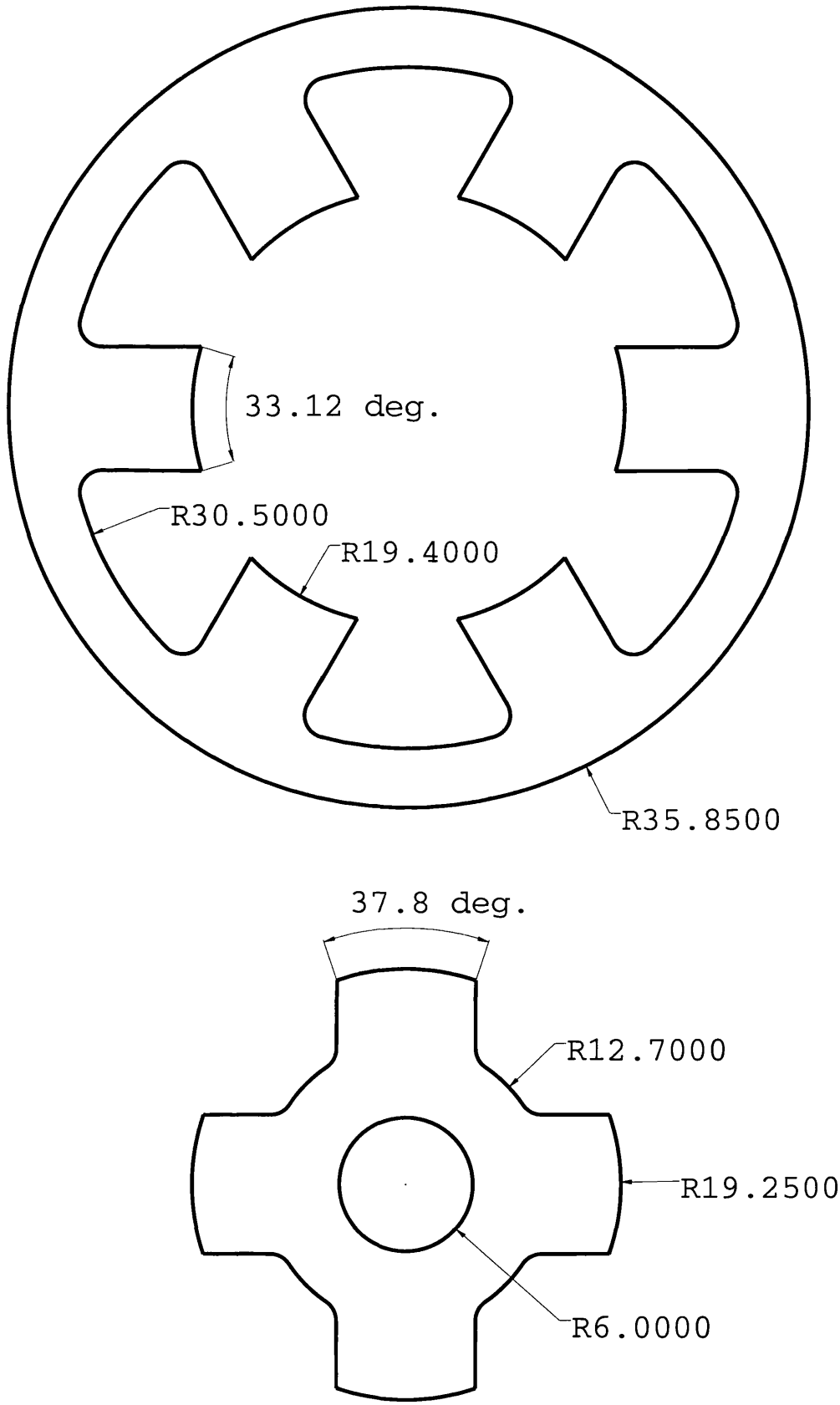

Figure B.6: Dimensions of the machine used for CGSM.

```
PC-SRD 7.0 for Windowß 9/30/98 7:20:12 PM C:\SPEED\PCSRD\cg_mot.srd
Gabriel
PC-SRD main title
PC-SRD sub-title

Dimensions:-------------------------------------------------------------
--

Rsh          6.000 mm      Ntp              1         Gap          0.110 mm
R0          12.700 mm      Nph              3         Lstk        50.800 mm
R1          19.250 mm      Nr               4         BetaR       37.800 mDeg
R2          30.500 mm      Ns               6         BetaS       33.120 mDeg
R3          35.850 mm      D1s          2.000 mm      D2s          2.000 mm
fil_R        2.000 mm      tpr_R        3.000 mDeg    tab          0.000 mm
fil_S        2.000 mm      tpr_S        3.000 mDeg    tpr_T        4.000 mDeg

Winding Data:----------------------------------------------------------
--

Np             110         TempC       50.000 DegC    Rph          2.874 ohm
Paths            1         SFill        0.300         Lau        118.369 mH
NSH              1         M.L.T.     145.388 mm      Lu         14.716 mH
WDia         0.523 mm      L/ends      69.483 mm      Lau/Lu       8.044
                           ACond        0.214 mm^2    Ext          0.000 mm
                           Aslot      157.296 mm^2    NwkPP            1
Coils/Ph     2.000         Tph        220.000         Nss              2

Control Data:----------------------------------------------------------
--

Vs          70.000 V       iHi          2.000 A       DuCy         1.000
rpm        800.000 rpm     iLo          2.000 A       Dwell       30.000 mDeg
Th0         50.000 mDeg    Rq           0.000 ohm     %Dwell      33.333 %
ThC         80.000 mDeg    Vq           0.000 V       Strk/Rev    12.000
ThZ         80.000 mDeg    Vd           0.000 V       Fph         53.333 Hz
ISLA             1         tq_ON        0.000 usec    tq_OFF       0.000 usec
CProfile     false         NChops           0         MeanChop    11.200 kHz

Performance:-----------------------------------------------------------
--

TorqSh   -9.23E+07 Nm      WCu          12.171 W      Erms        11.217 V
PowerSh  -7.73E+09 W       WIron    7.734E+09 W       Epk         21.066 V
Eff      -1.83E+10 %       Wwf          0.000 W       DegCW        0.100 Deg.
C/W
Sigma    -1.13E+08 psi     TotalLos 7.734E+09 W       TempRise 7.734E+08 DegC

Currents:--------------------------------------------------------------
--

IWPk         2.125 A       IWMean       0.762 A       IWrms        1.188 A
IQchPk       2.000 A       IQchMean     0.308 A       IQchRMS      0.769 A
IQcmPk       2.125 A       IQcmMean     0.647 A       IQcmRMS      1.132 A
IDchPk       2.125 A       IDchMean     0.454 A       IDchRMS      0.906 A
IDcmPk       1.971 A       IDcmMean     0.115 A       IDcmRMS      0.362 A
Jrms         5.539 A/mm^2  IDC(wfm)     0.579 A       DCripple     1.107 A
```

Figure B.7: PC-SRD file (machine used for CGSM) (1).

```
Iron Losses:-------------------------------------------------------------------
--

Rotor: Generic mild steel
WlbFeRY       9.684 W/kg    RCfCh         0.015         RCfa          1.800
WlbFeRP       5.567 W/kg    RCfCe     2.161E-05         RCfb          0.000
PRYE      7.949E+08 W       PRYH      3.285E+08 W       BRYMax        1.281 T
PRPE      4.061E+08 W       PRPH      1.654E+08 W       BRPMax        1.376 T

Stator: Generic mild steel
WlbFeSY      14.993 W/kg    SCfCh         0.015         SCfa          1.800
WlbFeSP       4.706 W/kg    SCfCe     2.161E-05         SCfb          0.000
PSYE      3.532E+09 W       PSYH      1.395E+09 W       BSYMax        1.604 T
PSPE      7.952E+08 W       PSPH      3.161E+08 W       BSPMax        1.555 T
WEC       5.528E+09 W       WHYS      2.205E+09 W       XFe           1.000
Stakf         0.970         IrnLos         Orig
WFe0R         8.817 W/kg    WFe0S         8.817 W/kg    FUnbal      252.404 lb

Supplementary Output:----------------------------------------------------------
--

WtCu          0.183 kg      RotJ      37437.075 kg-m2   DCLinkSP      0.605 A
WtFe      7.834E+08 kg      Resistiv 1.927E-08 ohm-m    ConvLoss      0.000 W
TotalWei  7.834E+08 kg      TFRho         1.118         TRPPpu        0.964
TRPP          0.531 Nm      TRrms         0.114 Nm      TRrmspu       0.207
LoopTork      0.360 Nm      WfmTork       0.551 Nm      WConv         0.189 J
Bm            1.900 T       Bs            1.300 T       Lau0        118.113 mH
Psim        259.954 mVs     Psis        177.864 mVs     Lu0           7.611 mH
im            7.280 A       i_s           1.503 A       Lss           0.476 mH
Xim           0.230         XLu           1.660         V2ETF        V3+lss
X_Np          1.000         X_Lstk        1.000         Ag          585.892 mm^2
CPU           4.927         PRS           3.810         Pslot         0.154
dLu           1.254 mH      dLau          0.256 mH      a_ETF         1.000
L_min        14.716 mH      L_max       118.369 mH      Lmax/Lmi      8.044
FluxPths     Normal         PsiMax      187.089 mVs     ThQ          92.375 mDeg
Th_X         52.250 mDeg    Th0_gen      87.625 mDeg    ThC_gen     127.750 mDeg
TRFmax_N    336.538 N

End of Design sheet------------------------------------------------------------
--
```

Figure B.8: PC-SRD file (machine used for CGSM) (2).

High resolution sensorless method

The measured magnetisation curves and the static torque curves of the 4 phase 8/6 SRM used in this setup were presented in section 2.3. The pictures of the test rig and the inverter are presented in Fig.B.9. The SRM is coupled to the PM load machine through a gear box with a ratio of 7:1. The load machine is a PM motor manufactured by Control Techniques Model No 142DSE300HAAA (DutymAx DS), its characteristics are summarised in Table B.2. The controller for the load machine is the Unidrive UNI-2402 rated at 7.5 kW from Control Techniques. The conventional power inverter with two diodes and two transistors per phase was used, the characteristic of the inverter are presented in Table B.3.

Poles	6
Continuous torque	23.2 Nm
Stall torque	26 Nm
Maximum speed	3000 rpm
k_t	1.6 Nm/Arms

Table B.2: PM load machine.

IGBT	Toshiba MG100J2YS50, 600 V and 100 A, $V_{drop,max} = 2.7$ V
DC-link capacitor	1500 μF, 385 V
Current sensors	LEM 50P/SP1, 1:1000
DC-link voltage used	100 V

Table B.3: Inverter components.

(a)

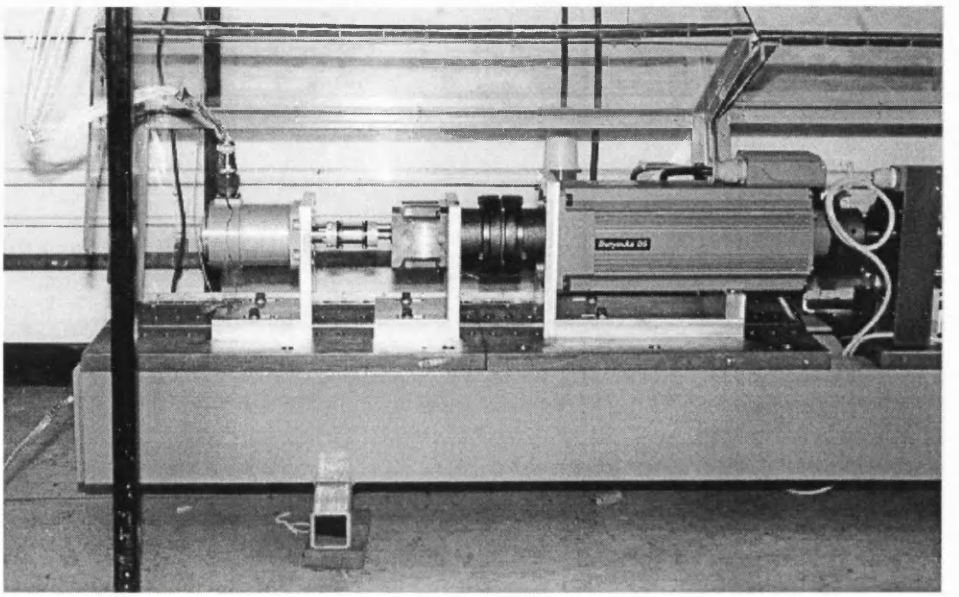

(b)

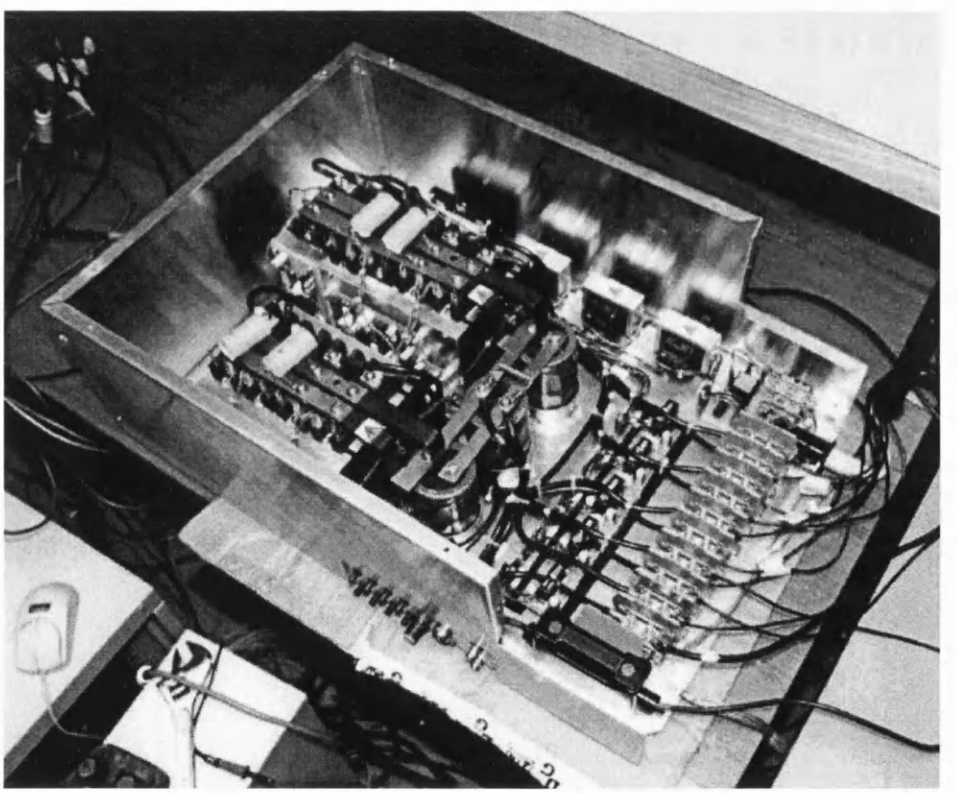

Figure B.9: Hardware setup overview, a: 4 phase 8/6 switched reluctance motor coupled to the load motor through a gear box with a ratio of 7:1, b: Classic four phase inverter.

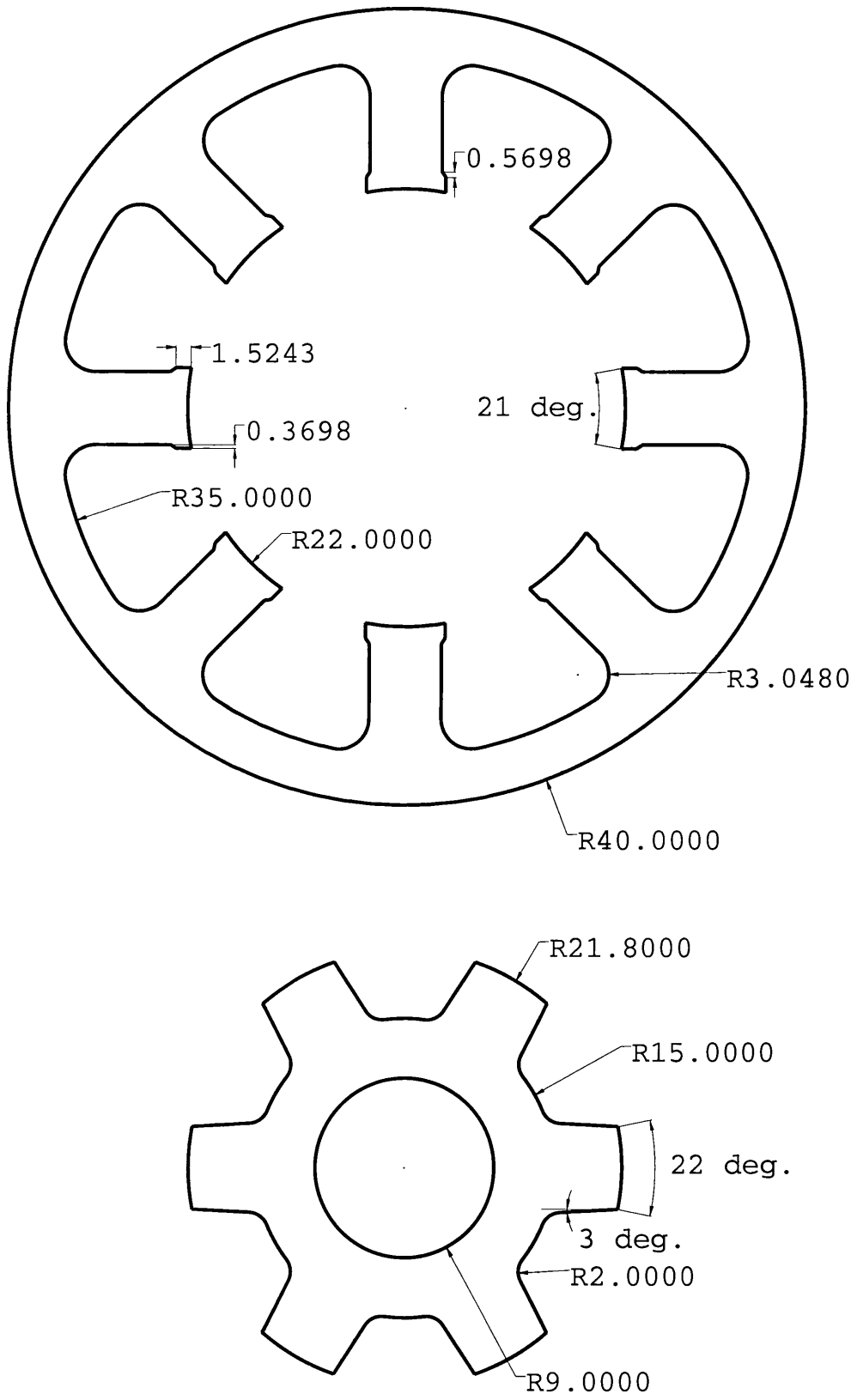

Figure B.10: Dimensions of the machine used for observer.

```
PC-SRD 7.0 for Windowß 9/30/98 7:21:43 PM C:\SPEED\PCSRD\ob_mot.srd
Gabriel
PC-SRD main title
PC-SRD sub-title

Dimensions:-------------------------------------------------------------
--

Rsh          9.000 mm      Ntp              1          Gap          0.240 mm
R0          15.000 mm      Nph              4          Lstk        70.000 mm
R1          21.800 mm      Nr               6          BetaR       22.000 mDeg
R2          35.000 mm      Ns               8          BetaS       21.000 mDeg
R3          40.000 mm      Dls          1.500 mm       D2s          0.500 mm
fil_R        2.000 mm      tpr_R        3.000 mDeg     tab          0.000 mm
fil_S        3.048 mm      tpr_S       -1.000 mDeg     tpr_T        4.000 mDeg

Winding Data:----------------------------------------------------------
--

Np             70          TempC      100.000 DegC     Rph          1.262 ohm
Paths           1          SFill        0.330          Lau         27.161 mH
NSH             1          M.L.T.     176.799 mm       Lu           4.309 mH
WDia         0.752 mm      L/ends      87.055 mm       Lau/Lu       6.303
                           ACond        0.444 mm^2     Ext          0.000 mm
                           Aslot      188.527 mm^2     NwkPP            1
Coils/Ph     2.000         Tph        140.000          Nss              2

Control Data:----------------------------------------------------------
--

Vs         100.000 V       iHi          5.000 A        DuCy         1.000
rpm       2000.000 rpm     iLo          5.000 A        Dwell       20.000 mDeg
Th0         30.000 mDeg    Rq           0.000 ohm      %Dwell      33.333 %
ThC         50.000 mDeg    Vq           2.200 V        Strk/Rev    24.000
ThZ         80.000 mDeg    Vd           1.800 V        Fph        200.000 Hz
ISLA            1          tq_ON        0.000 usec     tq_OFF       0.000 usec
CProfile     false         NChops           0          MeanChop    19.200 kHz

Performance:-----------------------------------------------------------
--

TorqSh   -2.76E+08 Nm      WCu          42.910 W       Erms         9.974 V
PowerSh  -5.79E+10 W       WIron    5.789E+10 W        Epk         18.917 V
Eff      -2.63E+10 %       Wwf          0.000 W        DegCW        0.100 Deg.
C/W
Sigma    -1.92E+08 psi     TotalLos 5.789E+10 W        TempRise 5.789E+09 DegC

Currents:--------------------------------------------------------------
--

IWPk         5.204 A       IWMean       1.897 A        IWrms        2.915 A
IQchPk       4.995 A       IQchMean     0.959 A        IQchRMS      2.129 A
IQcmPk       5.204 A       IQcmMean     1.550 A        IQcmRMS      2.744 A
IDchPk       5.204 A       IDchMean     0.938 A        IDchRMS      1.991 A
IDcmPk       4.904 A       IDcmMean     0.347 A        IDcmRMS      0.986 A
Jrms         6.560 A/mm^2  IDC(wfm)     2.450 A        DCripple     3.600 A
```

Figure B.11: PC-SRD file (machine used for observer) (1).

```
Iron Losses:-------------------------------------------------------------
--

Rotor: Generic mild steel
WlbFeRY      48.534 W/kg     RCfCh         0.015          RCfa          1.800
WlbFeRP      33.363 W/kg     RCfCe     2.161E-05          RCfb          0.000
PRYE      7.802E+09 W        PRYH      1.114E+09 W        BRYMax        0.800 T
PRPE      4.326E+09 W        PRPH      5.739E+08 W        BRPMax        1.153 T

Stator: Generic mild steel
WlbFeSY      69.576 W/kg     SCfCh         0.015          SCfa          1.800
WlbFeSP      32.617 W/kg     SCfCe     2.161E-05          SCfb          0.000
PSYE      2.926E+10 W        PSYH      4.027E+09 W        BSYMax        0.960 T
PSPE      9.551E+09 W        PSPH      1.234E+09 W        BSPMax        1.319 T
WEC       5.094E+10 W        WHYS      6.948E+09 W        XFe           1.000
Stakf         0.970          IrnLos         Orig
WFe0R         8.817 W/kg     WFe0S         8.817 W/kg     FUnbal      194.425 lb

Supplementary Output:----------------------------------------------------
--

WtCu          0.391 kg       RotJ      79822.073 kg-m2    DCLinkSP      2.514 A
WtFe      1.140E+09 kg       Resistiv  2.266E-08 ohm-m    ConvLoss     31.335 W
TotalWei  1.140E+09 kg       TFRho         1.314          TRPPpu        0.647
TRPP          0.894 Nm       TRrms         0.172 Nm       TRrmspu       0.125
LoopTork      0.846 Nm       WfmTork       1.381 Nm       WConv         0.221 J
Bm            1.600 T        Bs            1.300 T        Lau0         27.098 mH
Psim        141.047 mVs      Psis        114.601 mVs      Lu0           3.763 mH
im           29.809 A        i_s           4.219 A        Lss           0.237 mH
Xim           3.100          XLu           1.025          V2ETF        V3+lss
X_Np          1.000          X_Lstk        1.000          Ag          619.507 mm^2
CPU           4.365          PRS           2.855          Pslot         0.137
dLu           0.441 mH       dLau          0.063 mH       a_ETF         1.000
L_min         4.309 mH       L_max        27.161 mH       Lmax/Lmi      6.303
FluxPths     Normal          PsiMax       92.446 mVs      ThQ          60.500 mDeg
Th_X         32.875 mDeg     Th0_gen      59.500 mDeg     ThC_gen      87.125 mDeg
TRFmax_N    259.233 N

End of Design sheet------------------------------------------------------
--
```

Figure B.12: PC-SRD file (machine used for observer) (2).

Active clamp resonant dc-link switched reluctance motor

The measured magnetisation curves of the 4 phase SRM used in the test rig for the active clamp resonant SR inverter is depicted in Fig.B.13. The inverter used was the same described in the previous section. A picture of the active clamp resonant dc-link is shown in Fig.B.14. The classic switched reluctance inverter is underneath of the resonant circuit.

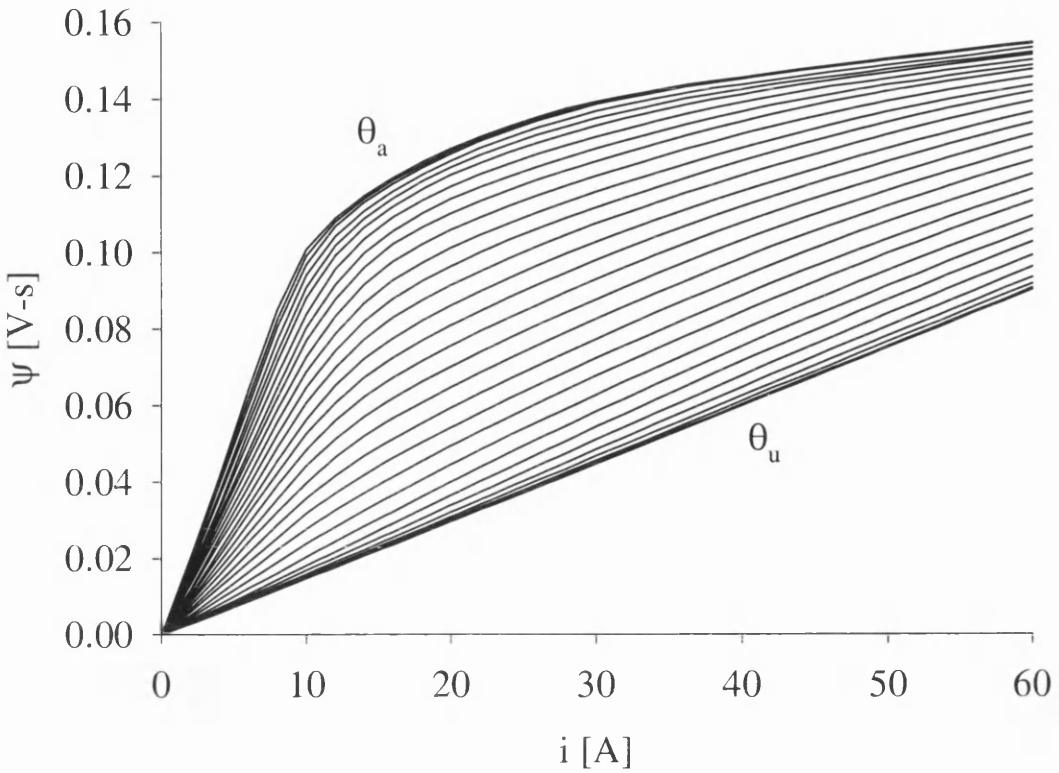

Figure B.13: Magcurves for one phase of the 4 phase SRM used.

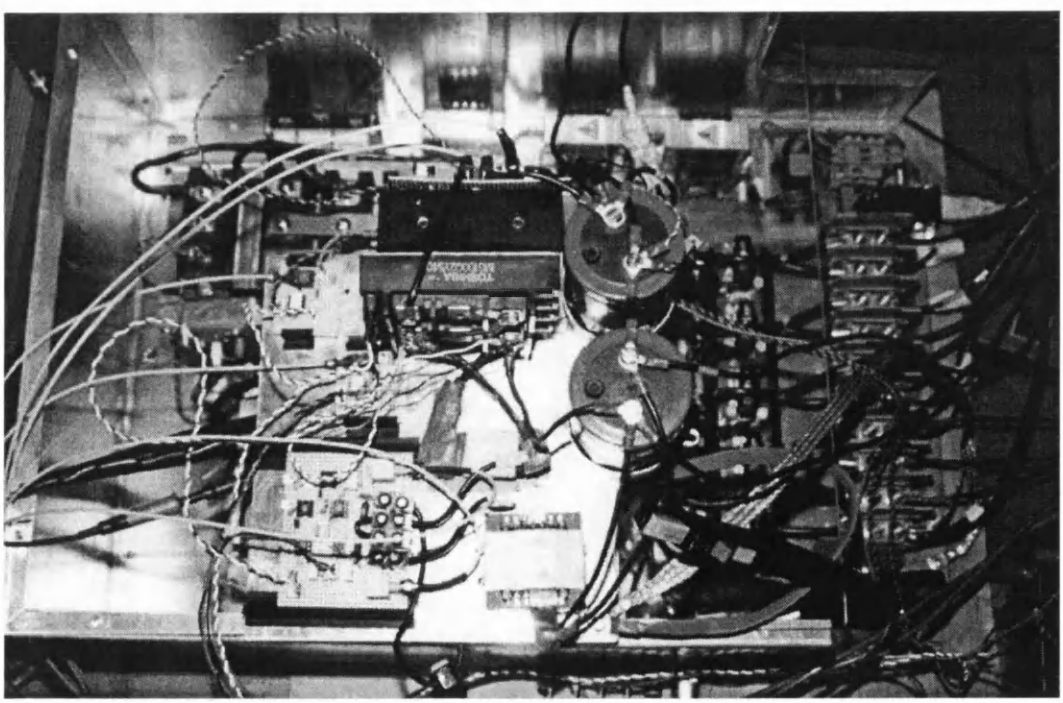

Figure B.14: Active clamp resonant dc-link switched reluctance inverter.

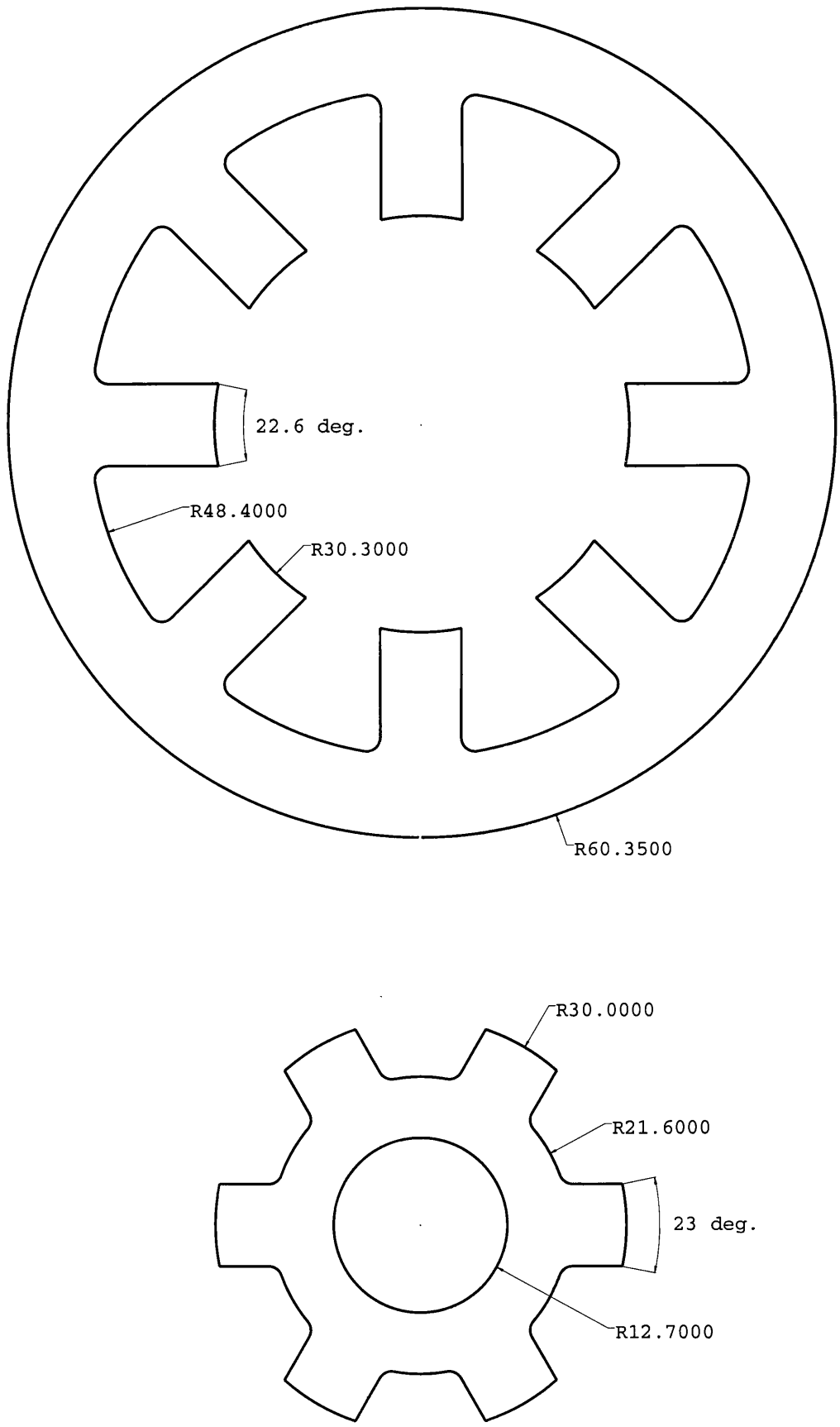

Figure B.15: Dimensions of the machine used for ACRDCL.

```
PC-SRD 7.0 for Windowß 9/30/98 7:04:40 PM c:\speed\pcsrd\re_mot.srd
Gabriel
PC-SRD main title
PC-SRD sub-title

Dimensions:-------------------------------------------------------------
--

Rsh          12.700 mm      Ntp              1          Gap          0.345 mm
R0           21.600 mm      Nph              4          Lstk        75.000 mm
R1           30.000 mm      Nr               6          BetaR       23.000 mDeg
R2           48.400 mm      Ns               8          BetaS       22.600 mDeg
R3           60.350 mm      D1s          2.000 mm       D2s          2.000 mm
fil_R         2.000 mm      tpr_R        3.000 mDeg     tab          0.000 mm
fil_S         3.048 mm      tpr_S        1.000 mDeg     tpr_T        4.000 mDeg

Winding Data:----------------------------------------------------------
--

Np              38          TempC      100.000 DegC     Rph          0.243 ohm
Paths            1          SFill        0.330          Lau          9.151 mH
NSH              1          M.L.T.     202.634 mm       Lu           1.457 mH
WDia         1.353 mm       L/ends      97.801 mm       Lau/Lu       6.279
                            ACond        1.438 mm^2     Ext          0.000 mm
                            Aslot      331.160 mm^2     NwkPP            1
Coils/Ph     2.000          Tph         76.000          Nss              2

Control Data:----------------------------------------------------------
--

Vs          100.000 V       iHi         10.000 A        DuCy         1.000
rpm        1000.000 rpm     iLo         10.000 A        Dwell       20.000 mDeg
Th0          30.000 mDeg    Rq           0.000 ohm      %Dwell      33.333 %
ThC          50.000 mDeg    Vq           2.200 V        Strk/Rev    24.000
ThZ          80.000 mDeg    Vd           1.800 V        Fph        100.000 Hz
ISLA             1          tq_ON        0.000 usec     tq_OFF       0.000 usec
CProfile     false          NChops           0          MeanChop    10.800 kHz

Performance:-----------------------------------------------------------
--

TorqSh   -3.75E+08 Nm        WCu          35.162 W       Erms        30.995 V
PowerSh  -3.93E+10 W         WIron    3.931E+10 W        Epk         59.869 V
Eff      -2.61E+10 %         Wwf           0.000 W       DegCW        0.100 Deg.
C/W
Sigma    -1.28E+08 psi       TotalLos 3.931E+10 W        TempRise 3.931E+09 DegC

Currents:--------------------------------------------------------------
--

IWPk         11.254 A        IWMean       3.678 A        IWrms        6.018 A
IQchPk        9.995 A        IQchMean     0.824 A        IQchRMS      2.816 A
IQcmPk       11.254 A        IQcmMean     3.341 A        IQcmRMS      5.826 A
IDchPk       11.254 A        IDchMean     2.854 A        IDchRMS      5.319 A
IDcmPk       10.155 A        IDcmMean     0.337 A        IDcmRMS      1.509 A
Jrms          4.185 A/mm^2   IDC(wfm)     1.946 A        DCripple     5.818 A
```

Figure B.16: PC-SRD file (machine used for ACRDCL) (1).

```
Iron Losses:-------------------------------------------------------------
--

Rotor: Generic mild steel
WlbFeRY      19.166 W/kg     RCfCh         0.015          RCfa          1.800
WlbFeRP      14.012 W/kg     RCfCe     2.161E-05          RCfb          0.000
PRYE      7.003E+09 W        PRYH      9.943E+08 W        BRYMax        0.699 T
PRPE      3.429E+09 W        PRPH      4.496E+08 W        BRPMax        1.041 T

Stator: Generic mild steel
WlbFeSY      10.711 W/kg     SCfCh         0.015          SCfa          1.800
WlbFeSP      10.632 W/kg     SCfCe     2.161E-05          SCfb          0.000
PSYE      1.654E+10 W        PSYH      2.490E+09 W        BSYMax        0.521 T
PSPE      7.433E+09 W        PSPH      9.735E+08 W        BSPMax        1.047 T
WEC       3.440E+10 W        WHYS      4.908E+09 W        XFe           1.000
Stakf         0.970          IrnLos         Orig
WFe0R         8.817 W/kg     WFe0S         8.817 W/kg     FUnbal      270.309 lb

Supplementary Output:----------------------------------------------------
--

WtCu          0.787 kg       RotJ      3.263E+05 kg-m2    DCLinkSP      2.100 A
WtFe      3.261E+09 kg       Resistiv  2.266E-08 ohm-m    ConvLoss     59.628 W
TotalWei  3.261E+09 kg       TFRho         1.314          TRPPpu        0.685
TRPP          1.427 Nm       TRrms         0.215 Nm       TRrmspu       0.103
LoopTork      1.100 Nm       WfmTork       2.084 Nm       WConv         0.288 J
Bm            2.100 T        Bs            1.300 T        Lau0          9.124 mH
Psim        159.428 mVs      Psis         98.693 mVs      Lu0           1.335 mH
im           56.462 A        i_s          10.785 A        Lss           0.083 mH
Xim           1.600          XLu           0.960          V2ETF        V3+lss
X_Np          1.000          X_Lstk        1.000          Ag          980.578 mm^2
CPU           4.906          PRS           3.421          Pslot         0.152
dLu           0.183 mH       dLau          0.027 mH       a_ETF         1.000
L_min         1.457 mH       L_max         9.151 mH       Lmax/Lmi      6.279
FluxPths     Normal          PsiMax       69.775 mVs      ThQ          54.000 mDeg
Th_X         31.000 mDeg     Th0_gen      66.000 mDeg     ThC_gen      89.000 mDeg
TRFmax_N    360.412 N

End of Design sheet------------------------------------------------------
--1
```

Figure B.17: PC-SRD file (machine used for ACRDCL) (2).

Appendix C

Circuit diagrams

This appendix presents the signal list for both MC68332 and TMS320C31 controllers. The circuit diagrams of the controllers boards and the schematic diagrams of the FPGA are also given.

SRM Controller
Motherboard Signal List
9/April/97 Gabriel Gallegos López

Pin	Signal	Micro	Comm.	Current	I/O	Function
1a	0V	•	•	•	•	Digital GND
2a	+5V	•	•	•	•	Digital VCC
3a	D0	•	•		•	332 Micro Data Bus (lsb)
4a	D2	•	•		•	332 Micro Data Bus
5a	D4	•	•		•	332 Micro Data Bus
6a	D6	•	•		•	332 Micro Data Bus
7a	D8	•	•		•	332 Micro Data Bus
8a	D10	•	•		•	332 Micro Data Bus
9a	D12	•				332 Micro Data Bus
10a	D14	•				332 Micro Data Bus
11a	A1	•	•		•	332 Micro Address Bus
12a	A3	•	•		•	332 Micro Address Bus
13a	A5	•				332 Micro Address Bus
14a	A7	•				332 Micro Address Bus
15a	TP0		•		•	Phase 4 Commutation
16a	TP2		•	•		Iph1
17a	TP4		•	•		Iph3
18a	TP6		•	•		Ph1 Pul.
19a	TP8		•	•		Ph3 Pul.
20a	TP10	•	•			INDEX Encoder
21a	TP12	•	•			CHB Encoder
22a	TP14		•		•	Phase 2 Commutation
23a	PQS0	•				332 Micro General Purpose I/O
24a	PQS2	•				332 Micro General Purpose I/O
25a	PQS4	•				332 Micro General Purpose I/O
26a	PQS6	•				332 Micro General Purpose I/O
27a	CS6	•				332 Micro Chip Select 6
28a	CS8	•			•	332 Micro Chip Select 8
29a	CS4	•				332 Micro Chip Select 4
30a	PWM1		•		•	PWM1 Signal Current Regulation
31a	+15V	•	•	•	•	+15V
32a	-15V	•	•	•	•	-15V

Notes: CS4, 5 and 6 are used by debug so should only be used as Write Only Functions

Table C.1: Back plane signal list of the MC68332 controller: row a tracks.

Pin	Signal	Micro	Comm.	Current	I/O	Function
1b	0V	•	•	•	•	Digital GND
2b	+5V	•	•	•	•	Digital VCC
3b	DSACK0	•				332 Micro
4b	DSACK1	•				332 Micro
5b	A8	•				332 Micro Address Bus
6b	A9	•				332 Micro Address Bus
7b	A10	•				332 Micro Address Bus
8b	A11	•				332 Micro Address Bus
9b	A12	•				332 Micro Address Bus
10b	Cut 0V					
11b						
12b						
13b						
14b						
15b						
16b						
17b						
18b						
19b						
20b						
21b						
22b						
23b						
24b						
25b	Cut 0V					
26b	Cut 0V					
27b	PWM4		•		•	PWM4 Signal Current Regulation
28b						
29b	DIR				•	DIR
30b	PWM2		•		•	PWM2 Signal Current Regulation
31b	+15V	•	•	•	•	+15V
32b	-15V	•	•	•	•	-15V

Table C.2: Back plane signal list of the MC68332 controller: row b tracks.

Pin	Signal	Micro	Comm.	Current	I/O	Function
1c	0V	•	•	•	•	Digital GND
2c	+5V	•	•	•	•	Digital VCC
3c	D1	•	•		•	332 Micro Data Bus
4c	D3	•	•		•	332 Micro Data Bus
5c	D5	•	•		•	332 Micro Data Bus
6c	D7	•	•		•	332 Micro Data Bus
7c	D9	•	•		•	332 Micro Data Bus
8c	D11	•	•		•	332 Micro Data Bus
9c	D13	•				332 Micro Data Bus
10c	D15	•				332 Micro Data Bus
11c	A2	•	•		•	332 Micro Address Bus
12c	A4	•	•			332 Micro Address Bus
13c	A6	•				332 Micro Address Bus
14c	IRQ7	•				332 Micro Interrupt 7
15c	TP1	•	•		•	Sensorless Pulses All Phases
16c	TP3		•	•		Iph2
17c	TP5		•	•		Iph4
18c	TP7		•	•		Ph2 Pul.
19c	TP9	•	•	•		Ph4 Pul.
20c	TP11	•	•			CHA Encoder
21c	TP13		•		•	Phase 1 Commutation
22c	TP15		•		•	Phase 3 Commutation
23c	PQS1	•	•		•	332 Micro General Purpose I/O
24c	PQS3	•				332 Micro General Purpose I/O
25c	PQS5	•				332 Micro General Purpose I/O
26c	CS5	•				332 Micro Chip Select 5
27c	CS7	•	•			332 Micro Chip Select 7
28c	CS3	•			•	332 Micro Chip Select 3
29c	RST	•				Master Reset Signal
30c	PWM3		•	•	•	PWM3 Signal Current Regulation
31c	+15V	•	•	•	•	+15V
32c	-15V	•	•	•	•	-15V

Table C.3: Back plane signal list of the MC68332 controller: row c tracks.

SRM DSP Controller
Motherboard Signal List
1/March/98 Gabriel Gallegos López

Pin	Signal	DSP	Comm.	ADC	Res	I/O	Function
1a	0V	•	•	•	•	•	Digital GND
2a	+5V	•	•	•	•	•	Digital VCC
3a	D0	•	•	•	•	•	TMS320C31 Data Bus (lsb)
4a	D2	•	•	•	•	•	TMS320C31 Data Bus
5a	D4	•	•	•	•	•	TMS320C31 Data Bus
6a	D6	•	•	•	•	•	TMS320C31 Data Bus
7a	D8	•	•	•		•	TMS320C31 Data Bus
8a	D10	•	•	•		•	TMS320C31 Data Bus
9a	D12	•					TMS320C31 Data Bus
10a	D14	•					TMS320C31 Data Bus
11a	A0	•	•	•	•	•	TMS320C31 Address Bus
12a	A2	•	•	•	•	•	TMS320C31 Address Bus
13a	A4	•			•		TMS320C31 Address Bus
14a	A6	•					TMS320C31 Address Bus
15a	COMM4		•			•	Phase 4 Commutation
16a	IRQ0	•	•				UP-SIGN Interrupt
17a							NOT USED
18a							NOT USED
19a							NOT USED
20a							NOT USED
21a							NOT USED
22a	COMM2		•			•	Phase 2 Commutation
23a							NOT USED
24a							NOT USED
25a							NOT USED
26a							NOT USED
27a	CS2	•	•				TMS320C31 Chip Select 2
28a	CS4	•				•	TMS320C31 Chip Select 4
29a	CS6	•	•	•			TMS320C31 Chip Select 6
30a	PWM1		•			•	PWM1
31a	+15V	•	•	•	•	•	+15V
32a	-15V	•	•	•	•	•	-15V

Table C.4: Back plane signal list of the TMS320C31 controller: row a tracks.

Pin	Signal	DSP	Comm.	ADC	Res	I/O	Function
1b	0V	•	•	•	•	•	Digital GND
2b	+5V	•	•	•	•	•	Digital VCC
3b	Cut 0V	•					NOT USED
4b	Cut 0V	•					NOT USED
5b	A7	•					TMS320C31 Address Bus
6b	A8	•					TMS320C31 Address Bus
7b	A9	•					TMS320C31 Address Bus
8b	A10	•					TMS320C31 Address Bus
9b	A11	•					TMS320C31 Address Bus
10b	Cut 0V						NOT USED
11b							
12b							
13b							
14b							
15b							
16b							
17b							
18b							
19b							
20b							
21b							
22b							
23b							
24b							
25b	Cut 0V						NOT USED
26b	Cut 0V						NOT USED
27b	PWM4		•			•	PWM4
28b							
29b	DIR		•				Direction of rotation
30b	PMW2		•		•	•	PWM2
31b	+15V	•	•	•	•	•	+15V
32b	-15V	•	•	•	•	•	-15V

Table C.5: Back plane signal list of the TMS320C31 controller: row b tracks.

Pin	Signal	DSP	Comm.	ADC	Res	I/O	Function
1c	0V	•	•	•	•	•	Digital GND
2c	+5V	•	•	•	•	•	Digital VCC
3c	D1	•	•	•	•	•	TMS320C31 Data Bus
4c	D3	•	•	•	•	•	TMS320C31 Data Bus
5c	D5	•	•	•	•	•	TMS320C31 Data Bus
6c	D7	•	•	•	•	•	TMS320C31 Data Bus
7c	D9	•	•	•		•	TMS320C31 Data Bus
8c	D11	•	•	•		•	TMS320C31 Data Bus
9c	D13	•					TMS320C31 Data Bus
10c	D15	•					TMS320C31 Data Bus
11c	A1	•	•	•	•	•	TMS320C31 Address Bus
12c	A3	•	•	•	•	•	TMS320C31 Address Bus
13c	A5	•					TMS320C31 Address Bus
14c							NOT USED
15c							NOT USED
16c							NOT USED
17c							NOT USED
18c							NOT USED
19c							NOT USED
20c							NOT USED
21c	Comm1		•			•	Phase 1 Commutation
22c	Comm3		•			•	Phase 3 Commutation
23c							NOT USED
24c							NOT USED
25c							NOT USED
26c	CS3	•					TMS320C31 Chip Select 5
27c	CS5	•			•		TMS320C31 Chip Select 7
28c	CS7	•					TMS320C31 Chip Select 3
29c		•					NOT USED
30c	PWM3		•	•		•	PWM3
31c	+15V	•	•	•		•	+15V
32c	-15V	•	•	•		•	-15V

Table C.6: Back plane signal list of the TMS320C31 controller: row c tracks.

Pin	Function	Programmed	Pin	Function	Programmed
12	$\overline{PWRDN}$		54	$\overline{RESET}$	
13	TCLKIN		55	DONE-$\overline{PG}$	
14	I/O	DB0	56	D7	
15	I/O	DB1	57	XTL1(OUT)	IOV2
16	I/O	DCL Pul.	58	D6	
17	I/O	DB3	59	I/O	Ph2 Pul.
18	I/O	DB4	60	D5	
19	I/O	DB5	61	$\overline{CS0}$	Ph3 Pul.
20	I/O		62	D4	PWM4
21	GND	GND	63	I/O	COM1
22	VCC	VCC	64	VCC	
23	I/O	DB7	65	GND	
24	I/O	DB8	66	D3	COM4
25	I/O	DB9	67	$\overline{CS1}$	COM2
26	I/O	DB10	68	D2	PWM3
27	I/O	DB11	69	I/O	COM3
28	I/O	IOV1	70	D1	PWM2
29	I/O	IOV3	71	RDY/$\overline{BUSY}$	
30	I/O	Ph1 Pul.	72	D0	PWM1
31	M1	(L)	73	DOUT	
32	M0	(L)	74	CCLK	
33	M2	(H)	75	A0	
34	HDC		76	A1	
35	I/O		77	A2	
36	$\overline{LDC}$	CS7	78	A3	
37	I/O	A1	79	I/O	IRefLD
38	I/O	A2	80	I/O	IOV4
39	I/O	A3	81	A15	
40	I/O	A4	82	A4	
41	INIT		83	A14	
42	VCC	VCC	84	A5	
43	GND	GND	1	GND	
44	I/O	DB2	2	VCC	
45	I/O	DB6	3	A13	
46	I/O		4	A6	
47	I/O	CHA Encoder	5	A12	
48	I/O	CHB Encoder	6	A7	
49	I/O	INDEX Encoder	7	I/O	
50	I/O	10 MHz CLK	8	A11	
51	I/O	332 EBL(PQS1)	9	A8	
52	I/O		10	A10	
53	XTL2(IN)		11	A9	

Table C.7: Commutation Board FPGA pin function (XC3195A-6 84pin)

Pin	Function	Programmed	Pin	Function	Programmed
12	$\overline{PWRDN}$		54	$\overline{RESET}$	
13	TCLKIN		55	DONE-$\overline{PG}$	
14	I/O	PMW1	56	D7	
15	I/O	PWM2	57	XTL1(OUT)	
16	I/O	PMW3	58	D6	
17	I/O	PMW4	59	I/O	SclOff (PI)
18	I/O		60	D5	
19	I/O	COMM1	61	$\overline{CS0}$	
20	I/O	COMM2	62	D4	DIR-DIN
21	GND	GND	63	I/O	
22	VCC	VCC	64	VCC	
23	I/O	COMM3	65	GND	
24	I/O	COMM4	66	D3	
25	I/O		67	$\overline{CS1}$	
26	I/O	CS3	68	D2	
27	I/O	CS8	69	I/O	
28	I/O	A1	70	D1	
29	I/O	A2	71	RDY/$\overline{BUSY}$	
30	I/O	A3	72	D0	
31	M1	(L)	73	DOUT	
32	M0	(L)	74	CCLK	
33	M2	(H)	75	A0	L1
34	HDC		76	A1	L2
35	I/O	DB0	77	A2	L2
36	$\overline{LDC}$		78	A3	L4
37	I/O	DB1	79	I/O	A-Switch
38	I/O	DB2	80	I/O	DIR-DB
39	I/O	DB3	81	A15	
40	I/O	DB4	82	A4	Sdc
41	INIT		83	A14	
42	VCC	VCC	84	A5	U1
43	GND	GND	1	GND	
44	I/O	DB5	2	VCC	
45	I/O	DB6	3	A13	
46	I/O	DB7	4	A6	U2
47	I/O	16 MHz CLK F2	5	A12	DOUT3
48	I/O	12 MHz CLK F1	6	A7	U3
49	I/O	DIR	7	I/O	B-Switch
50	I/O	SrOff (Im)	8	A11	DOUT2
51	I/O	SrOn (Vz)	9	A8	U4
52	I/O	SclOn (Id)	10	A10	DOUT1
53	XTL2(IN)		11	A9	Scl

Table C.8: I/O Board FPGA pin function (XC3064A-6 84pin)

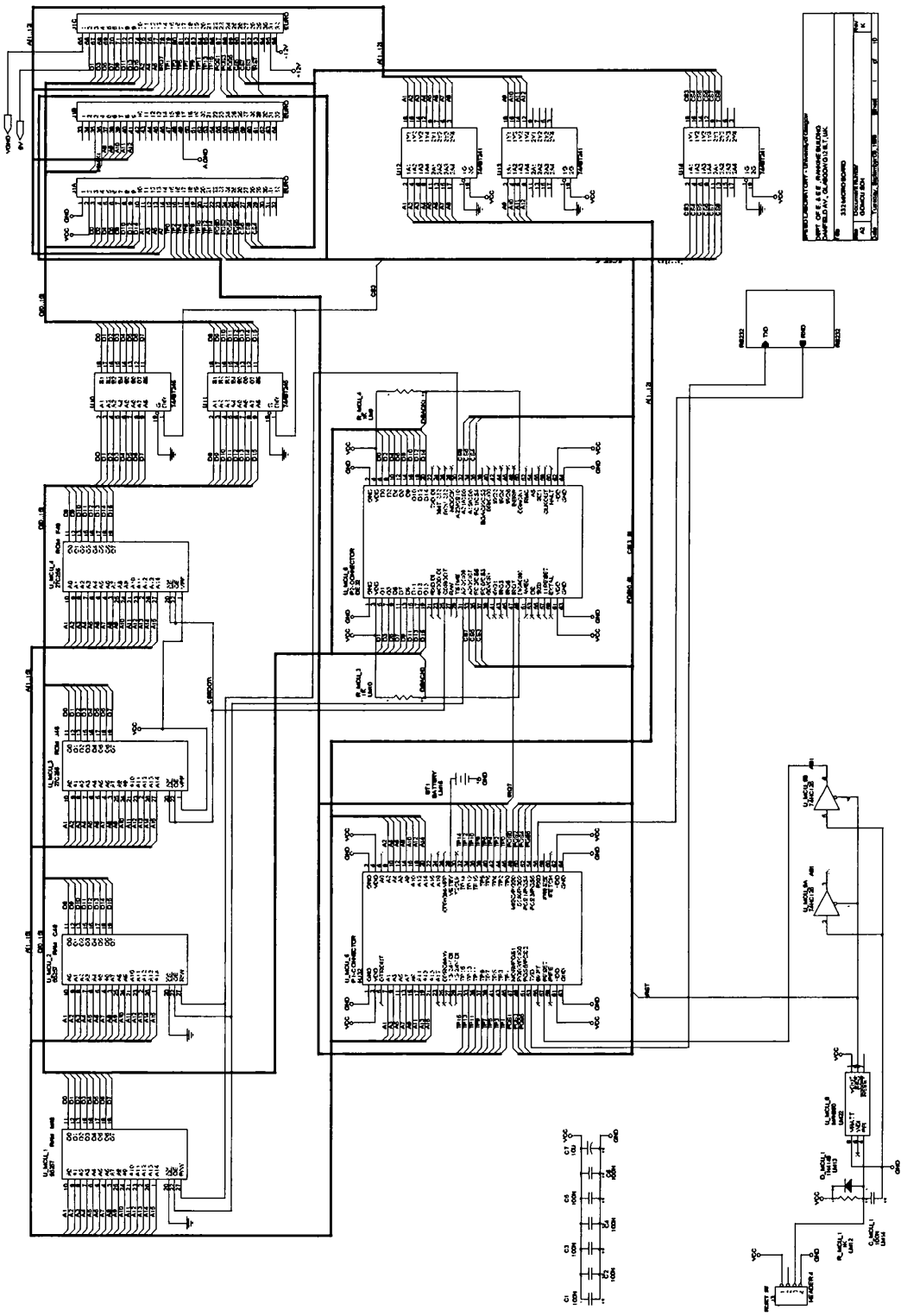

Figure C.1: Circuit diagram of the Microcontroller MC68332 board.

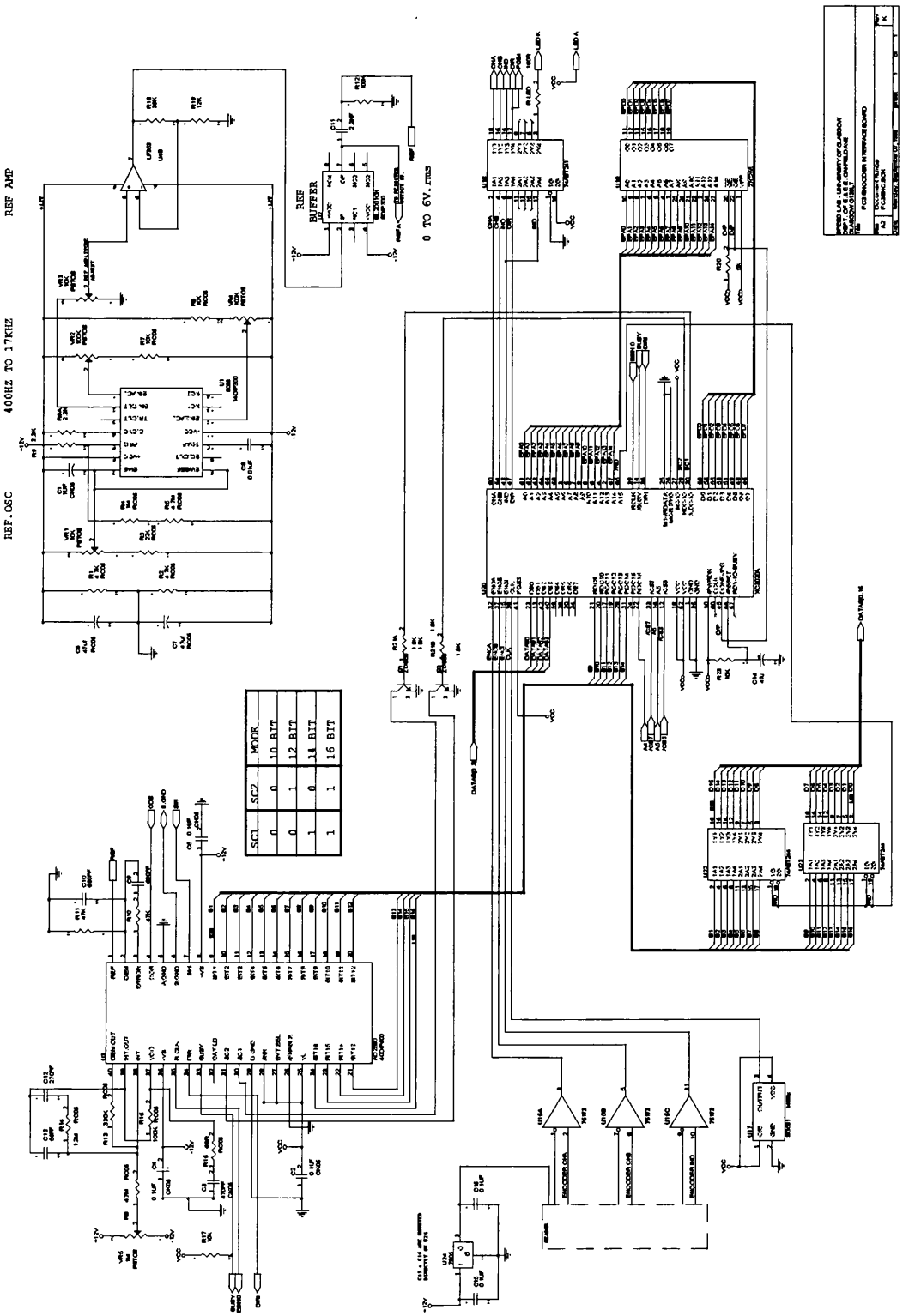

Figure C.2: Circuit diagram of the encoder board.

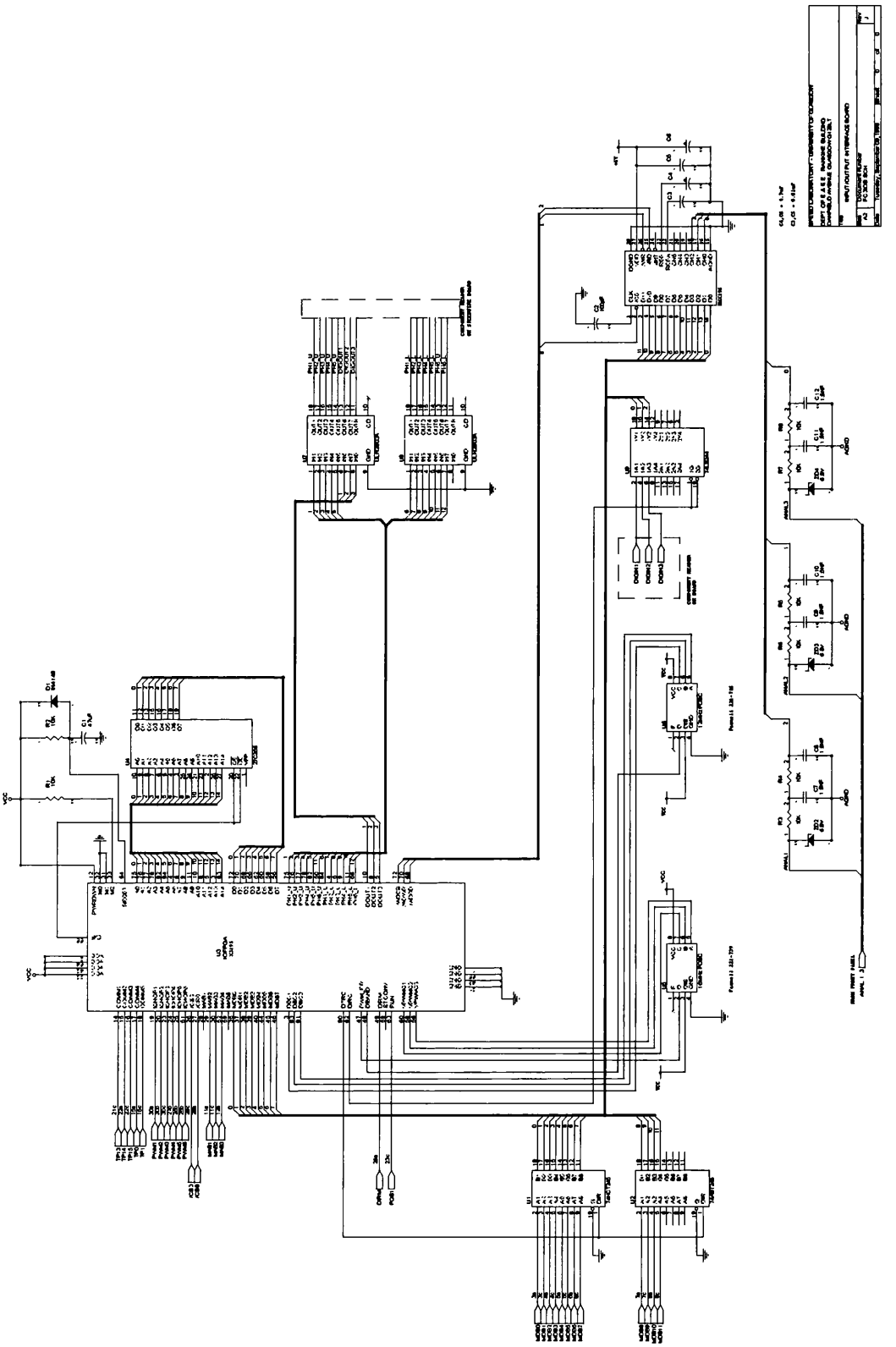

Figure C.3: Circuit diagram of the Input/Output board.

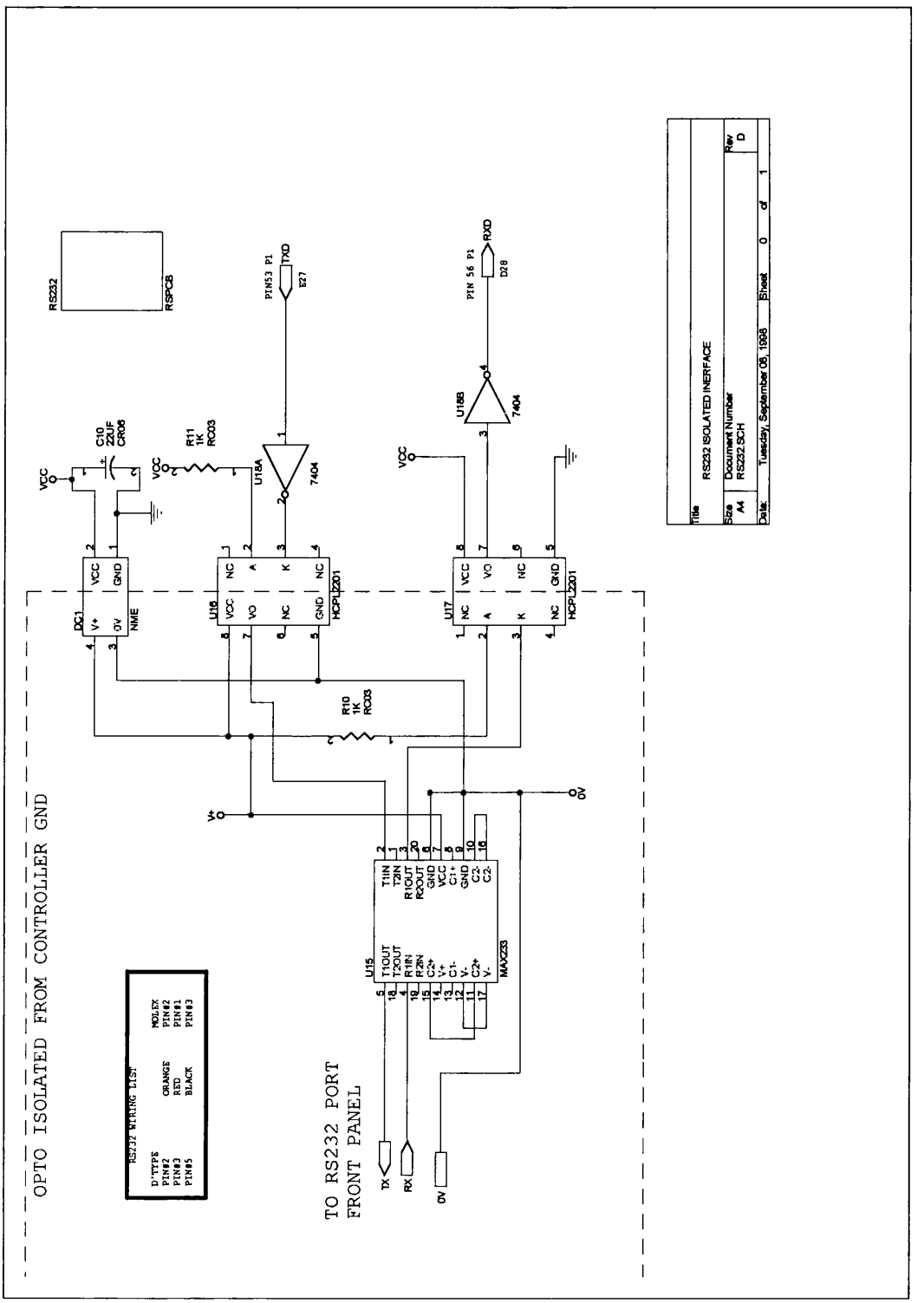

Figure C.4: Circuit diagram of the RS232 interphase.

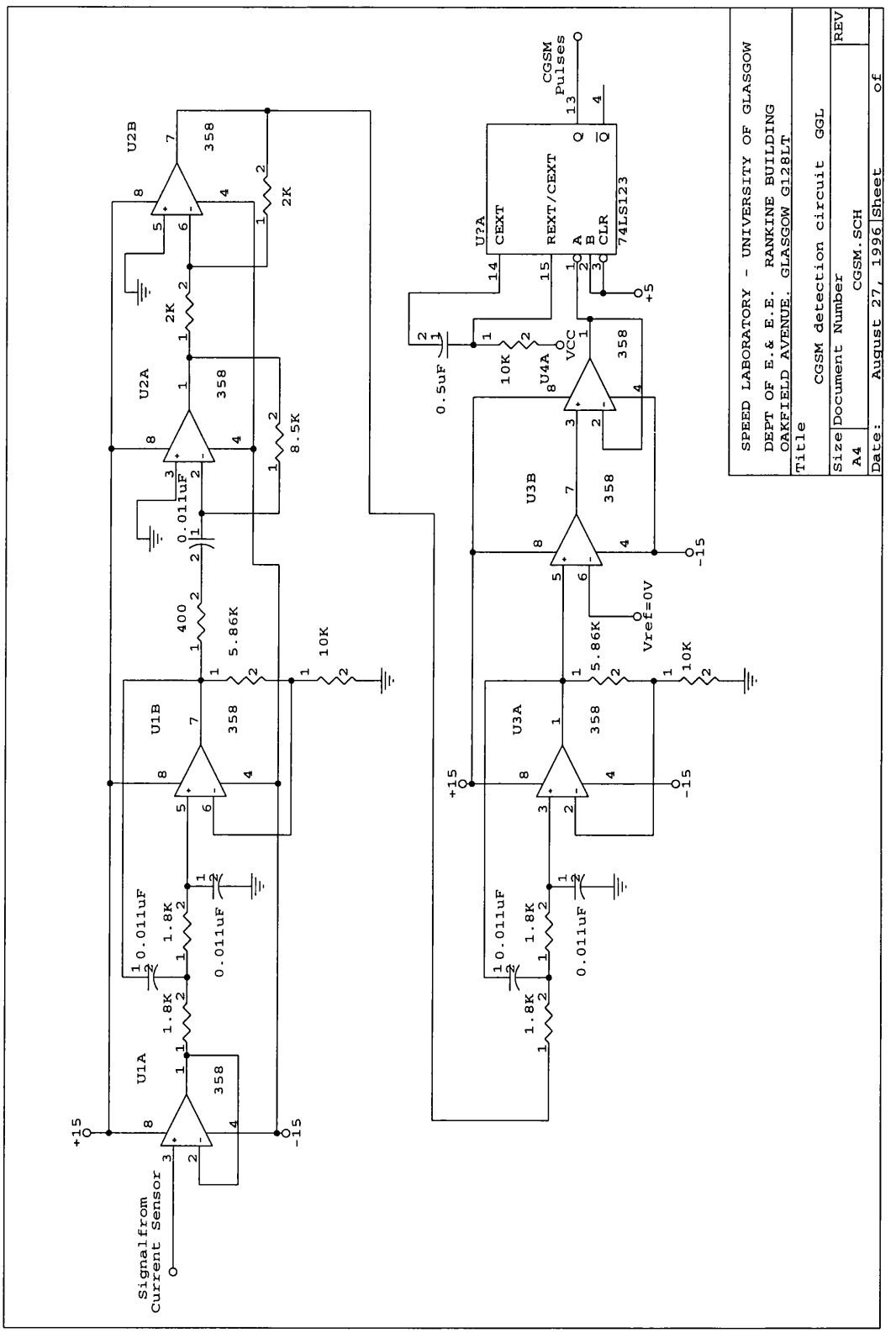

Figure C.5: Circuit diagram of the detection stage of CGSM.

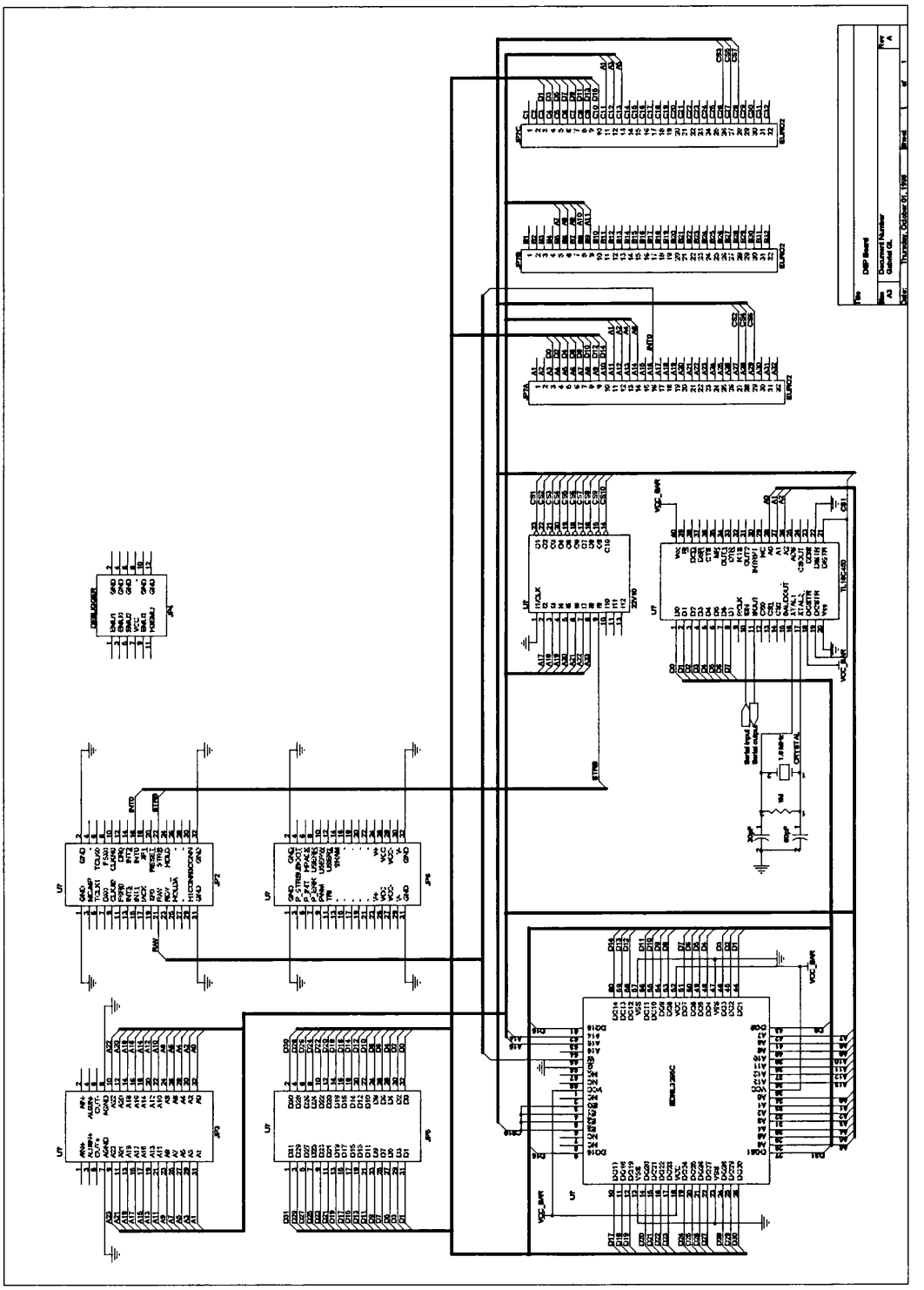

Figure C.6: Circuit diagram of the DSP TMS320C31 board.

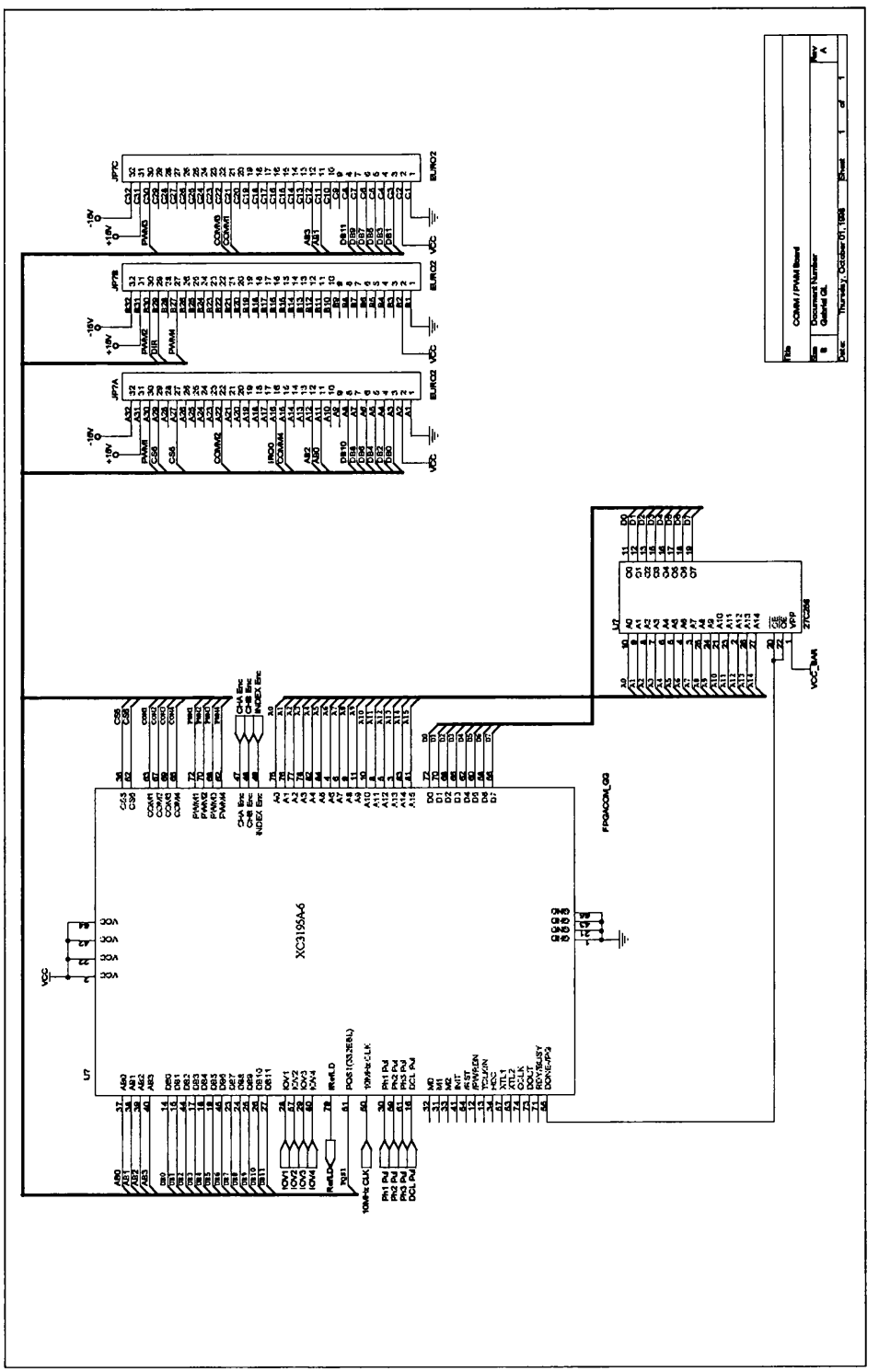

Figure C.7: Circuit of the commutation-PWM generator FPGA board.

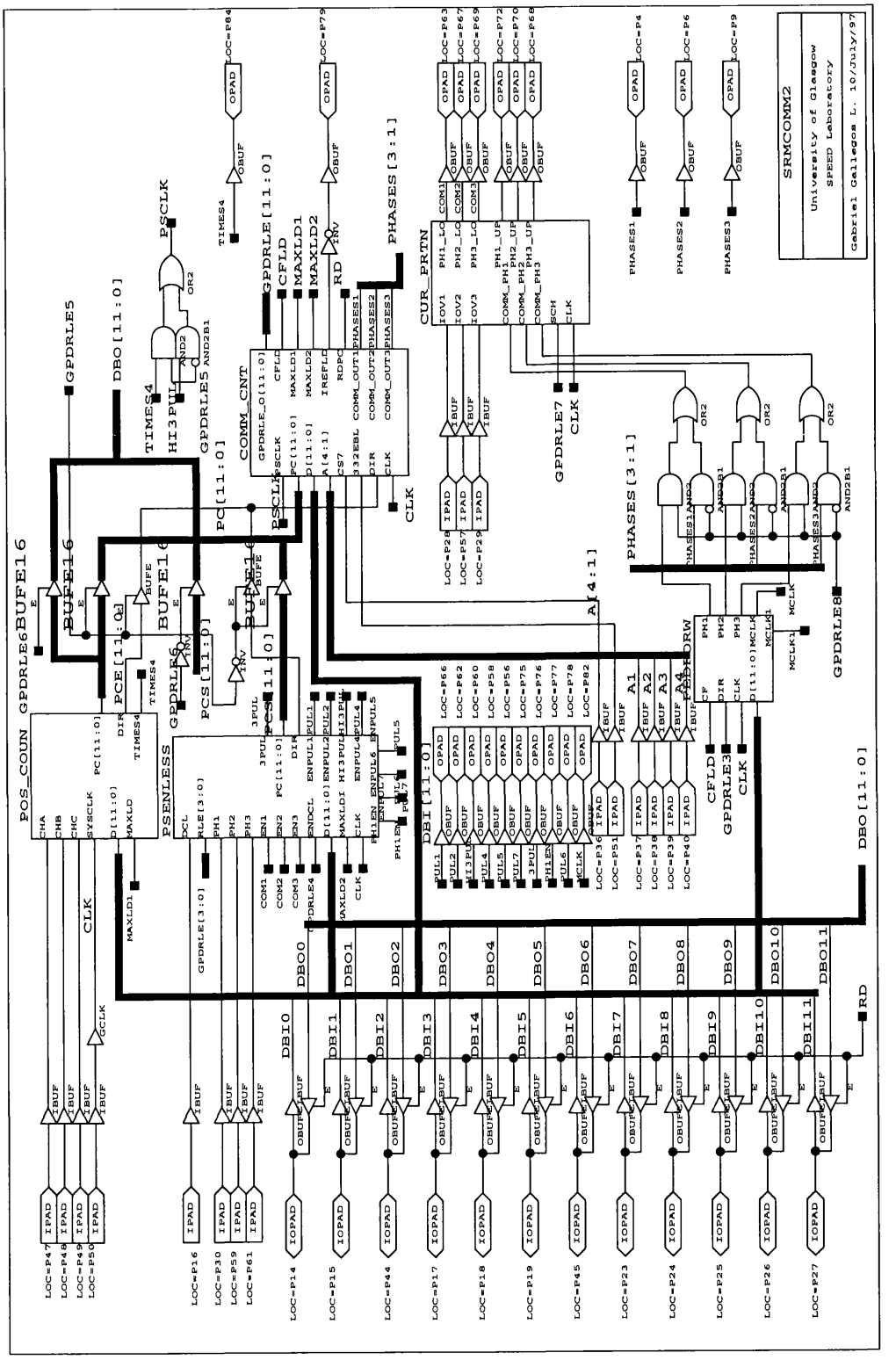

Figure C.8: Schematic diagram of the CGSM: top level.

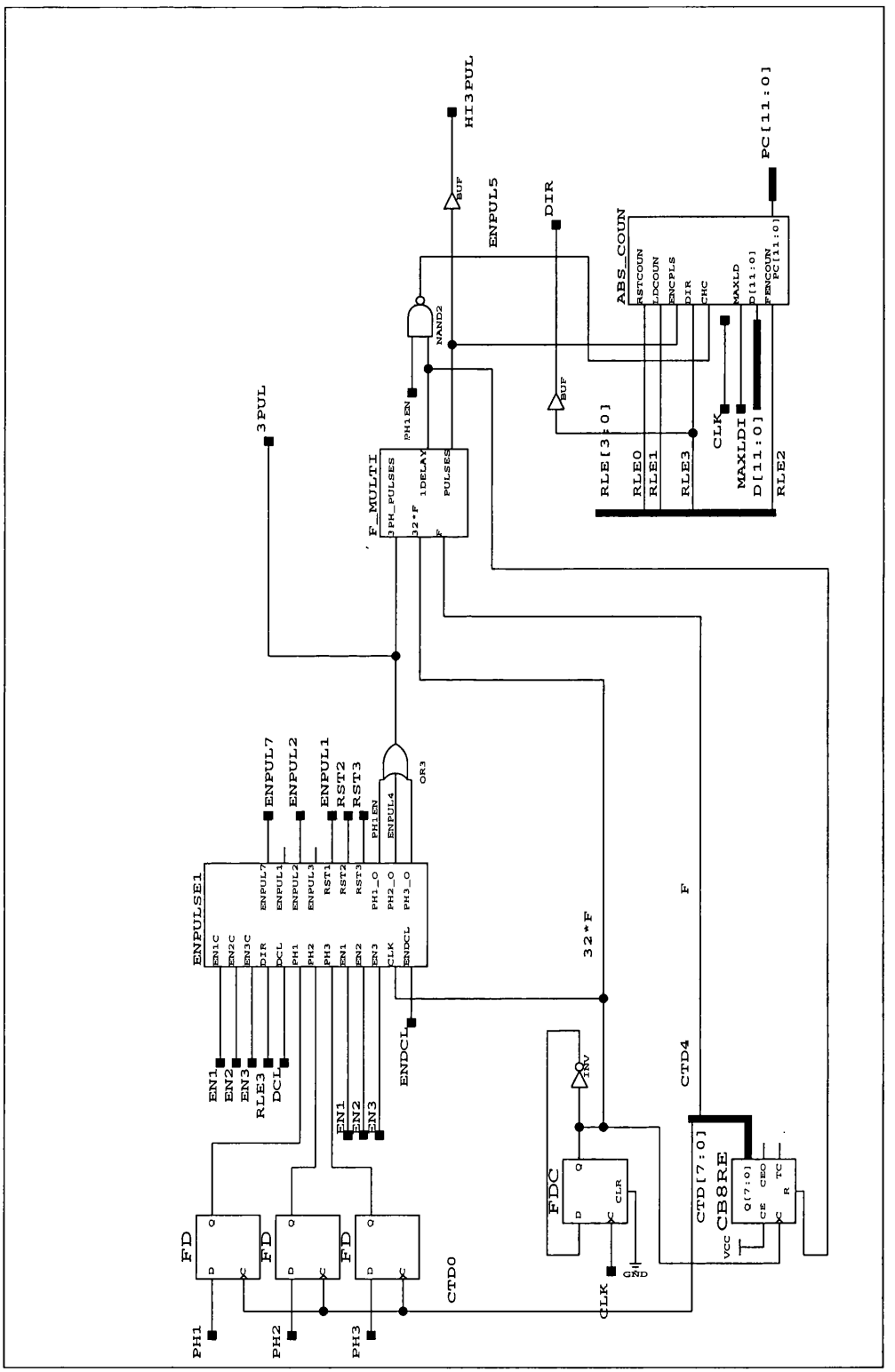

Figure C.9: Schematic diagram of the CGSM: sensorless pulses.

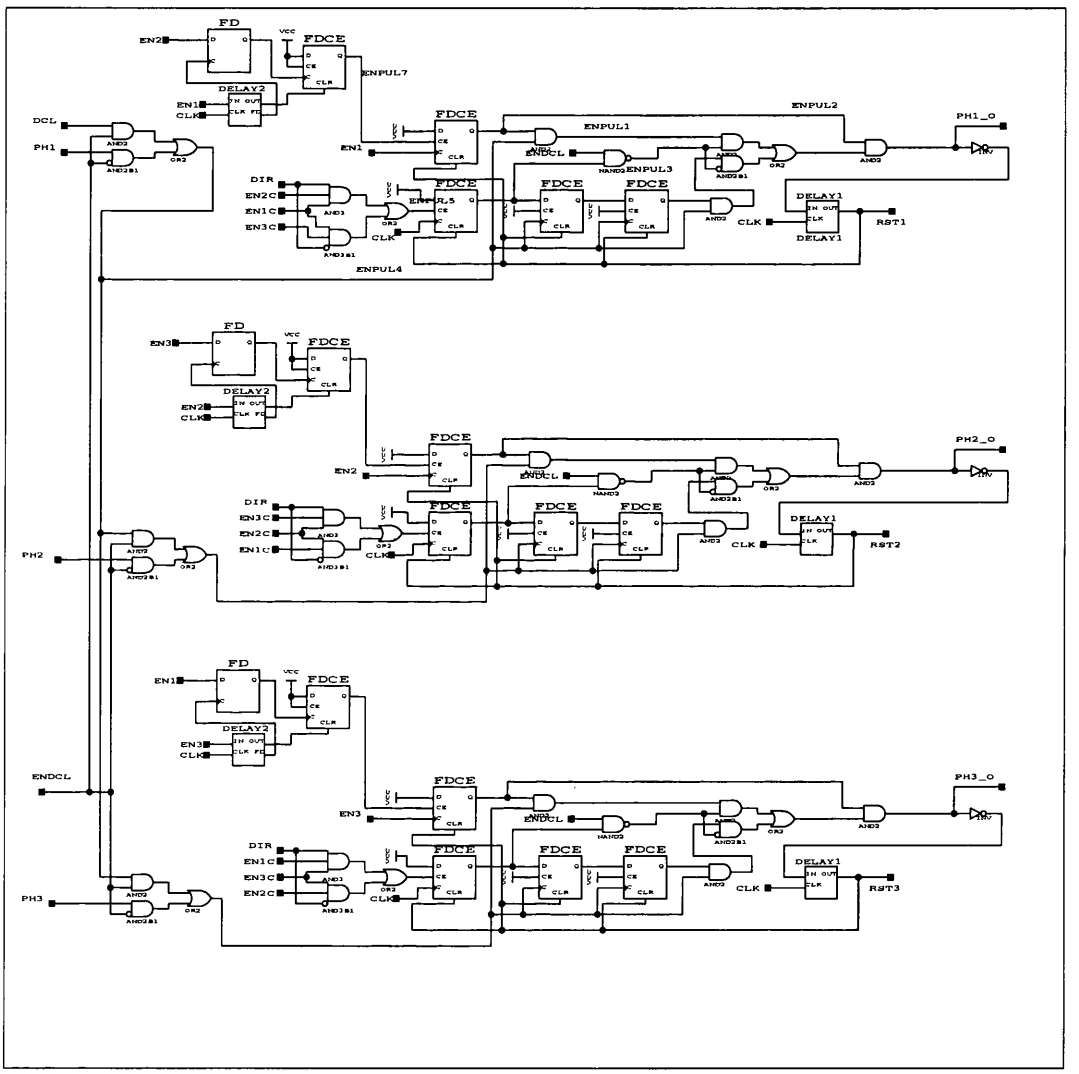

Figure C.10: Schematic diagram of the CGSM: enable sensorless pulses.

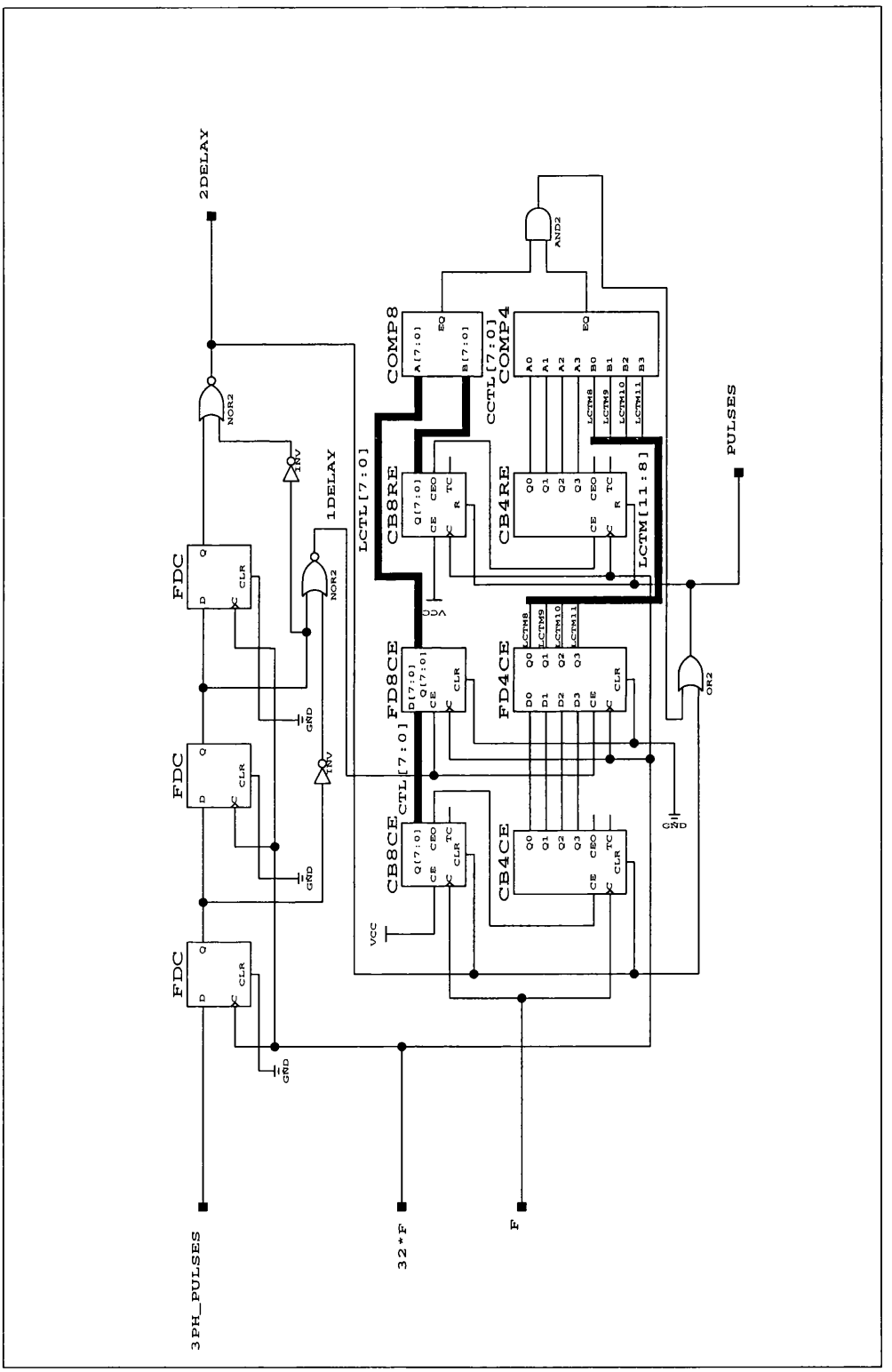

Figure C.11: Schematic diagram of the CGSM: PLL.

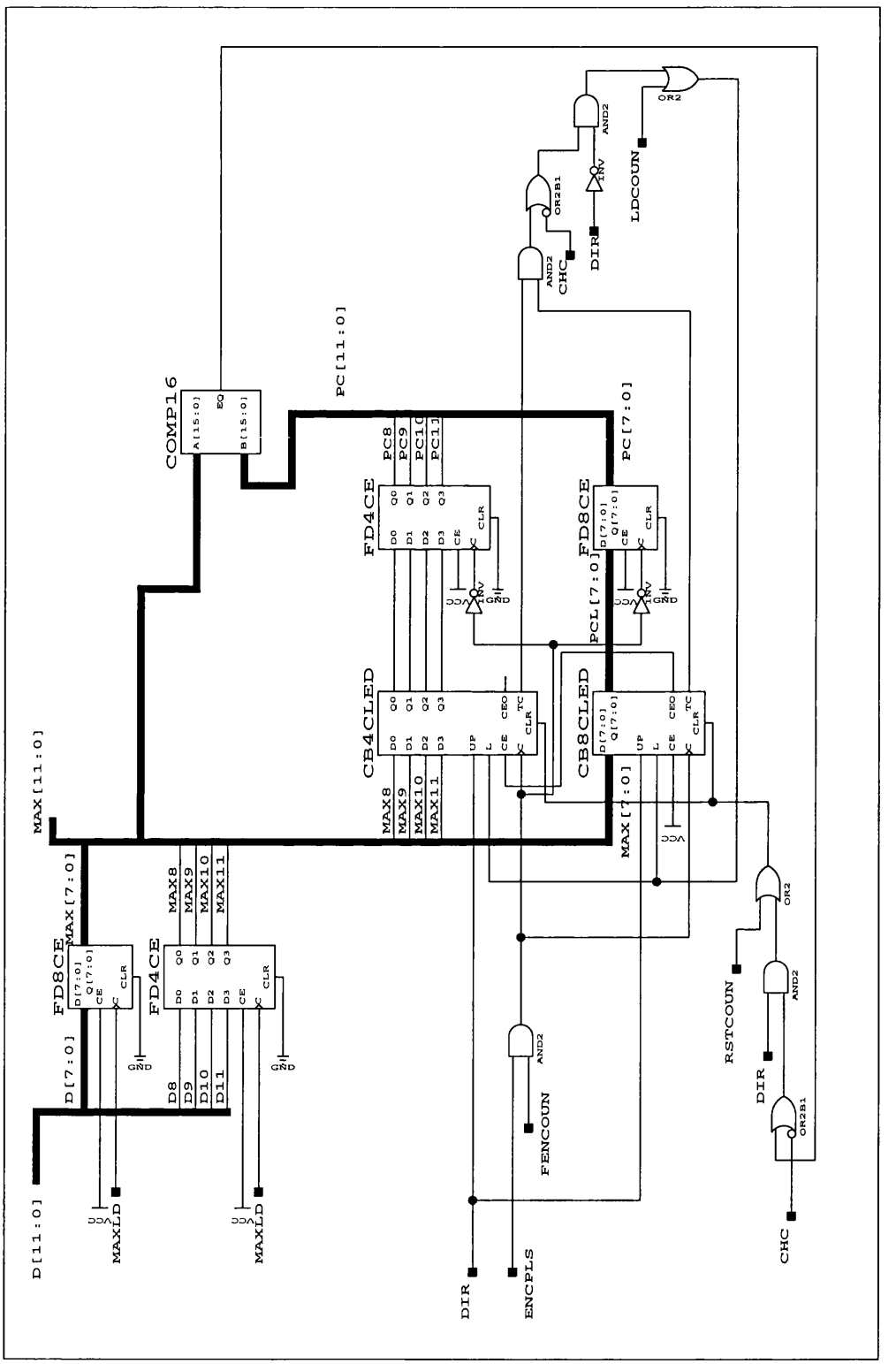

Figure C.12: Schematic diagram of the CGSM: position counter.

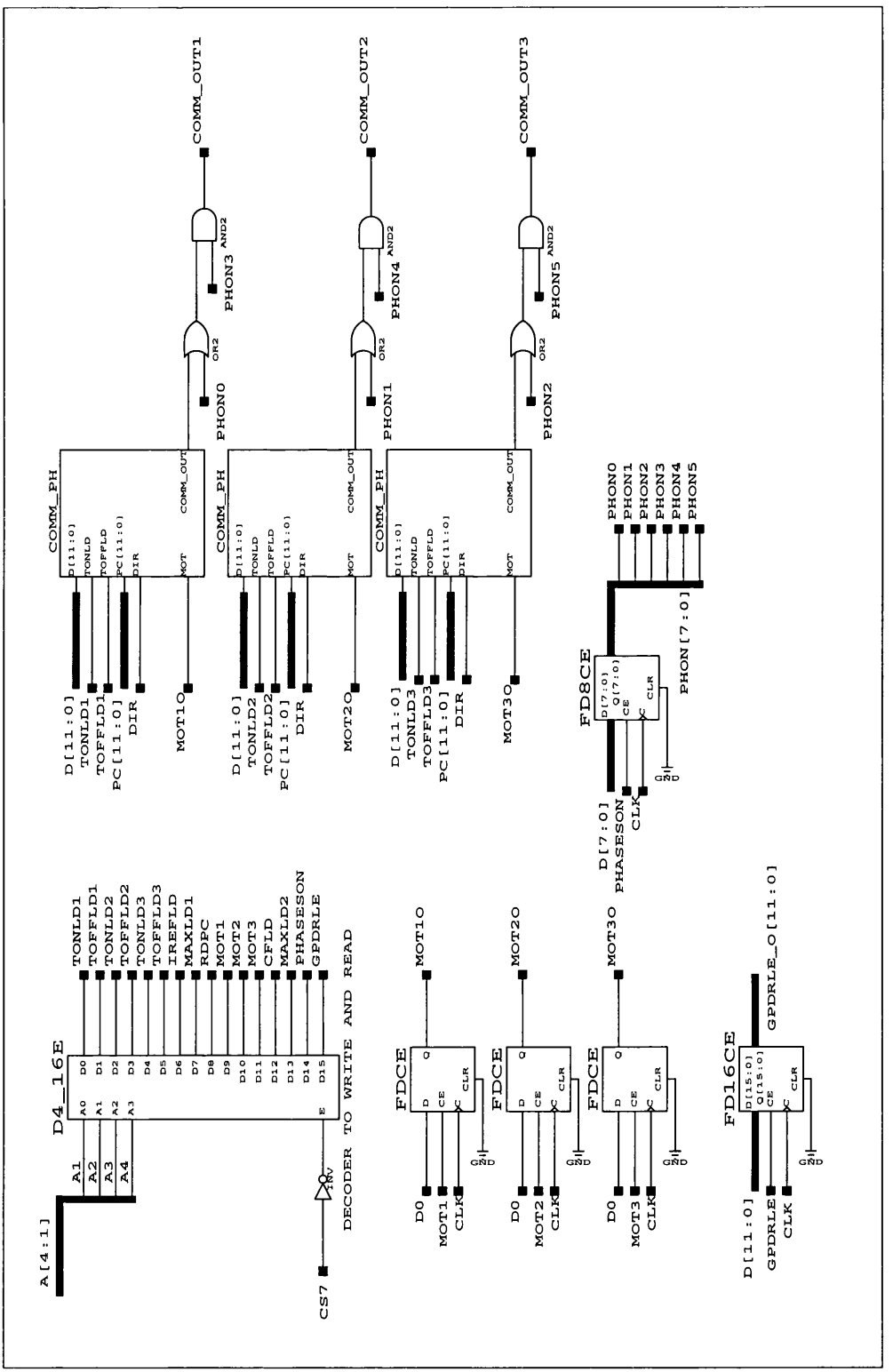

Figure C.13: Schematic diagram of the CGSM: commutation.

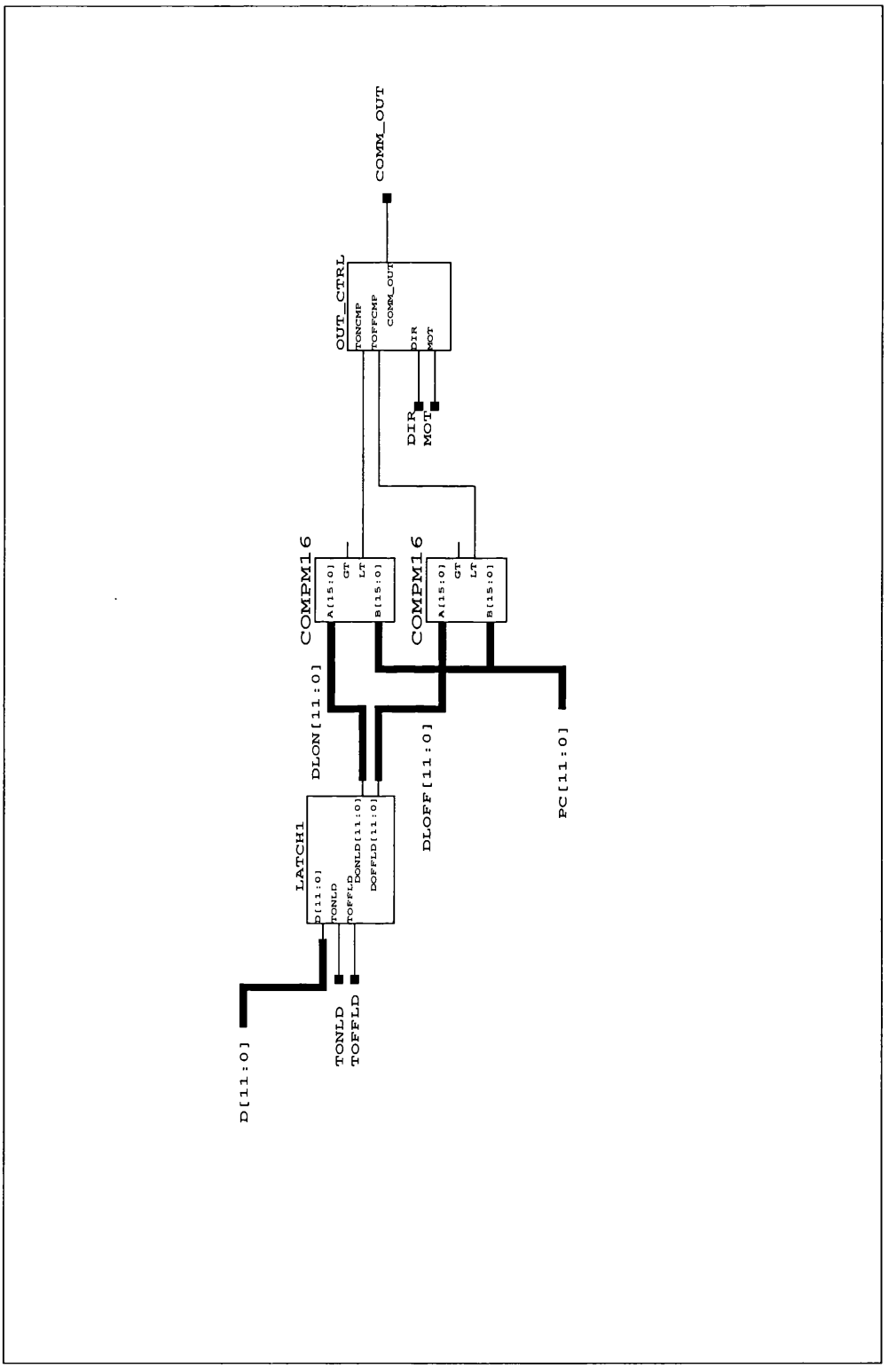

Figure C.14: Schematic diagram of the CGSM: one phase commutation.

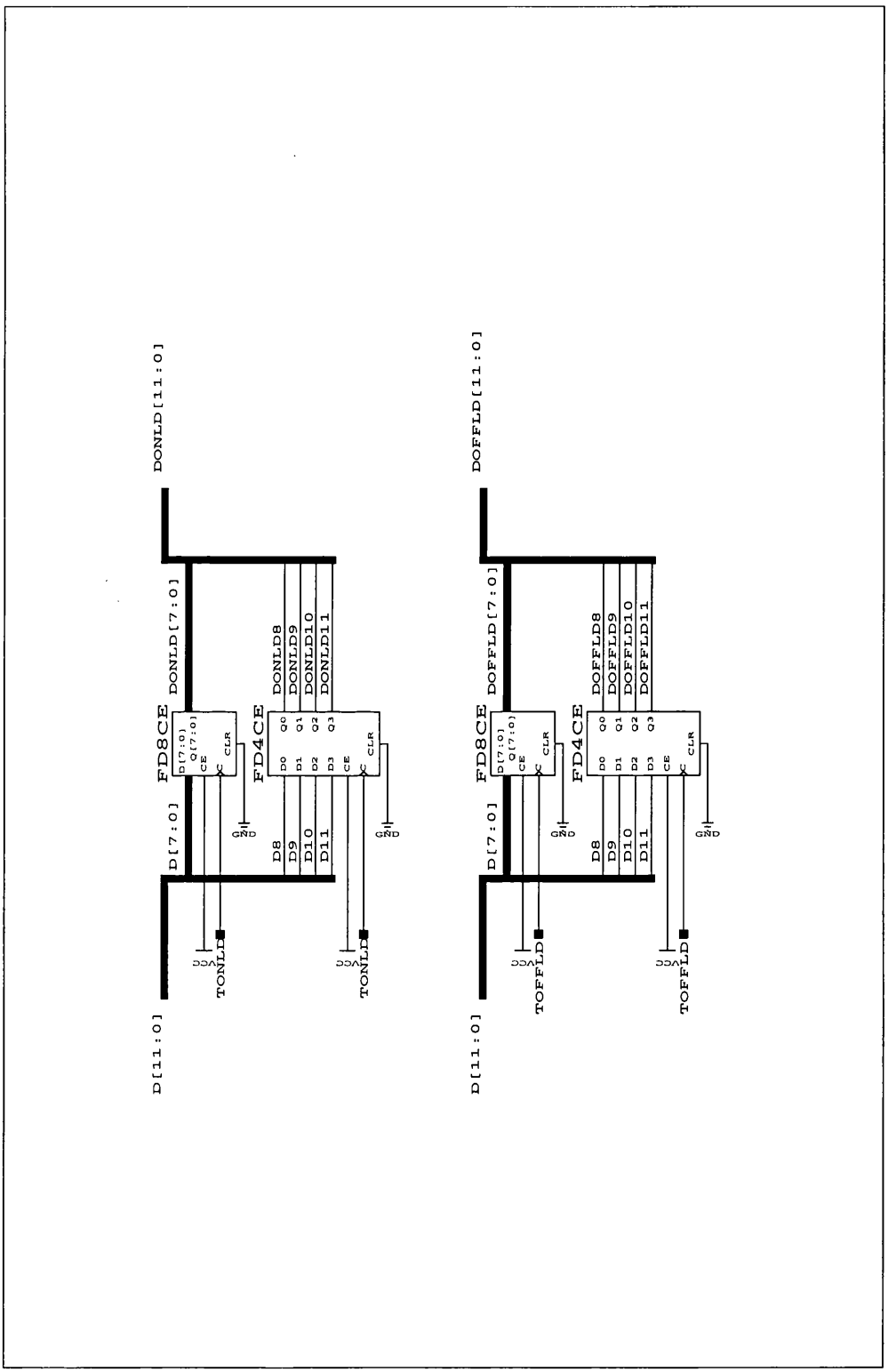

Figure C.15: Schematic diagram of the CGSM: commutation angles latch.

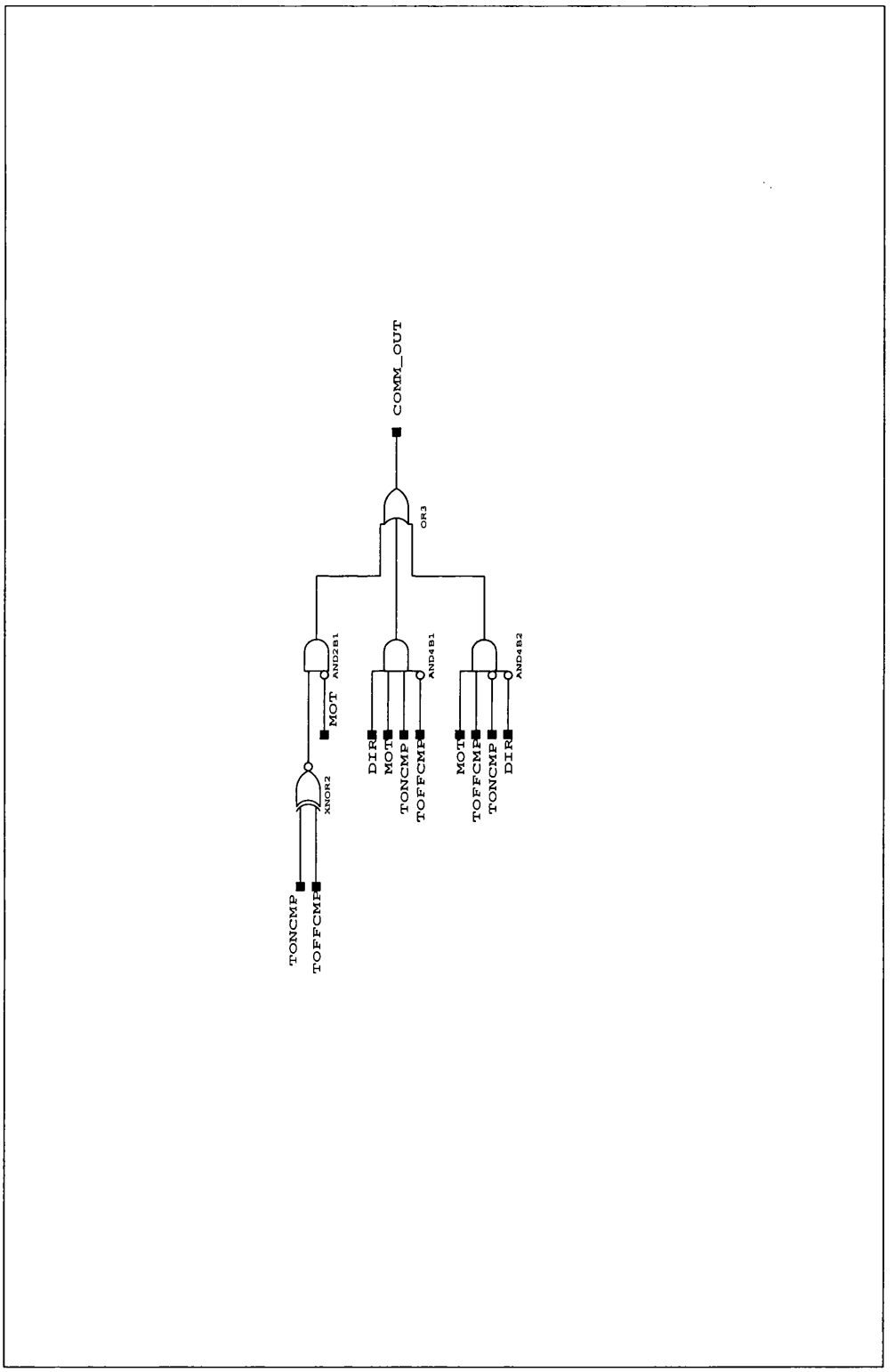

Figure C.16: Schematic diagram of the CGSM: commutation logic.

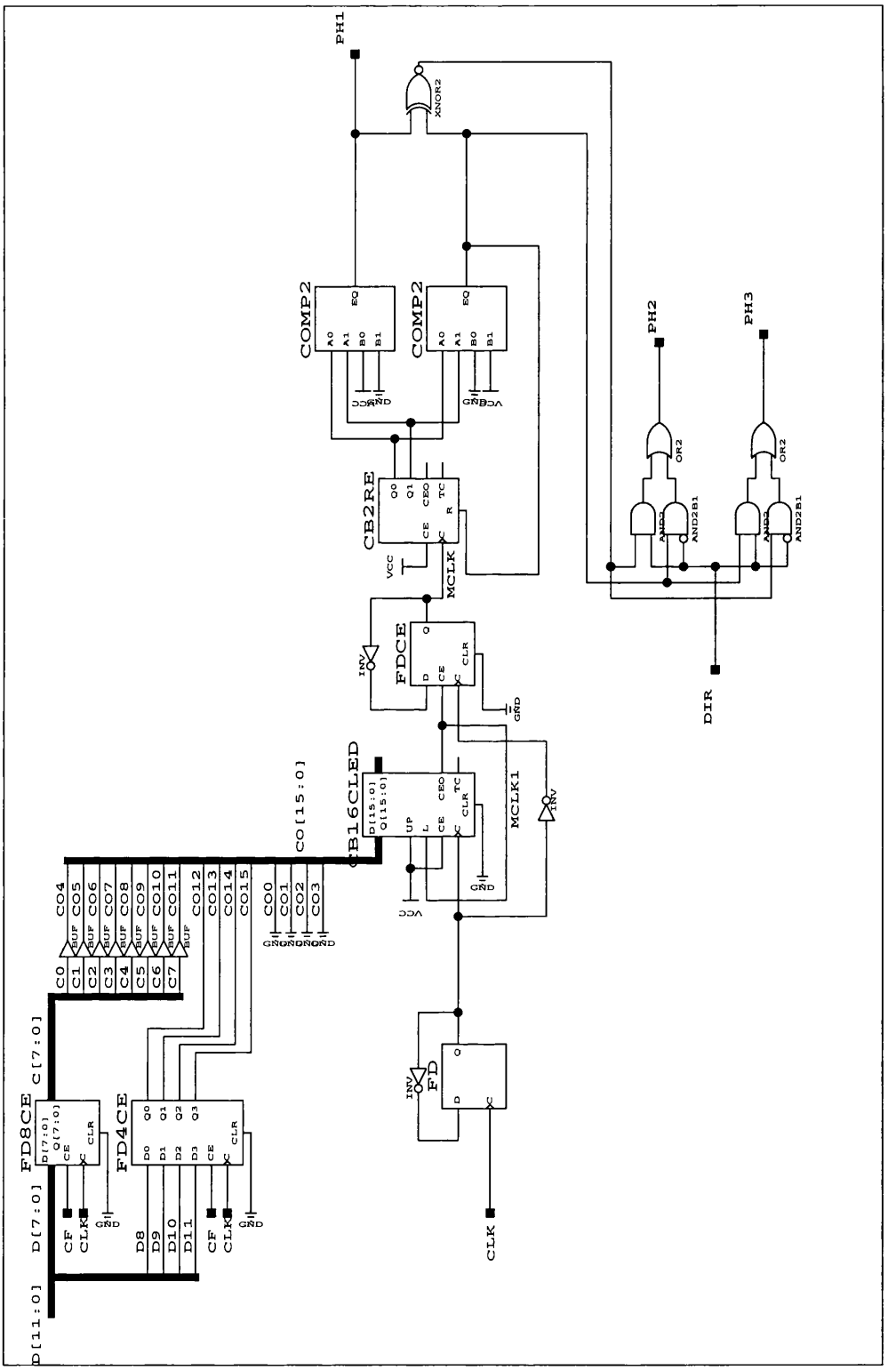

Figure C.17: Schematic diagram of the CGSM: fedforward commutation.

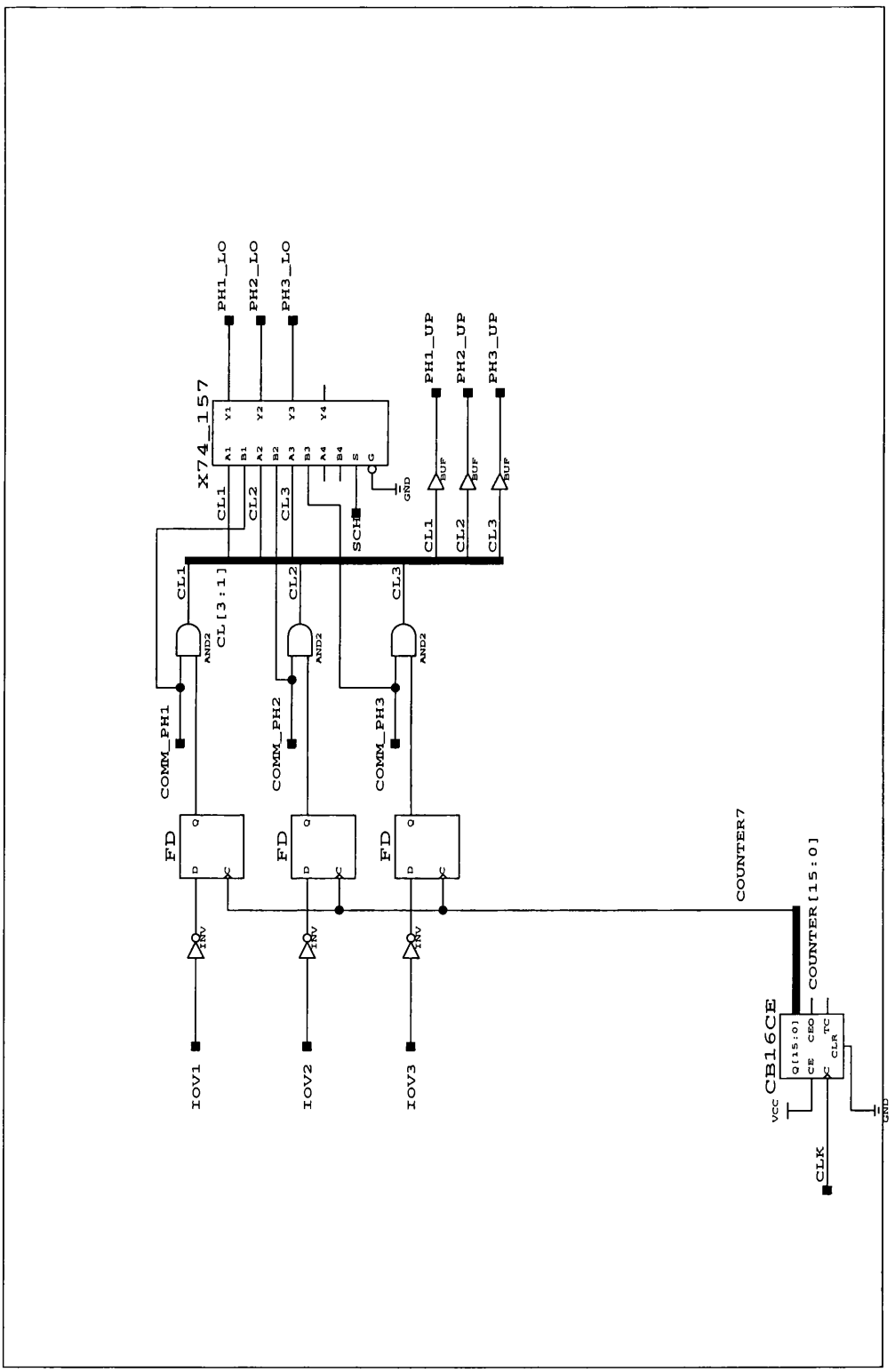

Figure C.18: Schematic diagram of the CGSM: current regulation.

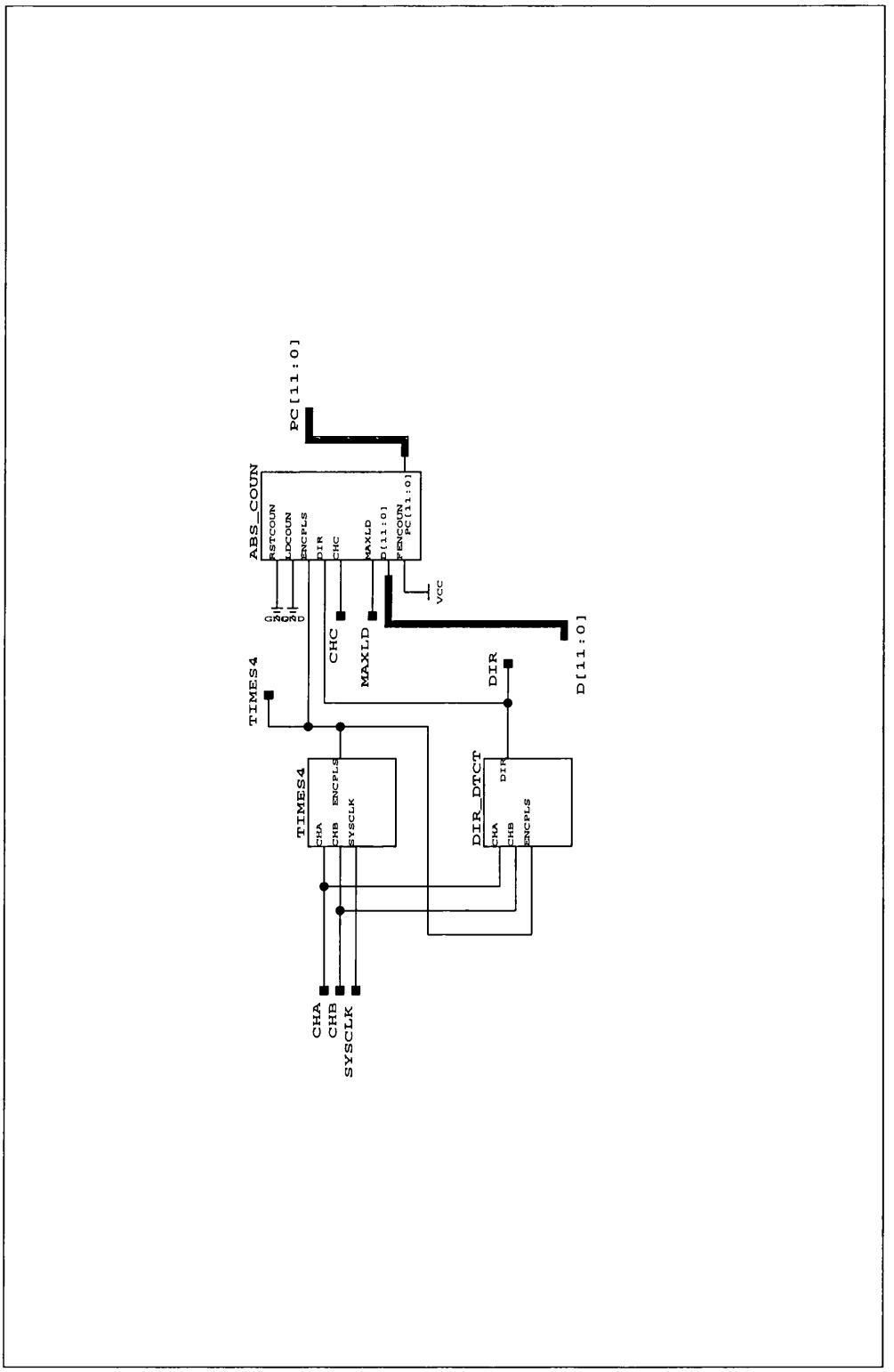

Figure C.19: Schematic diagram of the CGSM: encoder commutation.

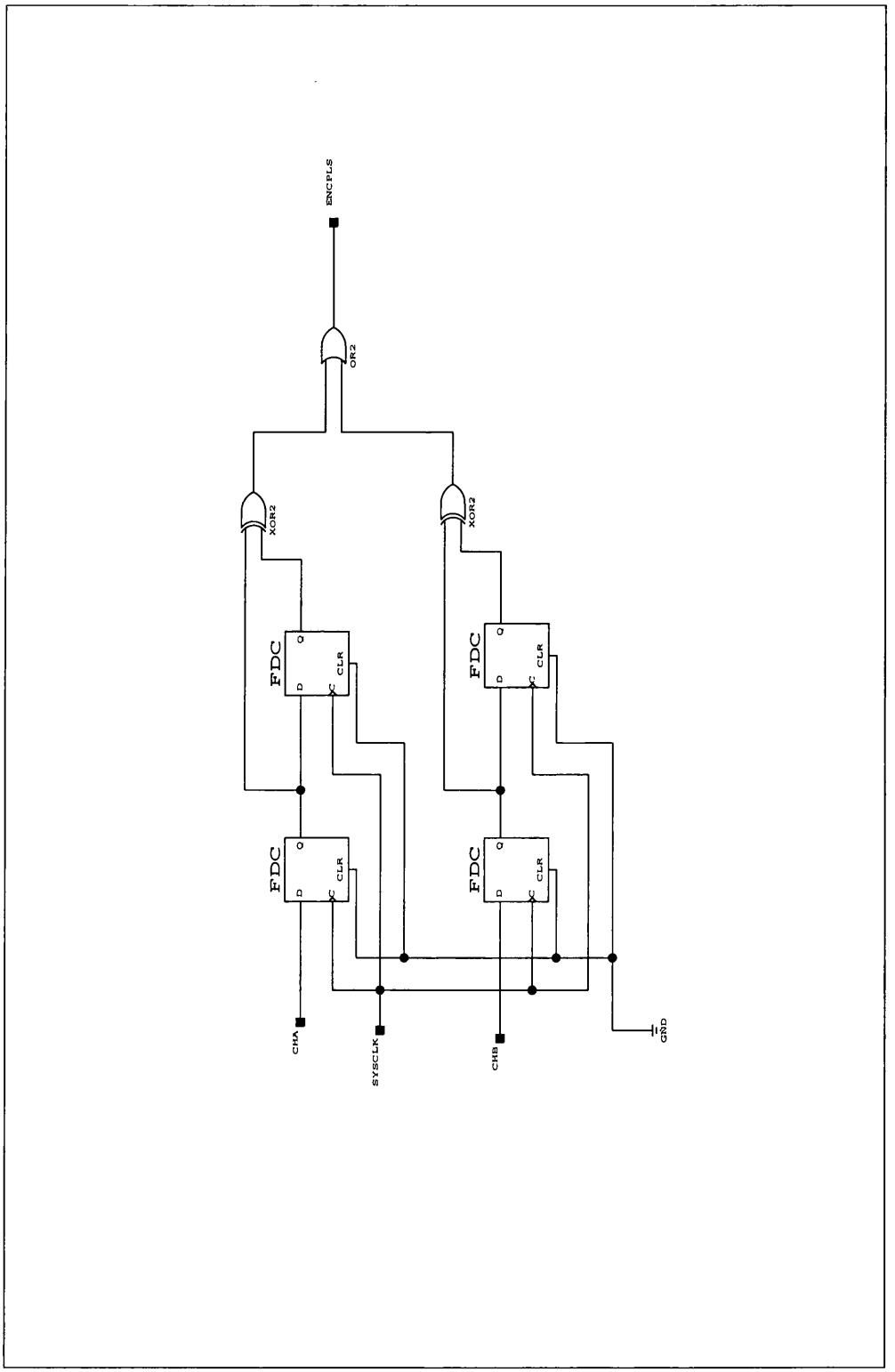

Figure C.20: Schematic diagram of the CGSM: 4 times encoder pulses.

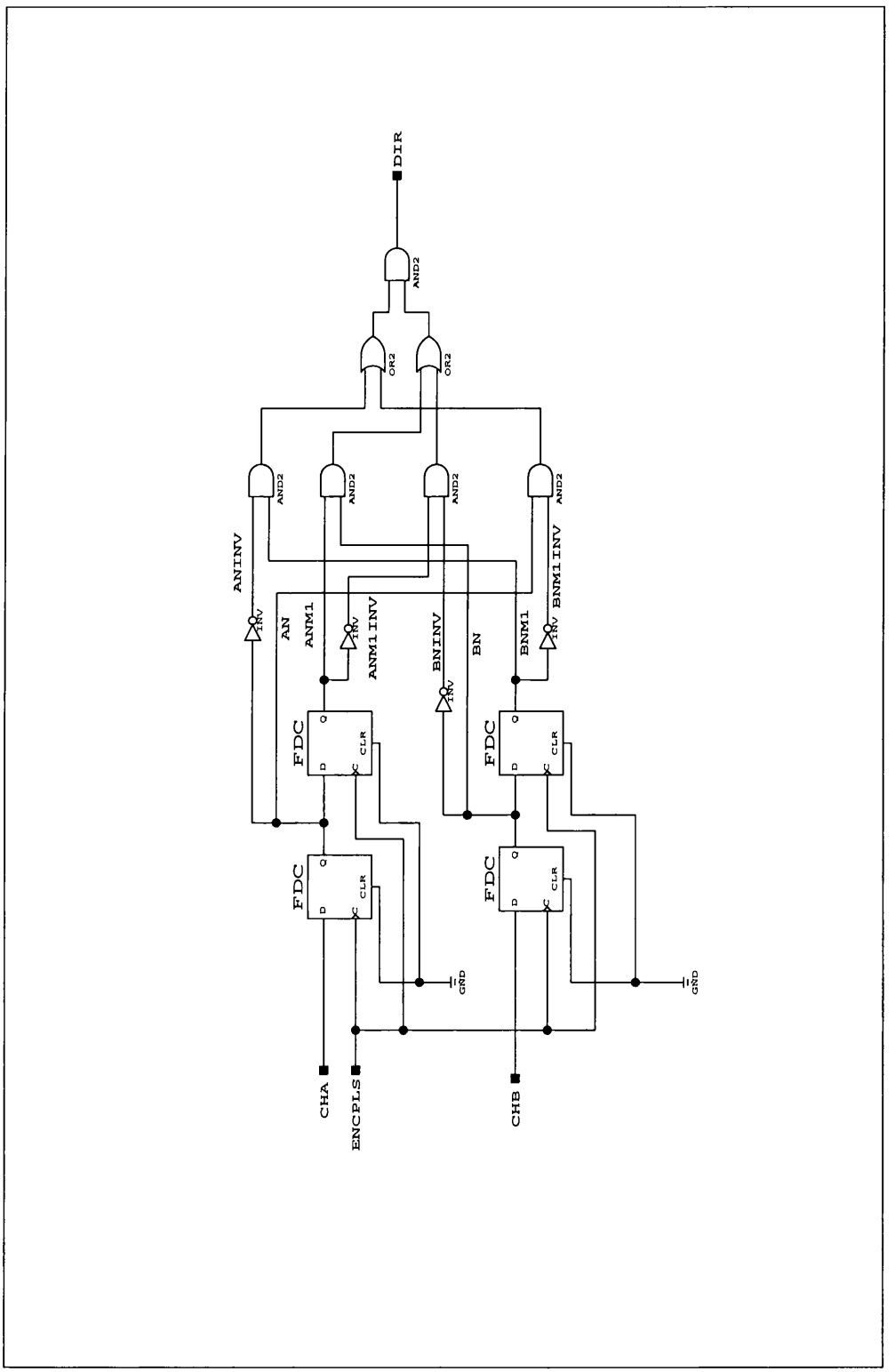

Figure C.21: Schematic diagram of the CGSM: direction detection from encoder.

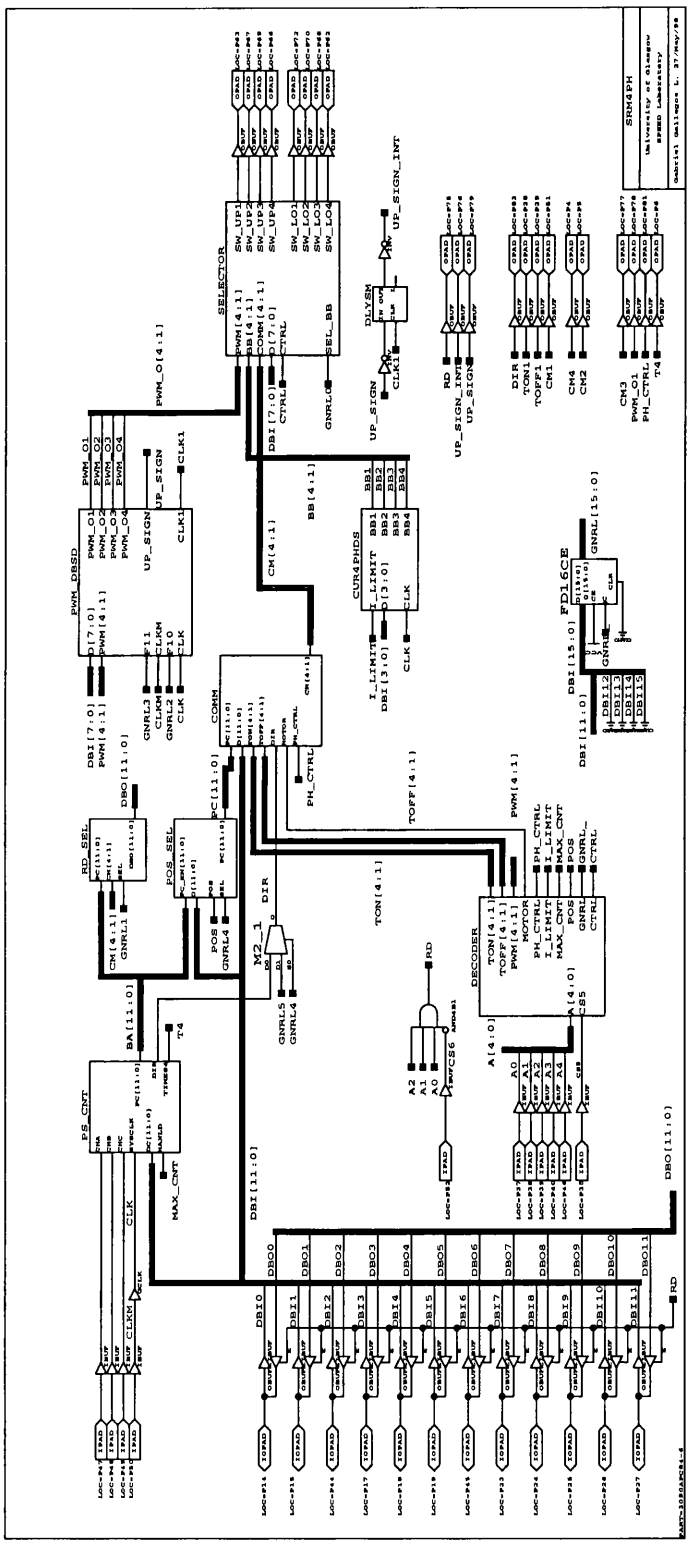

Figure C.22: Schematic diagram of the DSP controller: top level.

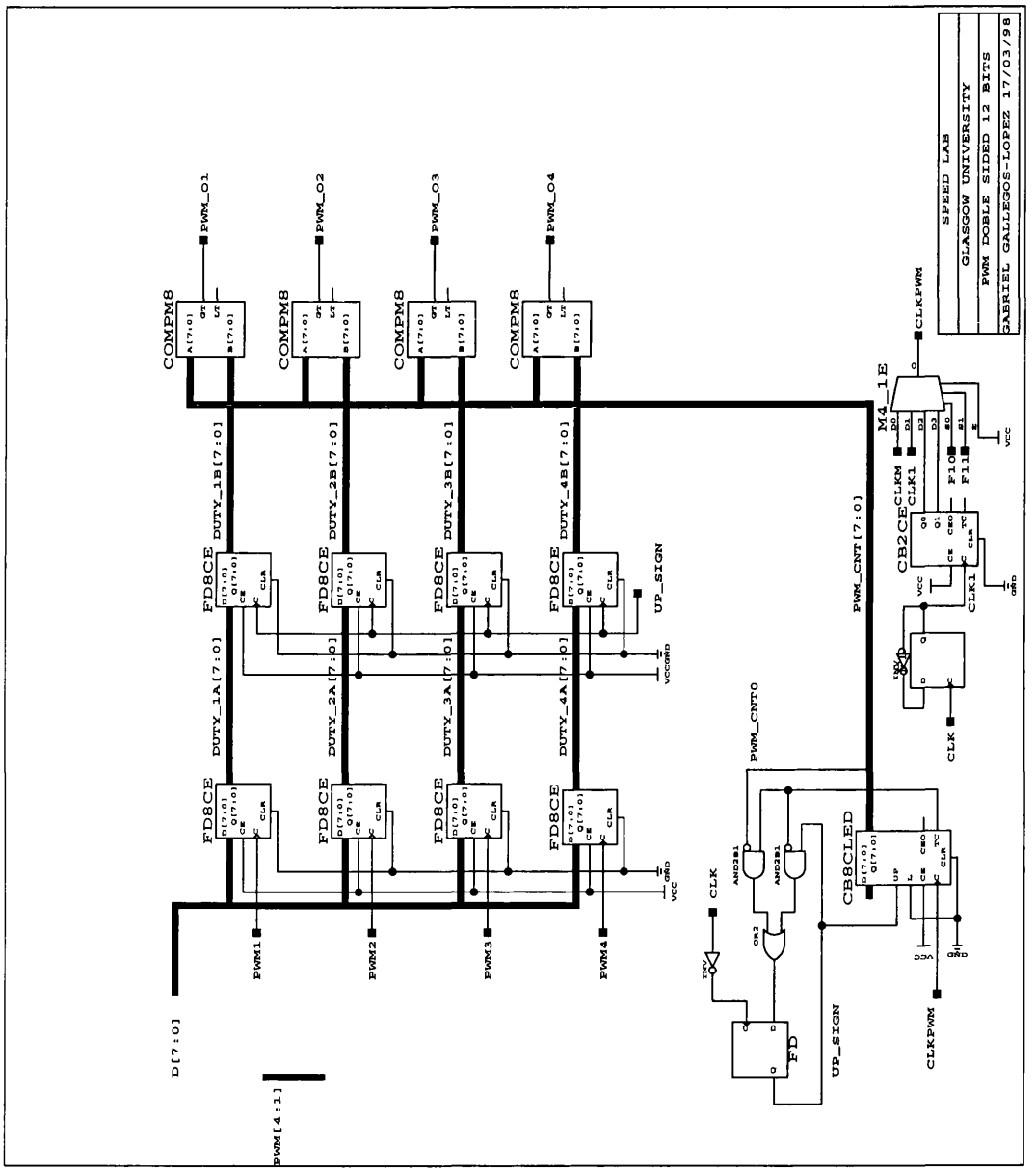

Figure C.23: Schematic diagram of the DSP controller: PWM modulator.

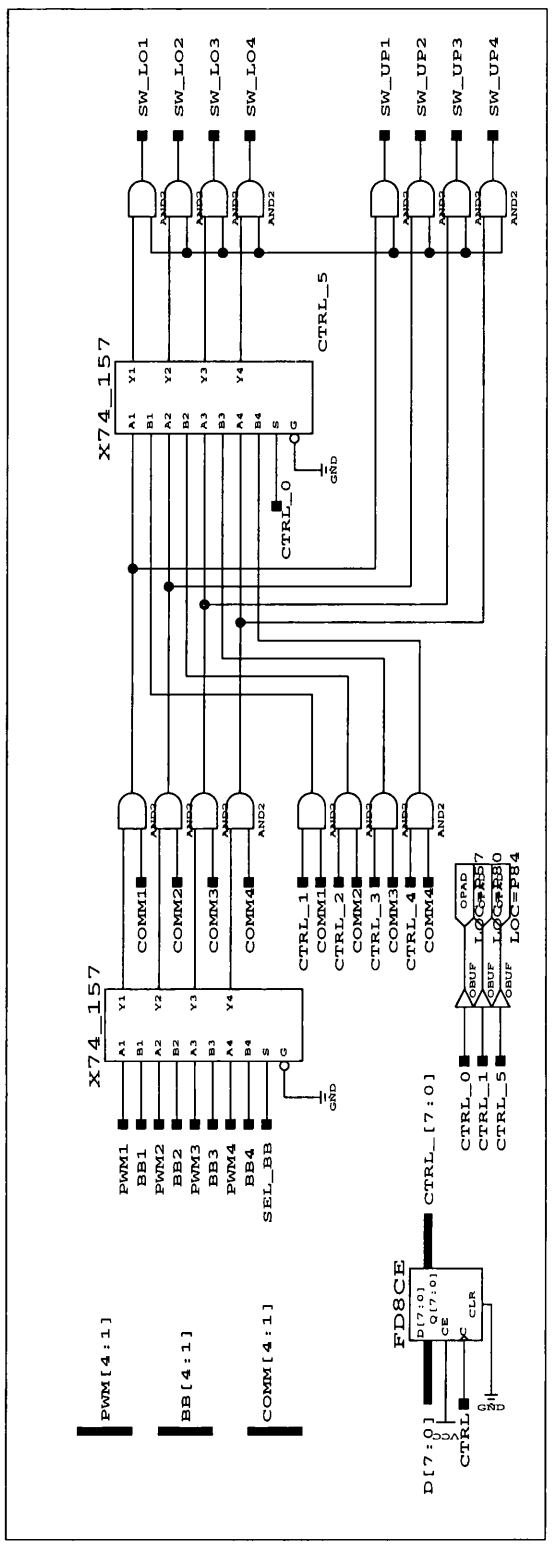

Figure C.24: Schematic diagram of the DSP controller: control mode logic, i.e. soft and hard switching, current Bang-Bang control.

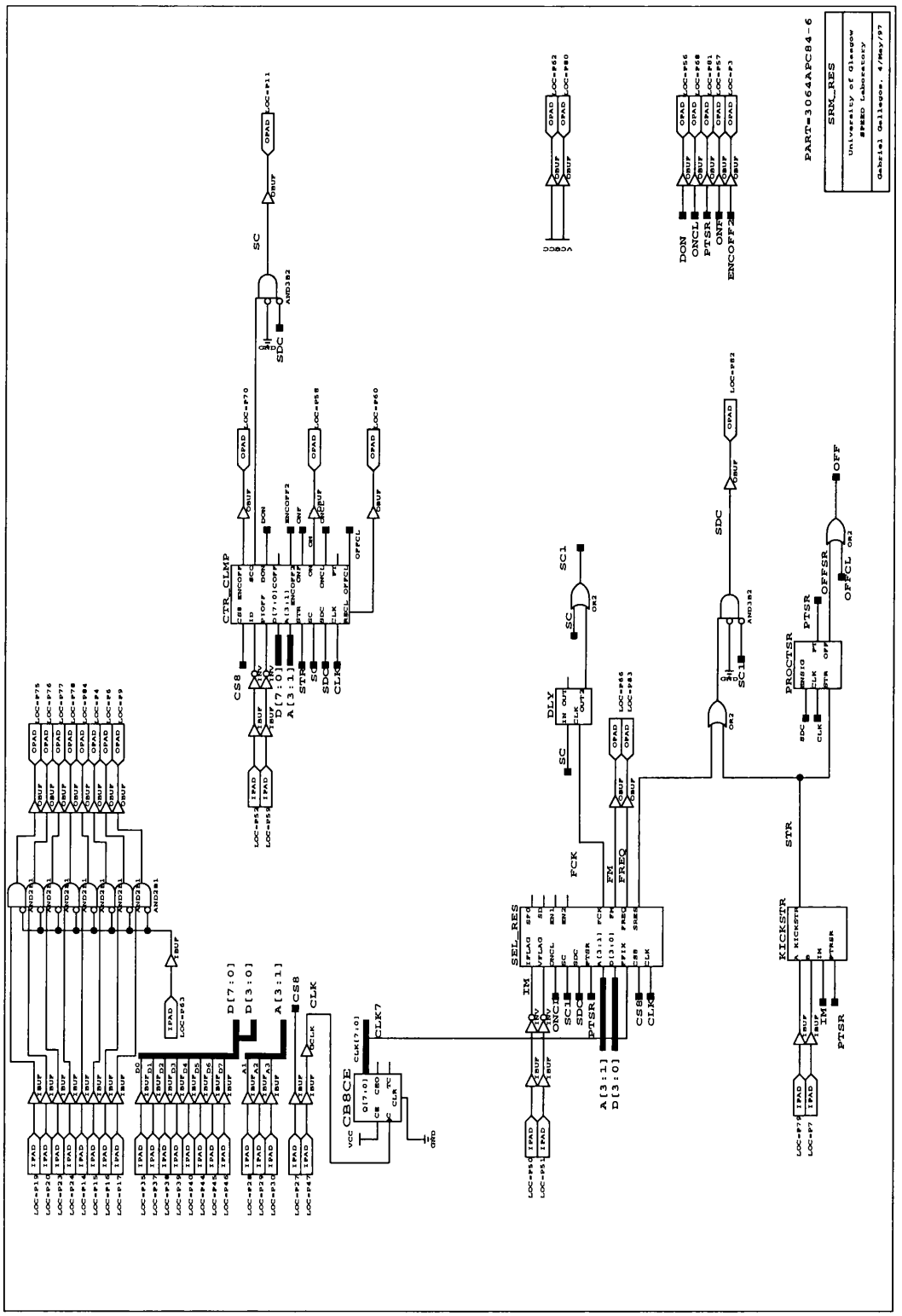

Figure C.25: Schematic diagram of the active resonant dc-link controller: top level.

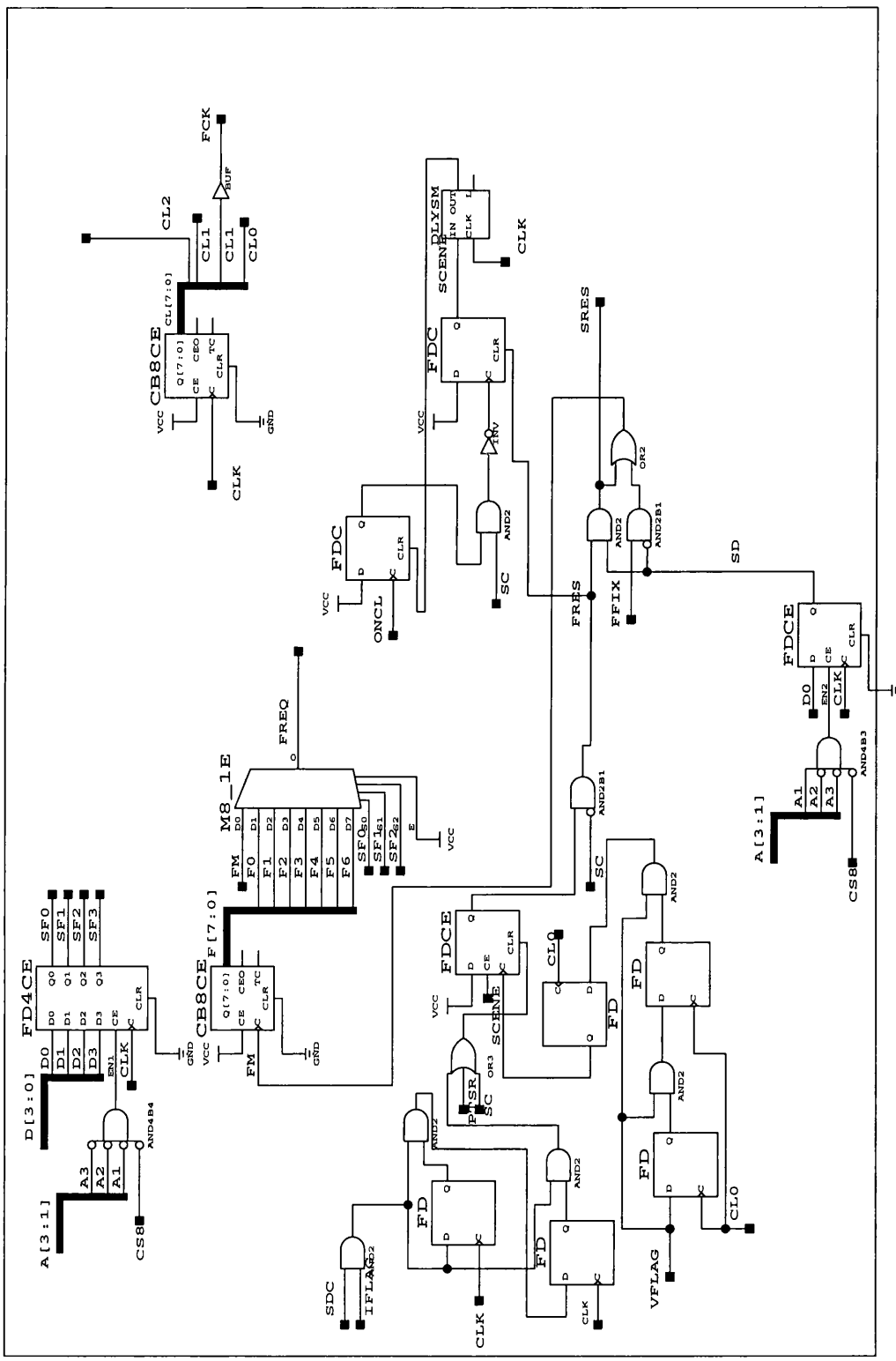

Figure C.26: Schematic diagram of the active resonant dc-link controller: control logic of the resonant IGBT S_{dc} and selection of synchronisation frequency.

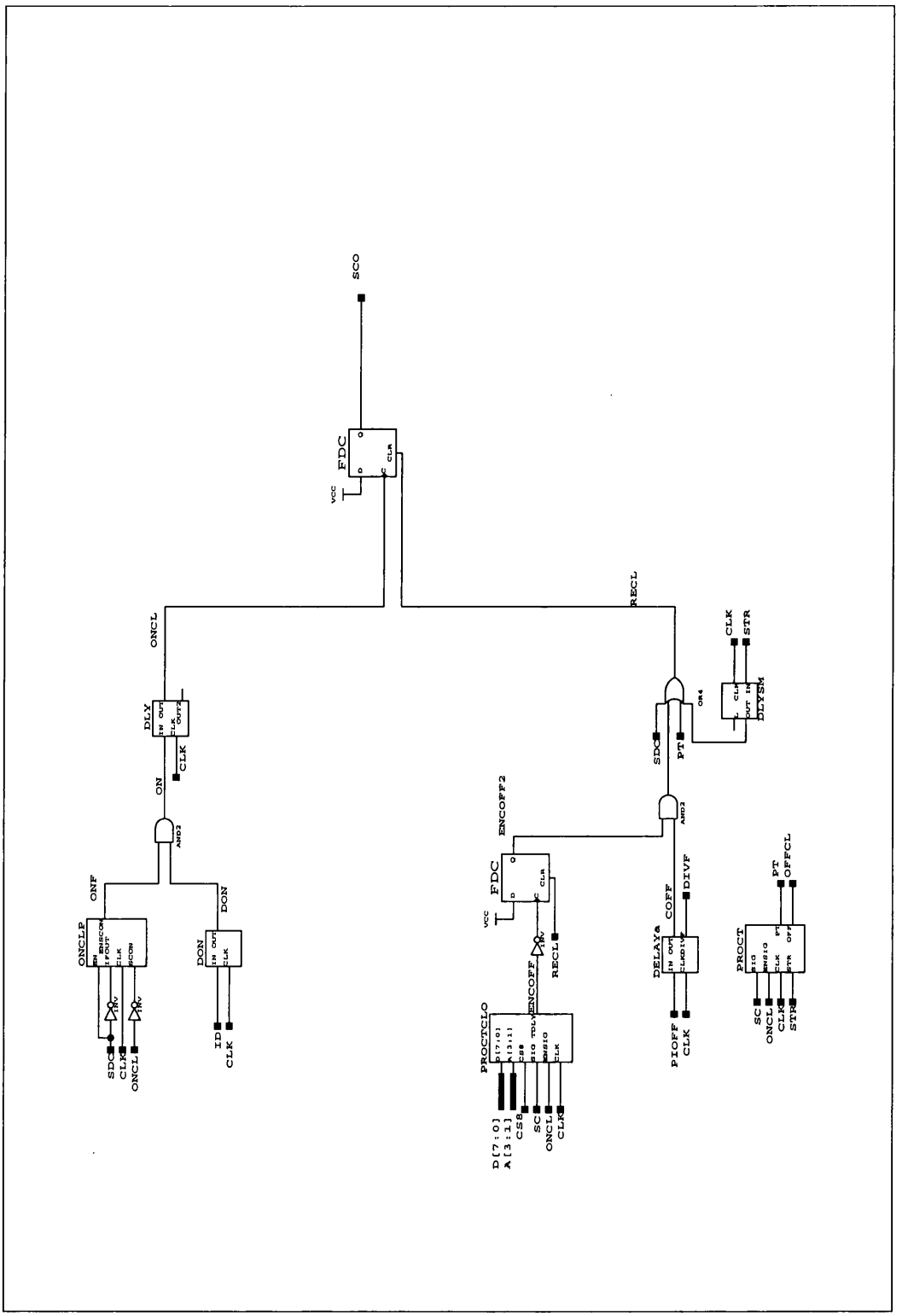

Figure C.27: Schematic diagram of the active resonant dc-link controller: control logic of the active clamp IGBT S_c.

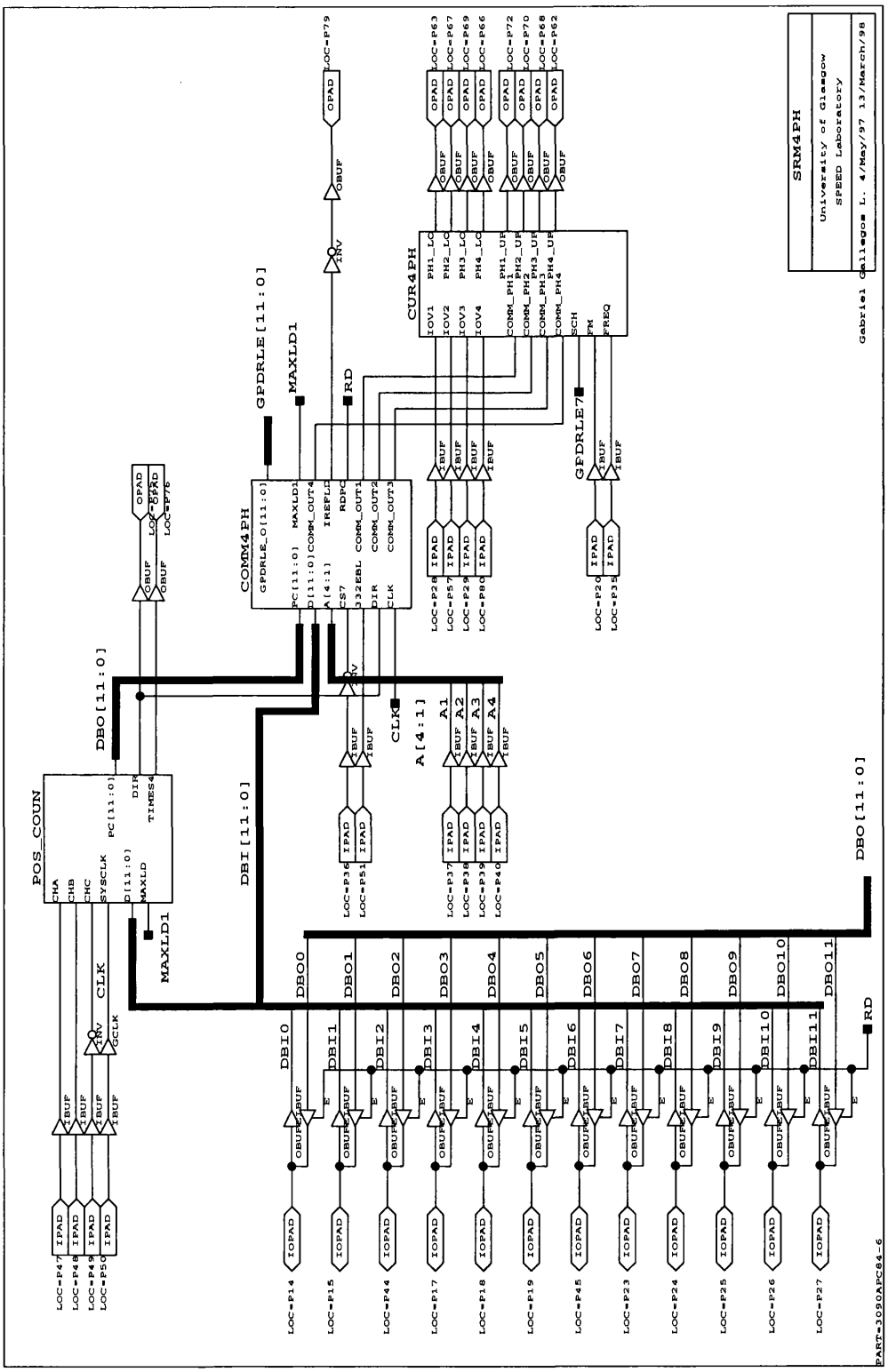

Figure C.28: Schematic diagram of the 4 phase SRM commutation control synchronised with the resonant frequency: top level.

Appendix D

Author's publications

1. *Gabriel Gallegos-López*, P.C. Kjær, T.J.E. Miller, High-grade Position Estimation for SRM Drives Using Flux linkage/Current Model, Proc. IAS'98, To be presented in IAS Annual Meeting in St. Louis, MO, USA, 1998

2. T.J.E. Miller, M. Glinka, M. McGilp, C. Cossar, *Gabriel Gallegos-López*, D. Ionel, M. Olaru, Ultra-fast Model of the Switched Reluctance Motor, Proc. IAS'98, To be presented in IAS Annual Meeting in St. Louis, MO, USA, 1998.

3. *Gabriel Gallegos-López*, P.C. Kjær, T.J.E. Miller, A New Rotor Position Estimation Method for Switched Reluctance Motors Using PWM Voltage Control IEEE Transaction IA, vol. 34, No. 4, pp. 832-840, July/August, 1998.

4. P.C. Kjær, *Gabriel Gallegos-López*, Single-sensor Current Regulation in Switched Reluctance Motor Drives, IEEE Transactions IA, vol. 34, No. 3, pp. 444-451, May/June, 1998.

5. *Gabriel Gallegos-López*, P.C. Kjær, T.J.E. Miller, A New Sensorless Method for Switched Reluctance Motor Drives Proc. IAS'97, vol.1, pp. 564-570, New Orleans, USA, 1997.

6. P.C. Kjær, *Gabriel Gallegos-López*, Single-sensor Current Regulation in Switched Reluctance Motor Drives, Proc. IAS'97, pp. 645-652, New Orleans, USA, 1997.

7. *Gabriel Gallegos-López*, P.C. Kjær, T.J.E. Miller, A New Rotor Position Estimation Method for Switched Reluctance Motors Using PWM Voltage Control Proc. EPE'97, vol. 3, pp. 3.580-3.585, Trondheim, Norway, 1997.

8. *Gabriel Gallegos-López*, P.C. Kjær, T.J.E. Miller, Active Clamp Resonant DC Link Inverter for Current-Controlled Switched Reluctance Motors, Proc. Power Conversion and Intelligent Motion, Nürnberg, Germany, 1997.

9. *Gabriel Gallegos-López*, P.C. Kjær, T.J.E. Miller, G.W. White, Simulation Study of Resonant DC Link Inverter for Current-Controlled Switched Reluctance Motors, Proc. PEDS, pp. 757-761, May, Singapore, 1997.

Bibliography

[1] S.A. Nasar. D.c. switched reluctance motor. *Proc. IEE*, 116(6):1048–1049, 1969.

[2] B.D. Bedford. Compatible permanent magnet or reluctance brushless motors and controlled switch circuits. *US Patent application*, (3678352), July 1972. General Electric Company.

[3] B.D. Bedford. Compatible brushless reluctance motors and controlled switch circuits. *US Patent application*, (3679953), July 1972. General Electric Company.

[4] M.R. Harris, V. Andjargholi, A. Hughes, P.J. Lawrenson, and B. Ertan. Limitations of reluctance torque in doubly-salient structures. *Proc. Int. Conf. on Stepping Motors and Systems*, pages 50–59, 1979.

[5] T.J.E. Miller. Converter volt-ampere requirements of the switched reluctance motor drive. *IEEE Transactions IA*, 21(5):1136–1144, 1985.

[6] P.J. Lawrenson, J.M. Stephenson, P.T. Blenkinsop, J. Corda, and N.N. Fulton. Variable-speed switched reluctance motors. *Proc. IEE B*, (4):253–265, July 1980.

[7] P.J. Lawrenson. A brief status review of switched reluctance drives. *Proc. EPE'92*, 2(3), 1992.

[8] C.A. Ferreira, S.R. Jones, W.S. Heglund, and W.D. Jones. Detailed design of a 30-kw switched reluctance starter/generator system for a gas turbine engine application. *IEEE Transactions IA*, 31(3):553–561, May/June 1995.

[9] E. Richter and C.A. Ferreira. Performance evaluation of a 250 kw switched reluctance starter generator. *Proc. IAS'95*, pages 434–440, 1995.

[10] C.A. Ferreira and E. Richter. About channel independence for multi channel switched reluctance generating systems. *Proc. IAS'96*, pages 816–821, 1996.

[11] D.E. Cameron, J.H. Lang, and S.D. Umans. The origin and reduction of acoustic noise in doubly salient variable-reluctance motors. *IEEE Transactions IA*, 28(6):1250–1255, November/December 1992.

[12] C.Y. Wu and C. Pollock. Analysis and reduction of vibration and acoustic noise in the switched reluctance drive. *IEEE Transaction IA*, pages 91–98, 1995.

[13] C. Pollock and C.Y. Wu. Acoustic noise cancellation techniques for switched reluctance drives. *Proc. IAS'95*, pages 448–455, 1995.

[14] A. Michaelides and C. Pollock. Reduction of noise and vibration in switched reluctance motors: new aspects. *Proc. IAS'96*, pages 771–778, 1996.

[15] Roy S. Colby, F.M. Mottier, and T.J.E. Miller. Vibration modes and acoustic noise in a four-phase switched reluctance motor. *IEEE Transactions IA*, 32(6):1357–1364, November/December 1996.

[16] M. Ilic-Spong, T.J.E. Miller, S.R. MacMinn, and J.S. Thorp. Instantaneous torque control of electric motor drives. *IEEE Transactions Power Electronics*, 2:55–61, January 1987.

[17] R.S. Wallace and D.G. Taylor. Low-torque-ripple switched reluctance motors for direct-drive robotics. *IEEE Transactions on Robotics and Automation*, 7(6):733–742, December 1991.

[18] R.S. Wallace and D.G. Taylor. A balanced commutator for switched reluctance motors to reduce torque ripple. *IEEE Transactions on Power Electronics*, 7(4):617–626, October 1992.

[19] F. Filicori, C.G. Lo Bianco, and A. Tonielli. Modeling and control strategies for a varible reluctance direct-drive motor. *IEEE Transactions IA*, 40(1):105–115, February 1993.

[20] I. Husain and M. Ehsani. Torque ripple minimization in switched reluctance motor drives by pwm current control. *IEEE Transactions on Power Electronics*, 11(1):83–88, 1996.

[21] A.M. Stankovic, G. Tadmor, and Z.J. Coric. Low torque ripple control of current-fed switched reluctance motors. *Proc. IAS*, pages 84–91, December 1996.

[22] P.C Kjaer, J.J. Gribble, and T.J.E. Miller. High-grade control of switched reluctance machines. *IEEE Transaction IA*, 33(6):1585–1593, November/December 1997.

[23] B.K. Bose, T.J.E. Miller, P.M. Szczesny, and W.H. Bicknell. Microcomputer control of switched reluctance motor. *IEEE Transaction Industrial Electronics*, IA-22:708–715, 1986.

[24] W.F. Ray, R.M. davis, and R.J. Blake. The control of sr motors. *Conference on Applied Motion Control*, pages 137–145, June 1986.

[25] T.J.E. Miller, P.G. Bower, R. Becerra, and M. Ehsani. Four-quadrant brushless reluctance motor drive. *IEE Conference on Power Electronics and Variable speed drives*, July 1988. London.

[26] R.C. Becerra, M. Ehsani, and T.J.E. Miller. Commutation of sr motors. *IEEE Transaction on Power Electronics*, 8(3):257–263, July 1993.

[27] P.H. Chappell, W.F. Ray, and R.J. Blake. Microprocessor control of a variable reluctance motor. *Proc. IEE Pt. B*, (2):51–60, March 1984.

[28] Gabriel Gallegos-López, P.C. Kjær, and T.J.E. Miller. A new rotor position estimation method for switched reluctance motors using pwm voltage control. *Proc. EPE'97*, 3:3.580–3.585, 1997. Trondheim, Norway.

[29] Gabriel Gallegos-López, P.C. Kjær, and T.J.E. Miller. A new sensorless method for switched reluctance motor drives. *Proc. IAS'97*, 1:564–570, 1997. New Orleans, USA.

[30] Gabriel Gallegos-López, P.C. Kjær, and T.J.E. Miller. A new rotor position estimation method for switched reluctance motors using pwm voltage control. *IEEE Transaction IA*, 34(4), July/August 1997.

[31] Gabriel Gallegos-López, P.C. Kjær, and T.J.E. Miller. High-grade position estimation for srm drives using flux linkage/current model. *Proc. IAS'98*, 1998. To be presented in IAS Annual Meeting in St. Louis, MO, USA.

[32] Gabriel Gallegos-López, P.C. Kjær, and T.J.E. Miller. Simulation study of resonant dc link inverter for current-controlled switched reluctance motors. *Proc. PEDS*, pages 757–761, May 1997. Singapore.

[33] Gabriel Gallegos-López, P.C. Kjær, and T.J.E. Miller. Active clamp resonant dc link inverter for current-controlled switched reluctance motors. *Proc. Power Conversion and Intelligent Motion*, 1997. Nürnberg, Germany.

[34] T.J.E. Miller. *Switched Reluctance Motors and their Control.* Number 31 in Monographs in electrical and electronic engineering. Magna Physics Publication, Clarendon Press, Oxford, 1993. ISBN 0-19-859387-2.

[35] G. Horst. *US Patent*, (5122697), 1992.

[36] P.J. Lawrenson, J.M. Stephenson, N.N. Fulton, and J. Corda. Switched reluctance motors for traction drives. *Ibid.*

[37] R.M. Davis et al. Inverter drive for switched reluctance motor: circuits and component ratings. *Proc. IEE B*, 128:126–136, March 1981.

[38] TJE Miller. Brushless reluctance motor drives. *IEE Power Engineering*, 1:283–289, 1987.

[39] R. Krishnan, S. Aravind, and P. Materu. Computer-aided design of electrical machines for variable speed applications. *Proc. IEEE-IECON*, pages 756–763, 1987. Cambridge.

[40] J.T. Bass, M. Ehsani, TJE MILLER, and R.L. Steigerwald. Development of a unipolar converter for switched reluctance motor drives. *IEEE Transactions IA*, 23:545–553, 1987.

[41] Slobodan Vukosavic and Victor R. Sefanovic. Srm inverter topologies: A comparative evaluation. *IEEE Transactions IA*, 27(6):1034–1047, November/December 1991.

[42] P. Sood. A dual-rail power converter for switched reluctance motor drives. *Patent pending.* ESCD - emerson Elecrtic, St. Louis.

[43] C. Cossar and T.J.E. Miller. Electromagnetic testing of switched reluctance motors. *ICEM'92*, 2:470–474, September 1992. Manchester.

[44] Pc-srd 6.91 user's manual. *SPEED Laboratory*, 1997. Glasgow.

[45] T.J.E. Miller, M. Glinka, M. McGilp, C. Cossar, Gabriel Gallegos-López, D. Ionel, and M. Olaru. Ultra-fast model of the switched reluctance motor. *Proc. IAS'98*, 1998. To be presented in IAS Annual Meeting in St. Louis, MO, USA.

[46] J.M. Stephenson and J. Corda. Computation of torque and current in double-salient reluctance motors from nonlinear magnetization data. *Pro. IEE*, 126(5):393–396, 1979.

[47] T.J.E. Miller and M. McGilp. Nonlinear theory of the switched reluctance motor for rapid computer-aided design. *Proc. IEE B*, 137(6):337–347, 1990.

[48] T.J.E. Miller, M. Glinka, M. McGilp, C. Cossar, G. Gallegos-López, D. Ionel, and M. Olaru. Ultra-fast model of the switched reluctance motor. *Proc. IAS'98*, 1998.

[49] D.J.W. Pulle. New data base for switched reluctance drive simulation. *Pro. IEE B*, 138(6):331–337, 1991.

[50] W.F. Ray and I.H. Al-Bahadly. Sensorless methods for determining the rotor position of switched reluctance motors. *Proc. of EPE'93*, 6:7–13, 1993.

[51] P.P. Acarnley, R.J. Hill, and C.W. Hooper. Detection of rotor position in stepping and switched reluctance motors by monitoring of current waveforms. *IEEE Transaction IE*, 32(3):215–222, 1985.

[52] T.J.E. Miller and J.T. Bass. Switched reluctance motor drive operating without a shaft position sensor. *US Patent*, (4611157), September 9 1986. General Electric Company.

[53] J.T. Bass, M. Ehsani, and T.J.E. Miller. Robust torque control of switched-reluctance motors without a shaft position sensor. *IEEE Transaction IE*, IE-33(33):212–216, 1986.

[54] J.L. Oldenkamp. Reversible switched reluctance motor operating without a shaft position sensor. *US Patent*, (5440218), August 8 1995. General Electric Company.

[55] S. Vukosavic et al. Sensorless operation of the sr motor with constand dwell. *Proc. IEEE PESC'90*, pages 451–454, 1990.

[56] R.J. Hill and P.P. Acarnley. Stepping motors and drive circuits therefor. *US Patent*, (4520302), May 28 1985. National Research Development Corporation, London, England.

[57] S.K. Panda and G.A.J. Amaratunga. Waveform detection technique for indirect rotor-position sensing of switched-reluctance motor drives. i. analysis. *IEE Proceedings B*, 140(1):80–88, January 1993.

[58] S.K. Panda and G.A.J. Amaratunga. Waveform detection technique for indirect rotor-position sensing of switched-reluctance motor drives. ii. experimental results. *IEE Proceedings B*, 140(1):89–96, January 1993.

[59] S.K. Panda and G.A.J. Amaratunga. Analysis of the waveform-detection technique for indirect rotor-position sensing of switched reluctance motor drives. *IEEE Transaction EC*, 6(3):476–483, September 1991.

[60] S.K. Panda and G.A.J. Amaratunga. Comparison of two techniques for closed-loop drive of vr step motors without direct rotor position sensing. *IEEE Transation IE*, 38(2):95–101, April 1991.

[61] I.J. Obradovic. Control apparatus and method for operating a switched reluctance motor. *US Patent*, (4777419), October 11 1988. Emerson Electric Co.

[62] J.G. Reichard and D.B. Weber. Switched reluctance electric motor with regeneration current commutation. *US Patent application*, (C.7566-2306), May 23 1989. A.O. Smith Corporation.

[63] G. Hedlund and H. Lundberg. Energizing system for a variable reluctance motor. *US Patent*, (5043643), August 27 1991. EMS Electronic Motor System AB.

[64] J.P. Lyons, S.R. MacMinn, and M.A. Preston. Flux/current methods for srm rotor position estimation. *Proc. IEEE-IAS'91*, pages 482–487, 1991.

[65] J.P. Lyons and S. MacMinn. Rotor position estimator for a switched reluctance machine. *US Patent*, (5097190), March 17 1992. General Electric Company.

[66] J.P. Lyons, S.R. MacMinn, and M.A. Preston. Discrete position estimator for a switched reluctance machine using a flux-current map comparator. *US Patent*, (5140243), August 18 1992. General Electric Company.

[67] W.F. Ray. Sensorless rotor position measurement in electric machines. *US Patent*, (5467025), November 14 1995. Switched Reluctance Drives Limited.

[68] W.F. Ray and I.H. Al-Bahadly. A sensorless method for determining rotor position for switched reluctance motors. *Conf. Proc. of Power electronics and variable-speed drives*, pages 13–17, October 1994.

[69] J.P. Lyons, S.R. MacMinn, and M.A. Preston. Rotor position estimation for a switched reluctance machine using a lumped paramenter flux/current model. *US Patent*, (5107195), April 21 1992. General Electric Company.

[70] P.P. Acarnley, C.D. French, and I.H. Al-Bahadly. Position estimation in switched-reluctance drives. *Proc. EPE'95*, 3:3.765–3.770, 1995.

[71] N. Ertugrul and P.P. Acarnley. A new algorithm for sensorless operation of permanent magnet motors. *IEEE Transaction IA*, 30(1):126–133, 1994.

[72] C. Elmas and H. Zelaya-De la Parra. Position sensorless operation of a switched reluctance drive based on observer. *Proc. EPE'93*, pages 82–87, 1993.

[73] A. Cheok and N. Ertugrul. A model free fuzzy logic based rotor position sensorless switched reluctance motor drive. *Proc. IEEE-IAS'96*, pages 76–83, 1996.

[74] L. Xu and J. Bu. Position transducerless control of a switched reluctance motor using minimum magnetizing input. *Proc. IEEE-IAS'97*, October 1997.

[75] E. Mese and D.A. Torrey. Sensorless position estimation for variable-reluctance machines using artificial neuronal networks. *Proc. IEEE-IAS'97*, October 1997.

[76] A.H. Lumsdaine and J.H. Lang. State observers for variable-reluctance motors. *IEEE Transaction IA*, 37(2):133–142, 1990.

[77] R.P. Bartos, T.H Houle, and J.H. Johnson. Switched reluctance motor with sensorless position detection. *US Patent*, (5256923), October 26 1993. A.O. Smith Corporation.

[78] P.K. Sood, J.L. Skinner, and D.M. Petty. Method and apparatus of operating a dynamoelectric machine using dc bus current profile. *US Patent*, (5420492), May 30 1995. Emerson Electric Co.

[79] J.G. Marcinkiewicz, J.S. Thorn, and J.L. Skinner. Improved sensorless commutation controller for a poly-phase dynamoelectric machine. *European Patent Application*, (95630049.5), November 29 1995. Emerson Electric Co.

[80] J.Y. Lim. Sensorless switched reluctance motor. *US Patent*, (5589751), December 31 1996. Goldstar Co., Ltd.

[81] S.R. MacMinn, W.J. Rzesos, P.M. Szczesny, and T.M. Jahns. Application of sensor integration techniques to switched reluctance motor drives. *Proc. IEEE-IAS'88*, pages 584–588, 1988.

[82] S.R. MacMinn and P.B. Roemer. Rotor position estimator for switched reluctance motor. *US Patent*, (4772839), September 20 1988. General Electric Company.

[83] S.R. MacMinn, C.M. Stephens, and P.M. Szezesny. Switched reluctance motor drive system and laundering apparatus employing same. *US Patent*, (4959596), September 25 1990. General Electric Company.

[84] T.G. Van Sistine. Switched reluctance motor providing rotor position detection at low speeds without a separate rotor shaft position sensor. *US Patent*, (5525887), June 11 1996. A.O. Smith Corporation.

[85] G. Hedlund and H. Lundberg. Motor energizing circuit. *US Patent*, (4868478), September 19 1989. EMS Electronic Motor System AB.

[86] M. Ehsani, I. Husain, and A.B. Kulkarni. Elimination of discrete position sensor and current sensor in switched reluctance motor drives. *IEEE Transaction IA*, 28(1):128–135, 1992.

[87] M. Ehsani, I. Husain, S. Mahajan, and K.R. Ramani. New modulation encoding techniques for indirect rotor position sensing in switched reluctance motors. *IEEE Transaction IA*, 30(1):85–91, 1994.

[88] M. Ehsani. Position sensor elimination technique for the switched reluctance motor drive. *US Patent*, (5072166), December 10 1991. The Texas A&M University System.

[89] M. Ehsani. Method and apparatus for sensing the rotor position of a switched reluctance motor without a shaft position sensor. *US Patent*, (5291115), March 1 1994. The Texas A&M University System.

[90] M. Ehsani. Method and apparatus for sensing the rotor position of a switched reluctance motor. *US Patent*, (5410235), April 25 1995. The Texas A&M University System.

[91] W.A. Harris, R. Goetz, and K.J. Stalsberg. Switched reluctance motor position by resonant signal injection. *US Patent*, (5196775), March 23 1993. Honeywell Inc.

[92] P. Laurent, M. Gabsi, and M. Multon. Sensorless rotor position analysis using resonant method for switched reluctance motor. *Proc. IEEE-IAS'93*, pages 687–694, 1993.

[93] P. Laurent, B. Multon, E. Hoang, and M. Gabsi. Sensorless rotor position measurement based on pwm eddy current variation for switched reluctance motor. *Proc. EPE'95*, 3:3.787–3.792, 1995.

[94] T.G. Van Sistine, R.P. Bartos, W.L. Mehlhorn, and T.H. Houle. Switched reluctance motor providing rotor position detection at high speeds without a separate rotor shaft position sensor. *US Patent*, (5537019), July 16 1996. A.O. Smith Corporation.

[95] R. Austermann. Circuit arrangement for commutating a reluctance motor. *US Patent*, (5180960), January 19 1993. U.S. Philips Corporation.

[96] I. Husain and M. Ehsani. Rotor position sensing in switched reluctance motor drives by measuring mutually induced voltages. *IEEE Transaction IA*, 30(3):665–672, 1994.

[97] J.P. Lyons and M.A. Preston. Low speed position estimator for switched reluctance machine using flux/current model. *US Patent*, (5525886), June 11 1996. General Electric Company.

[98] P.C. Kjær, F. Blaabjerg, J.K. Pedersen, P. Nielsen, and L. Andersen. A new indirect rotor position detection method for switched reluctance drives. *ICEM'94, Paris*, 2:555–560, 1994.

[99] K. Iizuka, H. Uzuhashi, M. Kano, T. Endo, and K. Mohri. Microcomputer control for sensorless brushless motor. *IEEE Transaction IA*, 21(3):595–601, 1985.

[100] S.R. MacMinn. Starting sequence for reluctance motor drives operating without a shaft position sensor. *US Patent*, (4642543), February 10 1987. General Electric Company.

[101] Motorola. *MC68332 - User's manual*, 1993.

[102] P.C. Kjær and Gabriel Gallegos-López. Single-sensor current regulation in switched reluctance motor drives. *Proc. IAS'97*, pages 645–652, 1997. New Orleans, USA.

[103] P.C. Kjær and Gabriel Gallegos-López. Single-sensor current regulation in switched reluctance motor drives. *IEEE Transactions IA*, 34(3):444–451, May/June 1998.

[104] Texas Instruments - Digital signal processing products. *TMS320C3x - User's guide*, revision l edition, July 1997.

[105] F. Blaabjerg, P.C. Kjær, P.O. Rasmussen, L. Christensen, S. Hansen, and J.R. Kristoffersen. Fast digital current control in switched reluctance motor drives without current feedback filters. *Proc. EPE'97*, 3:3.625–3.630, 1997.

[106] N. Mohan, T.M. Undeland, and W.P. Robbins. *Power electronics - converters, applications, and design.* John wiley & Sons, Inc, second edition, 1995. ISBN 0-471-30576-6.

[107] D.M.Divan. The resonant dc link converter - a new concept in static power conversion. *IEEE Transactions on Industry Applications*, 25(2):317–325, 1989.

[108] Jih-Sheng Lai and B.K. Bose. An induction motor drive using an improved high frequency resonant dc-link inverter. *Proc. IEEE PESC*, pages 792–799, 1990.

[109] D.M. Divan and G. Skibinski. Zero-switching-loss inverters for high-power applications. *IEEE Transactions on Industry Applications*, 25(4):634–643, 1989.

[110] D.M. Divan, G. Venkataramanan, and R.W. De Doncker. Design methodologies for soft switched inverters. *IEEE Transactions on Industry Applications*, 29(1):126–135, 1993.

[111] R.W. De Doncker and J.P. Lyons. An auxiliary quasi-resonant dc link inverter for switched reluctance machines. *Proceedings of 4th European Conference on Power Electronics and Applications*, pages 4.018–4.023, 1991. Firenze.

[112] S. Vukosavic and V.R. Stefanovic. Srm inverter topologies: A comparative evaluation. *IEEE Transactions on Industry Applications*, 27(6):1034–1047, 1991.

[113] H. Le-Huy, K. Slimani, and P. Viarouge. A current-controlled quasi-resonant converter for switched-reluctance motor. *IEEE Transactions on Industrial Electronics*, 38(5):355–362, 1991.

[114] T. Uematsu and R.G. Hoft. Resonant power electronic control of switched reluctance motor for electric vehicle propulsion. *Proceedings of PESC'95*, pages 264–269, 1995. Atlanta.

[115] R.W. De Doncker and J.P. Lyons. The auxiliary resonant commutated pole converter. *IEEE-IAS Conference Records*, pages 1228–1235, 1990.

[116] D.M. Divan, L. Malesani, P. Tenti, and V. Toigo. A synchronized resonant dc link converter for soft-switched pwm. *IEEE Transactions on Industry Applications*, 29(5):940–947, 1993.